Heterogene integratie van InAs/GaAs-kwantumdotlasers op siliciumfotonica

Heterogeneous Integration of InAs/GaAs Quantum Dot Lasers on Silicon Photonics

Sarah Uvin

Promotoren: prof. dr. ir. G. Roelkens, prof. dr. ir. D. Van Thourhout
Proefschrift ingediend tot het behalen van de graad van
Doctor in de ingenieurswetenschappen: fotonica

UNIVERSITEIT
GENT

Vakgroep Informatietechnologie
Voorzitter: prof. dr. ir. B. Dhoedt
Faculteit Ingenieurswetenschappen en Architectuur
Academiejaar 2019 - 2020

ISBN 978-94-6355-390-2
NUR 959
Wettelijk depot: D/2020/10.500/67

UNIVERSITEIT
GENT

Promotoren:
Prof. Dr. Ir. Günther Roelkens
Prof. Dr. Ir. Dries Van Thourhout

Examencommissie:

Prof. Dr. Ir. H. Van Landeghem (voorzitter)	Universiteit Gent
Prof. Dr. Ir. G. Roelkens (promotor)	Universiteit Gent
Prof. Dr. Ir. D. Van Thourhout (promotor)	Universiteit Gent
Prof. Dr. E. Bente	Technische Universiteit Eindhoven
Prof. Dr. Ir. Z. Hens	Universiteit Gent
Prof. Dr. Ir. B. Kuyken	Universiteit Gent
Dr. Ir. P. Ossieur	Universiteit Gent

Universiteit Gent
Faculteit Ingenieurswetenschappen en Architectuur

Vakgroep Informatietechnologie
Photonic Research Group
Technologiepark-Zwijnaarde 126 iGent, 9052 Gent, België

Tel.: +32-9-264 3316
Fax.: +32-9-264 3593

Dit werk kwam tot stand in het kader van een IWT doctoraatsbeurs voor strategisch basisonderzoek.

Dankwoord

9 januari 2013: tweede master in de fotonica, eerste deel mondeling examen nonlinear optics. Aanwezig: Sarah Uvin en Günther Roelkens. Nog op de planning: deel twee van het mondeling examen bij Roel Baets. Gemoedstoestand: zenuwen strak gespannen. Deze situatie kan beschouwd worden als de start van mijn doctoraat. Midden in het examen vraagt Günther, toen nog professor Roelkens voor mij, of ik geen zin heb om een doctoraat te komen doen rond lasers. Compleet overrompeld en met een brein in examenmodus is mijn eerste antwoord dat ik daar helemaal niet slim genoeg voor ben. Ik geef toe, niet de beste respons op een jobaanbieding. Inwendig roep ik al mijn gezond verstand bijeen en de conversatie eindigt zeker beter dan hij gestart is. Negen maanden later start ik als doctoraatsstudent in de Photonics Research Group.

Wat volgt zijn intense, drukke, plezante en waanzinnige jaren. Er worden honderden lasers gemaakt en ook twee kinderen. Er worden papers geschreven en een huis gekocht. Onderzoeksprojecten worden opgestart en kindertranen gedroogd. Kortom er wordt geleefd.

20 juni 2020, 2u53. Buiten is het donker en hierbinnen is het rustig. Een zeldzame sensatie in deze Corona-tijden, maar momenteel liggen al mijn huisgenoten vredig te slapen in hun eigen bed. Ik heb zonet de laatste punten en komma's in dit werk op hun plaats gezet en nu rest mij nog slechts 1 taak: iedereen bedanken. Ik heb de voorbije jaren veel dankwoorden gelezen en ze bestaan in alle vormen en maten. Je hebt de kort en bondige, maar ook de lange die een hoofdstuk op zichzelf vormen. Sommige zijn zakelijk, andere emotioneel, sommige grappig, andere droog. Dit dankwoord weet nog niet zo goed wat het zal worden: misschien het ”vermoeid-maar-opgeluchte” dankwoord of het “blijf-in-uw-kot” dankwoord. Enfin, ik zal er maar aan beginnen.

Onderzoek doe je niet alleen. Ik heb het geluk terecht te komen in de Photonics Research Group: een warme groep, waar mensen ambitieus zijn, maar minstens even hard supporteren voor hun collega's. Een groep waar altijd iemand je wil helpen of het nu gaat over het opstarten van een simulatie, het bouwen van een meetset-up of het leggen van elektriciteit in je huis (dankjewel Bart). Een groep waar mensen naar elkaar luisteren, zelfs als je je jonge, kinderloze, overwegend mannelijke collega's uitleg geeft over het nut van borstvoeding.

Daarom wil ik eerst en vooral de man bedanken met wie het allemaal begonnen is, het kloppend hart van onze groep: professor Roel Baets. Roel, jouw passie en enthousiasme hebben mij in de derde bachelor elektrotechniek overtuigd om te kiezen voor een master in de fotonica. Met bezieling leer jij jouw studenten over fotonica en in het bijzonder silicon photonics. Ik ben nog altijd ongelooflijk blij dat ik in dat derde jaar les van jou gekregen heb, het heeft mijn leven voorgoed veranderd.

Tijdens mijn doctoraat word ik begeleid door twee fantastische promotoren: Günther en Dries. Dat onderzoek niet altijd in een rechte lijn naar resultaten leidt, is niet onverwacht. Maar soms voelt het alsof je van de ene put in de andere sukkelt en de weg nooit een keertje gewoon recht wil lopen. Op zo'n moment was een meeting met jullie voldoende om er weer 200% voor te gaan. Jullie vonden altijd wel een nieuwe piste om te verkennen, of een nieuw onderzoeksproject om de gedachten mee te verzetten. Verder wil ik jullie ook nog bedanken voor de welgemeende proficiat toen ik niet een maar twee keer een zwangerschap kwam aankondigen tijdens mijn onderzoek. Ik kan het iedereen aanraden.

Ik wil ook graag de andere professoren in onze groep bedanken. Bart, Geert, Nicolas, Peter, Stephane en Wim het was een plezier om met jullie samen te werken.

Met zo'n lange lijst van professoren, kan het niet anders dan dat er een nog veel uitgebreider gezelschap van (post-)doctoraatstudenten rond loopt. Met het risico om mensen te vergeten, probeer ik jullie zo goed mogelijk te bedanken.

Over the years I shared my office with a lot of different people from all over the world. Yanlu, Nannicha, Pauline, Andrea, Jeroen, Sanja, Andrew, Yuting, Nayyera, Joan, Stijn, Chao, Zhongtao, Hendrik and Laurens (a very recent and thus only virtual office mate) it was a pleasure to work with all of you. Stijn, veel succes met de verbouwingen, hopelijk gaat het iets sneller vooruit dan bij ons...

Graag bedank ik ook mijn III-V- en transfer-printcollega's. *There are very few people who know how it feels to spend weeks in cleanroom hoping to produce the hero-laser, only to have it fail at the last metallization step, so I cherish you. Grigorij, I wish I would possess only half of your language skills. Javad, thank you for your kindness, it was always a pleasure talking to you. Jing, whenever I feel overwhelmed by my workload, I only have to look at you and I get the strength to keep going.* Kasper, de afgelopen jaren was jij zeer dikwijls mijn klankbord of het nu ging over het uitmeten van een mode-locked laser of de organisatie van de meetkamer. Bedankt voor al dat luisteren, ik heb veel van je geleerd. *Sulakshna, you are one of the most skilled cleanroom specialists that I have ever met. I am very happy that you were in team GaAs with me.* Meer recent werd het team GaAs uitgebreid met Jeroen, naast een excellente onderzoeker ook een zeer aangenaam gesprekspartner, het laatste van deze man hebben we nog niet gezien. Lange tijd bezig met obscure niet-lineaire materialen, maar recent overgekomen naar de

III-V-zijde is Artur. Ik ben nog steeds onder de indruk van de professionaliteit waarmee je je eerste III-V chip hebt ontworpen en gemaakt in de cleanroom, maar zeer weinigen zouden je dat na doen. *Bahawal is part of team DFB laser. Thank you for your valuable input.* Camiel, bedankt om aan te tonen dat het toch een goed idee was om III-V-a-Si-SiN couplers te maken. Aangezien transfer-printen hen nauw aan het hart ligt zorgen Gunther en Bart voor een gestage toestroom aan nieuwe studenten om het team te versterken: Tom, Dennis, Emad en Stijn, ik ben er zeker van dat jullie de nobele kunst van het transfer-printen in ere zullen houden.

Al laat bovenstaande opsomming misschien het tegendeel vermoeden, de Photonics Research Group is veel meer dan alleen transfer-printen. De meest uiteenlopende onderwerpen worden bestudeerd en onderzocht. Voor verdere uitleg hierover verwijs ik u graag door naar de website. Graag wil ik hier de bijhorende onderzoekers bedanken voor de voorbije jaren. *Clemens, Alex, Irfan, Mattias and Kristof: you had the most unexpected, weird and exotic conversations during lunch. It was a pleasure (and I will forward you the bill of my therapist).* Isaac, als je app ooit afgeraakt wil ik hem nog altijd graag eens testen. Ivo, succes met de verbouwing en bedankt voor het feedback-dag-idee. Anton, wij begrijpen elkaar. Pieter, samen met jou maakte ik mijn eerste laser(-cake), het is mij nooit meer gelukt om ze zo lekker te maken. *Antonio, we will meet again.* Suzanne, niemand beter om mee naar Japan te gaan. Ik hoop dat we onze woensdag-lunch-dates snel weer kunnen hervatten. Daan, bestaat er zoiets als een mannelijke hartsvriendin? Ik kijk er naar uit om met jou het leven te bespreken.

Een onderzoeksgroep zou nergens staan zonder zijn technische en administratieve staf. Voor de cleanroom hebben we eerst en vooral Steven. Bedankt voor de excellente samenwerking toen mijn zwangere buik en ik niet langer binnen mochten. Verder was jij het ook die me op het spoor bracht van het meest verschrikkelijke etchant KI:I2:DI. Het bracht me een heleboel kopzorgen, miserie en werkende lasers, waarvoor dank. Liesbet, ik moet toegeven dat het vooruitzicht van een babbel met jou aan de SEM, minstens even aanlokkelijk was als het bekijken van mijn chips. Bedankt hiervoor, ik zal er altijd met een warm gevoel aan terug denken. *Muhammad, thank you for delivering excellent e-beam samples.* Vaste waarde in de meetkamers is dan weer Michael, bedankt voor het vakkundig aan de praat krijgen van elk meetscript. Voor praktische meetproblemen kon ik achtereenvolgens terecht bij Jeroen, Jelle en Jasper. Ik wil allen bedanken voor de vlotte samenwerking. Jasper, het was altijd een plezier om met jou te babbelen en ik hoop dat we ondanks al de Corona-regels nog eens de kans gaan krijgen om samen te eten. Kristien, bedankt voor alle goede zorgen tijdens mijn doctoraat. Jij hebt nog een hele dikke knuffel te goed. Ilse en Ilse, het was een plezier om jullie aan mijn zijde te hebben bij het verzenden van pakjes en het uitgeven van projectbudgetten. Doen jullie toevallig ook belastingbrieven?

Alles begint en eindigt met familie. Zonder familie was ik waarschijnlijk nooit aan dit doctoraat begonnen. Zonder familie was er nu geen boek, dat ik zo trots aan jullie mag voorstellen. Het laatste deel van dit dankwoord is dan ook voor jullie.

Wanneer een doctoraatsstudent zijn titel behaalt, kijk ik altijd naar de familie. Meestal stralen zij nog harder dan de kersverse doctor. Die blinkende gezichten maken mij altijd redeloos gelukkig. Helaas, steekt Corona er in mijn geval een stokje voor. Mama en papa, ik zal jullie niet kunnen zien die dag. Maar eigenlijk is dat niet erg, want ik weet dat jullie gaan stralen en blinken voor mij. Jullie zijn mijn grootste supporters en die liefde en dat vertrouwen geeft mij al heel mijn leven vleugels om het leven zo goed mogelijk te leven. Ik zie jullie ongelooflijk graag, zonder jullie was dit alles nooit mogelijk geweest. Ik ging hier nog zoveel schrijven over de liefde voor boeken, mama, die je ons allemaal en nu ook mijn kinderen zo mooi hebt voorgeleefd en doorgegeven. Papa, ik ging schrijven over alles wat ik van je geleerd heb aan de eettafel, in de eerste plaats dat je altijd moet kunnen lachen en zeker met jezelf. Maar dat zou bijna een boek op zichzelf vullen. Daarom nog juist dit: jullie zien mij graag, altijd en dat betekent alles voor mij. Dank jullie wel.

Verder heb ik ook nog twee fantastische zussen. Charlotte en Louise, als ze ooit geen dokters, juffen of ingenieurs meer nodig hebben, kunnen we nog altijd samen in de film-business gaan. Wij lopen elkaars deur dan misschien niet plat, als er iets is kan ik altijd op jullie rekenen. En dan nog dit: *"Hey, baby. There ain't no easy way out. Hey, I will stand my ground. And I won't back down"*.

Ik heb het ongelooflijke geluk om nog vier grootouders te hebben. Oma en Opa uit Belsele en Oma en Opa Aalst, ik mis jullie. Jullie zijn er nog. Natuurlijk wel. Maar ik had jullie er zo graag bij gehad op mijn publieke verdediging. Ik luister graag naar jullie verhalen, ik eet graag jullie krieken met frikandon/ballekes: bij jullie op bezoek komen, voelt altijd als thuis komen. Geen enkel leven is zonder zorgen, maar als ik oud kan worden zoals jullie, dan mag ik mezelf gelukkig prijzen.

Via mijn vriend kreeg ik er niet alleen een zeer gezellige, kleurrijke, warme en liefdevolle schoonfamilie bij, ook een prachtige verzameling dieren maakt nu deel uit van mijn leven. In de categorie dingen die ik niet had verwacht ooit te zullen doen in mijn leven: 's nachts opstaan om aanwezig te zijn bij de geboorte van een boerenpaard, midden in de nacht een ontsnapt varken helpen vangen terwijl bovengenoemde vriend ziek in bed ligt, een online meeting vroegtijdig verlaten omdat een paar paarden door de draad zijn gesprongen, honden herkennen op Whatsapp aan hun manier van spreken,… en zo kan ik nog wel even door gaan. Lieve families De Groote en Van Buggenhout, stuk voor stuk zijn jullie mooie mensen en ik ben blij jullie te kennen. En Dirk, het was inderdaad mooi geregeld.

En dan kom ik bij de drie mensen die hier op een paar meter van mij liggen te slapen. Andreas, zonder jou was hier nu geen boek geweest en dat mag je heel letterlijk nemen. "Stop met simuleren, schrijf het gewoon op." "Leg je jury vast." "Leg je interne verdediging vast. Dan moet het wel af." En hij weet waarover hij spreekt, die Andreas, aangezien hij zichzelf al een paar jaar Dr. Ir. Andreas De Groote mag noemen. Uiteraard heb ik soms gevloekt, zeker toen ik opeens midden in volle Corona-lockdown, dit boek moest afwerken omdat de interne verdediging al vast lag. Maar het is gelukt. Duizendmaal dank voor al jouw aanmoedigingen. Andreas is natuurlijk veel meer dan een Dr. Ir.. Hij is ook de man die kasten, winkeltjes en een Corona-proof bureau maakt uit hout. Hij is de man die mij terug kan laten lachen als het voelt of de hemel naar beneden is gekomen, zelfs als zijn rationele brein de oorzaak van deze val niet volledig kan bevatten. Hij is de man die er voor zorgt dat ons nieuwe huis van elektriciteit is voorzien en nog een paar dingen. Hij is de man die mij uitdaagt de beste versie van mezelf te zijn. Hij is de vader van mijn kinderen. We zijn al tien jaar een top team. Twee drukke jobs, twee jonge kinderen, een verbouwing: we doen het wel even. Of zoiets. Al zullen we binnenkort toch eens tien dagen (of eerder tien weken) na elkaar moeten slapen, denk ik.

Lieve Irma, vorig weekend werd je alweer vier jaar. Mijn kleine baby is veranderd in een enthousiaste kleuter, die sinds kort kan fietsen zonder zijwieltjes, laserchips maakt op haar doe-alsof-werk en dingen zegt als “August als je op een grote en zware planeet staat, dan word je zo plat als een pannenkoek.” August, jij wordt ook al bijna twee. Als we even niet kijken klim je bovenop een ladder, ren je zo snel je kan naar de andere kant van het grootwarenhuis of verdwijn je naar de buren op zoek naar een kraan of tractor. Irma en August, lasers maken is leuk, maar jullie zijn zonder twijfel het beste, mooiste, spannendste, ongelooflijkste,... wat ik ooit gemaakt heb. Ik ben zo blij dat ik jullie mama ben.

Ik zou graag een speciaal woord van dank richten tot Scipio, onze 3 maand oude puppy. Heel erg bedankt om de kabel van mijn laptop met rust te laten, terwijl je trouw naast mij lag tijdens het werken. Misschien dat we wel een nieuwe oplader voor je papa zullen moeten kopen ...

Aaigem, Juni 2020
Sarah Uvin

Table of Contents

List of acronyms

A

AOM	Acousto-optic modulator
ACPML	Anti-colliding pulse mode-locking
AR	Anti-Reflection

B

BCB	Benzocyclobutene
BHF	Buffered hydrofluoride
BOX	Buried oxide

C

CMOS	Complementary metal oxide semiconductor
CMP	Chemical mechanical polishing
CPML	Colliding pulse mode-locking
CW	Continuous wave

D

DBR	Distributed Bragg reflector
DI	Deionized water
DFB	Distributed feedback
DUT	Device under test
DVS-BCB	Divinyl Siloxane bis-Benzocyclobutene
DWELL	Dot-in-a-well

E

EDFA	Erbium-doped fiber amplifier
EME	Eigenmode expansion
ESA	Electrical spectrum analyzer

F

FDTD	Finite difference time domain
FIB	Focused ion beam

G

GSG	Ground-signal-ground

I

IC	Integrate circuit
ICP	Inductively coupled plasma
IPA	Iso-propyl alcohol

L

LED	Light-emitting diode

M

MLL	Mode-locked laser
MPW	Multi-project wafer

O

OFDM	Orthogonal frequency division multiplexing
OSA	Optical spectrum analyzer

P

PDMS	Polydimethylsiloxane
PECVD	Plasma enhanced chemical vapour deposition
PIC	Photonic integrated circuit

Q

QD	Quantum dot
QW	Quantum well

R

RBW	Resolution bandwidth
RF	Radio frequency
RIE	Reactive ion etcher
RPM	Rotations per minute

S

SA	Saturable absorber
SCH	Separate confinement heterostructure
SCPML	Self-colliding pulse mode-locking
SEM	Scanning electron microscope
SHG-AC	Second harmonic generation autocorrelator
SMF	Single mode fiber
SMSR	Side-mode suppression ratio
SOI	Silicon on insulator
SSC	Spotsize converter

T

TE	Transverse electric
TDM	Time division multiplexing
TLM	Transmission line measurement
TM	Transverse magnetic
TP	Transfer printing

W

WDM	Wavelength division multiplexing

Nederlandstalige samenvatting

In het huidige big data tijdperk kent de vraag naar meer bandbreedte een ongeziene groei. Deze evolutie noopt tot de ontwikkeling van hoog-performante zender-ontvangers die deze hoge bandbreedtes aankunnen zonder buitensporig veel energie te verbruiken. Silicium-fotonica ontpopt zich tot een zeer belangrijk platform voor de realisatie van efficiënte, optische hogesnelheidszender-ontvangers [1]. Echter, momenteel verhindert het gebrek aan een kosten-effectieve integratie van de lichtbron op de silicium chip, het uitrollen van fotonische geïntegreerde circuits (PIC) gebaseerd op silicium in de datacom- en telecom-sector. Om mee te doen als competitieve technologie is het belangrijk om on-chip lasers te ontwikkelen die kunnen werken bij hoge omgevingstemperaturen en bovendien efficiënt licht kunnen koppelen naar het silicium golfgeleider circuit [2].

Ten gevolge van de drie dimensionale beperking van ladingsdragers in quantum dots (QD) zijn InAs/GaAs QD lasers inherent meer stabiel bij schommelingen in de omgevingstemperatuur tussen 20°C en 100°C in vergelijking met quantum well (QW) lasers [3]. Bovendien is hun drempelstroom zeer laag [4] en door de manier waarop ze worden gegroeid, hebben ze een breed winstspectrum in vergelijking met conventionele QW lasers. Hierdoor zijn ze ook een excellente kandidaat voor het maken van multi-golflengte lasers.

De integratie van QD lasers op het silicium-fotonica platform kan een uitgesproken kostenvoordeel opleveren in vergelijking met andere optische technologieën. Silicium kan gebruik maken van de CMOS fabricage-infrastructuur en de bijhorende schaalvoordelen. Tevens zorgt een dichte integratie van laser en silicium chip voor een vermindering van de koppelingsverliezen en een daling van de verpakkingskosten die onlosmakelijk verbonden zijn met multi-chip oplossingen. Laserbronnen rechtstreeks integreren op silicium laat bovendien toe om de bandbreedte van zender-ontvangers op te schalen tot Terabits/s [5]. Er zijn verschillende manieren om lasers te integreren met silicium-fotonische circuits. Gebruikelijke integratieconcepten zijn hetero-epitaxy van III-V materialen, flip-chip bonding en wafer bonding. Onlangs is ook transfer-printen naar voren gekomen als een veelbelovende integratietechniek.

Dit werk beschrijft het ontwerp, de fabricage en de karakterisatie van InAs/-GaAs quantum dot lasers geïntegreerd op silicium. Ten eerste, werd een nieuw proces ontwikkelt om InAs/GaAs QD materiaal te integreren op SOI met behulp van DVS-BCB wafer bonding en vervolgens lasers te fabriceren. We hebben ook de mogelijkheid onderzocht van getransfer-printe InAs/GaAs QD lasers. Parallel hieraan is uitgebreid onderzoek gedaan naar verschillende koppelingsmechanismen om licht van het III-V te koppelen naar de silicium golfgeleider. Dit leidde tot ’s werelds eerste single-mode InAs/GaAs QD laser geïntegreerd op en gekoppeld naar een siliciumchip. Bovendien werd hetzelfde QD epitaxiale materiaal ook gebruikt om verschillende soorten InAs/GaAs quantum dot mode-locked lasers te fabriceren. Om deze lasers te ontwerpen, werden eerst InP QW mode-locked lasers bestudeerd en gekarakteriseerd.

1 Fabricatie van heterogeen geïntegreerde InAs/GaAs quantum dot lasers

Bij de start van dit onderzoek bestonden er nog geen InAs/GaAs quantum dot lasers op silicium die in staat waren om licht te koppelen vanuit de III-V mesa in de silicium golfgeleider. Onze eerste taak bestond er dan ook uit om een fabricageproces te ontwikkelen dat dit wel mogelijk maakte. Door gebruik te maken van de oriëntatie van de kristalvlakken van het InAs/GaAs QD epitaxiaal materiaal konden we de wanden van de laser mesa onder een bepaalde hoek weg etsen. Dit kan helpen om efficiënte koppelingsstructuren te maken. We onderzochten een heleboel chemische mengsels die konden dienst doen voor het nat etsproces vooraleer we tot het eindproces kwamen zoals hieronder beschreven.

Een doorsnede van de III-V-op-silicium mesa wordt weergegeven in figuur 1a. Onderaan zien we een geplanarizeerde SOI wafer die de silicium golfgeleiders en spiegelroosters bevat. Deze zijn 180 nm diep geëtst in een 400 nm dikke silicium laag. De actieve III-V laag bestaat uit n-GaAs bodem-contactlaag (150 nm dik), een n-$Al_{0.4}Ga_{0.6}As$ bodem-mantellaag (70 nm dik), 9 InAs QD lagen gescheiden door GaAs bufferlagen, met een totale dikte van 352 nm, een p-type $Al_{0.4}Ga_{0.6}As$ mantellaag (1.5 μm dik) en een p^{++}-GaAs top-contactlaag (300 nm dik). De opsluitingsfactor van de optische mode ligt rond de 8.9 % in de actieve quantum dot zone en rond de 7.5% in de p-AlGaAs laag. Het materiaal werd gegroeid door Innolume.

Om de lasers te fabriceren, wordt in een eerste stap de InAs/GaAs QD structuur (typisch een chip van 1 cm bij 1 cm) gelijmd op een geplanarizeerde SOI chip met behulp van ultradunne divinylsiloxaan-bisbenzocyclobuteen (DVS-BCB). Na de bonding verwijderen we het GaAs substraat. Het grootste deel van dit substraat wordt verwijderd doormiddel van nat etsen in een HNO_3:H_2O_2:H_2O mengsel. De laatste 50 μm wordt weggeëtst in het meer selectieve NH_4OH:H_2O_2.

De III-V mesa en de adiabatische taper worden vervolgens gedefinieerd door middel van nat etsen. De GaAs en InAs lagen worden geëtst in citroen zuur:H_2O_2 en de AlGaAs lagen in KI:I_2:H_2O. De etssnelheid van de p-AlGaAs laag in KI:I_2:H_2O wordt gelimiteerd door de reactiesnelheid. Dit zorgt voor scheve laserwanden, waarvan de hoek wordt bepaald door de oriëntatie van de kristalvlakken. We kunnen dit zien in het SEM beeld van een FIB doorsnede van de III-V mesa dat wordt getoond in figuur 1b. Op die manier kunnen we de tip van de III-V taper smaller maken ook al maken we gebruik van 300 nm UV contact lithografie. Vervolgens

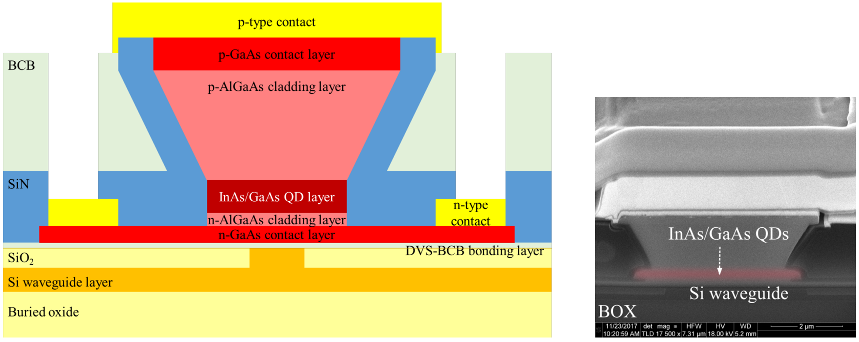

(a) (b)

Figuur 1: De InAs/GaAs QD-op-SOI laser mesa: (a) schematische doorsnede, (b) SEM beeld van een FIB doorsnede.

definiëren we het Ni/Ge/Au n-contact door middel van een lift-off proces. De lasers worden gepassiveerd met behulp van een 300 nm dikke SiN laag die wordt gedeponeerd met een PECVD. Daarna worden de structuren geplanarizeerd met DVS-BCB. In een volgende stap worden Ti/Au p-contacten gedeponeerd en de hele chip wordt in 30 seconden opgewarmd tot 430°C. Ten slotte vormen we via's en metalen probe pads.

2 Optische koppeling van III-V naar silicium

Licht koppelen vanuit een III-V mesa naar een silicium golfgeleider is verre van triviaal, zeker als we dit efficiënt willen doen, zonder licht terug te reflecteren, met een hoge tolerantie voor verkeerde uitlijning en zowel op geplanarizeerd SOI als in een put geëtst in een full platform silicium chip. Daarom hebben we in het kader van dit onderzoek verschillende koppelingsstructuren ontworpen, gesimuleerd en getest.

De traditionele dubbele adiabatische taper die wordt gebruikt in de meeste QW-op-SOI lasers heeft een uitstekende koppelingsefficiëntie. Deze structuur is dan ook zeer geschikt voor III-V-op-silicium lasers gemaakt via wafer bonding en wordt veelvuldig gebruikt doorheen dit werk. Helaas is ze zeer gevoelig aan slechte uitlijning. Dus voor III-V-op-silicium lasers gemaakt via transfer-printing met een uitlijningsprecisie van 1.0 μm (3 σ) is het nodig om de strutuur aan te passen om een goede koppelingsefficiëntie te behouden.

Een eerste kandidaat voor een meer tolerante koppelingsstructuur is de polymeer golfgeleider. In dit geval blijft de breedte van de III-V mesa onveranderd. Aan het einde van de mesa wordt een zeer brede polymeer golfgeleider gemaakt. Onder de polymeer golfgeleider bevindt zich een geïnverteerde taper gemaakt in het silicium. Deze taper trekt het licht naar beneden tot in de silicium golfgeleider. De grootste uitdaging bij deze structuur zit in het maken van ultra-propere en gladde laserfacetten. Tevens moet ook een goede anti-reflectie (AR) coating ontworpen worden om ongewenste reflecties tegen te gaan.

Een andere aanpak waarbij het niet nodig is om smalle tapers te etsen in de III-V mesa is de intracaviteit koppelaar. Via een silicium bocht onder de III-V mesa wordt een deel van het licht uitgekoppeld. Helaas is het met deze techniek niet mogelijk om single mode lasers te maken. Ondanks de voordelen verbonden aan deze structuur zoals een makkelijk fabricageproces, maakt eerder vermelde tekortkoming deze koppelaar ongeschikt voor de meeste toepassingen.

Wanneer we lasers willen integreren op een full platform silicium chip, moeten we rekening houden met de aanwezigheid van een micrometers dikke oxide-laag bovenop de silicium golfgeleiderlaag. Deze extra laag bevat onder andere de opwarmingselementen en de metaalbaantjes. Eerst wordt een opening gemaakt in deze back-end laag, zo kunnen de lasers vlakbij het silicium golfgeleider circuit geprint worden. Om opgewekte warmte vlot weg te kunnen leiden kan het een goed idee zijn om de lasers rechtstreeks bovenop het silicium substraat te plaatsen. In dat geval moet het licht vanuit het III-V gebuttkoppeld worden in een silicium golfgeleider. We hebben drie technieken bekeken om dit te doen: een geïnverteerde taper, een grote SiON golfgeleider en een drietandvormige structuur. Al deze structuren vertonen een vrij goede tolerantie ten opzichte van verkeerde uitlijning. Om een hoge koppelingsefficiëntie te bereiken is het wel uitermate belangrijk dat zowel het III-V facet als de verticale wand van de geëtste put glad en proper zijn.

Ten laatste bekeken we ook een koppelingsstructuur om licht vanuit het III-V te koppelen naar silicium nitride golfgeleiders. Aangezien silicium nitride golfgeleiders zeer lage optische verliezen hebben is dit voor veel toepassingen een zeer interessant platform. Echter, de lage brekingsindex van nitride zorgt er voor dat we geen gebruik kunnen maken van de traditionele dubbele adiabatische taper. Daarom hebben wij voorgesteld om een amorf silicium laag te gebruiken als overgang tussen het III-V en het silicium nitride. Simulaties beloofden efficiënte koppeling. Helaas was de fabricatie van dit type koppelaars zeer moeilijk.

Samenvattend is er geen enkele koppelingsstructuur die gelijktijdig voldoet aan alle eisen. Afhankelijk van de toepassing zal de ene of de andere structuur meer geschikt zijn.

3 InAs/GaAs quantum dot DFB lasers op silicium

Gebaseerd op de ontwikkelingen die hierboven werden beschreven, realiseerden we de allereerste single mode quantum dot DFB laser geïntegreerd op een silicium chip met efficiënte lichtkoppeling naar de silicium golfgeleider. Deze O-band laser produceert licht met een golflengte van 1300 nm of 1320 nm, afhankelijk van het ontwerp. De lasers werken continu tot en met de hoge omgevingstemperatuur van 100°C. De gemeten drempelstroomdichtheid is laag (353 A/cm^2) en de laser is single mode met een 40 dB onderdrukking van zijmodes. Deze lasers zijn dan ook geschikte kandidaten voor ongekoelde optische zender-ontvangers in datacenters.

Het ontwerp van de DFB laser wordt getoond in figuur 2a. De lasercaviteit bestaat uit een DFB rooster, gemaakt in de silicium-golfgeleider-laag, met daar bovenop een InAs/GaAs QD versterker geïntegreerd. De III-V sectie is 1000 μm lang (exclusief de 215 μm-lange adiabatische tapers aan weerskanten). De laser heeft tweede orde spiegelroosters met een periode van 400 nm, dit komt overeen met een Bragg golflengte van 1320 nm. De opsluitingsfactor van de optische mode in de actieve quantum dot zone ligt rond de 8.9 %. De koppeling van het laserlicht vanuit de hybride winstzone naar de silicium golfgeleiders gebeurt met behulp van een 215 μm-lange dubbele adiabatische taper. De III-V taper is stuksgewijs lineair en versmalt eerst snel (L = 35 μm) van een 3.7 μm brede mesa tot een 1.7 μm brede mesa. Vervolgens is er een tweede trage taper (L = 180 μm) waarbij het III-V nog verder versmalt terwijl de onderliggende silicium golfgeleider geleidelijkaan breder wordt.

Een doorsnede van de III-V-op-silicium golfgeleider wordt getoond in figuur 2b. Onderaan zien we een geplanarizeerde SOI wafer die de silicium golfgeleiders en spiegelroosters bevat. Deze zijn 180 nm diep geëtst in een 400 nm dikke silicium laag. De InAs/GaAs QD epitaxiale laag is hierop gelijmd met behulp van een 60 nm-dikke divinylsiloxaan-bisbenzocyclobuteen (DVS-BCB) bondingslaag.

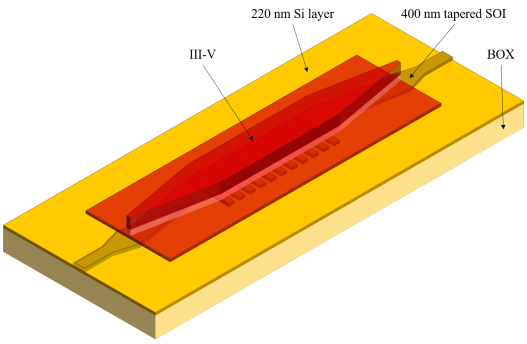

(a) 3D tekening van de III-V-op-silicium DFB laser

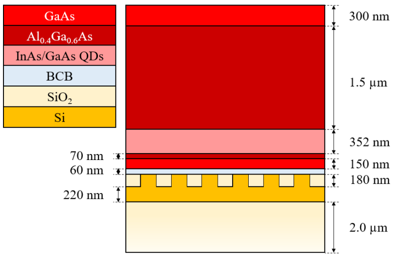

(b) Doorsnede van de laserstructuur

Figuur 2: Ontwerp van een III-V/Si verdeelde terugkoppeling (DFB)-laser.

De continue golf (CW) licht-stroom (LI) curve van de DFB laser wordt getoond in figuur 3a in functie van de temperatuur. De laser blijft werken tot een temperatuur van 100°C. Bij kamertemperatuur meten we uitgangsvermogens tot 2.5 mW in de golfgeleider. De CW drempelstroom als functie van de omgevingstemperatuur is geplot in figuur 3b. De laagst gemeten drempelstroom van 19 mA wordt bereikt bij 50°C omdat het winstspectrum en het roosterspectrum dan perfect op elkaar zijn afgestemd. Dit komt overeen met een drempelstroomdichtheid van 353 A/cm^2.

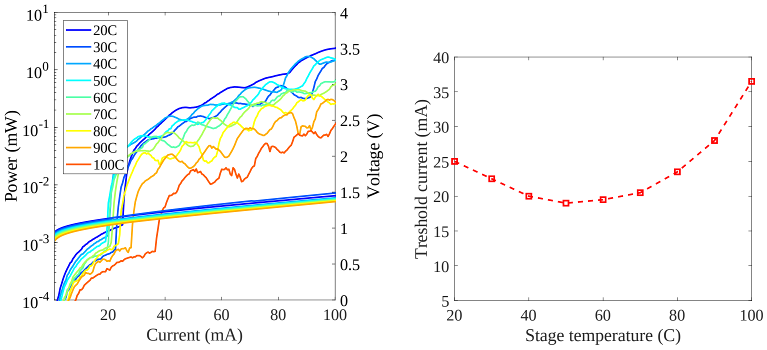

(a) **(b)**

Figuur 3: (a) LIV curve als een functie van de temperatuur. We tonen het optisch vermogen in de golfgeleider. (b) Drempelstroom als functie van de omgevingstemperatuur.

Het optisch spectrum bij een aandrijfstroom van 50 mA is weergegeven in figuur 4a voor verschillende temperaturen. Bij een temperatuur van 20°C werkt de laser rond 1321 nm. Met stijgende temperatuur schuift de lasergolflengte op naar langere golflengtes met een temperatuurscoëfficiënt van 0.1 nm/°C. De laser werkt single mode en heeft een zijmode onderdrukking van 40 dB. In figuur 4b wordt het optisch laserspectrum getoond bij kamertemperatuur voor verschillende aandrijfstromen. Wanneer de aandrijfstroom toeneemt verschijnen er op een bepaald moment hogere orde modes (bijvoorbeeld vanaf 90 mA bij 20°C). Dit wordt veroorzaakt door laterale hogere orde modes die aanwezig zijn in de lasercaviteit.

In de lasers die we hierboven hebben beschreven werken de III-V tapers niet optimaal. Dit veroorzaakt extra reflecties, extra verliezen en maakt het mogelijk voor hogere orde modes om uit te koppelen. We hebben de tapers proberen verbeteren door ze verder te vernauwen. Helaas zorgde dit ervoor dat meer en meer tapers stopten met werken als gevolg van defecten in het III-V materiaal. De laserwerking verbeteren zal dan ook hand in hand gaan met het verbeteren van het epitaxiaal materiaal.

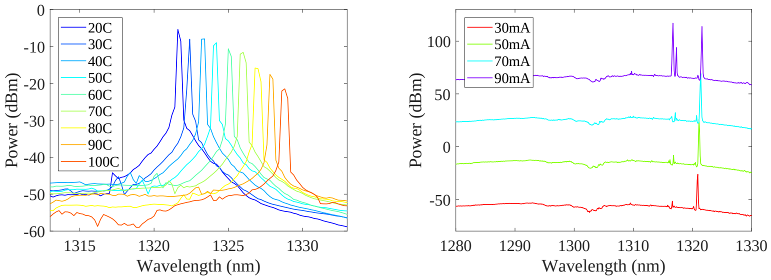

(a) **(b)**

Figuur 4: (a) Optisch spectrum als functie van de temperatuur voor een aandrijfstroom van 50 mA. (b) Optisch spectrum bij kamertemperatuur voor verschillende aandrijfstromen. De verschillende spectra zijn 40 dB uit elkaar geschoven voor de duidelijkheid.

4 Mode-locked lasers geïntegreerd op silicium

Om de beschikbare bandbreedte van een optische glasvezel maximaal te benutten is het uitermate belangrijk dat de optische zender-ontvangers in het systeem een goede spectrale efficiëntie hebben. Om hieraan te voldoen zijn lasers die meerdere golflengtes tegelijk kunnen genereren noodzakelijk. De mode-locked laser (MLL) genereert een frequentiekam bestaande uit verschillende longitudinale modes. De afstand tussen de modes wordt bepaald door de lengte van de laser. Bovendien zijn de fases van de verschillende modes aan elkaar gelinkt. Dit maakt de MLL tot een ideale kandidaat om het bandbreedte-probleem op te lossen. Het is reeds aangetoond dat (gestabiliseerde) glasvezel-gebaseerde mode-locked lasers kunnen dienen voor het genereren van een frequentiekam. Maar door hun lange lasercaviteit hebben deze lasers typisch een lage herhalingsfrequentie, waardoor de verschillende longitudinale modes te dicht bij elkaar staan om te kunnen dienen voor optische communicatie [6]. Door een MLL te integreren op een optische chip kan dit probleem worden opgelost. Hieraan zijn nog enkele extra voordelen verbonden: de on-chip MLL kan in grotere volumes geproduceerd worden en heeft een lager vermogensverbruik. Integreren we de MLL bovendien op een silicium platform, dan kunnen we gebruik maken van de laag-verlies silicium optische golfgeleiders om de lasercaviteit te vormen. Dit leidt tot betere werking van de laser.

In het kader van dit werk hebben we verschillende types MLLs ontworpen, gefabriceerd en uitgemeten. Een overzicht is weergegeven in figuur 5. Een lineaire MLL met een colliding pulse configuratie wordt getoond in figuur 5a. De laserstructuur bestaat uit een saturable absorber (SA) die in het midden van de lasercaviteit is geplaatst omgeven door twee halfgeleider optische versterkers. Twee pulsen circuleren in tegengestelde zin in de caviteit en komen elkaar enkel tegen in de SA. Dit leidt tot een verdubbeling van de herhalingsfrequentie of dus een

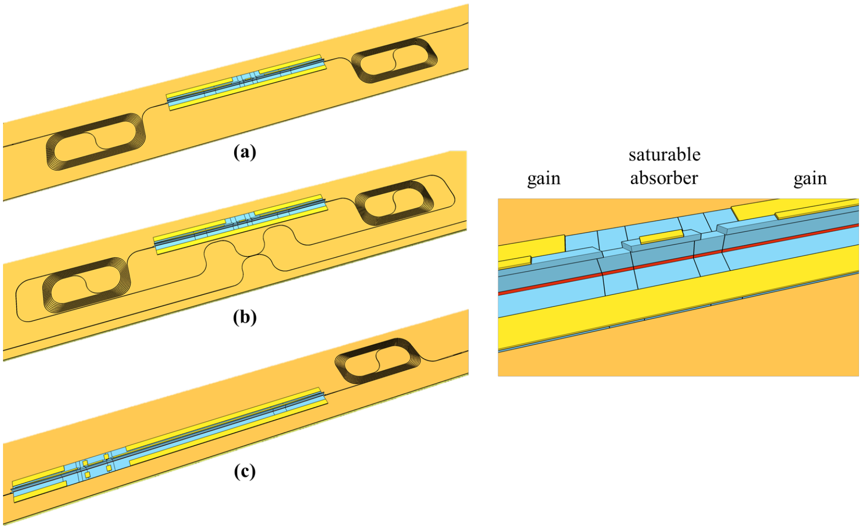

Figuur 5: Afbeelding van (a) een lineaire caviteit colliding pulse mode-locked laser, (b) een ring mode-locked laser en (c) een anti-colliding mode-locked laser.

halvering van de puls periode. Een gevolg van dit ontwerp is een hoge gevoeligheid van de laser voor de positie van de SA. Als de symmetrie niet perfect is, kan de harmonische mode-locking falen waardoor signalen verschijnen op de helft van de herhalingsfrequentie. In figuur 5b wordt een ring MLL weergegeven. Opnieuw propageren twee pulsen in de lasercaviteit in tegengestelde zin die elkaar enkel tegenkomen in de SA. Maar deze keer koppelt elke puls uit naar een andere uitgangsgolfgeleider. Hierdoor kan de frequentie niet verdubbelen en is de laser minder gevoelig aan de exacte positie van de SA. Figuur 5c is een tekening van een anti-colliding MLL. In dit geval wordt de SA geplaatst op de spiegel met de grootste verliezen. Dit leidt tot een toename van het uitgangsvermogen en een afname van de amplitude- en tijdsjitter.

Eerst en vooral hebben we het gedrag van verschillende 1550 nm InP quantum well mode-locked laser uitgemeten en geanalyseerd. We demonstreerden een 4.7 GHz lineaire MLL met een 36 kHZ 10 dB RF lijnbreedte en een 1.5 ps puls, een 4.7 GHz ring MLL met een 49 kHZ 10 dB RF lijnbreedte en een 4.83 GHz anti-colliding MLL met een 5 kHZ 10 dB RF lijnbreedte en een 3 ps puls. Om te voldoen aan de strenge eisen voor terabit per seconde coherente communicatie systemen wat betreft optische en elektrische lijnbreedte, onderzochten we ook hybride locking technieken en locking als gevolg van optische injectie. We konden aantonen dat optische injectie-locking leidt tot reductie van de 3 dB optische lijnbreedte van enkele MHz tot 50 kHz. In een experiment konden we aantonen dat, met een continu optisch injectie vermogen van slechts 0.1 mW, meer dan 50 longitudinale modes coherent gelocked waren aan de injectielaser en elkaar.

Gebaseerd op onze kennis van de InP quantum well lasers, onderzochten we vervolgens het potentieel van InAs/GaAs QD mode-locked lasers geïntegreerd op een silicium fotonisch platform. We hebben zowel lineaire als ring mode-locked lasers ontworpen, gefabriceerd en uitgemeten. We maakten een 18.8 GHz lineaire MLL met een 623 kHZ 3 dB RF lijnbreedte en een 20.3 GHz ring MLL met een 3 kHZ 3 dB RF lijnbreedte. Helaas was de optische 10 dB bandbreedte teleurstellend nauw. Beide structuren haalden niet meer dan een 3 nm bandbreedte ondanks het gebruik van quantum dots als actief materiaal. Waarom dit gebeurt, kunnen we momenteel niet volledig verklaren. Zeker is dat verdere optimalisatie van de verschillende laserparameters moet worden uitgevoerd en dat verder onderzoek naar deze lasers noodzakelijk is.

Referenties

[1] David AB Miller. *Rationale and challenges for optical interconnects to electronic chips*. Proceedings of the IEEE, 88(6):728–749, 2000.

[2] Zhiping Zhou, Bing Yin, and Jurgen Michel. *On-chip light sources for silicon photonics*. Light: Science & Applications, 4(11):e358, 2015.

[3] Mitsuru Sugawara and Michael Usami. *Quantum dot devices: Handling the heat*. Nature Photonics, 3(1):30–31, 2009.

[4] HY Liu, DT Childs, TJ Badcock, KM Groom, IR Sellers, M Hopkinson, RA Hogg, DJ Robbins, DJ Mowbray, and MS Skolnick. *High-performance three-layer 1.3-μm InAs-GaAs quantum-dot lasers with very low continuous-wave room-temperature threshold currents*. Photonics Technology Letters, IEEE, 17(6):1139–1141, 2005.

[5] Di Liang, Geza Kurczveil, Xue Huang, Chong Zhang, Sudharsanan Srinivasan, Zhihong Huang, M Ashkan Seyedi, Kate Norris, Marco Fiorentino, John E Bowers, and Raymond G Beausoleil. *Heterogeneous silicon light sources for datacom applications*. Optical Fiber Technology, 2017.

[6] Brian R Washburn, Scott A Diddams, Nathan R Newbury, Jeffrey W Nicholson, Man F Yan, and Carsten G Jrgensen. *Phase-locked, erbium-fiber-laser-based frequency comb in the near infrared*. Optics Letters, 29(3):250–252, 2004.

English summary

In the present Big Data era, the demand for higher bandwidths is increasing at an unprecedented pace. This trend requires high-performance interconnects that can sustain this high bandwidth without consuming exorbitant amounts of energy. Silicon photonics is emerging as an important platform for the realization of power-efficient, high-speed optical transceivers [1]. However, currently the lack of cost-effective integration of the light source limits silicon-based photonic integrated circuits (PIC) deployment in these fields. In order to become a competitive technology, on-chip lasers operating at high ambient temperature and with low-loss coupling to the silicon waveguide circuits are very important [2].

Due to the three dimensional confinement of carriers, InAs/GaAs quantum dot (QD) lasers inherently have a more stable performance over the 20°C-100°C temperature range compared to quantum well (QW) lasers [3]. Furthermore, they can achieve very low threshold current densities [4] and because of the way QDs are grown they have a wider gain spectrum compared to conventional QW lasers making this material system an excellent candidate for creating multi-wavelength transmitters.

The integration of QD lasers directly on the silicon photonics platform, leveraging the well-developed CMOS fabrication infrastructure and its economies of scale, can provide a distinct cost advantage over other optical technologies. At the same time it would reduce coupling losses and packaging costs inherent in multi-chip solutions. Furthermore, the integration of the laser source directly on silicon enables the scaling of the aggregate bandwidth of transceivers to the Terabit/s range. [5] There are multiple ways to integrate lasers with silicon photonic circuits. Typical integration schemes include hetero-epitaxy of III-V materials, flip-chip bonding and wafer bonding. Recently, also transfer-printing has emerged as a very promising integration technique.

This dissertation describes the design, fabrication and characterization of InAs/-GaAs quantum dot lasers integrated on silicon. Firstly, a new process is developed in order to integrate and fabricate InAs/GaAs QD lasers on SOI by means of DVS-BCB assisted wafer bonding. We also explored the option of transfer-printed InAs/GaAs QD lasers. In parallel, extensive research has been carried out into various coupling mechanism to couple light from the III-V into the silicon waveguide. This has led to the world's first single mode InAs/GaAs QD laser integrated

on and coupling to a silicon chip. Furthermore, the same QD epitaxial layerstack was also used to fabricate various types of InAs/GaAs quantum dot mode-locked lasers. In order to design these lasers, first InP quantum well based mode-locked lasers were characterized thoroughly to get a better understanding.

1 Fabrication of heterogeneously integrated InAs/-GaAs quantum dot lasers

At the start of this work InAs/GaAs quantum dot material was never integrated onto a silicon chip with the ability to couple light from the III-V into the silicon waveguide. So first we developed a fabrication process to realize exactly this. We wanted to use the crystal orientation of the epi in order to get faceted surfaces in the mesa, since this can help to create good coupling structures. We investigated a lot of potential wet etchants before we got to the final process described hereunder.

A schematic cross-section of the III-V-on-silicon waveguide structure is depicted in figure 1a. The laser consists of a planarized SOI wafer containing the silicon waveguides and gratings defined in a 400 nm thick silicon waveguide layer using 193 nm deep UV lithography (180 nm etch depth) fabricated in a CMOS pilot-line at imec. The III-V active region consists of an n-GaAs bottom contact layer (150 nm thick), an n-$Al_{0.4}Ga_{0.6}As$ bottom cladding layer (70 nm thick), 9 layers of InAs QDs separated by GaAs buffer layers, with a total thickness of 352 nm, a p-type $Al_{0.4}Ga_{0.6}As$ cladding layer (1.5 μm thick) and a p^{++}-GaAs top contact layer (300 nm thick). The confinement factor of the optical mode is 8.9% in the quantum dot layers and 7.5% in the p-AlGaAs layer. The epitaxial layer stack was grown by Innolume.

To fabricate the lasers, the InAs/GaAs QD epitaxial structure (typically a 1 cm by 1 cm die) is bonded to the planarized SOI using ultra-thin DVS-BCB adhesive bonding. After bonding, the GaAs substrate is removed. The major part of the GaAs substrate is removed by wet etching in HNO_3:H_2O_2:H_2O. The last 50 μm of the substrate is etched using more selective NH_4OH:H_2O_2.

The III-V mesa and spotsize converter are defined through wet etching, using citric acid:H_2O_2 and KI:I_2:H_2O for the GaAs/InAs and AlGaAs layers, respectively. The reaction rate limited wet etching of the p-AlGaAs cladding layer in KI:I_2:H_2O results in a faceted surface structure dependent on the crystal orientation. Therefore, the lasers should be parallel to the $[0\bar{1}\bar{1}]$ crystal plane of the GaAs wafer. This is illustrated in a scanning electron microscope (SEM) picture of a focused ion beam (FIB) cross-section of the III-V mesa shown in figure 1b. This allows creating undercut structures in the spot-size converter, which relaxes the lithography requirements in the definition of the III-V spotsize converter, which was realized using 300 nm UV contact lithography. Next, the Ni/Ge/Au n-contact was defined through a lift-off process. The devices were passivated using a 300 nm-thick silicon nitride layer deposited by plasma-enhanced chemical vapor deposition (PECVD). The lasers were then planarized with DVS-BCB. Thereafter

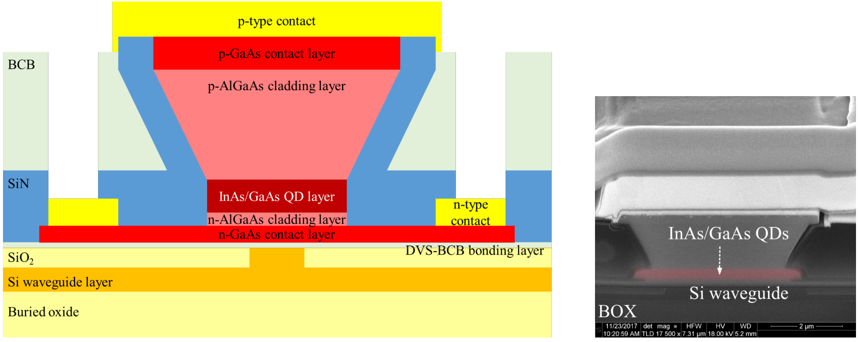

(a) **(b)**

Figure 1: The InAs/GaAs QD-on-SOI laser mesa: (a) schematic cross-section, (b) SEM picture of a FIB cross-section.

Ti/Au p-contacts were deposited on the p-GaAs contact layer and annealed at 430°C for 30 seconds. Finally vias were formed and probe pad metal was deposited in a ground-signal-ground (GSG) configuration.

2 Optical coupling schemes

Coupling light from the III-V mesa into a silicon waveguide is not trivial, especially if this needs to be done efficient, without back-reflections, with a high tolerance towards misalignment and both on planarized SOI and in the trench of a full platform silicon chip. Therefore we designed, simulated and tested several coupling structures.

The traditional spotsize converter used in many QW-on-SOI lasers has excellent coupling efficiency, but is very sensitive for misalignment. Therefore this structure is well suited for wafer bonded lasers and we used it throughout this work. But for lasers that are transfer-printed with a alignment accuracy of 1.5 μm (3 σ) the spotsize converter needs to be adapted to keep up its performance.

A first option for a more alignment tolerant coupler is the use of a polymer waveguide. The width of the III-V mesa is fixed and at the end a very wide polymer waveguide is attached. Underneath the polymer an inverted taper made in the silicon pulls all the light down into the silicon waveguide. Most challenging here is the need for clean lasing facets and a good anti-reflection (AR) coating to avoid back-reflections that may hamper good laser working.

Another approach that doesn't require narrow tapers to be etched in the III-V mesa, is the intracavity coupler. A silicon bend underneath the III-V mesa couples out some of the light. Unfortunately this technique doesn't allow us to make single mode lasers. So although this coupling mechanism has a lot of advantages like easy processing, this shortcoming makes it unsuitable for most applications.

When we want to integrate a laser on a full silicon platform, we have to take into account the back-end stack that contains the heaters and all metal. A trench is opened in this back-end so the laser can be printed close to the silicon waveguide circuits. For good heat-sinking, printing the laser directly onto the silicon substrate is a good idea. Then we need butt-coupling from the III-V into the silicon waveguide circuit. We explored three different techniques: an inverted taper, a big SiON waveguide and a trident-like structure. All show decent misalignment tolerance. However, in order to have a good coupling efficiency, it is important that both the III-V facet and the vertical facet of the etched well are smooth and clean.

Finally, we also researched coupling of light from III-V into silicon nitride waveguides. Due to the very low losses of silicon nitride waveguides, this is also a promising material platform. But the low refractive index of nitride prevents the use of a traditional spotsize converter. We proposed to use an amorphous silicon layer as an intermediate between the III-V and nitride. In simulation the coupling efficiency was promising, however the fabrication proved to be quite a challenge.

In the end there is no one coupling technology that fits all and depending on the application one or the other will be the better choice.

3 InAs/GaAs quantum dot DFB lasers on silicon

Based on the developments described above, we demonstrated the first single mode quantum dot DFB laser on a silicon substrate with efficient coupling of light to a silicon waveguide. We demonstrated high temperature operation with CW lasing up to 100°C. Threshold current densities as low as 353 A/cm^2 were measured. The laser showed single mode behavior with a side-mode suppression ratio of 40 dB. These devices are attractive candidates for uncooled WDM systems in data centers.

The device geometry of the DFB laser is shown in figure 2a. The laser cavity consists of a DFB grating defined in the silicon waveguide layer with the III–V gain region bonded on top. The III-V gain section is 1000 μm long (not including the 215 μm-long spotsize converters on each side). Second order DFB gratings were used with a grating period of 400 nm and a duty cycle of 70%, which corresponds with a Bragg wavelength of 1320 nm. The confinement factor of the optical mode in the quantum dot active region is around 8.9 %. A 215 μm-long tapered spotsize converter is used to couple the light from the hybrid gain section into the passive silicon waveguides. The III-V taper is a piecewise linear taper that quickly tapers (L = 35 μm) from a 3.7 μm mesa width to an 1.7 μm wide waveguide width after which a slower adiabatic taper (L = 180 μm) is implemented by tapering both the III-V and silicon waveguide structure.

A cross-sectional diagram of the III-V-on-silicon waveguide structure is depicted in figure 2b. It consists of a planarized SOI wafer containing the silicon waveguides and gratings defined in a 400 nm thick silicon waveguide layer using 193 nm deep UV lithography (180 nm etch depth). The GaAs quantum dot epitaxial layer stack is adhesively bonded to the planarized silicon-on-insulator (SOI) using a 60 nm-thick divinylsiloxane-bisbenzocyclobutene (DVS-BCB) bonding layer.

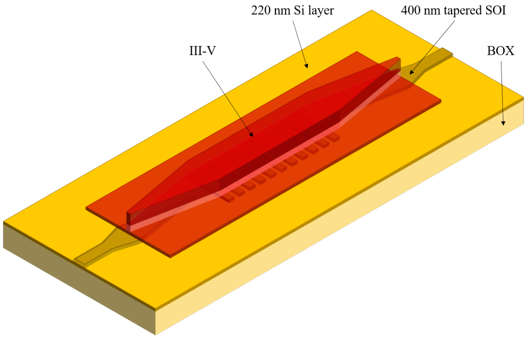

(a) 3D view of the III-V-on-silicon DFB laser

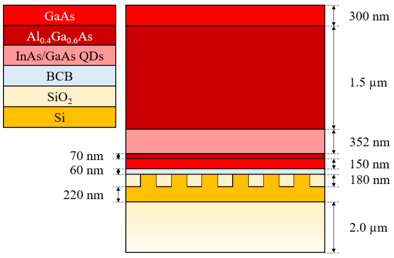

(b) Cross-sectional diagram of the laser structure

Figure 2: III-V/Si distributed feedback laser design.

The continuous wave (CW) light-current (LI) characteristic of the DFB laser is shown in figure 3a, as a function of temperature. Lasing is observed up to 100°C. We measure output powers up to 2.5 mW in the waveguide at room temperature. The CW threshold current as a function of stage temperature is shown in figure 3b. The lowest threshold current is 19 mA, reached at 50°C. This corresponds with a threshold current density of 353 A/cm^2.

The optical spectrum as a function of temperature for a drive current of 50 mA is plotted in figure 4a. Laser emission at 20°C is observed around 1321 nm. With increasing temperature the laser output wavelength shifts to longer wavelengths with a temperature coefficient of 0.1 nm/°C. We see single mode operation and a side-mode suppression ratio of 40 dB. figure 4b shows the optical spectrum as a function of drive current at room temperature. At higher drive currents (e.g. from 90 mA at 20°C) higher order modes appear. This is due to lateral higher order modes that exist in the laser mesa.

In the devices described above, suboptimal III-V tapers caused residual reflections, extra losses and the existence of higher order modes. We tried to improve the

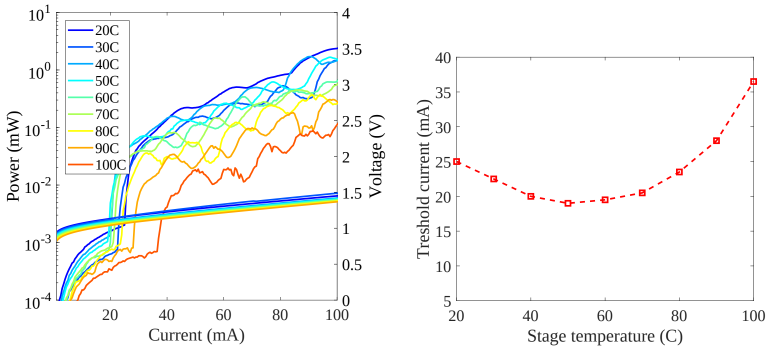

(a) **(b)**

Figure 3: (a) LIV curve as a function of temperature. The power in the waveguide is plotted. (b) Threshold current data as a function of stage temperature.

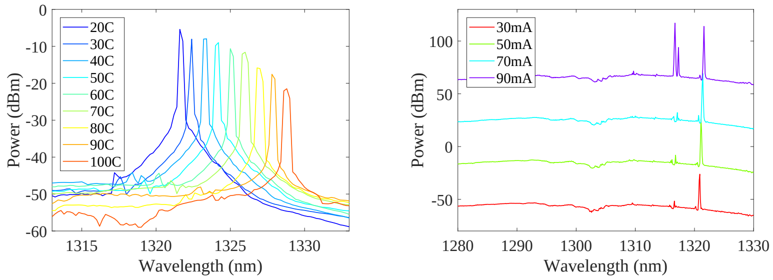

(a) **(b)**

Figure 4: (a) Optical spectrum for a drive current of 50 mA as a function of temperature. (b) Optical spectra for different drive currents at room temperature. The different spectra are shifted 40 dB apart for clarity.

tapers by making them narrower. However, when we make the tapers more narrow, more and more of them are taken out by defects in the III-V material. Improving the laser working will go hand in hand with improving the epitaxial material.

4 Mode-locked lasers integrated on silicon

In order to use the available optical fiber bandwidth effectively, the spectral efficiency of optical transceivers is of utmost importance. Therefore, there is a great need for multi-wavelength lasers. The frequency comb generated by a mode-locked laser, can be the perfect solution. Because of the mode-locking, the laser lines have inherently a distinct phase relation, while the frequency spacing is determined by the repetition rate of the laser. It has been shown that (stabilized) mode-locked fiber lasers can serve as a frequency comb source, however, these lasers have typically a low repetition rate (and hence too small frequency spacings for optical communication) because of the long laser cavity length [6]. Integrating mode-locked lasers on chip could overcome this problem, and has additionally a clear advantage in volume factor and power consumption. The integration of mode-locked lasers on a silicon photonics platform allows using low-loss silicon waveguide structures to form the laser cavity, which positively affects the laser performance.

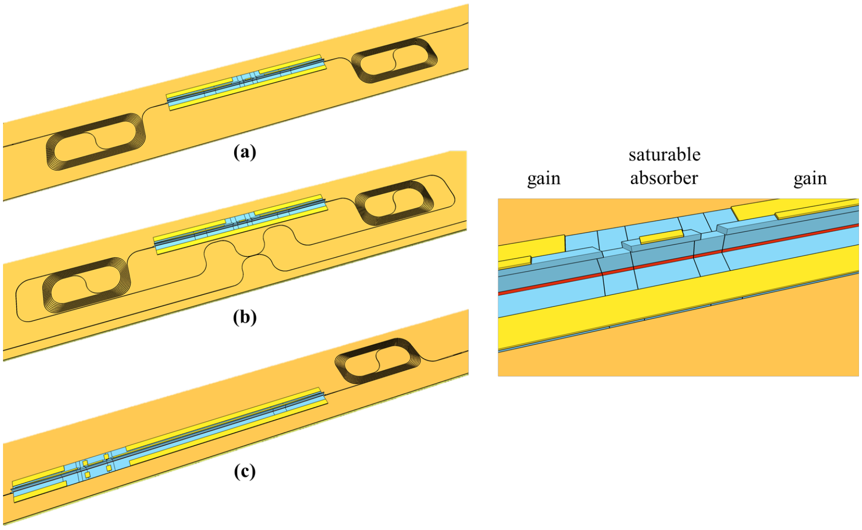

Figure 5: Illustration of (a) the linear cavity colliding pulse mode-locked laser, (b) the ring mode-locked laser and (c) the anti-colliding mode-locked laser.

In this work we designed, fabricated and characterized various types of mode-locked lasers as is shown in figure 5. A linear MLL realized in a colliding pulse configuration is shown in figure 5a. The structure of the laser comprises a saturable absorber (SA) section located in the middle of the resonator cavity between two semiconductor optical amplifier (SOA) sections. Two counter-propagating pulses circulate in the cavity and only interact in the saturable absorber. This leads to a doubling of the repetition frequency and thus a halving of the pulse period. Due to its geometry, this design is very sensitive to any mismatch in the saturable absorber position. When the symmetry is not perfect, the harmonic mode-locking can fail and tones at half the repetition frequency can appear. In figure 5b a ring mode-locked laser is depicted. Two pulses propagate in the ring cavity in opposite directions and collide in the SA. Since the two pulses couple to different output waveguides, the frequency is not doubled as is the case in linear colliding pulse configurations. This means that in the ring mode-locked laser no spurious tones appear when the SA is not placed exactly in the middle. Figure 5c shows a drawing of an anti-colliding pulse mode-locked laser. In this case the SA is placed next to the low reflectivity mirror. This leads to an increase in output power and a reduction in amplitude and timing jitter compared with the self-colliding pulse designs.

Firstly we characterized 1550 nm InP quantum well mode-locked lasers of the different types. We showed a 4.7 GHz linear MLL with a 36 kHZ 10 dB RF line width and a 1.5 ps pulse, a 4.7 GHz ring MLL with a 49 kHZ 10 dB RF line width and a 4.83 GHz anti-colliding MLL with a 5 kHZ 10 dB RF line width and a 3 ps pulse. In order to meet the stringent requirements of terabits per second coherent communications in terms of line width and phase stability, we used hybrid mode-locking and injection locking techniques to improve the optical and electrical line width of the MLL. We demonstrated that under optical injection locking the 3 dB optical line width is reduced from a $\sim$MHz line width to a 50 kHz line width. With a CW injection power as low as 0.1 mW, coherence between more than 50 mode-locked laser modes and the CW laser is experimentally confirmed.

Based on the InP quantum well lasers, we explored the potential of InAs/-GaAs QD mode-locked lasers integrated on a silicon photonics platform. We designed, fabricated and tested both linear colliding pulse MLLs and ring MLLs. Quantum-dot-based comb lasers were shown with both constellations. We showed a 18.8 GHz linear MLL with a 623 kHZ 3 dB RF line width and a 20.3 GHz ring MLL with a 3 kHZ 3 dB RF line width. However, the optical 10 dB bandwidth was disappointingly small, around 3 nm for both structures and the cause for this is not fully understood at the moment. Since this is a first iteration, the different design parameters of the laser cavity are not yet optimized and more research is necessary.

References

[1] David AB Miller. *Rationale and challenges for optical interconnects to electronic chips*. Proceedings of the IEEE, 88(6):728–749, 2000.

[2] Zhiping Zhou, Bing Yin, and Jurgen Michel. *On-chip light sources for silicon photonics*. Light: Science & Applications, 4(11):e358, 2015.

[3] Mitsuru Sugawara and Michael Usami. *Quantum dot devices: Handling the heat*. Nature Photonics, 3(1):30–31, 2009.

[4] HY Liu, DT Childs, TJ Badcock, KM Groom, IR Sellers, M Hopkinson, RA Hogg, DJ Robbins, DJ Mowbray, and MS Skolnick. *High-performance three-layer 1.3-μm InAs-GaAs quantum-dot lasers with very low continuous-wave room-temperature threshold currents*. Photonics Technology Letters, IEEE, 17(6):1139–1141, 2005.

[5] Di Liang, Geza Kurczveil, Xue Huang, Chong Zhang, Sudharsanan Srinivasan, Zhihong Huang, M Ashkan Seyedi, Kate Norris, Marco Fiorentino, John E Bowers, and Raymond G Beausoleil. *Heterogeneous silicon light sources for datacom applications*. Optical Fiber Technology, 2017.

[6] Brian R Washburn, Scott A Diddams, Nathan R Newbury, Jeffrey W Nicholson, Man F Yan, and Carsten G Jrgensen. *Phase-locked, erbium-fiber-laser-based frequency comb in the near infrared*. Optics Letters, 29(3):250–252, 2004.

1

Introduction

Today, silicon photonics offers wafer based manufacturing and integration of a variety of optical functions (modulation, detection, filtering, multiplexing of wavelengths, etc.), with the significant exception being the light source, which normally is a laser. To date, this laser is a separate component that needs to be integrated with the silicon photonic chip in a back-end packaging step. No industrially scalable (i.e. suitable for high volume manufacturing) and high-yield process exists to integrate lasers with the silicon photonic chip and supporting electronics on 300 mm wafers. In addition, it is important that the selected laser technology can handle the high temperatures that typically occur inside the racks of large data centers, an application field where silicon photonics is expected to make a large impact. In this work we report the design, fabrication and characterization of single mode laser sources based on InAs/GaAs quantum dot epitaxy integrated on the silicon photonics platform by means of wafer bonding. We are also exploring the potential of InAs/GaAs quantum dot mode-locked lasers integrated on a silicon photonics platform and compare it with an extensive characterization of integrated InP quantum well mode-locked lasers. In this introductory chapter we provide the context for our research, look into the state-of-the-art regarding InAs/GaAs quantum dot lasers on silicon and present the outline of the rest of the dissertation.

1.1 Optical interconnects and photonics

Electronic ICs are today omnipresent in our society. They are part of every aspect of our life. They form the heart of our computers and smartphones. We can find them in the cars we drive and the fitbits we wear to monitor our health. Therefore, electronics can be considered as one of the most important technologies of the 20th century. At the core of this digital revolution lies the CMOS industry which mass produces all the necessary electronic chips.

Today, a new life-changing technology has emerged. Photonics, the science and technology that uses light for information gathering, processing and transport, is considered the information technology of the 21st century: it makes the internet as we know it today possible. Thanks to the development of the optical fiber and the semiconductor laser, we are interconnected with the entire world. Currently 99% of the data traffic that is crossing oceans is carried by undersea optical fibers. As of 2020, one estimates that there are over 1.2 million kilometers of submarine cables in service globally [1]. In figure 1.1 all submarine cables present and used today are depicted, without them the internet as we know it, would be impossible.

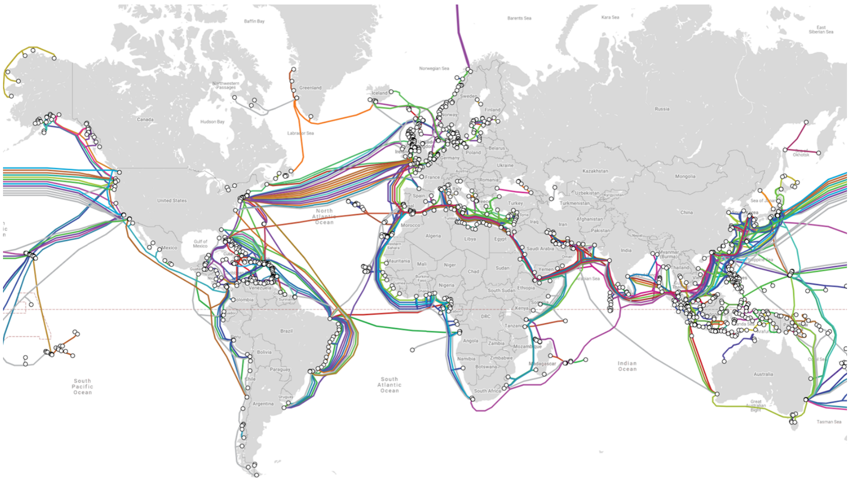

Figure 1.1: Submarine optical fiber cables are connecting the whole world. [1]

Fiber optic networks are not only used for long distance communication (telecommunication), but also inside data centers (data communication). Fibers are used to make connections within data center racks, between data center racks and between data center buildings. At the start and the end of each fiber, there is need for an optical transceiver. Optical transceivers serve both as an optical transmitter that converts an electrical signal into a light signal and an optical receiver that accepts the light signal and converts it back into an electrical signal.

Due to the ever increasing number of connected devices and people [2], the demand for higher bandwidths is increasing at an unprecedented pace. This trend requires high-performance interconnects that can sustain this high bandwidth without consuming exorbitant amounts of energy. Furthermore the continuously growing popularity of cloud based software applications is putting data center operators under severe pressure [3]. Since this evolution will probably not stop anytime soon, solutions that can be easily scaled up to higher bandwidths are preferred. This is illustrated in figure 1.2. Because of this, electronic and photonic systems need to be made ever more performant and lower-cost and one wants to realize the entire system on a single chip or in a single package. Since electrical interconnects have an inherent bandwidth limitation, there is a trend, and also a strong need, to switch from electrical to optical links at increasingly shorter distances, and employ them for rack-to-rack, board-to-board, chip-to-chip and intra-chip interconnects.

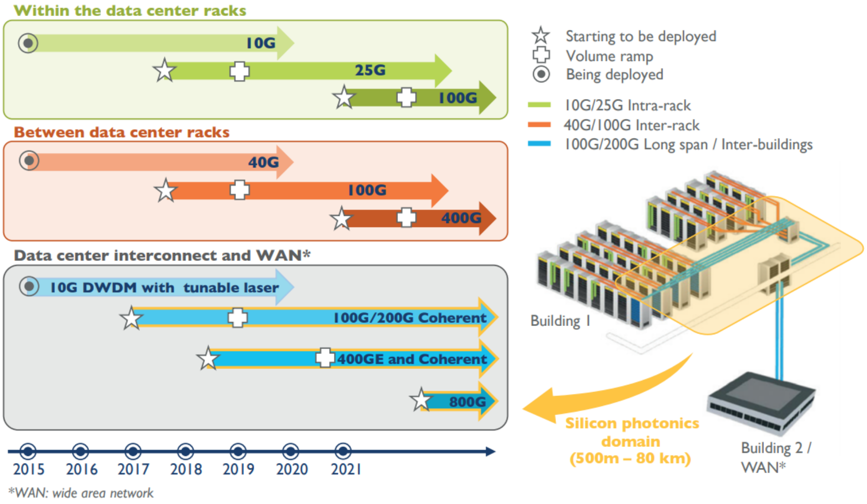

Figure 1.2: Status of optical transceivers migration to higher speed in datacom, driven by cloud datacenter networks and high performance computing interconnects. Source: Yole Developpement, June 2020

This trend was already started approximately two decades ago and pushed the development of integrated photonics, where optical devices and circuits are integrated on semiconductor chips. Photonic integrated circuits (PICs) can be made on different material platforms such as indium phosphide [4, 5] or silicon [6].

Silicon photonics is emerging as a powerful technology for the integration of optical functions on a chip [7]. It is also the only technology that can directly benefit from the CMOS industry and its economy of scale, since silicon photonics integrated circuits are made in silicon-on-insulator (SOI), a material platform that is used for high performance CMOS circuits. [8]

1.2 Silicon photonic integrated circuits

The photonics SOI platform is based on the strong optical confinement resulting from the high index contrast between silicon (n $\approx$ 3.45) and SiO_2 (n $\approx$ 1.45). This allows to scale down photonic waveguides to a few hundred nanometers and make bends with small bend radii. Because of this, a very large number of optical components can be combined on one single PIC [9]. Not only are these waveguides small, they can also be fabricated with low optical losses (typically less than 1 dB/cm). If very low losses are needed, rib waveguides can be used with losses smaller than 0.5 dB/cm [10, 11]. The silicon photonics platform has an impressive toolbox of high-performance passive optical devices. There are low-loss crossings and splitters available. Spectral filters [12] can be realized from high-Q ring resonators [13], wavelength demultiplexers based on arrayed waveguide gratings (AWGs) [14], Mach-Zehnder interferometers (MZI) [15] and planar concave gratings (PCG) [16]. Furthermore, easy interfacing with single mode fibers can be achieved using vertical chip-to-fiber grating couplers [17]. An example of a silicon photonics platform is shown in figure 1.3.

Next to passive components, silicon photonics also offers a variety of active devices integrated on chip like thermo-optic phase shifters [18], high-speed germanium photodetectors [19], electro-absorption modulators (EAM) [20] and carrier-based electro-optic modulators [21].

The significant exception to all the above is the light source, which normally is a laser [22]. High performance semiconductor lasers (as well as other opto-electronic components) are realized in III-V semiconductors. Therefore, there is a need for the integration of III-V semiconductors on silicon photonic ICs, in order to complete the toolkit for the realization of complex and advanced photonic systems-on-chip.

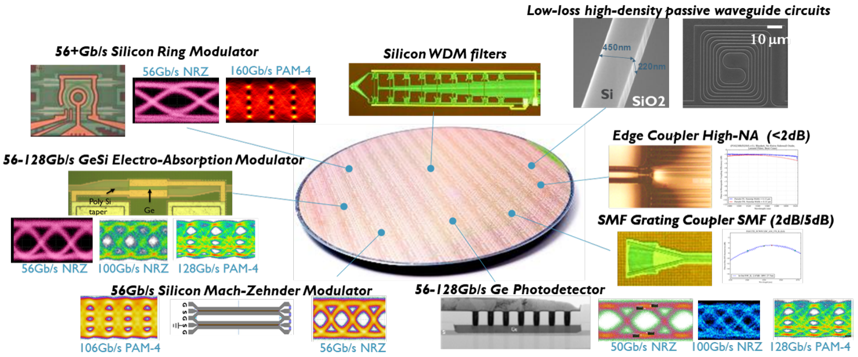

Figure 1.3: imec's fully integrated silicon photonics platform for 1310 nm/1550 nm wavelengths (based on [23]).

1.3 Heterogeneous III-V-on-silicon integration

There are many possible ways to integrate lasers with silicon optical circuits ranging from hetero-epitaxy of group III-V materials to co-packaging of a prepackaged laser to a separate silicon photonics chip. The advantages and disadvantages of the main technologies are described briefly below.

Fiber coupling an external packaged laser to the silicon chip The easiest way to achieve laser integration with a silicon chip is by fiber pigtailing an external III-V laser to the chip. The advantages of such an approach are that a high-end III-V laser can be temperature-controlled separately from the silicon chip and the yield of the two components can be optimized separately. But it is not an integrated solution and has a larger footprint, degraded performance due to coupling loss and reflections at each fiber coupling point, less scalability, and high cost from multiple packaging steps. This makes fiber coupling less attractive for low-cost applications.

Flip-chip and pick-and-place assembly of a laser Here, a prefabricated laser is attached to the silicon-on-insulator (SOI) chip using flip-chip, micro-packaging [24] or a micro-optical bench [25]. Either mechanical stops or machine vision is used to passively or actively align the laser to the silicon waveguide. This is illustrated in figure 1.4. Currently, the use of a micro-packaged laser (coined a LaMP), comprising a III-V laser diode on a micro-optical bench and including a ball lens, isolator and mirror to focus the light on a grating coupler defined in the Si PIC, pioneered by Luxtera, has the highest maturity to integrate III-V semiconductor lasers on silicon photonic integrated circuits [26]. While this approach has several advantages (use of mature InP technology, wafer-level assembly, packaging, test and burn-in of the LaMP, integration on the back-end stack of a silicon photonic wafer), the complexity of the LaMP itself and its sequential active alignment on the silicon photonic wafer make it an expensive solution. Moreover, the fact that a grating coupler structure is used for optical interfacing limits the coupling efficiency and bandwidth, and no waveguide-in/waveguide-out components such as semiconductor optical amplifiers (SOAs) – key components in advanced photonic integrated circuits – have been integrated using this approach.

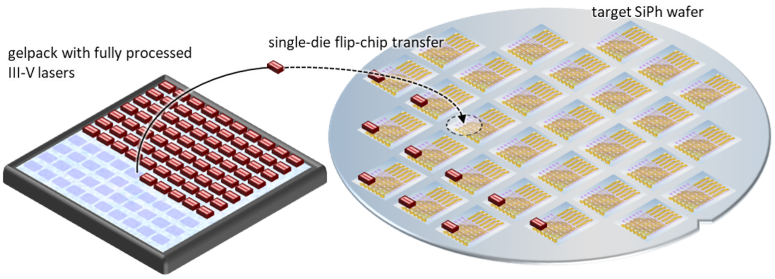

Figure 1.4: Die-level integration of an external packaged laser by flip-chipping. Picture courtesy: Wim Bogaerts.

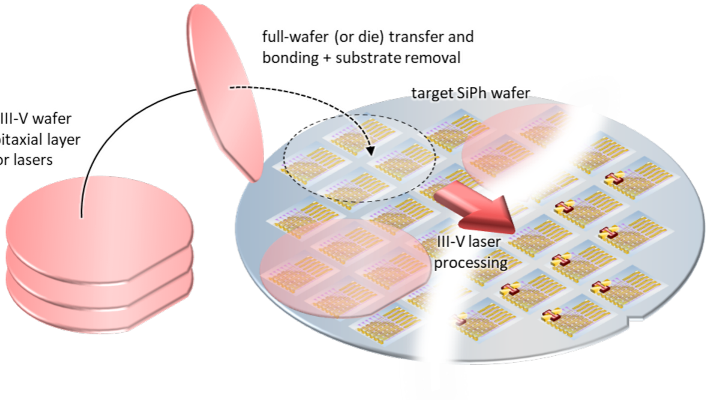

Figure 1.5: Heterogeneous integration of III-V lasers on an SOI waveguide circuit by means of wafer bonding. Picture courtesy: Wim Bogaerts.

Epitaxial growth of III-V layers Epitaxial growth of III-V layers on silicon has been widely investigated. Recently, a lot of progress has been made in the epitaxial growth of InAs/GaAs QD lasers on silicon working at 1.3 μm [27, 28]. However, direct epitaxy typically introduces a substantial crystalline defect density resulting in lower quality material, which can adversely affect device performance and reliability. Also the high growth temperatures are incompatible with the current silicon photonics process flow. Furthermore, some intermediate layers (like Ge or GaP) are often used to enable the growth process and reduce the defect density. These layers prevent efficient coupling of the laser light into the silicon circuit layer. Nonetheless, the epitaxial growth of InAs/GaAs QD lasers on silicon is evolving rapidly and there are huge research efforts to improve this technology, making this a technology that will probably gain more and more importance in the future [29].

Bonding technology Wafer bonding involves bonding an unpatterned III-V die or wafer to an SOI wafer either by interfacial bonds (direct) or by using a ”glue” (adhesive), and processing it further to fabricate the integrated laser. This is depicted in figure 1.5.

Direct or molecular bonding is one the most applied bonding techniques since it is used to create silicon-on-insulator (SOI). Since 2006, direct bonding is also successfully used to integrate III-V material on the silicon platform, when Fang *et al* from UCSB have demonstrated an electrically pumped III-V-on-silicon evanescent laser [30]. SOI is produced at temperatures above 800°C. Since III-V materials evaporate at such temperatures, an O_2 plasma-assisted bonding has been developed. The typical process flow is shown in figure 1.6a.

Divinylsiloxane-benzocyclobutene (DVS-BCB) is one of the most popular materials for adhesive bonding. A thin layer ($<$100 nm) of diluted DVS-BCB that is spin-coated on the SOI sample, is applied as glue between the SOI and the III-V die. Because we use an intermediate bonding layer, even though it is thin, there is a slightly larger tolerance to particle contamination and surface roughness. Although DVS-BCB has a low thermal conductivity, since the layer is very thin simulations show that the difference in heat dissipation at the bond interface is small. Also in 2006, Roelkens *et al* from Ghent University reported for the first time electrically injected thin film laser diodes integrated on and coupled to an SOI waveguide circuit by means of adhesive bonding [31]. The typical process flow is shown in figure 1.6b.

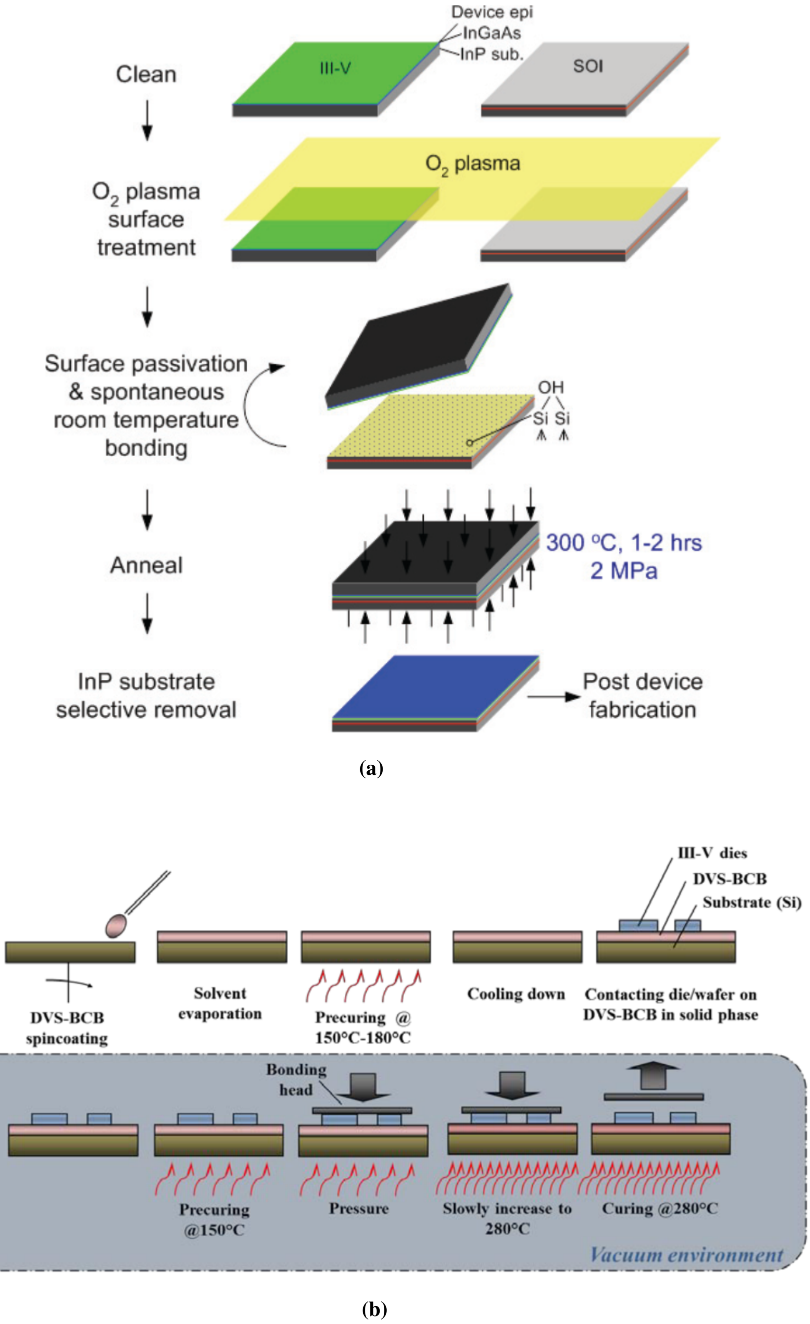

Figure 1.6: Process flow of (a) O2 plasma assisted direct bonding of InP on SOI; (b) die-to-die/wafer adhesive bonding via DVS-BCB. Reproduced from reference [32, 33].

Thus far laser integration on SOI focused mainly on QW-based active material, as was done in the Photonics Research Group [32]. Recently however, also the wafer bonding of 1.3 μm InAs/GaAs QD material sparked some research interest.

The tolerance to large bonding misalignment and simple packaging means that this architecture is suitable for low-cost and high-volume applications with a high number of lasers, while the minimal coupling loss between the laser and the silicon waveguide lends itself to applications that require power efficiency. Moreover, the direct integration between materials permits the realization of a bunch of new functions, like creating laser cavities in the silicon layer, etc. A disadvantage of this technique is the waste of III-V material, since the III-V on top of ”non-laser-area” on the Si photonic chip is etched away and thus lost. Furthermore, the III-V substrate is etched away as well [34]. Also the laser cannot be tested until all fabrication is finished.

Micro transfer printing Micro-transfer-printing (μTP) is a technology where materials or devices can be selectively removed from their source wafer and transferred in parallel to a new platform as a printing process. The TP process relies on the ability to release the components from their initial substrate, generally through undercut etching, together with a patterned stamp and an associated tool to pick and place arrays of components in a parallel process. This process can be applied to many different materials and structures and it makes very efficient use of materials. Additionally, significant (order of magnitude) cost savings can be attained due to the simplification and reduction in number of packaging steps. [35]

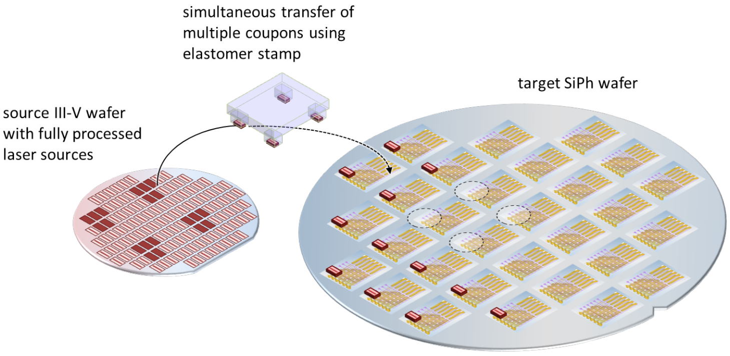

Figure 1.7: Micro transfer printing of III-V coupons on a silicon waveguide platform. Picture courtesy: Wim Bogaerts.

1.4 Quantum dots

Currently, in almost all commercial photonic integrated circuits (PICs) quantum wells (QWs) are the gain medium of choice. However, when confronted with high temperatures, QW-based-lasers show a substantial performance degradation. The lack of thermal robustness is a large obstacle on the way to use these lasers for datacom applications. The last two decades tremendous progress has been made in quantum dot (QD) epitaxial growth, enabling now the fabrication of QD structures that facilitate the generation of light with high efficiency, also at high temperatures. We believe that QD-based lasers can be very attractive to substitute conventional QW-based lasers because of their more favorable properties, as explained below.

The idea of a QD laser was first proposed by Arakawa and Sakaki in 1982 [36]. However, despite many attempts, functional devices were not realized until ten years later, following the development of self-assembly techniques during epitaxial growth [37, 38] which allowed the realization of the first quantum dot lasers emitting at 1 μm in 1994 [39]. By the year 2000, QD lasers started to outperform their QW counterparts [40].

Quantum dots – tiny clusters of semiconductor material with dimensions of only a few nanometers – are sometimes referred to as ”artificial atoms” because the charge carriers occupy only a restricted set of energy levels rather like electrons in an atom. Because of this, quantum dot lasers can show [29, 41–43]:

- Very low threshold current densities [44].
- A more stable performance over the 20°C-100°C temperature range compared to quantum well lasers [45].
- Reduced sensitivity to crystalline defects [46].
- Improved stability against optical feedback [47], paving the way to isolator-free PICs.
- Chirp[1] free operation [48].

Because of the way QDs are grown, there is a Gaussian distribution of dot sizes with a corresponding Gaussian distribution of emission frequencies. This effect leads to inhomogeneous broadening, the FWHM (full width at half maximum) of which is typically around 40-60 nm. This results in a wider gain spectrum compared with conventional quantum well lasers making this material system an excellent candidate for creating multi-wavelength transmitters.

In this work, an InAs/GaAs-based quantum dot epitaxial layer stack from the German company INNOLUME will be used. These QDs allow us to create lasers that operate in the 1.2 - 1.3 μm wavelength range [49].

---

[1] Chirp is determined from the shift of the wavelength a laser exhibits during current modulation. This is an important parameter for directly modulated lasers.

1.4.1 Electronic density of states of quantum dots

In 1963, Kroemer proposed a pair of heterojunction injectors in order to improve the performance of semiconductor lasers [50]. But it was not until the demonstration of the first double heterostructure semiconductor laser in 1970 by Alferov [51] that the importance of carrier confinement to the active region was recognized. Since then, quantum structured lasers have received much attention.

As illustrated in figure 1.8, reducing one or more dimensions of the active material greatly impacts the density of states and the corresponding thermal energy distribution of the electrons and holes. When confining the carriers in one dimension, as is the case for quantum wells, the density of states is changed to a Heaviside step function, resulting in the concentration of most of the injected carriers in an narrow energy range near the bottom of the conduction band and/or top of the valence band. This leads to a lower threshold current and improved temperature stability compared with a bulk active region. When reducing all three dimensions to create a quantum dot, the density of states becomes a delta-function, very much like atoms and the above positive effects are further enhanced [52].

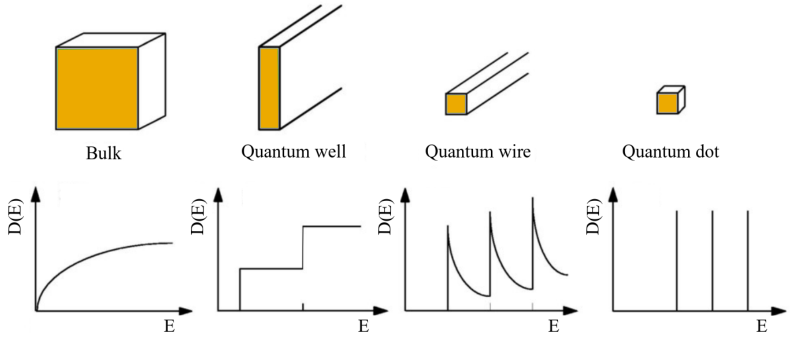

Figure 1.8: Effect of the reduced dimensionality. Schematic diagram of the density of states D(E) of bulk, quantum well, quantum wire and quantum dot material.

However in real semiconductor systems, we move away slightly from the ideal delta-function-like density of states. When growing the quantum dots, various dot sizes will appear, depending on the crystal growth conditions. These variations lead to inhomogeneous broadening, ΔE_{inh}, of the optical properties of a dot ensemble. The realistic density of states of a quantum dot structure is the superposition of the discrete states of the individual dots as is show in figure 1.9a. Luckily, the inhomogeneous broadening can be a few times smaller than the energy level spacing, such that the quantum dot structure still has separated energy levels. Furthermore, during growth a thin wetting layer of dot material appears (see section

1.4.2). This layer will act as a quantum well connecting all dots in that layer. Taking into account the above effects, a more realistic density of states is shown in figure 1.9b. [29]

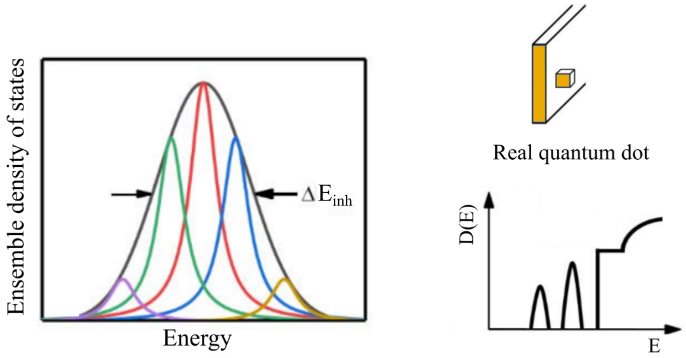

Figure 1.9: (a) Inhomogeneous broadening for a quantum dot state. (b) The density of states, D(E), of a quantum dot structure including inhomogeneous broadening and the wetting layer. Based on [29].

1.4.2 Self-organized growth of quantum dots

In case of a sufficiently deep localizing potential, when the motion of charge carriers in a semiconductor crystal is limited to a very small volume, the density of states becomes quantized. When assuming a 3D rectangular shape of the QD and an infinite barrier potential, the corresponding conduction-band energy levels are given by

$$E_c^{n_x,n_y,n_z} = E_{c,0} + \frac{\hbar^2\pi^2}{2m_e^*}\left(\frac{n_x^2}{L_x^2} + \frac{n_y^2}{L_y^2} + \frac{n_z^2}{L_z^2}\right) \tag{1.1}$$

with $E_{c,0}$ the conduction-band edge, m_e^* the electron effective mass, $L_{x,y,z}$ the QD dimensions and $n_{x,y,z} = 1, 2, 3, \ldots$ the quantum numbers. [53]

In order to be useful for laser devices the quantum dots have a lower and upper size limit [54]. Since at least one energy level for the holes and electrons should be available in the quantum dot, the minimal size is related to the conduction band offset ΔE_c. For a spherical QD, the minimal diameter D_{min} can be calculated by inserting equation 1.1 in:

$$E_{c,1} - E_{c,0} < \Delta E_c \tag{1.2}$$

and thus

$$D_{min} = \frac{\pi\hbar}{\sqrt{2m_e^*\Delta E_c}} \tag{1.3}$$

The maximum size of a quantum dot is defined by the spacing between neighboring energy levels. If the spacing approaches the thermal energy kT, population of higher-energy levels cannot be neglected. As a rule of thumb, the spacing should be 3 times larger than the thermal energy kT:

$$kT \leq \frac{1}{3}(E_{c,2} - E_{c,1}) \tag{1.4}$$

This leads to dot dimensions between 4 nm and 20 nm for the InAs/GaAs quantum dot system [43].

In order to grow high quality quantum dots with the right size, a high density and uniformly spread out over the wafer, a wide variation of techniques was investigated, for example QDs based on lithographic patterning of QWs [55] and quantum dots grown on patterned substrates [56]. However, the quantum dots used in this work are self-assembled quantum dots based on the Stranski-Krastanov (SK) growth mechanism. This is the most commonly used technique for the growth of high quality quantum dots. In this method crystalline layers of InAs are deposited on a GaAs substrate. Due to the lattice mismatch between the two materials (around 7 $\%$) the layer is strained. When a critical thickness is reached, 3D pyramidally-shaped islands form through the Stranski-Krastanov transition. Not all the atoms form these dots, a small layer remains on the surface forming the wetting layer. This is illustrated in figure 1.10a. The dot size and areal density depend on the growth parameters like growth rate and growth temperature [57, 58]. Next, another layer of semiconductor material is deposited to cap the quantum dots. During capping, the apex of the pyramid gets removed and the side facets become steeper as shown in figure1.10b [59]. Figure 1.10c shows a microscope image of a quantum dot layer before capping.

1.4.3 Quantum dot lasers

When designing a semiconductor laser we need to take into account certain important characteristics. Before discussing what happens when the active medium consists of quantum dots, we give a brief overview of the basic laser properties.

A first important laser parameter is the threshold current density j_{thr}. This is the current density needed such that the material gain compensates the internal losses (absorption and scattering losses) and the mirror losses. At this point the laser starts lasing. The gain at threshold g_{thr} can be written as:

$$\Gamma g_{\text{thr}} = \alpha_i + \alpha_m \tag{1.5}$$

with α_i, the internal losses, α_m the mirror losses and Γ the optical confinement factor. The latter is the ratio of the total light intensity and the light intensity in the active layer. One can see it as a measure for the overlap between the QDs and

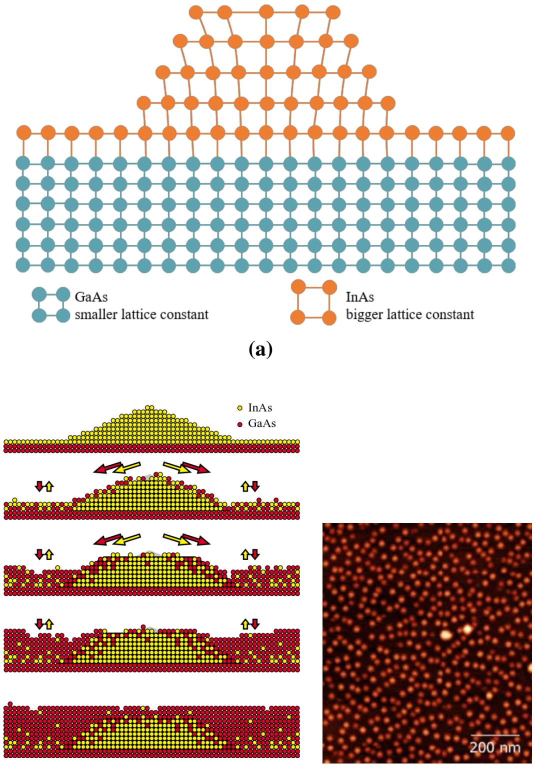

(a)

(b) (c)

Figure 1.10: (a) Illustration of the structure of an InAs/GaAs quantum dot [60]; (b) model for the capping process of the QD structure [59]; (c) atomic force microscope image of an uncapped quantum dot layer [29]

the optical mode. Γg_{thr} is called the modal gain. It is the modal gain that needs to overcome all losses in order to obtain lasing. When we stack N active layers on top of each other, the optical confinement factor Γ and thus the modal gain should be multiplied with a factor N, provided the intensity of the optical mode stays more or less uniform over the different layers. This can be a solution when a single active layer has not sufficient modal gain to start lasing. However, note that if a single active layer is sufficient to reach lasing threshold, the transparency current density will also increase with a factor N because more carriers are needed to fill all the states to reach population inversion [43].

Also important is the behavior of the laser with increasing temperature. When the temperature is rising, more carriers will be located in higher energy states. Therefore, the carrier density at a given energy state is decreasing and the threshold current is rising. The temperature dependence of the threshold current is given by:

$$j_{\mathrm{thr}}(T) = j_{\mathrm{thr}}(T_1) exp(\frac{T - T_1}{T_0}) \tag{1.6}$$

where T_1 is a given base temperature. T_0 is called the characteristic temperature of the laser: the higher this temperature, the more stable the threshold current with temperature.

1.4.3.1 The ideal quantum dot laser

When Arakawa and Sasaki [36] predicted the quantum dot laser, they assumed an ideal active layer of quantum dots: a collection of dots having identical optical and electrical properties (meaning no inhomogeneous broadening), where the carriers are strongly confined. Based on this description, very nice laser properties have been predicted [54].

Because of the 3D confinement in a quantum dot, the injected carriers are squeezed in a narrower energy range than is the case for quantum wells or bulk material. This results in a steeper dependence of the optical gain on injection current. Furthermore is the threshold current reduced because population inversion is reached with fewer injected carriers. In [61] it was theoretically demonstrated that the material gain spectrum of ideal quantum dots is much narrower than that of multidimensional structures and the maximum material gain is larger. This is plotted in figure 1.11a. The predicted threshold current densities of comparable quantum dots, wires, wells and bulk are plotted in figure 1.11b.

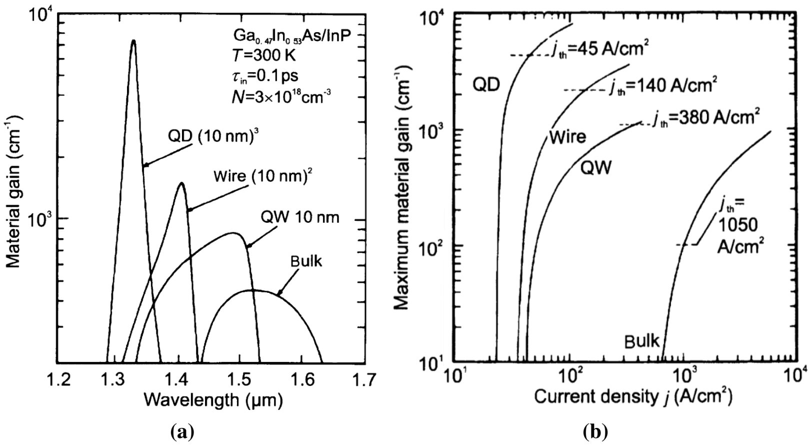

(a) (b)

Figure 1.11: (a) Gain spectra for a quantum dot, wire, well and bulk. The confined lateral dimensions are each 10 nm. (b) Maximum material gain as a function of current density. The dashed line indicates the threshold. [54]

In an ideal quantum dot laser, we assume a δ-function-like density of states, and thus infinite barriers for the carrier confinement. Because of this the lasing threshold becomes independent of temperature and the characteristic temperature T_0 equals infinity.

1.4.3.2 The real quantum dot laser

As already described in section 1.4.1 and shown in figure 1.9, the density of states of a real set of quantum dots differs considerably from the ideal delta-function states, mostly due to the inhomogeneous broadening. Because of this, the behavior of a real quantum dot laser is different from the ideal one.

A first very noticeable change is the transformation of the narrow gain spectrum caused by an ensemble of identical quantum dots to a broad gain spectrum. For some broadband applications, like mode-locked lasers, tunable lasers and optical amplifiers, this can be used as an advantage. By changing the crystal growth conditions the extent of the inhomogeneous broadening can be influenced.

Every dot present in the active layer acts as an independent emitter and each dot can only exhibit stimulated emission for a photon energy corresponding to the energy levels of the QD. So the gain produced at a certain photon energy is not tied to the gain at another photon energy. This means that at a certain wavelength only a subset of the dots contributes to the gain, resulting in a very small confinement factor. So despite a high material gain, the modal gain is low. On the other hand, quantum dots being independent emitters also has positive implications. In a quantum dot mode-locked laser, each mode will interact with a different subset of quantum dots. Since charge carriers cannot freely move between dots, neighboring modes will not compete for carriers.

Despite the inhomogeneous broadening, the electron energy levels are still well separated. However, since the hole energy levels are more closely spaced, the injected holes get thermally broadened [62]. This reduces the temperature stability. This problem can be mitigated by better growth quality and p-type modulation doping [63]. Through this measures, the effect of temperature is small compared to quantum well lasers. This is demonstrated in this work in chapter 4. In [64] CW lasing was demonstrated up till 220°C, a record high temperature for semiconductor lasers.

In early works regarding quantum dot lasers, one hypothesized that a phonon bottleneck would degrade the laser performance: due to a lack of phonons with the right energy, the transition of carriers between the discrete energy levels of the quantum dots was predicted to be slowed significantly [65]. Luckily, efficient Auger recombination processes limited these effects, and moreover they caused ultra fast carrier dynamics. This is illustrated in figure 1.12. When the carrier density in the wetting layer surrounding the quantum dots is low, the relaxation and capture processes are mainly phonon assisted. However, as the laser pumping increases, the carrier density in the wetting layer increases as well and the carriers get captured in the quantum dots. Due to the Pauli exclusion principle the number of carriers allowed in the quantum dot energy states is limited. So the quantum dot states get filled and the relaxation and capture of carriers gets saturated. All extra carriers injected in the system form a carrier reservoir in the wetting layer. The high density of carriers in the reservoir increases the Auger assisted capture speed. Moreover due to the high confinement of carriers in the quantum dot states, Auger scattering results in a fast transfer of carriers from the excited state to the ground state [66]. This allows for carriers to relax very rapidly to the dot ground state and results in sub-picosecond gain recovery times [67].

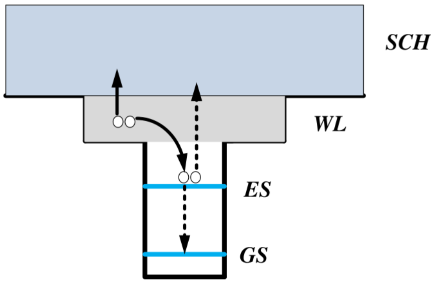

Figure 1.12: Carrier capture and relaxation processes through Auger processes lead to ultrafast carrier dynamics in quantum dots (SCH: separate confinement heterostructure, WL: wetting layer, ES: excited state and GS: ground state). [66]

Finally, the linewidth enhancement factor α in semiconductor quantum dot lasers can be very low. This is important because this factor determines the laser linewidth and the laser sensitivity for undesired back-reflections [68]. The laser linewidth scales as:

$$\Delta\nu \propto (1+\alpha^2) \tag{1.7}$$

while the laser stability against undesired reflections is defined by the critical feedback level:

$$f_{\text{crit}} \propto \frac{1+\alpha^2}{\alpha^4} \tag{1.8}$$

The linewidth enhancement factor is related to the coupling of the real and imaginary part of the complex susceptibility in the laser medium and is given by

$$\alpha = -\frac{dn_r/dN}{dn_i/dN} = -\frac{4\pi}{\lambda}\frac{dn_r/dN}{dg/dN} \tag{1.9}$$

with N the carrier density, n_r the real part and n_i the imaginary part of the refractive index and dg/dN the differential gain. Lower values of α can be obtained for materials with a symmetric gain spectrum and a high differential gain. In the case of a QD laser with a dot ensemble showing a perfect Gaussian energy distribution, the gain spectrum is highly symmetric [43]. Typical values of α for quantum well materials are in the range of 3 to 5, while for quantum dot materials values around and even below zero have been demonstrated [69].

1.5 Quantum dot lasers on silicon – state-of-the-art

Multiple ways to integrate InAs/GaAs quantum dot lasers with silicon photonic circuits are already demonstrated. Typical integration schemes include hetero-epitaxy of III-V materials [28], flip-chip bonding [70] and wafer bonding (described in this work).

Below we will give an overview of the most important achievements of the last years.

1.5.1 Epitaxial growth

The realization of an on-chip light source is essential for silicon photonics technology. To allow for high production volumes, low-cost and high-yield fabrication is indispensable. Since silicon has an indirect bandgap and group IV-based light emitters will not be up to the mark in the foreseeable future, heterogeneous integration with III-V materials becomes necessary. Currently, III-V lasers integrated through bonding [32] or transfer-printing [71] show the best performance and the best opportunity for commercial usage. However, the direct epitaxial growth of III-V materials onto the silicon wafer is perceived as the solution to this problem in the long term [72].

However, monolithic integration of III-V materials onto the silicon platform is quite challenging due to large material dissimilarities between III-V materials and group IV materials. This leads to the formation of antiphase boundaries (APB), the formation of threading dislocations (TD) and the creation of thermal cracks, which all can hamper good laser performance. Although this is very problematic for QW lasers grown on silicon, QD devices are more robust towards defects. Most notably, they are less sensitive to threading dislocations than QW structures. Threading dislocations are a result of the lattice mismatch between the silicon and the III-V material. As a result, strain appears in the grown epilayer. The strain energy increasing with increasing thickness. At some point during the growth the accumulated strain is relaxed through (among others) threading dislocations. This defect propagates through the III-V material acting as a non-radiative recombination center reducing the device performance [73]. As is illustrated in figure 1.13, a threading dislocation only kills a few dots and leaves the rest unharmed and capable of providing optical gain, while a quantum well is cut in two influencing a lot of carriers [74].

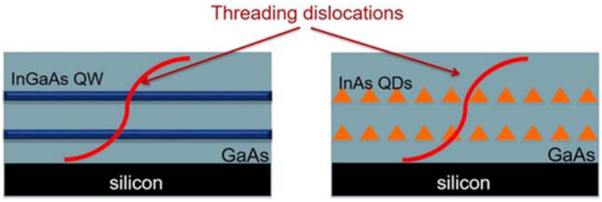

Figure 1.13: Schematic illustration of the influence of threading dislocations on QWs and QDs [73].

Since epitaxial growth of GaAs directly on silicon causes so many problems, many research efforts are done to use Ge or Ge-on-Si substrates. Due to the small lattice mismatch, Ge can act as a bridge between the GaAs III-V material and the silicon. In 2012 the first electrically pumped CW 1.3 μm InAs/GaAs quantum dot laser monolithically grown on a Ge-on-Si substrate was demonstrated showing a threshold current density of 163 A/cm^2 by researchers from UCL [75]. In 2014, UCSB researchers showed CW lasing operation up to 119°C [76].

Since the Ge layer prevents the laser light coupling into the silicon waveguide layer because of absorption, direct integration without an intermediate Ge layer remains the goal. To prevent the formation of antiphase boundaries, InAs/GaAs QD lasers are grown on the Si (100) substrate with a 4°off-cut towards the [011] plane [77]. In 2016, high-performance electrically pumped CW 1310 nm InAs/-GaAs quantum dot lasers were realized on this platform by Chen *et al* from UCL. They showed a low threshold current density of 62.5 A/cm^2, operation up to 120 °C and good reliability at room temperature [78].

In order to fully use the CMOS-compatibility of the silicon photonics platform, the ultimate goal is the epitaxial growth of InAs/GaAs QD lasers on (001) Si substrates. The first successful demonstration of an electrically pumped CW 1.3 μm InAs/GaAs quantum dot laser on this platform was shown in 2017 by UCSB researchers, using a combination of MOCVD and MBE growth. A GaP layer is used as a buffer between the device layers and the silicon. Laser operation was shown up to 90°C [79]. In 2019, Kwoen *et al* from the University of Tokyo reported high-temperature (over 100°C) CW operation of an InAs/GaAs QD laser directly grown on on-axis Si (001) substrates through the use of only MBE, simplifying the fabrication process considerably [27]. Very recently, Wan *et al* from UCSB showed a CW InAs/GaAs QD laser directly grown on nominal Si (001) substrates. No GaP, Ge buffer layers or substrate patterning is required [80]. Although non of the above lasers actually couples into a silicon waveguide, the unpatterned growth technique of [80] might significantly de-risk the technology from a performance standpoint, warranting discussion for more advanced photonic integration.

1.5.2 Wafer bonding

Epitaxial growth is a promising technology for the future, but non of the laser devices described above can already couple light into the silicon waveguide circuit. Today, hetero-integration based on wafer bonding is the most mature technology and has been widely adopted in industry by among others Intel [81].

Although wafer bonding is a very well established technology for QW lasers [82], at the start of this work only very few InAs/GaAs based quantum dot lasers were bonded on SOI.

The first InAs/GaAs QD lasers bonded on silicon substrates were reported by researchers from Tokyo University in 2012. They fabricated Fabry-Pérot lasers by means of direct bonding. Since current injection was done through the GaAs/Si interface, as can be seen on figure 1.14, they had to use p-type silicon instead of SOI. They reported CW 1.28 μm lasing at room temperature with a threshold current density of 480 A/cm^2. [83, 84]

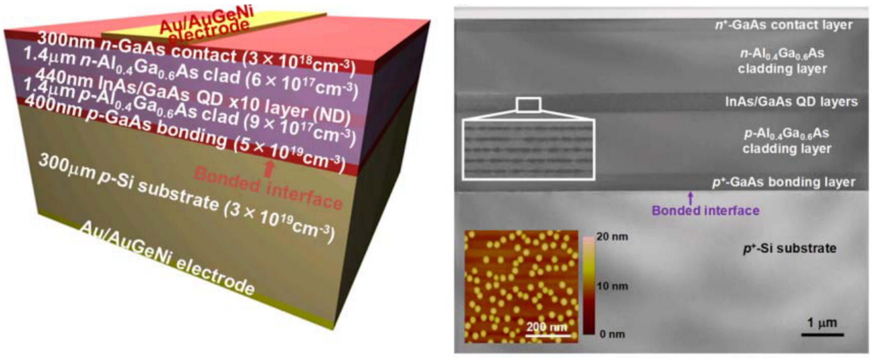

Figure 1.14: InAs/GaAs QD laser on Si substrate: cross-sectional diagram of the different epi-layers and a transmission electron microscope image of the laser [84].

The same group also demonstrated InAs/GaAs QD lasers on SOI substrates by metal-stripe wafer bonding in 2015 [85]. In this approach metal stripes were used both as a bonding intermediate layer and an electrode. Although the metal facilitates the bonding, it also complicates the coupling to an underlying silicon waveguide circuit.

For the first time, in 2016, two research groups showed InAs/GaAs QD lasers directly bonded on a silicon substrate with efficient coupling of light to a silicon waveguide under the QD gain region. Since both electrical contacts are now laterally formed on the III-V, low-loss coupling of the laser light to a silicon waveguide is possible. Both Kurczveil *et al* from Hewlett-Packard Labs [86] and Jang *et al* from Tokyo University [87] showed CW operation up to 100°C.

In 2018, the first single mode InAs/GaAs QD laser heterogeneously integrated on a Si photonics waveguide circuit was demonstrated as part of this work. The InAs/GaAs epi material was bonded on the SOI by means of adhesive bonding. Single mode lasing around 1300 nm with a side-mode suppression ratio higher than 40 dB was demonstrated. High temperature operation with CW lasing up to 100°C is obtained. Threshold current densities as low as 205 A/cm^2 were measured [88].

1.6 Outline

This work consists of 7 chapters of which the content is summarized below.

At the start of this work, only very few quantum dot lasers integrated on the silicon platform existed [75, 84] and non of them could couple light into a silicon waveguide. Therefore, a big part of my research was spent in cleanroom in order to develop the necessary processes. The results are described in chapter 2. We start with a description of the general lay-out of the laser that is shared by all the different types of lasers discussed later on. Since wet etching is a big part of the fabrication process, an overview of the different chemical etchants and their main properties is presented. Armed with this knowledge, the fabrication of heterogeneously integrated InAs/GaAs quantum dot lasers is described in detail. Most of the work focuses on wafer bonded lasers, but we have also investigated the option of transfer-printed lasers which is described at the end of the chapter.

It is one thing to put a III-V laser on top of a silicon chip, but to couple the laser light efficiently into a silicon waveguide is something else entirely. In chapter 3 we describe different methods to couple light from a III-V gain chip into a silicon waveguide. This list is by no means exhaustive but all methods described were fabricated and tested.

In chapter 4 the core work of this PhD project is addressed. An extensive discussion is presented on the design, fabrication and characterization of single mode InAs/GaAs quantum dot DFB lasers on a silicon substrate with coupling to a silicon waveguide.

The next two chapters focus on mode-locked lasers: the lasers in chapter 5 are based on InGaAsP/InP quantum wells, where the mode-locked lasers described in chapter 6 are based on InAs/GaAs quantum dots. In chapter 5 three different designs of mode-locked lasers are discussed in detail. Next, the linear cavity colliding pulse mode-locked laser design is used to demonstrate a narrow line width frequency comb source by injection of a narrow line width CW tone in the mode-locked laser. We were able to reduce the optical laser line width to 50 kHz for a

4.71 GHz repetition rate mode-locked laser. This line width is narrow enough to enable coherent data transmission with advanced modulation formats. Two locking techniques are explored. In chapter 6 we explored the potential of InAs/GaAs QD mode-locked lasers integrated on a silicon photonics platform. Based on the mode-locked lasers presented in chapter 5, we designed, fabricated and tested both linear colliding pulse MLLs and ring MLLs. Quantum-dot-based comb lasers were shown with both constellations.

In the conclusive chapter 7, the results of this works are summarized and an outlook to the future is provided.

1.7 List of publications

The results obtained within this work have been published in various papers and presented at various conferences.

1.7.1 Publications in international journals

1. J. Goyvaerts, S. Kumari, S. Uvin, J. Zhang, R. Baets, A. Gocalinska, E. Pelucchi, B. Corbett, G. Roelkens, ”Transfer-print integration of GaAs p-i-n photodiodes onto silicon nitride waveguides for near infrared applications”, (submitted)

2. K. Van Gasse, S. Uvin, V. Moskalenko, S. Latkowski, G. Roelkens, E. Bente, B. Kuyken, ”Recent advances in the photonic integration of mode-locked laser diodes”, *IEEE Photonics Technology Letters* (invited), 31(23), p.1870–1873 (2019)

3. J. Juvert, T. Cassese, S. Uvin, A. De Groote, B. Snyder, L. Bogaerts, G. Jamieson, J. Van Campenhout, G. Roelkens, D. Van Thourhout, ”Integration of etched facet, electrically pumped, C-band Fabry-Pérot lasers on a silicon photonic integrated circuit by transfer printing”, *Optics express*, 26(17), p.21443–21454 (2018)

4. S. Uvin, S. Kumari, A. De Groote, S. Verstuyft, G. Lepage, P. Verheyen, J. Van Campenhout, G. Morthier, D. Van Thourhout, G. Roelkens, ”1.3 μm InAs/GaAs quantum dot DFB laser integrated on a Si waveguide circuit by means of adhesive die-to-wafer bonding”, *Optics express*, 26(14), p.18302–18309 (2018)

5. G. Chen, J.J. Goyvaerts, S. Kumari, J. Van Kerrebrouck, M. Muneeb, S. Uvin, Y. Yu, G. Roelkens, ”Integration of high-speed GaAs metal-semiconductor-metal photodetectors by means of transfer printing for 850 nm wavelength photonic interposers”, *Optics express*, 26(5) p.6351–6359 (2018)

6. A. Katumba, J. Heyvaert, B. Schneider, S. Uvin, J. Dambre, P. Bienstman, ”Low-loss photonic reservoir computing with multimode photonic integrated circuits”, *Scientific reports*, 8(1), p.1–10 (2018).
7. N. Ye, G. Muliuk, A. J. Trindade, C. Bower, J. Zhang, S. Uvin, D. Van Thourhout, G. Roelkens, ”High-alignment-accuracy transfer printing of passive silicon waveguide structures”, *Optics express*, 26(2), p.2023–2032 (2018)
8. K. Van Gasse, Z. Wang, S. Uvin, B. De Deckere, J. Mariën, L. Thomassen, G. Roelkens, ”Ka-band to L-band frequency downconversion based on III–V-on-silicon photonic integrated circuits”, *CEAS Space Journal*, 9(4), p.531–541 (2017)
9. S. Dhoore, S. Uvin, D. Van Thourhout, G. Morthier, G. Roelkens, ”Novel adiabatic tapered couplers for active III–V/SOI devices fabricated through transfer printing”, *Optics express*, 24(12), p.12976–12990 (2016)
10. S. Uvin, S. Keyvaninia, F. Lelarge, G. Duan, B. Kuyken, G. Roelkens, ”Narrow line width frequency comb source based on an injection-locked III–V-on-silicon mode-locked laser”, *Optics express*, 24(5) p.5277–5286 (2016)
11. G. Roelkens, A. Abbasi, P. Cardile, U.D. Dave, A. De Groote, Y. De Koninck, S. Dhoore, X. Fu, A. Gassenq, N. Hattasan, Q. Huang, S. Kumari, S. Keyvaninia, B. Kuyken, L. Li, P. Mechet, M. Muneeb, D. Sanchez, H. Shao, T. Spuesens, A. Subramanian, S. Uvin, M. Tassaert, K. Van Gasse, J. Verbist, R. Wang, Z. Wang, J. Zhang, J. Van Campenhout, Y. Xin, J. Bauwelinck, G. Morthier, R. Baets, D. Van Thourhout, ”III-V-on-Silicon Photonic Devices for Optical Communication and Sensing”, *Photonics* (invited), 2, p. 969–1004 (2015)
12. S. Keyvaninia, S. Uvin, M. Tassaert, Z. Wang, X. Fu, S. Latkowski, J. Marien, L. Thomassen, F. Lelarge, G. Duan, G. Lepage, P. Verheyen, J. Van Campenhout, E. Bente, G. Roelkens, ”III–V-on-silicon anti-colliding pulse-type mode-locked laser”, *Optics Letters*, 40(13), p.3057–3060 (2015)
13. S. Keyvaninia, S. Uvin, M. Tassaert, X. Fu, S. Latkowski, J. Marien, L. Thomassen, F. Lelarge, G. Duan, P. Verheyen, G. Lepage, J. Van Campenhout, E. Bente, G. Roelkens, ”Narrow-linewidth short-pulse III-V-on-silicon mode-locked lasers based on a linear and ring cavity geometry”, *Optics express*, 23(3), p.3221–3229 (2015)
14. G. Roelkens, U.D. Dave, A. Gassenq, N. Hattasan, C. Hu, B. Kuyken, F. Leo, A. Malik, M. Muneeb, E.M.P. Ryckeboer, D. Sanchez, S. Uvin, R. Wang, Z. Hens, R. Baets, Y. Shimura, F. Gencarelli, B. Vincent, R. Loo, J. Van Campenhout, L. Cerutti, J.B. Rodriguez, E. Tournie, X. Chen, M.

Nedeljkovic, G. Mashanovich, L. Shen, N. Healy, A. C. Peacock, X. Liu, R. Osgood, W. M. J. Green, ”Silicon-based photonic integration beyond the telecommunication wavelength range”, *IEEE Journal of Selected Topics in Quantum Electronics* (invited), 20(4), p.8201511 (2014)

15. U.D. Dave, S. Uvin, B. Kuyken, S. Selvaraja, F. Leo, G. Roelkens, ”Telecom to mid-infrared spanning supercontinuum generation in hydrogenated amorphous silicon waveguides using a Thulium doped fiber laser pump source”, *Optics express*, 21(26), p.32032–32039 (2013)

16. G. Roelkens, U.D. Dave, A. Gassenq, N. Hattasan, C. Hu, B. Kuyken, F. Leo, A. Malik, M. Muneeb, E.M.P. Ryckeboer, S. Uvin, Z. Hens, R. Baets, ”Silicon-based heterogeneous photonic integrated circuits for the mid-infrared”, *Optical Materials Express* (invited), 3(9), p.1523–1536 (2013)

1.7.2 Publications in international conferences

1. G. Roelkens, J. Zhang, A. De Groote, J. Juvert, N. Ye, S. Kumari, J. Goyvaerts, G. Muliuk, S. Uvin, G. Chen, B. Haq, B. Snyder, J. Van Campenhout, D. Van Thourhout, A. Trindade, C.A. Bower, J. O’Callaghan, R. Loi, B. Roycroft, B. Corbett, ”Transfer printing for silicon photonics transceivers and interposers”, *IEEE Optical Interconnects Conference (OI) 2018* (invited), United States, p.13–14 (2018)

2. B. Kuyken, K. Van Gasse, S. Keyvaninia, S. Uvin, S. Latkowski, E. Bente, Z. Wang, G. Roelkens, ”Integrated modelocked comb lasers for spectroscopy applications”, *Lasers and Electro-Optics CLEO Pacific Rim*, W2F–4 (2018)

3. S. Uvin, S. Kumari, A. De Groote, S. Verstuyft, G. Morthier, D. Van Thourhout, G. Roelkens, ”InAs/GaAs quantum dot 1.3 μm DFB laser heterogeneously integrated on a silicon waveguide circuit”, *European Conference on Integrated Optics (ECIO)*, Spain, p.125–127 (2018)

4. J. Juvert, T. Cassese, S. Uvin, A. De Groote, B. Snyder, P. De Heyn, P. Verheyen, A. J. Trindade, C. Bower, M. Romagnoli, G. Roelkens, D. Van Thourhout, ”Integration of III-V light sources on a silicon photonics circuit by transfer printing”, *IEEE 14th International Conference on Group IV Photonics (GFP)*, Germany, p.171–172 (2017)

5. G. Muliuk, N. Ye, S. Uvin, A. Ribeiro, C. Bower, D. Van Thourhout, G. Roelkens, ”Transfer printing of silicon-on-insulator devices on silicon nitride waveguide circuits: design of coupling structures and process development”, *IEEE Photonics Society Benelux*, Belgium (2016)

6. K. Van Gasse, Z. Wang, S. Uvin, J. Marien, L. Thomassen, G. Roelkens, ”Ka-to-L-band frequency down-conversion using a micro-photonic IIIV-on-silicon mode-locked laser and Mach-Zehnder modulator”, *International Conference on Space Optics*, France (2016)

7. G. Roelkens, U.D. Dave, S. Keyvaninia, F. Leo, S. Uvin, K. Van Gasse, Z. Wang, S. Latkowski, E. Bente, B. Kuyken, ”Frequency comb generation in III-V-on-silicon photonic integrated circuits”, *Advanced Photonics Congress - IPR* (invited), Cananda, IM2A–5 (2016)

8. S. Uvin, S. Keyvaninia, F. Lelarge, G.H. Duan, B. Kuyken, G. Roelkens, ”Narrow Line Width Injection-locked III-V-on-silicon Mode-locked Laser”, *18th European Conference on Integrated Optics (ECIO)*, Poland, (2016)

9. S. Uvin, S. Keyvaninia, D. Van Thourhout, G. Roelkens, ”A novel approach of integrating III-V on the silicon nitride platform”, *IEEE Photonics Society Benelux* (2015)

10. G. Roelkens, A. Abbasi, S. Keyvaninia, S. Uvin, K. Van Gasse, Z. Wang, U.D. Dave, B. Kuyken, G. Morthier, D. Van Thourhout, ”III–V-on-silicon photonic integrated circuits for communication and sensing applications”, *28th IEEE Photonics Conference (IPC)* (invited), United States, p.593–594 (2015)

11. S. Uvin, S. Keyvaninia, M. Tassaert, Z. Wang, X. Fu, S. Latkowski, J. Marien, L. Thomassen, F. Lelarge, G. Duan, G. Lepage, P. Verheyen, J. Van Campenhout, E. Bente, G. Roelkens, ”1.7 kHz RF linewidth III-V-on-silicon mode-locked laser”, *IEEE 12th International Conference on Group IV Photonics (GFP)* (invited), p.25–26 (2015)

12. G. Roelkens, S. Keyvaninia, Y. De Koninck, S. Uvin, A. Abbasi, K. Van Gasse, Z. Wang, G. Morthier, D. Van Thourhout, R. Baets, ”III-V-on-silicon photonic integrated circuits for optical interconnects”, *IEEE Summer Topicals* (invited), Bahamas, p.144–145 (2015)

13. G. Roelkens, U.D. Dave, A. Gassenq, N. Hattasan, C. Hu, B. Kuyken, F. Leo, A. Malik, M. Muneeb, E.M.P. Ryckeboer, D. Sanchez, S. Uvin, R. Wang, Z. Hens, R. Baets, Y. Shimura, F. Gencarelli, B. Vincent, R. Loo, J. Van Campenhout, L. Cerutti, J.B. Rodriguez, E. Tournie, X. Chen, M. Nedeljkovic, G. Mashanovich, L. shen, N. Healy, A. Peacock, X. Liu, R. Osgood, W.M.J. Green, ”Long-wavelength silicon photonic integrated circuits”, *11th International Conference on Group IV Photonics (GFP)* (invited), France, p.23-24 (2014)

14. G. Roelkens, U.D. Dave, A. Gassenq, N. Hattasan, C. Hu, B. Kuyken, F. Leo, A. Malik, M. Muneeb, E.M.P. Ryckeboer, S. Uvin, Z. Hens, R. Baets, Y. Shimura, F. Gencarelli, B. Vincent, R. Loo, J. Van Campenhout, L. Cerutti, J.B. Rodriguez, E. Torunie, X. Chen, M. Nedeljkovic, G. Mashanovich, L. Shen, N. Healy, A.C. Peacock, X. Liu, R. Osgood, W. Green, ”Mid-IR heterogeneous silicon photonics”, *Conference on Silicon Photonics IX* (invited), United States, p.899316 (6 pages) (2014)

15. S. Uvin, U.D. Dave, B. Kuyken, S. Selvaraja, F. Leo, G. Roelkens, ”Mid-infrared to telecom-band stable supercontinuum generation in hydrogenated amorphous silicon waveguides”, *IEEE Photonics Conference (IPC)*, United States, p.380–381 (2013)

References

[1] TeleGeography, 2020. `https://www.submarinecablemap.com/`.

[2] CISCO. *Cisco Annual Internet Report (2018-2023)*, 2020. White paper.

[3] Qi Zhang, Lu Cheng, and Raouf Boutaba. *Cloud computing: state-of-the-art and research challenges*. Journal of internet services and applications, 1(1):7–18, 2010.

[4] Xaveer Leijtens. *JePPIX: the platform for Indium Phosphide-based photonics*. IET optoelectronics, 5(5):202–206, 2011.

[5] Meint Smit, Xaveer Leijtens, Erwin Bente, Jos van der Tol, Huub Ambrosius, David Robbins, Mike Wale, Norbert Grote, and Martin Schell. *A generic foundry model for InP-based photonic ICs*. In OFC/NFOEC, pages 1–3. IEEE, 2012.

[6] Bahram Jalali and Sasan Fathpour. *Silicon photonics*. Journal of lightwave technology, 24(12):4600–4615, 2006.

[7] P De Dobbelaere, A Dahl, A Mekis, B Chase, B Weber, B Welch, D Foltz, G Armijo, G Masini, G McGee, et al. *Advanced silicon photonics technology platform leveraging a semiconductor supply chain*. In 2017 IEEE International Electron Devices Meeting (IEDM), pages 34–1. IEEE, 2017.

[8] David Thomson, Aaron Zilkie, John E Bowers, Tin Komljenovic, Graham T Reed, Laurent Vivien, Delphine Marris-Morini, Eric Cassan, Léopold Virot, Jean-Marc Fédéli, et al. *Roadmap on silicon photonics*. Journal of Optics, 18(7):073003, 2016.

[9] Dan-Xia Xu, Jens H Schmid, Graham T Reed, Goran Z Mashanovich, David J Thomson, Milos Nedeljkovic, Xia Chen, Dries Van Thourhout, Shahram Keyvaninia, and Shankar K Selvaraja. *Silicon photonic integration platform—Have we found the sweet spot?* IEEE Journal of Selected Topics in Quantum Electronics, 20(4):189–205, 2014.

[10] Pieter Dumon, Wim Bogaerts, Vincent Wiaux, Johan Wouters, Stephan Beckx, Joris Van Campenhout, Dirk Taillaert, Bert Luyssaert, Peter Bienstman, Dries Van Thourhout, et al. *Low-loss SOI photonic wires and ring resonators fabricated with deep UV lithography*. IEEE Photonics Technology Letters, 16(5):1328–1330, 2004.

[11] Minh A Tran, Duanni Huang, Tin Komljenovic, Jonathan Peters, Aditya Malik, and John E Bowers. *Ultra-low-loss silicon waveguides for heterogeneously integrated silicon/III-V photonics*. Applied Sciences, 8(7):1139, 2018.

[12] Wim Bogaerts, Shankar Kumar Selvaraja, Pieter Dumon, Joost Brouckaert, Katrien De Vos, Dries Van Thourhout, and Roel Baets. *Silicon-on-insulator spectral filters fabricated with CMOS technology*. IEEE journal of selected topics in quantum electronics, 16(1):33–44, 2010.

[13] Wim Bogaerts, Peter De Heyn, Thomas Van Vaerenbergh, Katrien De Vos, Shankar Kumar Selvaraja, Tom Claes, Pieter Dumon, Peter Bienstman, Dries Van Thourhout, and Roel Baets. *Silicon microring resonators*. Laser & Photonics Reviews, 6(1):47–73, 2012.

[14] M Gehl, D Trotter, A Starbuck, A Pomerene, AL Lentine, and C DeRose. *Active phase correction of high resolution silicon photonic arrayed waveguide gratings*. Optics express, 25(6):6320–6334, 2017.

[15] Sarvagya Dwivedi, Alfonso Ruocco, Michael Vanslembrouck, Thijs Spuesens, Peter Bienstman, Pieter Dumon, Thomas Van Vaerenbergh, and Wim Bogaerts. *Experimental extraction of effective refractive index and thermo-optic coefficients of silicon-on-insulator waveguides using interferometers*. Journal of Lightwave Technology, 33(21):4471–4477, 2015.

[16] Joost Brouckaert, Wim Bogaerts, Pieter Dumon, Dries Van Thourhout, and Roel Baets. *Planar concave grating demultiplexer fabricated on a nanophotonic silicon-on-insulator platform*. Journal of Lightwave Technology, 25(5):1269–1275, 2007.

[17] Dries Van Thourhout, Günther Roelkens, Roel Baets, Wim Bogaerts, Joost Brouckaert, Peter Debackere, Pieter Dumon, Stijn Scheerlinck, Jonathan Schrauwen, Dirk Taillaert, et al. *Coupling mechanisms for a heterogeneous silicon nanowire platform*. Semiconductor Science and Technology, 23(6):064004, 2008.

[18] Nicholas C Harris, Yangjin Ma, Jacob Mower, Tom Baehr-Jones, Dirk Englund, Michael Hochberg, and Christophe Galland. *Efficient, compact and*

low loss thermo-optic phase shifter in silicon. Optics express, 22(9):10487–10493, 2014.

[19] Hongtao Chen, Michael Galili, P Verheyen, P De Heyn, G Lepage, J De Coster, S Balakrishnan, P Absil, L Oxenlowe, J Van Campenhout, et al. *100-Gbps RZ data reception in 67-GHz Si-contacted germanium waveguide pin photodetectors*. Journal of Lightwave Technology, 35(4):722–726, 2016.

[20] Jochem Verbist, Michiel Verplaetse, SA Srivinasan, Peter De Heyn, Timothy De Keulenaer, Ramses Pierco, Renato Vaernewyck, Arno Vyncke, Philippe Absil, Guy Torfs, et al. *First real-time 100-Gb/s NRZ-OOK transmission over 2 km with a silicon photonic electro-absorption modulator*. In Optical Fiber Communication Conference, pages Th5C–4. Optical Society of America, 2017.

[21] Graham T Reed, G Mashanovich, FY Gardes, and DJ Thomson. *Silicon optical modulators*. Nature Photonics, 4(8):518–526, 2010.

[22] Richard Soref. *The past, present, and future of silicon photonics*. IEEE Journal of selected topics in quantum electronics, 12(6):1678–1687, 2006.

[23] Abdul Rahim, Jeroen Goyvaerts, Bertrand Szelag, Jean-Marc Fedeli, Philippe Absil, Timo Aalto, Mikko Harjanne, Callum Littlejohns, Graham Reed, Georg Winzer, et al. *Open-access silicon photonics platforms in Europe*. IEEE Journal of Selected Topics in Quantum Electronics, 25(5):1–18, 2019.

[24] Peter De Dobbelaere, Ali Ayazi, Yuemeng Chi, Anders Dahl, Scott Denton, Steffen Gloeckner, Kam-Yan Hon, Steve Hovey, Yi Liang, Michael Mack, et al. *Packaging of Silicon Photonics Systems*. In Optical Fiber Communication Conference, pages W3I–2. Optical Society of America, 2014.

[25] Bradley Snyder, Brian Corbett, and Peter O Brien. *Hybrid Integration of the Wavelength-Tunable Laser With a Silicon Photonic Integrated Circuit*. Journal of Lightwave Technology, 31(24):3934–3942, 2013.

[26] Luxtera, 2020. `http://www.luxtera.com/`.

[27] Jinkwan Kwoen, Bongyong Jang, Katsuyuki Watanabe, and Yasuhiko Arakawa. *High-temperature continuous-wave operation of directly grown InAs/GaAs quantum dot lasers on on-axis Si (001)*. Optics express, 27(3):2681–2688, 2019.

[28] Mengya Liao, Siming Chen, Jae-Seong Park, Alwyn Seeds, and Huiyun Liu. *III–V quantum-dot lasers monolithically grown on silicon*. Semiconductor Science and Technology, 33(12):123002, 2018.

[29] Justin C Norman, Daehwan Jung, Zeyu Zhang, Yating Wan, Songtao Liu, Chen Shang, Robert W Herrick, Weng W Chow, Arthur C Gossard, and John E Bowers. *A review of high-performance quantum dot lasers on silicon*. IEEE Journal of Quantum Electronics, 55(2):1–11, 2019.

[30] Alexander W Fang, Hyundai Park, Oded Cohen, Richard Jones, Mario J Paniccia, and John E Bowers. *Electrically pumped hybrid AlGaInAs-silicon evanescent laser*. Optics express, 14(20):9203–9210, 2006.

[31] Gnther Roelkens, Dries Van Thourhout, Roel Baets, R Nötzel, and Meint Smit. *Laser emission and photodetection in an InP/InGaAsP layer integrated on and coupled to a Silicon-on-Insulator waveguide circuit*. Optics express, 14(18):8154–8159, 2006.

[32] Günther Roelkens, Liu Liu, Di Liang, Richard Jones, Alexander Fang, Brian Koch, and John Bowers. *III-V/silicon photonics for on-chip and intra-chip optical interconnects*. Laser & Photonics Reviews, 4(6):751–779, 2010.

[33] Shahram Keyvaninia, Muhammad Muneeb, Stevan Stankovic, PJ Van Veldhoven, Dries Van Thourhout, and Günther Roelkens. *Ultra-thin DVS-BCB adhesive bonding of III-V wafers, dies and multiple dies to a patterned silicon-on-insulator substrate*. Optical Materials Express, 3(1):35–46, 2013.

[34] Justin C Norman, Daehwan Jung, Yating Wan, and John E Bowers. *Perspective: The future of quantum dot photonic integrated circuits*. APL Photonics, 3(3):030901, 2018.

[35] John Justice, Chris Bower, Matthew Meitl, Marcus B Mooney, Mark A Gubbins, and Brian Corbett. *Wafer-scale integration of group III-V lasers on silicon using transfer printing of epitaxial layers*. Nature Photonics, 6(9):610–614, 2012.

[36] Y Arakawa and Hiroyuki Sakaki. *Multidimensional quantum well laser and temperature dependence of its threshold current*. Applied Physics Letters, 40(11):939–941, 1982.

[37] L Goldstein, F Glas, JY Marzin, MN Charasse, and G Le Roux. *Growth by molecular beam epitaxy and characterization of InAs/GaAs strained-layer superlattices*. Applied Physics Letters, 47(10):1099–1101, 1985.

[38] J-Y Marzin, J-M Gérard, A Izraël, D Barrier, and G Bastard. *Photoluminescence of single InAs quantum dots obtained by self-organized growth on GaAs*. Physical review letters, 73(5):716, 1994.

[39] N Kirstaedter, NN Ledentsov, M Grundmann, D Bimberg, VM Ustinov, SS Ruvimov, MV Maximov, Ps S Kop'ev, Zh I Alferov, U Richter, et al. *Low threshold, large T/sub o/injection laser emission from (InGa) As quantum dots*. Electronics Letters, 30(17):1416–1417, 1994.

[40] Dieter Bimberg and Udo W Pohl. *Quantum dots: promises and accomplishments*. Materials Today, 14(9):388–397, 2011.

[41] EU Rafailov, MA Cataluna, and Wilson Sibbett. *Mode-locked quantum-dot lasers*. Nature photonics, 1(7):395–401, 2007.

[42] Nadya Anscombe. *Join up the quantum dots*. Nature Photonics, 1(7):360–361, 2007.

[43] Dieter Bimberg, M Grundmann, F Heinrichsdorff, NN Ledentsov, VM Ustinov, AE Zhukov, AR Kovsh, MV Maximov, YM Shernyakov, BV Volovik, et al. *Quantum dot lasers: breakthrough in optoelectronics*. Thin Solid Films, 367(1):235–249, 2000.

[44] HY Liu, DT Childs, TJ Badcock, KM Groom, IR Sellers, M Hopkinson, RA Hogg, DJ Robbins, DJ Mowbray, and MS Skolnick. *High-performance three-layer 1.3-μm InAs-GaAs quantum-dot lasers with very low continuous-wave room-temperature threshold currents*. Photonics Technology Letters, IEEE, 17(6):1139–1141, 2005.

[45] Mitsuru Sugawara and Michael Usami. *Quantum dot devices: Handling the heat*. Nature Photonics, 3(1):30–31, 2009.

[46] Alan Y Liu, Sudharsanan Srinivasan, Justin Norman, Arthur C Gossard, and John E Bowers. *Quantum dot lasers for silicon photonics*. Photonics Research, 3(5):B1–B9, 2015.

[47] Alan Y Liu, Tin Komljenovic, Michael L Davenport, Arthur C Gossard, and John E Bowers. *Reflection sensitivity of 1.3 μm quantum dot lasers epitaxially grown on silicon*. Optics express, 25(9):9535–9543, 2017.

[48] J Duan, H Huang, D Jung, Z Zhang, J Norman, JE Bowers, and F Grillot. *Semiconductor quantum dot lasers epitaxially grown on silicon with low linewidth enhancement factor*. Applied Physics Letters, 112(25):251111, 2018.

[49] A Kovsh, A Gubenko, I Krestnikov, D Livshits, S Mikhrin, J Weimert, L West, G Wojcik, D Yin, C Bornholdt, et al. *Quantum dot comb-laser as efficient light source for silicon photonics*. In Photonics Europe, pages 69960V–69960V. International Society for Optics and Photonics, 2008.

[50] Herbert Kroemer. *A proposed class of hetero-junction injection lasers*. Proceedings of the IEEE, 51(12):1782–1783, 1963.

[51] Zh I Alferov. *AlAs-GaAs heterojunction injection lasers with a low room-temperature threshold*. Sov. Phys. Semicond., 3:1107–1110, 1970.

[52] Nikolai N Ledentsov, M Grundmann, F Heinrichsdorff, Dieter Bimberg, VM Ustinov, AE Zhukov, MV Maximov, Zh I Alferov, and JA Lott. *Quantum-dot heterostructure lasers*. Selected Topics in Quantum Electronics, IEEE Journal of, 6(3):439–451, 2000.

[53] Shun Lien Chuang. *Physics of photonic devices*, volume 80. John Wiley & Sons, 2012.

[54] Dieter Bimberg, Marius Grundmann, and Nikolai N Ledentsov. *Quantum dot heterostructures*. John Wiley & Sons, 1999.

[55] H Qiang, Fred H Pollak, Y-S Tang, PD Wang, and CM Sotomayor Torres. *Characterization of process-induced strains in GaAs/Ga0. 7Al0. 3As quantum dots using room-temperature photoreflectance*. Applied physics letters, 64(21):2830–2832, 1994.

[56] KC Rajkumar, A Madhukar, K Rammohan, DH Rich, P Chen, and L Chen. *Optically active three-dimensionally confined structures realized via molecular beam epitaxical growth on nonplanar GaAs (111) B*. Applied physics letters, 63(21):2905–2907, 1993.

[57] Arvind Baskaran and Peter Smereka. *Mechanisms of stranski-krastanov growth*. Journal of Applied Physics, 111(4):044321, 2012.

[58] JX Chen, Alexander Markus, Andrea Fiore, U Oesterle, RP Stanley, JF Carlin, Romuald Houdre, M Ilegems, L Lazzarini, L Nasi, et al. *Tuning InAs/-GaAs quantum dot properties under Stranski-Krastanov growth mode for 1.3 μm applications*. Journal of applied physics, 91(10):6710–6716, 2002.

[59] Holger Eisele, Andrea Lenz, Robert Heitz, Rainer Timm, Mario Dähne, Yevgeniy Temko, Takayuki Suzuki, and Karl Jacobi. *Change of InAs/GaAs quantum dot shape and composition during capping*. Journal of Applied Physics, 104(12):124301, 2008.

[60] Qingqing Duan. *Nano-Photonic Systems Incorporating Single III-V Semiconductor Quantum Dots*. PhD thesis, University of Sheffield, 2019.

[61] Mashiro Asada, Yasuyuki Miyamoto, and Yasuharu Suematsu. *Gain and the threshold of three-dimensional quantum-box lasers*. IEEE Journal of quantum electronics, 22(9):1915–1921, 1986.

[62] OB Shchekin and DG Deppe. *1.3 μm InAs quantum dot laser with T o= 161 K from 0 to 80 C.* Applied Physics Letters, 80(18):3277–3279, 2002.

[63] Justin C Norman, Zeyu Zhang, Daehwan Jung, Chen Shang, MJ Kennedy, Mario Dumont, Robert W Herrick, Arthur C Gossard, and John E Bowers. *The importance of p-doping for quantum dot laser on silicon performance*. IEEE Journal of Quantum Electronics, 55(6):1–11, 2019.

[64] T Kageyama, K Nishi, M Yamaguchi, R Mochida, Y Maeda, K Takemasa, Y Tanaka, T Yamamoto, M Sugawara, and Y Arakawa. *Extremely high temperature (220 C) continuous-wave operation of 1300-nm-range quantum-dot lasers*. In The European Conference on Lasers and Electro-Optics, page PDA_1. Optical Society of America, 2011.

[65] Mitsuru Sugawara, Kohki Mukai, and Hajime Shoji. *Effect of phonon bottleneck on quantum-dot laser performance*. Applied physics letters, 71(19):2791–2793, 1997.

[66] Mahdi Razm-Pa and Farzin Emami. *Phonon Bottleneck and Auger Recombination Effect on the Perfermance of a Self-assembled Quantum Dot Laser*. Silicon, 10(4):1513–1521, 2018.

[67] Holger Schmeckebier and Dieter Bimberg. *Quantum-dot semiconductor optical amplifiers for energy-efficient optical communication*. In Green Photonics and Electronics, pages 37–74. Springer, 2017.

[68] Heming Huang, Jianan Duan, Bozhang Dong, J Norman, D Jung, JE Bowers, and F Grillot. *Epitaxial quantum dot lasers on silicon with high thermal stability and strong resistance to optical feedback*. APL Photonics, 5(1):016103, 2020.

[69] Weng W Chow, Zeyu Zhang, Justin C Norman, Songtao Liu, and John E Bowers. *On quantum-dot lasing at gain peak with linewidth enhancement factor α H= 0.* APL Photonics, 5(2):026101, 2020.

[70] Nobuaki Hatori, Yutaka Urino, Takanori Shimizu, Makoto Okano, Tsuyoshi Yamamoto, Masahiko Mori, Takahiro Nakamura, and Yasuhiko Arakawa. *Quantum Dot Laser for a Light Source of an Athermal Silicon Optical Interposer*. In Photonics, volume 2, pages 355–364. Multidisciplinary Digital Publishing Institute, 2015.

[71] Jing Zhang, Grigorij Muliuk, Joan Juvert, Sulakshna Kumari, Jeroen Goyvaerts, Bahawal Haq, Camiel Op de Beeck, Bart Kuyken, Geert Morthier, Dries Van Thourhout, et al. *III-V-on-Si photonic integrated circuits realized using micro-transfer-printing*. APL photonics, 4(11):110803, 2019.

[72] Zhiping Zhou, Bing Yin, and Jurgen Michel. *On-chip light sources for silicon photonics*. Light: Science & Applications, 4(11):e358, 2015.

[73] Qiang Li and Kei May Lau. *Epitaxial growth of highly mismatched III-V materials on (001) silicon for electronics and optoelectronics*. Progress in Crystal Growth and Characterization of Materials, 63(4):105–120, 2017.

[74] Zizhuo Liu, Constanze Hantschmann, Mingchu Tang, Ying Lu, Jae-Seong Park, Mengya Liao, Shujie Pan, Ana M Sanchez, Richard Beanland, Mickael Martin, et al. *Origin of defect tolerance in InAs/GaAs quantum dot lasers grown on silicon*. Journal of Lightwave Technology, 2019.

[75] Andrew Lee, Qi Jiang, Mingchu Tang, Alwyn Seeds, and Huiyun Liu. *Continuous-wave InAs/GaAs quantum-dot laser diodes monolithically grown on Si substrate with low threshold current densities*. Optics Express, 20(20):22181–22187, 2012.

[76] Alan Y Liu, Chong Zhang, Justin Norman, Andrew Snyder, Dmitri Lubyshev, Joel M Fastenau, Amy WK Liu, Arthur C Gossard, and John E Bowers. *High performance continuous wave 1.3 μm quantum dot lasers on silicon*. Applied Physics Letters, 104(4):041104, 2014.

[77] R Fischer, D Neuman, H Zabel, H Morkoc, C Choi, and N Otsuka. *Dislocation reduction in epitaxial GaAs on Si (100)*. Applied physics letters, 48(18):1223–1225, 1986.

[78] Siming Chen, Wei Li, Jiang Wu, Qi Jiang, Mingchu Tang, Samuel Shutts, Stella N Elliott, Angela Sobiesierski, Alwyn J Seeds, Ian Ross, et al. *Electrically pumped continuous-wave III–V quantum dot lasers on silicon*. Nature Photonics, 2016.

[79] Alan Y Liu, Jon Peters, Xue Huang, Daehwan Jung, Justin Norman, Minjoo L Lee, Arthur C Gossard, and John E Bowers. *Electrically pumped continuous-wave 1.3 μm quantum-dot lasers epitaxially grown on on-axis (001) GaP/Si*. Optics Letters, 42(2):338–341, 2017.

[80] Yating Wan, Chen Shang, Justin Norman, Bei Shi, Qiang Li, Noelle Collins, Mario Dumont, Kei May Lau, Arthur C Gossard, and John E Bowers. *Low threshold quantum dot lasers directly grown on unpatterned quasi-nominal (001) Si*. IEEE Journal of Selected Topics in Quantum Electronics, 26:1–9, 2020.

[81] Intel. *Intel Silicon Photonics 100G PSM4 Optical Transceiver Brief*, 2017. `https://www.intel.com/content/www/us/en/architecture-and-technology/silicon-photonics/optical-transceiver-100g-psm4-qsfp28-brief.html`.

[82] Tin Komljenovic, Duanni Huang, Paolo Pintus, Minh A Tran, Michael L Davenport, and John E Bowers. *Heterogeneous III-V silicon photonic integrated circuits*. Proceedings of the IEEE, 2018.

[83] Katsuaki Tanabe, Katsuyuki Watanabe, and Yasuhiko Arakawa. *1.3 μm InAs/GaAs quantum dot lasers on Si rib structures with current injection across direct-bonded GaAs/Si heterointerfaces*. Optics express, 20(26):315–321, 2011.

[84] Katsuaki Tanabe, Katsuyuki Watanabe, and Yasuhiko Arakawa. *III-V/Si hybrid photonic devices by direct fusion bonding*. Scientific reports, 2, 2012.

[85] Yuan-Hsuan Jhang, Katsuaki Tanabe, Satoshi Iwamoto, and Yasuhiko Arakawa. *InAs/GaAs Quantum Dot Lasers on Silicon-on-Insulator Substrates by Metal-Stripe Wafer Bonding*. Photonics Technology Letters, IEEE, 27(8):875–878, 2015.

[86] Géza Kurczveil, Di Liang, Marco Fiorentino, and Raymond G Beausoleil. *Robust hybrid quantum dot laser for integrated silicon photonics*. Optics Express, 24(14):16167–16174, 2016.

[87] Bongyong Jang, Katsuaki Tanabe, Satoshi Kako, Satoshi Iwamoto, Tai Tsuchizawa, Hidetaka Nishi, Nobuaki Hatori, Masataka Noguchi, Takahiro Nakamura, Keizo Takemasa, et al. *Demonstration of a hybrid silicon evanescent quantum dot laser*. In OptoElectronics and Communications Conference (OECC) held jointly with 2016 International Conference on Photonics in Switching (PS), 2016 21st, pages 1–3. IEEE, 2016.

[88] Sarah Uvin, Sulakshna Kumari, Andreas De Groote, Steven Verstuyft, Guy Lepage, Peter Verheyen, Joris Van Campenhout, Geert Morthier, Dries Van Thourhout, and Gunther Roelkens. *1.3 μm InAs/GaAs quantum dot DFB laser integrated on a Si waveguide circuit by means of adhesive die-to-wafer bonding*. Optics express, 26(14):18302–18309, 2018.

2

Fabrication of heterogeneously integrated InAs/GaAs quantum dot lasers

Silicon photonics is a powerful technology, but because of the indirect bandgap of silicon, the realization of an efficient, electrically pumped laser is a challenge. This requires the integration of III-V semiconductor lasers on the silicon photonic platform. The classical integration approach involves either fiber pigtailing an external laser [1] or attaching a micro-packaged III-V laser [2, 3] to the silicon circuit using active alignment techniques. While these are viable solutions for the integration of single laser diodes, these approaches don't scale well. Therefore, heterogeneous integration of III-V materials on the silicon platform through wafer-bonding [4–6] and more recently through transfer printing [7, 8] has been widely explored.

Currently, most heterogeneously integrated lasers are realized on the InP platform, using a quantum well active region. Using this platform, e.g. distributed feedback lasers (DFB) [9, 10], tunable lasers [11] and mode-locked lasers [12] have been demonstrated. However, when confronted with high temperatures, InP-lasers suffer from a large increase in threshold current and decrease of slope efficiency [13, 14]. The lack of thermal robustness is a large obstacle on the way to use this lasers for datacom applications.

The last few years, tremendous progress has been made in quantum dot (QD) epitaxial growth, enabling the fabrication of QD structures that facilitate the gen-

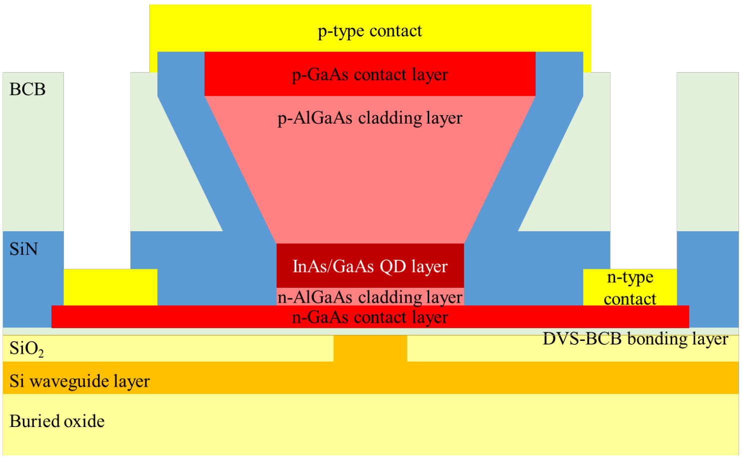

Figure 2.1: Cross-section of the III-V/Si laser.

eration of light with high wall-plug efficiency. We believe that QDs can be very attractive to substitute conventional InP-based lasers because of their more favorable properties. GaAs-based quantum dot lasers inherently have a more stable performance over the 20-100°C temperature range [15, 16]. Moreover, they have a small linewidth enhancement factor, enabling direct modulation and are insensitive to optical feedback [17, 18].

In this chapter we will discuss the fabrication of heterogeneously integrated III-V-on-Si quantum dot lasers. We will focus mainly on the use of adhesive die-to-wafer bonding, but at the end of the chapter transfer printing of GaAs-based lasers is also discussed. All processing is done in the Ghent University cleanroom.

2.1 General layout of the III-V/Si lasers

A schematic cross-section of the III-V-on-silicon waveguide structure is depicted in figure 2.1. The laser consists of a planarized SOI wafer containing the silicon waveguides and gratings defined in a 400 nm thick silicon waveguide layer, using 193 nm deep UV lithography (180 nm etch depth), fabricated in a CMOS pilot-line at imec. The GaAs quantum dot epitaxial layer stack is adhesively bonded to the planarized silicon-on-insulator (SOI) using a 60 nm-thick divinylsiloxane-bisbenzocyclobutene (DVS-BCB) bonding layer.

We based the design of the epitaxial layer stack on monolithic InAs/GaAs QD gain stacks reported in literature [19, 20] and we adapted them to make them suitable for wafer bonding. The III-V active region consists of an n-GaAs bottom contact layer (150 nm thick), an n-$Al_{0.4}Ga_{0.6}As$ bottom cladding layer (70 nm thick), 9 layers of InAs QDs separated by GaAs buffer layers, with a total thickness of

#	Layer	Mole fraction (x)	Thickness	Doping
15	n-GaAs contact		150 nm	(n) 3×10^{18}cm^{-3}
14	graded SCH n-Al$_x$Ga$_{1-x}$As	0.4 – 0	10 nm	(n) 10^{17}cm^{-3}
13	n-Al$_x$Ga$_{1-x}$As cladding	0.4	50 nm	(n) 10^{17}cm^{-3}
12	graded SCH n-Al$_x$Ga$_{1-x}$As	0 – 0.4	10 nm	(n) 10^{17}cm^{-3}
11	GaAs		10 nm	i
10	GaAs barrier / In$_x$Ga$_{1-x}$As QW / InAs QD	0.15	8x35 / 9x5 / 9x0.8 nm	nid
9	GaAs		10 nm	i
8	graded SCH p-Al$_x$Ga$_{1-x}$As	0.4 – 0	10 nm	(p) 9×10^{17}cm^{-3}
7	p-Al$_x$Ga$_{1-x}$As cladding	0.4	1500 nm	(p) 9×10^{17}cm^{-3}
6	graded SCH p-Al$_x$Ga$_{1-x}$As	0 – 0.4	10 nm	(p) 9×10^{17}cm^{-3}
5	p-GaAs contact		300 nm	(p) 5×10^{19}cm^{-3}
4	sacrificial Al$_x$Ga$_{1-x}$As	0.85	70 nm	i
3	sacrificial GaAs		40 nm	i
2	etch stop Al$_x$Ga$_{1-x}$As	0.85	800 nm	i
1	GaAs		500 nm	i
0	GaAs substrate			

Table 2.1: Epitaxial layer stack of the InAs/GaAs QD laser

352 nm, a p-type Al$_{0.4}$Ga$_{0.6}$As cladding layer (1.5 μm thick) and a p^{++}-GaAs top contact layer (300 nm thick). The confinement factor of the optical mode is 8.9% in the quantum dot layers and 7.5% in the p-AlGaAs layer. The details are presented in table 2.1. In this work, GaAs-based quantum dot layer stacks from the German company INNOLUME are used. These QDs allow us to create lasers that operate in the 1.1 - 1.3 μm wavelength range.

The layerstack is the same for both the DFB lasers and mode-locked lasers demonstrated in this work. Consequently, both structures share a common fabrication process, hence the lasers will be processed together and only one common fabrication process needs to be developed to realize the two different laser structures.

Both during the bonding and during the mesa definition we make frequent use of wet etch steps. We investigated and tested a lot of potential wet etchants before we got to the final process. That is why we start the chapter with an overview of the various etchants that are used in manufacturing. We then go through the entire process.

2.2 Wet etching

Wet chemical etching of GaAs and AlGaAs layers is a technique that is widely used during the fabrication of circuits and components on GaAs. Due to the abundance of chemical solutions and the pure chemical action of the etchant, a very high selectivity of GaAs over Al$_x$Ga$_{1-x}$As and vice versa is within reach. Moreover, opposite to dry etching, wet chemical processing is impact-free: the surface is not exposed to radiation and ion-bombardments.

Like almost all wet etching processes of semiconductors, in a first step the surface is oxidized by an oxidizing agent (mostly H_2O_2). Next, the resultant oxide material is dissolved in an acid or base. These two etch steps lead to 2 types of etchants: reaction rate limited and diffusion rate limited etchants dependent on which etch step is the fastest. This distinction will have a big influence on the etch profile [21].

In diffusion limited etching, the speed limiting factor of the etch process is the transport of active etch components to the surface or of the reaction products away from the surface. This means that:

- The etchant has a polishing character: a surface protrusion leads locally to a higher supply speed, while in a trough the etch process slows down. This results in the leveling of the surface.
- The etch rate increases with stirring of the liquid etchant.
- The etch rate is relatively insensitive to temperature variations.
- Etching doesn't depend on crystal orientation.
- The etch rate is proportional to the square root of the etching time.

In reaction rate limited etching, the limiting factor is the chemical reaction rate. This means that:

- The etch rate is unaffected by stirring of the liquid etchant.
- The etch rate changes with temperature.
- The etch rate is linearly proportional with the etching time.
- Etching results in a faceted surface structure dependent on the crystal orientation.

In this work we used (100)-GaAs substrates. The etch profiles in the 2 perpendicular directions $[0\bar{1}\bar{1}]$ and $[01\bar{1}]$, as indicated in figure 2.2 differ thoroughly when using a reaction rate limited etchant. Since an As-surface has an abundance of free electrons where a Ga-surface has a scarcity of electrons, depending on the etchant (acid or base) one or the other will act as an etch stop [22]. In this work we will use this property to create undercut structures in the spotsize converters of the lasers, which relaxes the lithography requirements.

Besides the oxidizing and dissolving agents, there is usually also a diluent (mostly deionized water (DI)) present in the etchant. Given the many possible components in an etchant, not only multiple reactions at the surface of the semiconductor can occur, but also reactions between the different components can take place. In turn, these reactions also affect what happens on the surface. Because of this, most etch processes are developed rather by trial and error and intuition

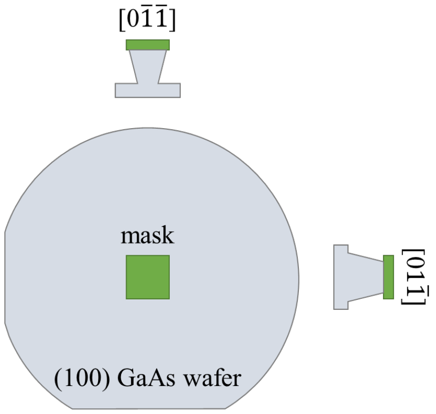

Figure 2.2: Etch profiles of a (100) GaAs substrate for the mask aligned to the [0$\bar{1}\bar{1}$] and [01$\bar{1}$] crystal direction.

than based on a thorough theoretical background. Therefore, the scope of this section is not to provide a theoretical explanation of the different etch processes that were used to fabricate the lasers. Rather we want to give an overview of the etchants used in this work. We will discuss the advantages and disadvantages of the different etchants, the observables during etching and ideal etching conditions.

As shown in Table 2.1, the layer thicknesses of the laser stack vary between tens of nanometers and hundreds of nanometers. In order to have good control over the etch process, we are typically looking for etch speeds between 100nm/min and 1μm/min. Even when the etchant is highly selective, controllable etch speeds are still important to avoid massive undercut during etching.

2.2.1 Non-selective wet etching of GaAs and AlGaAs

2.2.1.1 Sulfuric-based etching

When etching GaAs and AlGaAs in H_2SO_4:H_2O_2:H_2O, hydrogen peroxide (H_2O_2) acts as the oxidizing agent and sulfuric acid (H_2SO_4) dissolves the oxidized surface. In order to slow down the etch speed we can dilute the etchant in DI water.

The etching of GaAs and AlGaAs in H_2SO_4:H_2O_2:H_2O can be both diffusion and reaction rate limited depending on the concentrations of the different components in the etchant and the fraction of aluminum in the AlGaAs alloy. In general we see a transition of a reaction rate limited to a diffusion limited process with increasing Al-percentage, since the oxidation speed increases with increasing Al mole fraction.

A first etching solution used to fabricate the heterogeneously integrated quantum dot lasers, is the commonly used 1:1:18. Etch rates vary between 200 nm/min for GaAs and 300 nm/min for $\mathrm{Al}_{0.4}\mathrm{Ga}_{0.6}\mathrm{As}$. The etching solution is prepared 10 minutes before etching to allow the etchant to return to room temperature after mixing, because mixing the H_2SO_4:H_2O_2:H_2O etch solution is an exothermic process. Firstly, we use this etchant to etch away the n-GaAs contact layer (150 nm), which is sitting directly on top of the DVS-BCB bonding layer. Selectivity is needed nor wanted. On top of the n-GaAs contact layer is a 10 nm thick graded SCH n-$\mathrm{Al}_x\mathrm{Ga}_{1-x}\mathrm{As}$, were the concentration of aluminum varies between 0.0 and 0.4. This layer is partially removed in an earlier step during the etching of the n-$\mathrm{Al}_{0.4}\mathrm{Ga}_{0.6}\mathrm{As}$ cladding layer, using a selective etchant. But some aluminum containing material might still be present as the etch rate of the selective etchant slows down with decreasing aluminum concentration. Therefore, the non-selective H_2SO_4:H_2O_2:H_2O (1:1:18) makes sure to remove everything still present. Since the n-GaAs layer is immediately on top of the SOI, the etch process cannot etch away too much. Secondly, the etch solution is used when we want to isolate part of the top p-GaAs contact layer. This requires etching completely through the p-contact layer and around 100 nm in the p-$\mathrm{Al}_{0.4}\mathrm{Ga}_{0.6}\mathrm{As}$ cladding layer. Since the p-cladding has a thickness of 1.5 μm it is safe to rely on timing alone to determine when to stop etching.

Secondly we use a 5s dip in a 1:1:40 etch solution before depositing the p- and n-contacts. This ensures a fresh surface of GaAs on which the contacts can be deposited, like also described in [23].

2.2.1.2 Nitric-based etching

The first step after bonding the III-V die on the SOI substrate is the removal of the GaAs substrate. Since this substrate has a thickness of 450 μm, we remove the major part of the substrate with a fast non-selective etch solution HNO_3:H_2O_2:H_2O (1:4:1). At room temperature, this etch solution has an etch rate around 5 μm/min. The advantages of a nitric acid-based etchant are that it is repeatable, easy and no contaminations arise. We etch the substrate until 50 μm of GaAs is left. For the remainder of the substrate we need a selective etchant to make sure we stop at the etch stop layer. This will be discussed in section 2.2.2.2.

2.2.2 Selective wet etching of GaAs over AlGaAs

2.2.2.1 Citric-based etching

The laser mesa contains multiple GaAs-layers that we want to etch away in a controlled manner without introducing huge undercut. Furthermore, the active layer contains multiple $\mathrm{In}_{0.15}\mathrm{Ga}_{0.85}\mathrm{As}$ layers that need to be etched in order to define the laser mesa. The $C_6H_8O_7$:H_2O_2 (4:1) solution has an etch rate of 250 nm/min in GaAs and around 280 nm/min in $\mathrm{In}_{0.15}\mathrm{Ga}_{0.85}\mathrm{As}$ and a selectivity of around

100 to 1 over $Al_{0.4}Ga_{0.6}As$ [21]. H_2O_2 acts as the oxidizing agent and citric acid ($C_6H_8O_7$) dissolves the oxidized surface.

The $C_6H_8O_7$:H_2O_2 (4:1) etch solution is prepared 15 minutes in advance and put on a shaker to allow the citric acid and hydrogen peroxide to mix and come to room temperature. The 300 nm p-contact layer on top of the 1.5 μm p-$Al_{0.4}Ga_{0.6}As$ cladding is removed selectively by immersing it into the citric acid solution for 1 minute and 10 seconds. Also, the 352 nm active QD layer (for details see layer 10 in table 2.1) on top of the 50 nm n-$Al_{0.4}Ga_{0.6}As$ cladding is etched in 1 minute and 25 seconds. Once the $Al_{0.4}Ga_{0.6}As$ surface is exposed the sample surface appears to be light pink. Although the etchant is selective, over-etching is unwanted to avoid the p-contact layer to become too thin.

Furthermore, the $C_6H_8O_7$:H_2O_2 (4:1) is also used to remove the sacrificial 40 nm GaAs on top of the 70 nm thick $Al_{0.85}Ga_{0.15}As$ sacrificial layer by exposing the GaAs surface to the etchant for 30 seconds. The sample color changes to blue when the $Al_{0.85}Ga_{0.15}As$ layer is reached.

2.2.2.2 Ammonia-based etching

For the removal of the GaAs substrate (thickness: 450 μm) after bonding, we need a high etching speed. Furthermore, a high selectivity to the etch stop layer ($Al_{0.85}Ga_{0.15}As$) is needed. For this we use a NH_4OH:H_2O_2 (1:19) etching solution. This solution has an etch rate of approximately 3-4 μm/min. Since this etch rate slows down over time, we will only use this solution to etch the last 50 μm of the substrate. Moreover, we noticed that the ammonia-based etchant introduced quite some non-uniformity on the sample. Because of the selectivity of GaAs over the $Al_{0.85}Ga_{0.15}As$ etch stop layer in NH_4OH:H_2O_2 (1:19) this is no problem in a 50 μm etch step. However, when the etching step takes too long, the risk of etching away the etch stop layer increases. Therefore, the first 400 μm of the substrate is etched away with a nitric-based solution, as described in section 2.2.1.2.

The origin of this non-uniformity and the etching speed that is difficult to reproduce lies in the principle behind the etching. The basic principle of oxidizing the surface through the presence of H_2O_2 is retained, however vigorous agitation of the etchant is needed to mechanically remove the GaAs-oxide. After the oxide has been loosened the process can restart. AlGaAs is believed to form a stronger oxide, more difficult to remove than the less stable GaAs-oxide, hence explaining the selectivity. [22]

During etching, the NH_4OH:H_2O_2 (1:19) etching solution is stirred the entire time. Since the etch rate is variable, we rely on the color change of the sample to determine if the etch process is finished. The appearance of a reddish color indicates that the $Al_{0.85}Ga_{0.15}As$ etch stop layer is reached. Typically the discoloration starts in one corner of the sample after which the color slowly spreads over the sample and a rainbow pattern appears when the $Al_{0.85}Ga_{0.15}As$ layer gets oxidized. When the sample is all colorful, the substrate is completely removed. We also noticed small bubbles appearing on the sample surface during etching, slowing down the etch speed. We believe them to be O_2-bubbles caused by the dissociation of the hydrogen peroxide in a basic environment. When these bubbles are too numerous, it can help to lift the sample out of the etchant so the bubbles disappear before continuing the etch process.

2.2.3 Selective wet etching of AlGaAs over GaAs

Where there are multiple etchants available to selectively etch GaAs over AlGaAs, it is much harder to find etchants that selectively etch AlGaAs over GaAs, especially when the aluminum concentration is not very high (e.g. 40% in both cladding layers).

Moreover, as already explained in section 2.1, we want undercut structures in the spot-size converter. This allows us to make much smaller taper tips in the III-V than would normally be possible with our contact lithography tool. In practice this means we need a reaction limited etchant that etches along the crystal planes to etch the thick 1.5 μm p-$Al_{0.4}Ga_{0.6}As$ cladding layer. By carefully choosing the orientation of the III-V die with respect to the SOI, the realization of very narrow taper tips becomes possible.

2.2.3.1 KI:I_2 etching

One of the most important steps is the etching of the 1.5 μm thick p-$Al_{0.4}Ga_{0.6}As$ cladding layer. Since this layer is considerably thicker than the other device layers, the etch profile of this layer determines mostly how the laser mesa will look like. As already explained we are looking for a large contact surface, but a small taper tip. So preferably after etching, the p-$Al_{0.4}Ga_{0.6}As$ cladding layer looks something like a reverse triangle.

We only found one etchant that could etch $Al_{0.4}Ga_{0.6}As$ selectively over GaAs and was also reaction rate limited: an iodine-potassium iodide solution, $KI:I_2:H_2O$ (83.5 g:48.8 g:72 ml). The etch principle of this solution is not so well known. In literature [22, 24] it is mostly described as a redox reaction. In such a system, the oxidation (the reaction limit in the etch process) is determined by the concentration of the oxidizer relative to the concentration of the reducer. Dissolving the oxide layer is determined by the pH of the solution.

In figure 2.3 we see a scanning electron microscope (SEM) picture of a focused ion beam (FIB) cross-section of two perpendicular stripes of an $Al_{0.4}Ga_{0.6}As$ layer. We can clearly see that the etching happens along the crystal planes, as is also described in literature [25]. For the laser mesa we are interested in a big contact surface, but small taper tip, so we want our laser mesas to look like figure 2.3b.

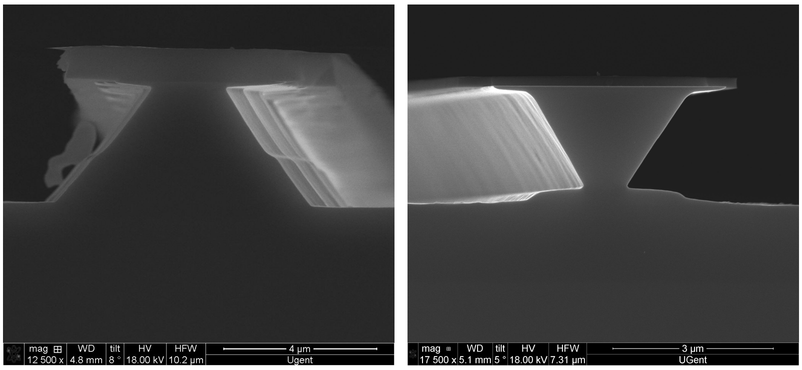

(a) Resist mask along the $(01\bar{1})$ direction **(b)** Resist mask along the $(0\bar{1}\bar{1})$ direction

Figure 2.3: Etch profiles of $Al_{0.4}Ga_{0.6}As$ in an $KI:I_2:H_2O$ etch solution. Since the the process is reaction rate limited, the etching occurs along the crystal planes.

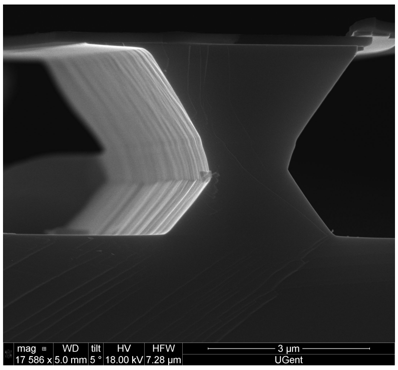

Figure 2.4: An offset appears during etching of $Al_{0.4}Ga_{0.6}As$ in an $KI:I_2:H_2O$ etch solution.

When looking at a cross-section of the stripe before the etch process is completely finished, we see an offset in the etch profile, as is shown in figure 2.4. Etching for a longer time, makes this offset move down until it completely vanishes. This is something we have to take into account when using height measures to assess the progress of the etching. We can use a profilometer to measure the height difference between the III-V surface and the mask. However, according to this measurement when the measured height is equal to the layer thickness of the layer we want to etch, it seems like the etching is finished. In reality we need to continue etching until the offset is completely gone.

The $KI:I_2:H_2O$ etch solution is used to etch the 1.5 μm thick p-$Al_{0.4}Ga_{0.6}As$

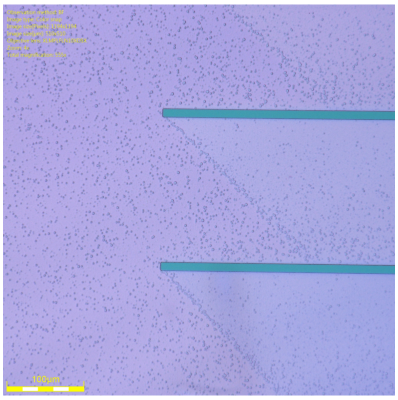

Figure 2.5: Residue of the etching of $Al_{0.4}Ga_{0.6}As$ in an $KI{:}I_2{:}H_2O$ etch solution.

cladding layer and stop on the GaAs barrier around the active layer. Since the solution is dark brown, it is not possible to see the surface of the chip during etching, let alone any color change. Moreover we also need to etch until the offset has vanished completely. We found that it takes around 30 seconds to etch completely through the 1.5 μm thick AlGaAs cladding layer. Another 30 seconds is needed to get rid of the offset.

The residue of etching AlGaAs in $KI{:}I_2{:}H_2O$ can stick firmly to the etched surface and when it sticks, it is impossible to remove again. An example of this is shown in figure 2.5. Therefore it is of paramount importance to hold the sample vertically in the etch solution and stir continuously. When removing the sample from the solution flowing water should be applied immediately for at least 1 minute to end up with a clean sample.

2.2.3.2 HF-based etching

Etching of $Al_{0.4}Ga_{0.6}As$ in HF has been reported to be very slow at room temperature, with an etch rate around 10 nm/min. The etch rate increases rapidly for aluminum concentrations of 58% and above. [26]. Therefore, we cannot use HF to etch our laser mesa.

However, a 10 second dip in diluted HF (40 ml HF (40%): 760 ml DI) can be useful to remove (native) oxides on a GaAs surface.

2.2.3.3 HCl-based etching

Although there is little data available on etching AlGaAs in hydrocloric acid (HCl), we can use this etchant, commonly used in the InP world, to etch AlGaAs with an Al composition higher than 0.6 [27, 28]. Therefore, it is unsuited to etch the laser mesa, but well suited to remove the $Al_{0.85}Ga_{0.15}As$ etch stop and sacrificial layers. The GaAs-layers are not etched in HCl, it only removes the GaAs-oxide, should there be one. Due to the dangers associated with etching in HF, we prefer a dip in HCl to remove native oxide.

A (1:1) HCl:H_2O solution is used to etch the 800 nm thick $Al_{0.85}Ga_{0.15}As$ etch stop layer. Before etching, the solution was allowed to cool down to room temperature for 30 minutes. The $Al_{0.85}Ga_{0.15}As$ etch stop layer is etched by immersing the III-V-on-SOI sample in the solution for 2 minutes immediately after the rainbow pattern appeared during the substrate removal in NH_4OH:H_2O_2. The AlGaAs layer is removed completely when all colors are gone and the surface is shiny again. The 70 nm thick $Al_{0.85}Ga_{0.15}As$ sacrificial layer is also removed in a HCl:H_2O (1:1) solution.

Secondly, HCl can also be used for digital etching. In most etch processes oxidizing and dissolving the oxidized material happen simultaneously. However, digital etching separates both steps so that each reaction is independent from the other. In this way the etch depth is controlled perfectly and the resulting surface is extremely smooth [29]. First the GaAs is oxidized by putting it in H_2O_2 for 1 minute. A stable native oxide (thickness around 1.15 nm) of GaAs is formed by a self-limiting process, leaving the sample for a longer time in the H_2O_2 will not impact the oxide thickness. Next, the chip is thoroughly rinsed to avoid mixing of the H_2O_2 with the HCl solution. After that the chip is put in a HCl:H_2O (1:1) solution to etch away the oxide layer. The unreacted GaAs underneath is unaffected. Next, the chip is rinsed again. This process can be repeated for many cycles.

At the end of the substrate removal procedure and right before the deposition of the nitride hard mask, we use 3 cycles of digital etching to ensure a clean and smooth p-GaAs surface.

2.2.4 Overview of the etchants

Table 2.2 summarizes all the different etchants used to realize the heterogeneously integrated InAs/GaAs quantum dot lasers.

Material	**Solution**	**Proportions**	**Etch rate**	**Note**
GaAs	H_2SO_4:H_2O_2:H_2O	1:1:18	200 nm/min	
		1:1:40		
	HNO_3:H_2O_2:H_2O	1:4:1	5 μm/min	Etch speed not uniform over surface
	$C_6H_8O_7$:H_2O_2	4:1	250 nm/min	
	NH_4OH:H_2O_2	1:19	3-4 μm/min	Constant stirring required. Etch speed slows down over time
	HF dip	40ml HF (40%): 760ml DI	-	Remove native oxide
	HCl:H_2O dip	1:1	-	Remove native oxide
	HCl:H_2O and H_2O_2		around 1.5 nm/cycle	Digital etching
$Al_{0.4}Ga_{0.6}As$	H_2SO_4:H_2O_2:H_2O	1:1:18	300 nm/min	
	KI:I_2:H_2O	83.5g:48.8g:72ml	750-1500 nm/min	
$Al_{0.85}Ga_{0.15}As$	HCl:H_2O	1:1	400 nm/min	
InAs/InGaAs QDs	$C_6H_8O_7$:H_2O_2	4:1	280 nm/min	

Table 2.2: Overview of the etchants used to fabricate the lasers.

2.3 Fabrication of the lasers

The fabrication of heterogeneously integrated lasers on silicon is not straightforward. In addition to developing a robust and repeatable chip fabrication process, it is very important to design a proper set of lithographic masks. First we discuss mask design, then we talk about the adhesive bonding of GaAs-based III-V material. Subsequently we look at the post-bonding process flow in more detail.

2.3.1 Mask design

The first step in fabricating lasers is to carefully design the lithographic contact masks. Figure 2.6 shows an image of the full mask layout including the silicon layers (pink) and the III-V layers (other colors). Except for the lasers, the mask also contains a number of other structures:

1. **Alignment markers for silicon and post-bond processing:** The markers consist of a cross surrounded by Vernier rectangles. The former allow for coarse alignment, whereas the latter can be used for very precise alignment. We use both global and local markers. The global markers are etched in the silicon and located as far away from the laser structures as the size of the silicon chip will allow (not visible in figure 2.6). The reason for this distance is twofold: first, after bonding all markers on the silicon close to the laser structures are covered by the epi. Second, the further the markers are spaced from each other, the more accurate alignment can be done. Typically these global markers are used during the first lithographic step where the III-V laser mesa's are positioned with respect to the underlying SOI structures. During this step, the local markers are defined surrounding the laser structures, as can be seen in figure 2.6. These markers are used for the rest of the post-bond processing.
2. **TLM structures:** Metal contacts may be the most common reason optoelectronic devices fail and therefore having sufficient test structures is important. The TLM (transmission line method) test structures allow us to measure the contact resistivity and sheet resistance of both n- and p-contact in detail. The distance between two contacts varies from 4 to 50 μm.
3. **Etch markers:** During wet etching we want to monitor the progress of the etching and the amount of undercut without needing to do a focused ion beam (FIB) cross-section too many times. Etch markers are stripes in the III-V with different widths ranging from 2 to 12 μm. We have both stripes parallel with the laser structures and perpendicular to the laser structures since the etching can be dependent on the crystal planes. The more etch markers fly off, the more undercut has happened.

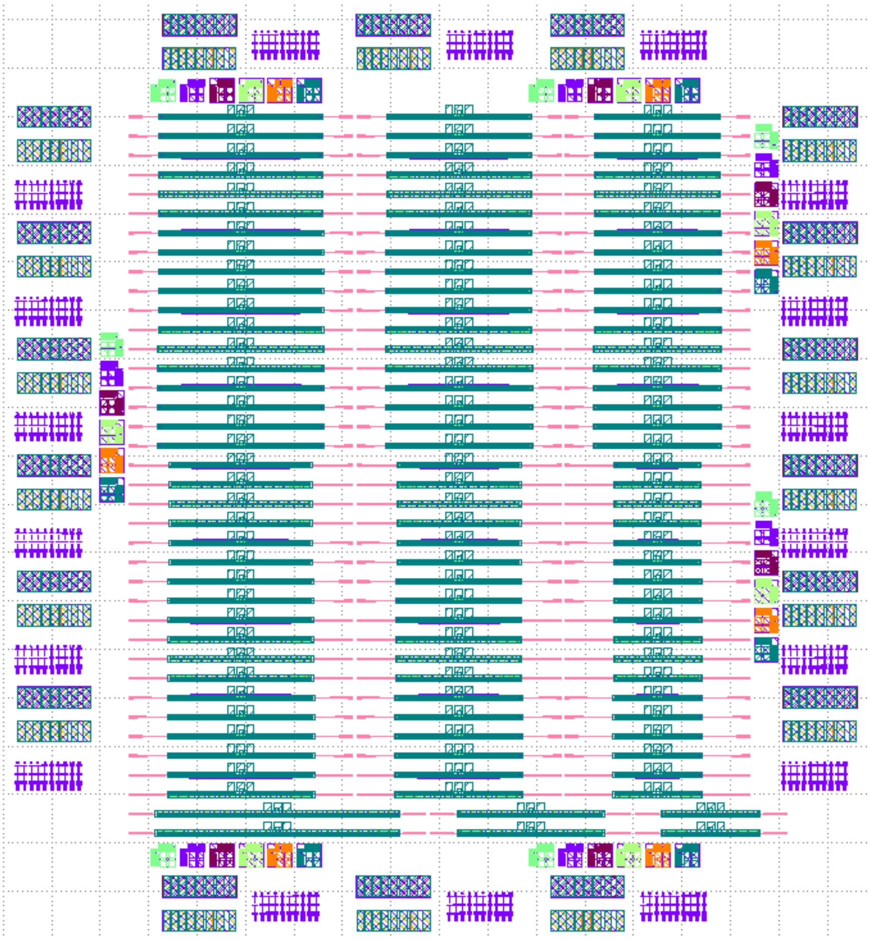

Figure 2.6: Full mask layout for the DFB lasers, including the silicon layers (pink) and III-V layers (other colours).

A microscope image of the extra structures during processing is shown in figure 2.7.

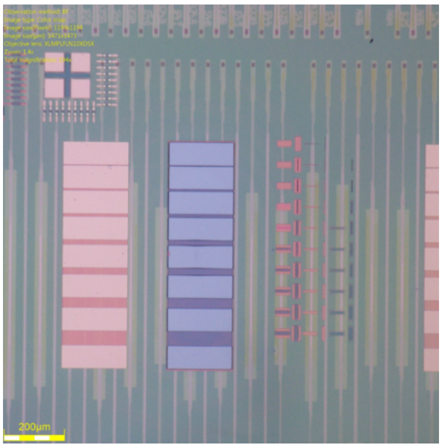

Figure 2.7: Microscope image of the alignment markers, TLM structures and etch markers right before the deposition of the p-contacts.

2.3.2 Adhesive bonding

Wafer bonding involves bonding an unpatterned III-V die or wafer to an SOI chip either by interfacial bonds (direct) or by using a ”glue” (adhesive), and processing it further to fabricate the integrated laser [5]. While direct bonding can be used to transfer GaAs epi onto an SOI waveguide wafer, adhesive bonding using DVS-BCB offers some significant advantages and will be used in this work. The relaxed requirements on surface cleanliness, contamination and surface roughness combined with the planarization capability of DVS-BCB, offer a significant reduction in surface preparation.

Preparation of the SOI sample

An SOI die is cleaved from a multi-project wafer (MPW). Protective photoresist is removed with acetone and iso-propylalcohol (IPA). Afterward the remaining polymers are removed by a 10 minute O_2-plasma etch. Subsequently a diluted DVS-BCB solution is spin-coated at 3000 rpm on the SOI die. Mesithylene is used for dilution, where for a 60 nm bonding layer thickness on top of the waveguide a 1:6 DVS-BCB:mesithylene dilution is needed. A partial cure of 30 min at 180 °C ensures flatness across the entire die.

Preparation of the III-V sample

To achieve a good bonding, it is important to start with very clean bond interfaces. Therefore sacrificial layers are often present in the epitaxial layer stack that are removed just before the bonding. However experience has learned that the less the sample is touched before the bonding, the less chance there is of dirt getting on the sample. So we chose to not include sacrificial layers in our layer stack. To protect the wafer, resist is spin-coated upon arrival of the wafer in the cleanroom.

When preparing a new sample, first a piece of III-V is cleaved from the wafer taking into account the crystal orientation of the epi material as shown in figure 2.2. The minor flat (the $[0\bar{1}\bar{1}]$ crystal plane) should be parallel to the lasers. Typically, the cleaved die is a 1.1 cm × 1.0 cm rectangle. Second, the resist is removed by spraying acetone and IPA on the sample. Third, the sample is put in the PECVD to deposit a 10 nm thin SiO_2 layer for better adhesion. The sample is not touched again until the actual bonding.

Bonding

Both dies are now brought into contact by flipping the III-V die upside down and placing it on the DVS-BCB coated SOI die. A set of pyrex carrier wafers is used to keep the III-V and SOI die in place. The whole is then loaded in the bonding machine. Machine bonding is employed to control the pressure applied on the sample, resulting in an improvement of thickness uniformity of the bonding layer. A Suss MicroTec ELAN CB6/8L wafer bonding machine is used in this work.

In the bonder, the temperature is increased step by step. After the sample reaches 150 °C, a pressure between 85 mbar and 100 mbar is applied. The exact pressure depends on the size and thickness of the III-V die. While the bonder is applying pressure, the temperature is further increased, first to 180 °C and then to 250 °C. This happens all in vacuum. After the pressure head is lifted, the sample remains at 250 °C for another hour to bake. Afterwards it is slowly cooled down to finalize the bonding process. We now have an SOI sample with a GaAs-based epitaxial layer stack bonded to it, as shown in figure 2.9a. In figure 2.8 an SEM picture of a thin DVS-BCB bonding layer in between planarized SOI and the QD epitaxial layerstack is shown.

Substrate removal

Next the 450 μm thick substrate is removed. An overview of the substrate removal process flow is presented in figure 2.9.

- **Protect the DVS-BCB:** Before removing the GaAs substrate, a wax (CrystalBond 509) [30] is applied around the die to protect the edges of the III-V and the DVS-BCB bond-interface during the etching process. CrystalBond

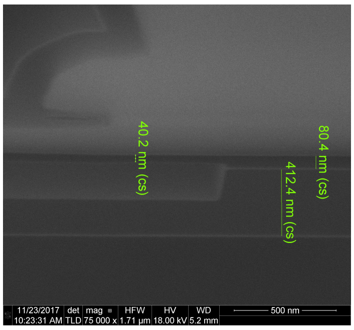

Figure 2.8: SEM picture of a FIB cross-section of the thin DVS-BCB bonding layer in between the SOI and the InAs/GaAs QD layerstack.

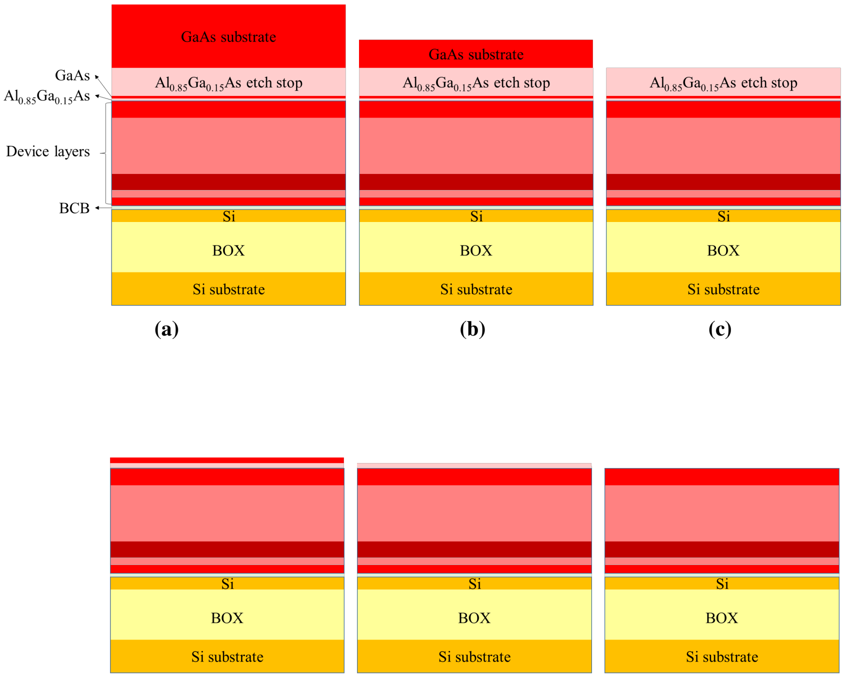

(a) (b) (c)

(d) (e) (f)

Figure 2.9: Schematic process flow for the removal of the GaAs substrate.

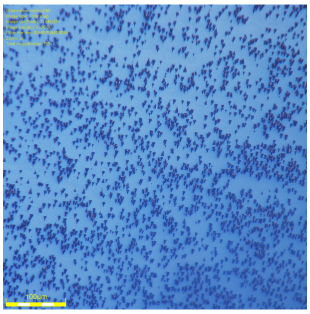

Figure 2.10: Grass formed as result of a reaction between nitric-etch-residue and the ammonia etch.

509 can be dissolved in acetone. The CrystalBond 509 wax exhibits strong adhesion and high chemical resistance which makes it suitable for sidewall protection during the substrate removal process. The wax is melted by heating it to 125 °C in a glass petri dish. With the help of a sharp cotton tip, the melted wax is carefully applied at the edges of the bonded III-V. We have to make sure no wax is present on top of the III-V die since this effectively blocks the substrate removal.

- **Nitric acid etch:** We remove the major part of the substrate with a fast non-selective etch solution HNO_3:H_2O_2:H_2O (1:4:1). At room temperature, this etch solution has an etch rate around 5 μm/min and gives rise to non-uniformity across the sample, typically around 30 μm. Since the etchant is not selective it is important to stop when 50 μm of the substrate is left. This is illustrated in figure 2.9b. When the nitric-based etching is finished, the sample must be rinsed thoroughly by keeping it under running water for at least 5 minutes. This to avoid a reaction between nitric residue and the ammonia-based etchant that follows, since this gives rise to ”grass” on the sample which is impossible to remove. A picture of this is shown in figure 2.10.

- **Ammonia etch:** The remainder of the substrate is removed in NH_4OH:H_2O_2 (1:19). As explained in section 2.2.2.2 the solution should be stirred the entire time. Since the etch rate is uncontrollable, we rely on color change to know when we reached the $Al_{0.85}Ga_{0.15}As$ etch stop layer. Typically this takes around 20 to 30 minutes. When the sample is all colorful, the substrate is completely removed.

- **Remove the etch stop layer:** As illustrated in figure 2.9c in a next step we remove the 800 nm thick $Al_{0.85}Ga_{0.15}As$ etch stop layer. This layer is removed selectively in $HCl:H_2O$ (1:1) in 2 to 3 minutes and stops on the GaAs sacrificial layer. The III-V surface is now nice and shiny.

- **Remove wax and ears:** At the edge of the bonded III-V die some GaAs bulk material may sometimes remain, called ears. This unevenness can negatively affect the optical lithography in subsequent steps during the laser fabrication. Therefore, a sharp scalpel is used to scratch the ears away from the bonded III-V die. The sample is protected in advance by spin-coating a thick layer of resist. This way we can prevent scraped particles from sticking to the III-V surface.
- **Remove sacrificial layers:** Lastly the sacrificial GaAs and $Al_{0.85}Ga_{0.15}As$ layers are removed. The 40 nm thick GaAs layer is removed in $C_6H_8O_7:H_2O_2$ (4:1) by exposing the GaAs surface to the etchant for 30 seconds. The sample color changes to blue when the $Al_{0.85}Ga_{0.15}As$ layer is reached. The 70 nm thick $Al_{0.85}Ga_{0.15}As$ layer is removed selectively in $HCl:H_2O$ (1:1). The exposed p-GaAs contact layer is subsequently subjected to 3 cycles of digital wet etching by alternating the exposure of the GaAs surface to H_2O_2 and $HCl:H_2O$ (1:1) for 1 min in separate steps. This etch step completely removes possible residues from the AlGaAs etching and ensures a very clean interface with the p-contacts.

2.3.3 Process flow: details of the individual processing steps

An overview of the fabrication process flow is presented in figure 2.11.

P-mesa definition

First a 300 nm thick SiNx layer that acts as hard mask is deposited on top of the p-GaAs surface via PECVD at 270°C. After patterning of the SiNx layer through optical contact lithography, the hard mask is defined through reactive ion etching (RIE) (figure 2.11a). Preferably, the hard mask is deposited immediately after the digital wet etch such that there is no chance to contaminate the GaAs surface.

The 300 nm thick p-GaAs contact layer is etched in a $C_6H_8O_7:H_2O_2$ (4:1) solution for 1 minute (figure 2.11b). Although the etchant is selective, we do not etch longer than necessary to avoid undercut of the mask, since more etch steps that attack the side of the p-GaAs contact layer are still to come.

Next, the 1.5 μm thick p-$Al_{0.4}Ga_{0.6}As$ cladding layer is wet etched in $KI:I_2:H_2O$ (figure 2.11c). As explained in section 2.2.3.1, it is not straightforward to monitor the progress of the etching. Therefore, we put etch markers with different widths in our design. At the start of the mesa etch all etch markers, even the most narrow are still intact. When the etching continues, the markers fly off one by one, nicely visualizing the etch progress. This is illustrated in figure 2.12.

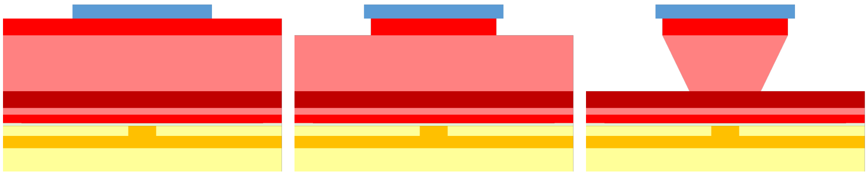

(a) p-mesa SiN hard mask

(b) p-GaAs contact layer etch

(c) p-AlGaAs cladding layer etch

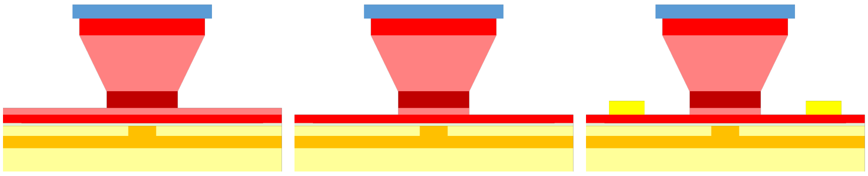

(d) QD layer etch

(e) n-AlGaAs cladding layer etch

(f) n-metal

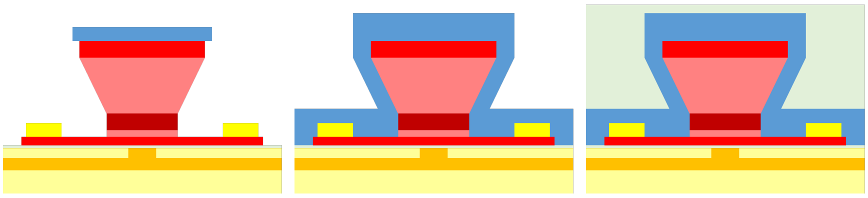

(g) Island etch

(h) Passivation

(i) Planarization

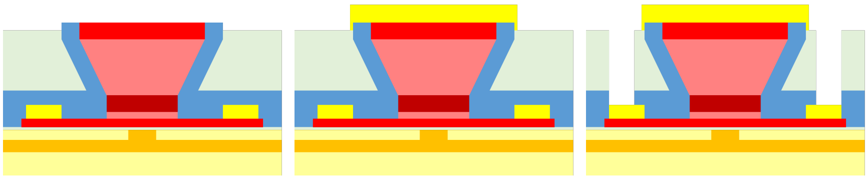

(j) DVS-BCB and SiN opening for p-contacts

(k) p-metal

(l) Via definition

Figure 2.11: Process flow for the III-V on Si laser fabrication showing cross-sections at the various processing steps

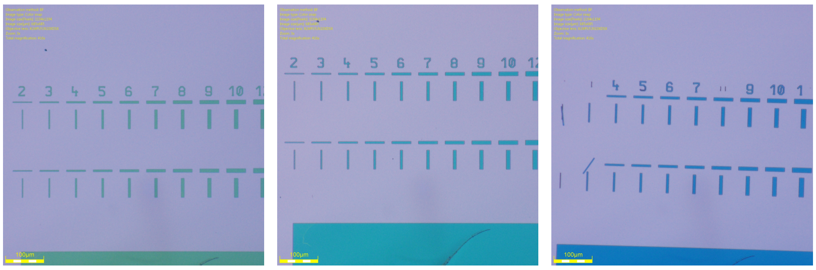

(a) At the start of the mesa etch

(b) After 30s etching in KI:I_2:H_2O

(c) After 60s etching in KI:I_2:H_2O

Figure 2.12: Microscope images of the etch markers that visualize the etch progress during etching in KI:I_2:H_2O.

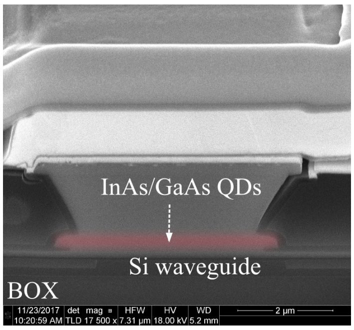

Figure 2.13: SEM picture of a FIB cross-section of the laser mesa.

Thereafter, the 352 nm thick QD active region is etched in $C_6H_8O_7$:H_2O_2 (4:1) in 1 minute and 25 seconds (figure 2.11d). Once the n-$Al_{0.4}Ga_{0.6}As$ surface underneath is exposed the sample surface appears to be light pink. Although the etchant is selective, over-etching is still unwanted to avoid the higher up p-contact layer to become to small.

Lastly, the 50 nm thick n-$Al_{0.4}Ga_{0.6}As$ cladding layer is etched away by dipping the sample for 10 seconds in KI:I_2:H_2O (figure 2.11e). The sample now has a pink, yellowish color.

The reaction rate limited wet etching of the p-AlGaAs cladding layer in KI:I_2:H_2O results in a V-shaped structure dependent on the crystal orientation. This is beneficial for the adiabatic tapered coupler used to couple light from the GaAs waveguide to the underlying silicon waveguide. This is illustrated in a scanning electron microscope (SEM) picture of a focused ion beam (FIB) cross-section of the III-V mesa shown in figure 2.13.

We noticed that all the above described wet etch processes sometimes fail to continue after the sample is exposed to air. We believe this is caused by oxidation of the surface when in contact with air. This problem is simply resolved by dipping the sample in buffered hydrofluoric acid (BHF) or HCl:H_2O (1:1) for 5 seconds before continuing with the etching.

N-type contact metallization

The n-type ground contact structures are defined through an image-reversal optical contact lithography step (figure 2.11f). First, we dip our sample in H_2SO_4:H_2O_2:H_2O (1:1:40) for 5 seconds to ensure a fresh surface of n-GaAs on which the contacts are deposited. Next, a 30:20:50 nm Ni:Ge:Au + 40:50 nm Ti:Au metallurgy is used. The extra Ti:Au improves the protection of the contact during a later via definition step. In figure 2.14 a microscope image of the sample after lift-off is shown.

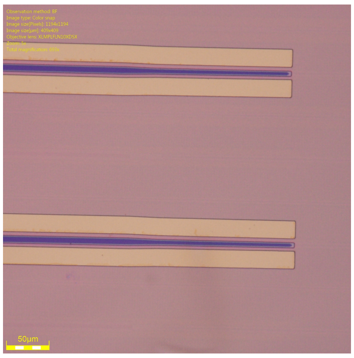

Figure 2.14: Microscope image of two laser mesa's after n-contact metallization.

Island definition

During the island definition the individual laser structures are electrically isolated from each other. The islands are patterned through optical contact lithography after which the bottom n-type GaAs contact layer is etched in the non-selective H_2SO_4:H_2O_2:H_2O (1:1:18). This step is shown in figure 2.11g.

Planarization

A 300 nm thick conformal SiNx layer is deposited through PECVD (figure 2.11h). Afterward an undiluted DVS-BCB layer is spin-coated to planarize the sample (figure 2.11i). A typical 50 nm topography is achieved. The planarized sample is then etched back through RIE. First the DVS-BCB is etched back in an SF_6/O_2

RIE plasma. Subsequently, around 150 nm to 200 nm of the 600 nm thick SiNx layer is etched away in an $CF_4/H_2/SF_6$ RIE plasma.

P-type contact metallization

Another image-reversal optical contact lithography step is used to define the p-type contact. First the remainder of the SiNx above the p-type GaAs contact layer is removed through RIE (figure 2.11j). Just before deposition, a short (5 seconds) H_2SO_4:H_2O_2:H_2O (1:1:40) dip removes any oxidized layer and ensures a fresh p-GaAs surface. Next 40:150 nm Ti:Au is deposited by sputtering in the Univex. After lift-off the sample is annealed at 430°C for 30 seconds. This is illustrated in figure 2.11k.

Via etching

Then openings are defined to reach the n-type ground contact. The DVS-BCB material and underlying SiNx layer are removed through RIE (figure 2.11l).

Final metallization

Finally, probe pad metal was deposited in a ground-signal-ground (GSG) configuration. Figure 2.15 shows a microscope top image of an array of fully processed DFB lasers.

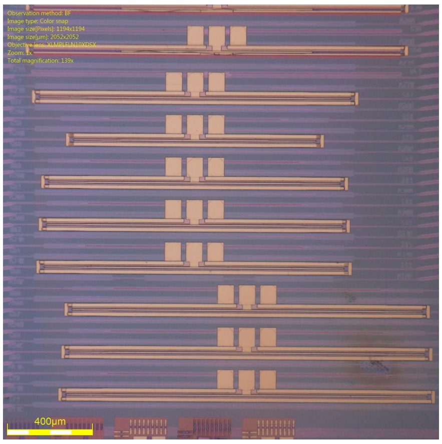

Figure 2.15: Optical microscope image of a fabricated chip with a set of DFB lasers.

2.4 Transfer-printing of GaAs-based lasers on the silicon photonics platform

Micro-transfer-printing (μTP) is a technology in which devices or materials are selectively picked from a source wafer (or substrate) and printed in parallel to a host wafer (or any other suitable platform). This is illustrated in figure 2.16.

(a) Patterned stamp with multiple posts

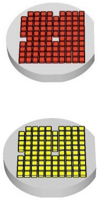

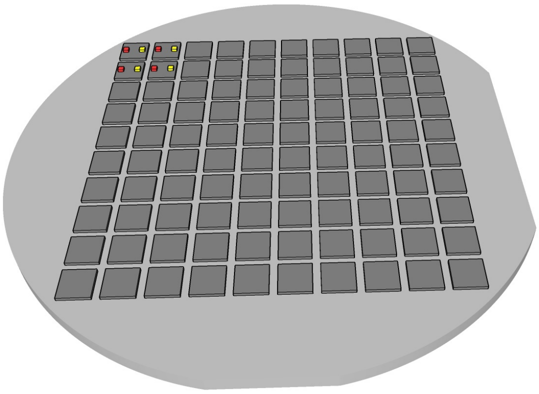

(b) Two source substrates with patterned coupons

(c) SOI target substrate with four printed coupons of each source in top left.

Figure 2.16: Transfer-printing of four coupons of two different III-V source wafers to SOI. The stamp with multiple posts ensures the high throughput, while the small coupons allow for spatial design freedom. The area magnification is readily apparent as the entire SOI wafer can be populated using the small III-V wafers. Picture courtesy from Andreas De Groote [31].

This is done by releasing components from the source wafer through undercut etching and picking these components up using a suitably microstructured elastomeric stamp. The stamp is manufactured by casting polydimethylsiloxane (PDMS) against a microfabricated master wafer. The process can be applied on many different wafer or substrate materials and structures. [32] This approach shows a lot of advantages:

- It makes very efficient use of III-V material. The III-V wafer (here the source wafer) can be completely used for lasers. There is no need to etch part of it away like is the case with bonding, where the minimum die size that can be handled is limited. So the III-V loss is kept to a minimum.
- One small III-V wafer can be used for the realization of several complex

silicon photonic integrated circuit wafers. This is called area magnification. It is illustrated in figure 2.16.

- Lasers can be tested before integration on 200 mm or 300 mm active silicon wafers.
- The number of lasers that is printed can easily be upscaled.
- The number of post-processing steps on the full platform is kept to a minimum.
- The development of this technique will ultimately permit the integration of multiple other functions onto the silicon photonics platform.

2.4.1 Fabrication process

In figure 2.17 the various process steps prior to the actual printing are displayed. First the laser mesa is etched as displayed in figure 2.17a. Since this process was mainly developed for butt-coupled lasers, dry etching is used to etch the mesa in order to have a flat coupling section. Next the whole structure is protected by depositing 250 nm silicon nitride (SiNx), as shown in figure 2.17b. This is followed by two litho steps to define the n- and p-contacts, similar as described in section 2.3.3 (see figure 2.17c). Next, the SiNx is etched away to expose the release layer, as is shown in figure 2.17d. To avoid oxidation of the release layer, it is an option to not completely etch away the n-GaAs contact layer in step a. In that case this layer is removed now in citric acid. Subsequently, anchors are defined by locally etching through the release layer and around 100 nm into the GaAs substrate, depicted in figure 2.17e. It is important to avoid too much undercut in this step, otherwise different anchors might connect to each other and the release layer might become isolated during the encapsulation. In figure 2.17f we see that there is no photoresist on the front and back of the laser. In order to couple the light efficiently into the silicon coupling structures (explained in detail in chapter 3) it is important to make the distance between the III-V device and the silicon coupler as small as possible. If the width of the SiNx layer is chosen smart it can act as an anti-reflection coating. Finally, the release layer is etched as shown in figure 2.17g.

We tested different options for the release layer. The first option is an 800 nm thick InAlP-layer. This layer is an excellent candidate, since it can be etched very selectively in a HCl solution while the post-etching residues are kept to a minimum [33]. This results in a very smooth surface at the bottom of the coupon. However, a thick InAlP-layer might have a negative impact on the quality of the device due to epitaxy concerns. In figure 2.18 a microscope image of the coupons

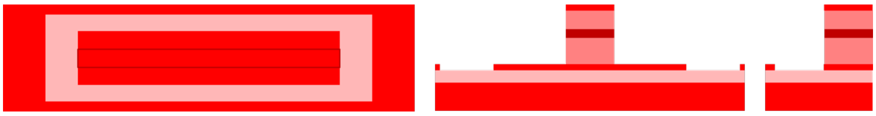

(a) Laser after mesa etch

(b) Passivation with SiNx

(c) Define the contacts (2 litho steps)

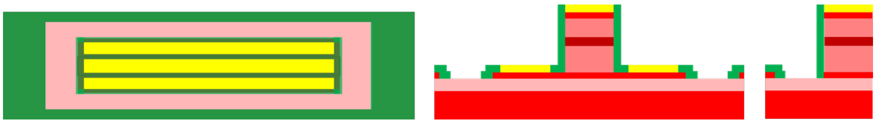

(d) Open streets

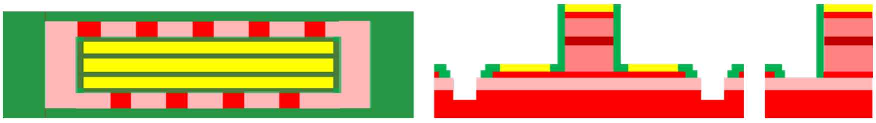

(e) Define anchors

(f) Encapsulate with photoresist

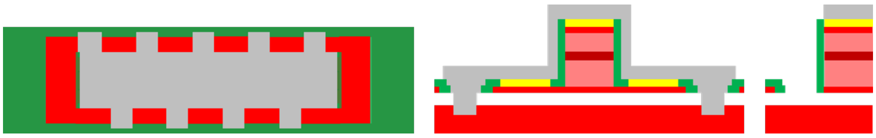

(g) Etch of the release layer

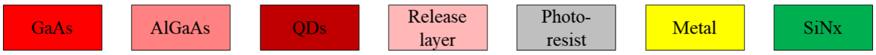

(h)

Figure 2.17: Process flow for the transfer-printing of the III-V laser showing top view, cross-sections and side view at the various processing steps

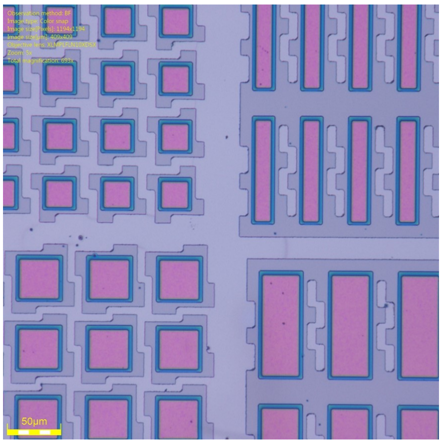

Figure 2.18: Optical microscope image of the test coupons right after the anchor definition in case of an InAlP release layer.

right after the anchor definition (step 2.17e) is shown. In order to define the anchors, diluted hydrochloric acid HCl:H_2O (1:5) with an etch rate of 200 nm/min is used to etch through the release layer in a controlled manner, followed by 30 seconds of $C_6H_8O_7$:H_2O_2 (4:1) to etch into the GaAs substrate. To completely remove the release layer in the final etch step, the sample is put in HCl:H_2O (1:1) for 5 minutes.

The second option is a 1 μm $\mathrm{Al}_x\mathrm{Ga}_{1-x}\mathrm{As}$ layer with a very high aluminum concentration (x = 0.9-0.95). First, the release layer becomes very sensitive to oxidation which makes the process leading up to the release more challenging. Second, the sample is dirty after the release etch due to etching residues. Extra cleaning steps before printing (e.g. by means of digital etching as described in [34]) become necessary. However, since the lasers are long and skinny we are able to rinse well underneath our structures and printing is still possible. Diluted hydrochloric acid HCl:H_2O (1:1) with an etch rate of 1 μm/min is used to etch away the release layer both for the anchor definition and the final release etch which takes approximately 30 minutes.

In the end we were able to demonstrate successful picking and printing of both layer stacks. But we think InAlP is the most suited choice for releasing thin film membranes with respect to ease of processing. This is in line with the the findings reported in [8].

The above research formed the starting point for the CALADAN project, started on January 1st 2019. CALADAN is an European H2020 project which focuses upon the micro-transfer-printing technology to integrate GaAs quantum dot lasers and high-speed SiGe BiCMOS chips onto 300 mm silicon photonic wafers. The purpose of the project is to demonstrate Terabit/s capable optical transceivers for the datacom market segment.

2.5 Conclusion

At the start of this work almost all III-V-on-Si lasers were based on InP QW gain material. InAs/GaAs quantum dot material was never integrated onto a silicon chip with the ability to couple light from the III-V into the silicon waveguide. Therefore, we developed a new fabrication process to realize exactly this. After a thorough investigation of possible wet etchants we got to the final process described in this chapter. The most challenging step of the laser fabrication is the definition of the mesa. Since we need narrow III-V tapers in order to create good coupling structures, we used the crystal orientation of the epi to get faceted surfaces. The appearance of the mesa is largely determined by the 1.5 μm p-AlGaAs cladding layer. Due to the aluminum in this layer, most etchants are diffusion limited and therefore not useful to create undercut structures. We only found one etchant that could etch $\mathrm{Al}_{0.4}\mathrm{Ga}_{0.6}\mathrm{As}$ selectively over GaAs and was also reaction rate limited: an iodine-potassium iodide solution, $KI:I_2:H_2O$ (83.5 g:48.8 g:72 ml). After extensive development we were able to realize working lasers based on this etchant.

We also explored the possibility to create GaAs-based heterogeneously integrated lasers on silicon by means of transfer-printing instead of wafer bonding. We tested different options for the release layer: an 800 nm thick InAlP-layer and a 1 μm $\mathrm{Al}_x\mathrm{Ga}_{1-x}\mathrm{As}$ layer with a very high aluminum concentration (x = 0.9-0.95). In the end we were able to demonstrate successful picking and printing of both layer stacks.

References

[1] Fuad E Doany, Benjamin G Lee, Solomon Assefa, William MJ Green, Min Yang, Clint L Schow, Christopher V Jahnes, Sheng Zhang, Jonathan Singer, Victor I Kopp, et al. *Multichannel high-bandwidth coupling of ultradense silicon photonic waveguide array to standard-pitch fiber array*. Lightwave Technology, Journal of, 29(4):475–482, 2011.

[2] Bradley Snyder, Brian Corbett, and Peter O Brien. *Hybrid Integration of the Wavelength-Tunable Laser With a Silicon Photonic Integrated Circuit*. Journal of Lightwave Technology, 31(24):3934–3942, 2013.

[3] Peter De Dobbelaere, Ali Ayazi, Yuemeng Chi, Anders Dahl, Scott Denton, Steffen Gloeckner, Kam-Yan Hon, Steve Hovey, Yi Liang, Michael Mack, et al. *Packaging of Silicon Photonics Systems*. In Optical Fiber Communication Conference, pages W3I–2. Optical Society of America, 2014.

[4] Guang-Hua Duan, Christophe Jany, Alban Le Liepvre, Alain Accard, Marco Lamponi, Dalila Make, Peter Kaspar, Guillaume Levaufre, Nils Girard, François Lelarge, et al. *Hybrid III–V on Silicon Lasers for Photonic Integrated Circuits on Silicon*. IEEE Journal of selected topics in quantum electronics, 20(4):158–170, 2014.

[5] Günther Roelkens, Liu Liu, Di Liang, Richard Jones, Alexander Fang, Brian Koch, and John Bowers. *III-V/silicon photonics for on-chip and intra-chip optical interconnects*. Laser & Photonics Reviews, 4(6):751–779, 2010.

[6] Tin Komljenovic, Michael Davenport, Jared Hulme, Alan Y Liu, Christos T Santis, Alexander Spott, Sudharsanan Srinivasan, Eric J Stanton, Chong Zhang, and John E Bowers. *Heterogeneous silicon photonic integrated circuits*. Journal of Lightwave Technology, 34(1):20–35, 2016.

[7] Andreas De Groote, Paolo Cardile, Ananth Z Subramanian, Alin M Fecioru, Christopher Bower, Danae Delbeke, Roel Baets, and Günther Roelkens. *Transfer-printing-based integration of single-mode waveguide-coupled III-V-on-silicon broadband light emitters*. Optics Express, 24(13):13754–13762, 2016.

[8] Brian Corbett, Ruggero Loi, Weidong Zhou, Dong Liu, and Zhenqiang Ma. *Transfer print techniques for heterogeneous integration of photonic components*. Progress in Quantum Electronics, 2017.

[9] Stevan Stankovic, Richard Jones, Matthew N Sysak, John M Heck, Günther Roelkens, and Dries Van Thourhout. *Hybrid III–V/Si Distributed-Feedback Laser Based on Adhesive Bonding*. IEEE PHOTONICS TECHNOLOGY LETTERS, 24(23):2155, 2012.

[10] Chong Zhang, Sudharsanan Srinivasan, Yongbo Tang, Martijn JR Heck, Michael L Davenport, and John E Bowers. *Low threshold and high speed short cavity distributed feedback hybrid silicon lasers*. Optics Express, 22(9):10202–10209, 2014.

[11] Sören Dhoore, Anna Köninger, Ralf Meyer, Gunther Roelkens, and Geert Morthier. *Electronically tunable distributed feedback (DFB) laser on silicon*. Laser & Photonics Reviews, 13(3):1800287, 2019.

[12] Zhechao Wang, Kasper Van Gasse, Valentina Moskalenko, Sylwester Latkowski, Erwin Bente, Bart Kuyken, and Gunther Roelkens. *A III-V-on-Si ultra-dense comb laser*. Light: Science & Applications, 6(5):e16260, 2017.

[13] Matthew N Sysak, Di Liang, Raymond Beausoleil, Richard Jones, and John E Bowers. *Thermal management in hybrid silicon lasers*. In Optical Fiber Communication Conference. Optical Society of America, 2013.

[14] M Lamponi, Shahram Keyvaninia, C Jany, F Poingt, F Lelarge, G De Valicourt, Günther Roelkens, Dries Van Thourhout, S Messaoudene, J-M Fedeli, et al. *Low-threshold heterogeneously integrated InP/SOI lasers with a double adiabatic taper coupler*. Photonics Technology Letters, IEEE, 24(1):76–78, 2012.

[15] EU Rafailov, MA Cataluna, and Wilson Sibbett. *Mode-locked quantum-dot lasers*. Nature photonics, 1(7):395–401, 2007.

[16] Nadya Anscombe. *Join up the quantum dots*. Nature Photonics, 1(7):360–361, 2007.

[17] D Bimberg, N Kirstaedter, NN Ledentsov, Zh I Alferov, PS Kop'Ev, and VM Ustinov. *InGaAs-GaAs quantum-dot lasers*. IEEE Journal of selected topics in quantum electronics, 3(2):196–205, 1997.

[18] Zeyu Zhang, Daehwan Jung, Justin Norman, Weng W Chow, and John E Bowers. *Linewidth enhancement factor in InAs/GaAs quantum dot lasers and its implication in isolator-free and narrow linewidth applications*. IEEE Journal of Selected Topics in Quantum Electronics, 2019.

[19] Alan Y Liu, Chong Zhang, Justin Norman, Andrew Snyder, Dmitri Lubyshev, Joel M Fastenau, Amy WK Liu, Arthur C Gossard, and John E Bowers. *High performance continuous wave 1.3 μm quantum dot lasers on silicon*. Applied Physics Letters, 104(4):041104, 2014.

[20] Dieter Bimberg, M Grundmann, F Heinrichsdorff, NN Ledentsov, VM Ustinov, AE Zhukov, AR Kovsh, MV Maximov, YM Shernyakov, BV Volovik, et al. *Quantum dot lasers: breakthrough in optoelectronics*. Thin Solid Films, 367(1):235–249, 2000.

[21] Gregory C DeSalvo, Wen F Tseng, and James Comas. *Etch rates and selectivities of citric acid/hydrogen peroxide on GaAs, Al0. 3Ga0. 7As, In0. 2Ga0. 8As, In0. 53Ga0. 47As, In0. 52Al0. 48As, and InP*. Journal of The Electrochemical Society, 139(3):831–835, 1992.

[22] Peter Van Daele. *Studie van ets-en depositiestappen bij opto-elektronische integratie in III-V halfgeleiders*. Phd-thesis, Universiteit Gent, Faculteit van de Toegepaste Wetenschappen, 1987.

[23] BK Sehgal, VR Balakrishnan, R Gulati, and SP Tewari. *Analysis of Electrical Properties of Ti/Pt/Au Schottky Contacts on (n) GaAs Formed by Electron Beam Deposition and RF Sputtering*. Journal of Semiconductor Technology and Science, 3(1):1, 2003.

[24] Dong Hyun Kim and Hee Chul Lee. *Selective lateral etching of Al0. 3Ga0. 7As/GaAs heterojunction structure using the redox solution of I2/KI*. Japanese journal of applied physics, 36(3A):L253, 1997.

[25] Andrzej Malag, Jacek Ratajczak, and Jerzy Gazecki. *AlGaAs/GaAs heterostructure characterization by wet chemical etching*. Materials Science and Engineering: B, 20(3):332–338, 1993.

[26] P Kumar, S Kanakaraju, and DL DeVoe. *Sacrificial etching of AlxGa1-xAs for III–V MEMS surface micromachining*. Applied Physics A, 88(4):711–714, 2007.

[27] Sulakshna Kumari. *GaAs VCSEL Integration on SiN Waveguide Circuits: Design, Technology and Devices*. PhD thesis, Ghent University, 2017.

[28] C Zhang, D Lubyshev, TN Jackson, DL Miller, and TS Mayer. *The Effect of Al0. 7Ga0. 3As Etch Stop Removal on the Preparation of Wafer-Bonded Compliant Substrates*. Journal of the Electrochemical Society, 146(4):1597–1601, 1999.

[29] Gregory C DeSalvo, Christopher A Bozada, John L Ebel, David C Look, John P Barrette, Charles LA Cerny, Ross W Dettmer, James K Gillespie, Charles K Havasy, Thomas J Jenkins, et al. *Wet chemical digital etching of GaAs at room temperature*. Journal of The Electrochemical Society, 143(11):3652–3656, 1996.

[30] Ted Pella. *Crystalbond^{TM}Adhesives Product Numbers 821-1, 821-2, 821-3, 821-4, 821-6*. `https://www.tedpella.com/technote_html/821-1-2-3-4-6-TN.pdf`.

[31] Andreas De Groote. *Heterogeneous integration of multibandgap III-V semiconductor light sources on silicon photonics*. PhD thesis, Ghent University, 2017.

[32] John Justice, Chris Bower, Matthew Meitl, Marcus B Mooney, Mark A Gubbins, and Brian Corbett. *Wafer-scale integration of group III-V lasers on silicon using transfer printing of epitaxial layers*. Nature Photonics, 6(9):610–614, 2012.

[33] Cheng-Wei Cheng, Kuen-Ting Shiu, Ning Li, Shu-Jen Han, Leathen Shi, and Devendra K Sadana. *Epitaxial lift-off process for gallium arsenide substrate reuse and flexible electronics*. Nature communications, 4:1577, 2013.

[34] Guanyu Chen, Jeroen Goyvaerts, Sulakshna Kumari, Joris Van Kerrebrouck, Muhammad Muneeb, Sarah Uvin, Yu Yu, and Gunther Roelkens. *Integration of high-speed GaAs metal-semiconductor-metal photodetectors by means of transfer printing for 850 nm wavelength photonic interposers*. Optics express, 26(5):6351–6359, 2018.

3

Optical coupling schemes

Silicon photonics, leveraging the well-developed CMOS fabrication infrastructure and its economy of scale, is emerging as an important platform for the realization of power-efficient, high-speed optical transceivers [1]. It allows lower power consumption and enables the scaling of the aggregate bandwidth of transceivers to the Terabit/s range. Today, optical modulators [2], multiplexers and photodetectors [3] suitable for high-performance optical transceivers have already been demonstrated on a silicon-on-insulator (SOI) platform. However, currently the lack of cost-effective integration of the light source limits silicon-based photonic integrated circuits (PIC) deployment in these fields.

As explained in chapter 1, in order to become a competitive technology, on-chip lasers operating at high ambient temperature and with low-loss coupling to the silicon waveguide circuits are very important [4]. This requires the integration of III-V semiconductor lasers on the silicon photonic platform combining the advantages of both material systems. SOI waveguides allow high density integrated photonics due to the high omnidirectional index contrast and the small features achievable using deep UV lithography. III-V materials allow active functions like optical amplification and laser action. The classical integration approach involves either fiber pigtailing an external laser [5] or attaching a micro-packaged III-V laser [6, 7] to the silicon circuit using active alignment techniques. While these are viable solutions for the integration of single laser diodes, these approaches don't scale well.

Wafer bonding technologies have been proposed to tackle this issue, either based on direct [8, 9] or adhesive [10–12] bonding. These technologies provide a dense integration with the silicon circuit and do not require high precision placement accuracy of the III-V. The tolerance to large bonding misalignment and simple packaging means that this architecture is suitable for low-cost and high-volume applications with a high number of lasers. The minimal coupling loss between the laser and the silicon waveguide lends itself to applications that require power efficiency. Moreover, the direct integration of materials permits the realization of a number of new functions, like laser cavities in the silicon layer. A disadvantage of this technique is the waste of III-V material, since the III-V on top of a ”non-laser-area” is etched away and thus lost.

A technology that addresses the above problems is micro-transfer-printing (μTP or just transfer printing). In this approach, materials or devices can be selectively picked from their source wafer and transferred in parallel to a new platform as a printing process. The TP process relies on the ability to release the components from their initial substrate, generally through undercut etching, together with a patterned stamp and an associated tool to pick and place arrays of components in a parallel process. This process can be applied to many different materials and structures and it makes very efficient use of materials. Additionally, significant (order of magnitude) cost savings can be attained due to the simplification and reduction in number of packaging steps. [13]

Whether we use wafer bonding or transfer printing, in both cases we must be able to achieve low loss optical coupling from the III-V mesa to the silicon waveguide circuits. In this chapter several types of structures for optical coupling will be presented and analyzed. We will evaluate their sensitivity to misalignment, their robustness in case of deviating dimensions and their ease of processing. Some coupling techniques are suitable for both technologies, others only for one of the two. Note that the quality of the coupling is also defined by the optical device which uses the coupler structure. When the coupler is inside the laser cavity, good coupling is very critical and we should aim for coupling losses as low as possible. If the coupler is no part of the laser cavity, higher losses can be tolerated.

3.1 Double adiabatic taper coupler

A first coupling structure to efficiently couple light between the III-V waveguide layer and the silicon waveguide layer is the adiabatically tapered III-V/SOI coupler [14]. This coupler is commonly employed in heterogeneously integrated InP-on-silicon devices [15–17] and was therefore an obvious candidate to realize InAs/GaAs QD lasers integrated on SOI.

A schematic of the coupling structure is shown in figure 3.1. To couple the light from the GaAs mesa to the underlying silicon waveguide an adiabatic tapered coupler is used. By simultaneously varying the waveguide dimensions along the coupling structure, the effective indices of the fundamental local modes of the

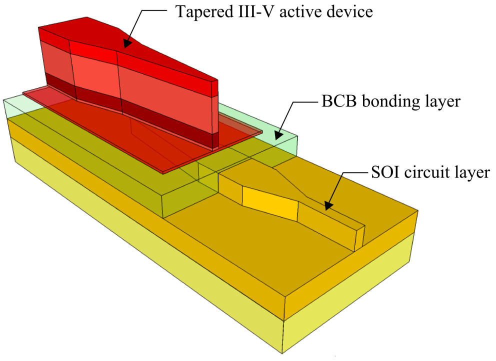

Figure 3.1: Schematic of the adiabatic-taper-based coupling scheme.

unperturbed waveguides (i.e. the GaAs and silicon waveguide) can be increased or decreased. In this way the light is gradually ”pushed down” from the III-V active device into the silicon waveguide. If the spatial waveguide variations occur gradual enough, no light is coupled to higher-order modes and we can speak of an adiabatic taper.

For the simulations we consider a 400 nm thick silicon waveguide layer with a 180 nm etch depth. Such a silicon waveguide layer thickness enables efficient light coupling from the III-V to the SOI waveguide in heterogeneously integrated III-V/SOI devices. The silicon substrate and silicon device layer are separated by a 2 μm-thick BOX layer. The InAs/GaAs quantum dot epitaxial layer stack is adhesively bonded to the planarized silicon-on-insulator (SOI) using a 60 nm-thick DVS-BCB bonding layer (n = 1.53). The III-V active region consists of an n-GaAs bottom contact layer (150 nm thick), an n-$Al_{0.4}Ga_{0.6}As$ bottom cladding layer (70 nm thick), 9 layers of InAs QDs separated by GaAs buffer layers, with a total thickness of 352 nm, a p-type $Al_{0.4}Ga_{0.6}As$ cladding layer (1.5 μm thick) and a p^{++}-GaAs top contact layer (300 nm thick). This is the same layer stack that was used to fabricate the lasers as described in chapter 2. The details of the assumed epitaxial layer stack are shown in Table 2.1. Extensive use is made of the commercially available software Fimmwave, an optical mode solver from Photon Design [18]. The Eigenmode Expansion (EME) method [19] is used to simulate the light propagation in the proposed coupling structures. The influence of misalignment is simulated by means of Lumerical Mode Solutions [20]. Simulations are carried out for transverse electric (TE)-polarized light at a wavelength of 1310 nm.

3.1.1 Optimization of the coupling section

The details of the spotsize converter coupling section are shown in figure 3.2a and 3.2b. The optical mode initially resides in the III-V mesa. The confinement factor of the optical mode is 8.9% in the quantum dot layers and 15% in the p-AlGaAs layer. First, while no silicon waveguide is present yet, the III-V waveguide rapidly tapers down from 3 μm to 1 μm. No light is lost, the coupling in this first taper is 100%.

In the second part of the coupling structure the waveguide width of the silicon waveguide is increasing while the width of the III-V is decreasing. At the start of this taper, the light is residing mostly in the III-V waveguide. This means that the initial width of the silicon waveguide is not critical: the coupling at the interface is perfect for widths up to 400 nm. For the rest of the simulations we will use $w_{\text{Si,start}}$ = 150 nm.

The coupling efficiency strongly depends on the width of the III-V taper tip ($w_{\text{III-V,end}}$) and the width of the silicon waveguide at the end of the spotsize converter ($w_{\text{Si,end}}$). In figure 3.2c the taper coupling efficiency is plotted as a function of the III-V taper tip for different silicon waveguide widths assuming a perfect adiabatic taper. When the taper tip is narrow ($<$ 400 nm), the width of the silicon doesn't matter that much, since the mode is pushed down anyway. However when the III-V taper tip broadens, the coupling efficiency decreases more rapidly when ($w_{\text{Si,end}}$) is smaller. Since the fabrication of the tapers is one of the most critical steps during processing, some variety in taper width may occur. So for robustness, it is better to opt for a broader silicon waveguide width. Figure 3.2d shows the coupling efficiency as a function of taper length for different width parameters. The broader the III-V taper tip, the faster the spotsize converter is adiabatic, but the overall coupling is lower.

In figure 3.2e the influence of the DVS-BCB thickness (h_{BCB}) on the coupling efficiency is plotted assuming a perfectly adiabatic taper. A realistic III-V taper tip of 500 nm is assumed. When perfect tapers are assumed thicker DVS-BCB leads to better coupling, since the changes at the interfaces are less abrupt due to the DVS-BCB. However, when we look at the graphs plotted in figure 3.2f, we see a trade-off needs to be made. The thicker the DVS-BCB, the longer it takes before the taper is adiabatic. Since extra losses exist in the III-V tapers (among other as a result of side-wall recombination and incomplete pumping of the taper) that are not taken into account in these simulations, it is not desirable to have very long tapers. For this work we will use h_{BCB} = 60 nm leading to a coupling efficiency around 96% and adiabatic coupling for lengths longer than 150 μm.

Simulations show that reflections at the taper tip are close to zero as long as the tip width is below 500 nm. With wider tips, the reflections increase up to 3 % for $w_{\text{III-V,end}}$=1 μm and $w_{\text{Si,end}}$=1.5 μm.

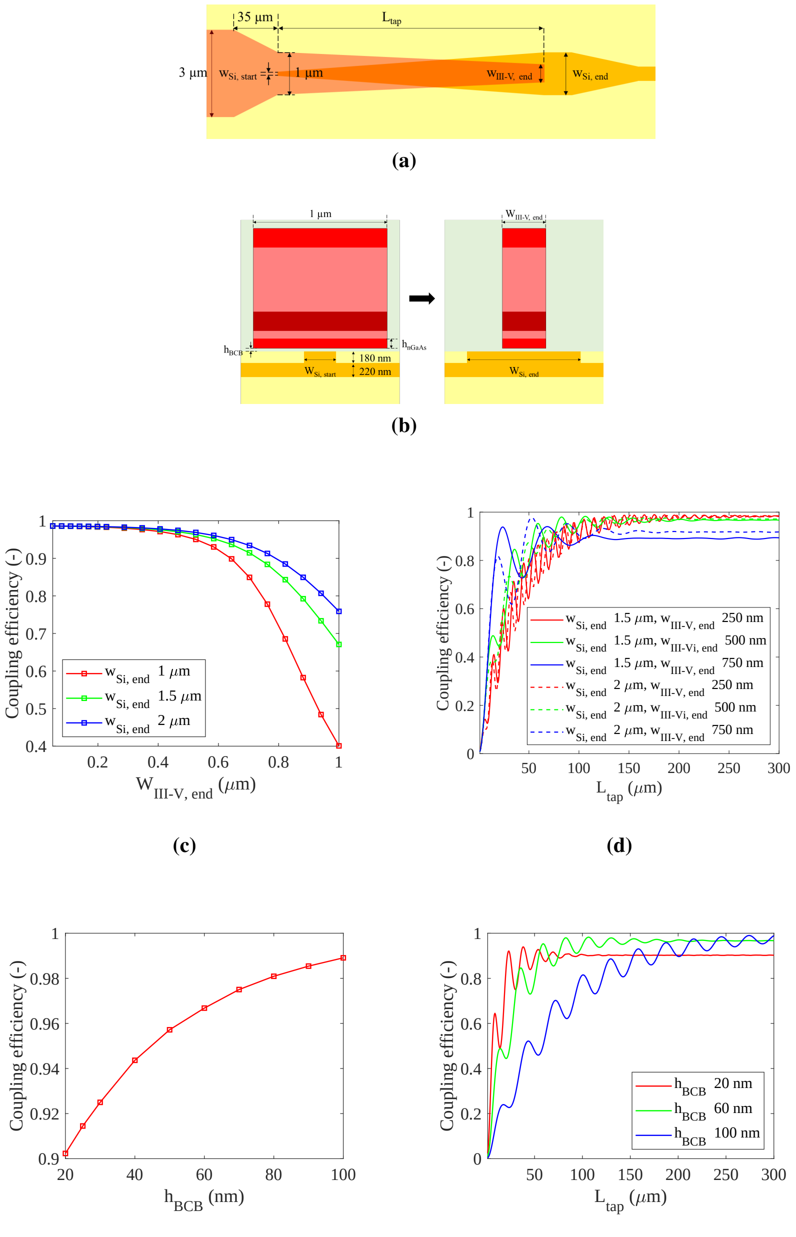

Figure 3.2: Optimization of the spotsize converter coupling section. (a) Top view of the taper coupling section; (b) Cross-sectional view along the taper; (c) Influence of the III-V taper tip width ($w_{\text{III-V, end}}$) on the coupling efficiency for different silicon waveguide widths ($w_{\text{Si, end}}$) assuming a perfect adiabatic taper (h_{BCB} = 60 nm); (d) Taper coupling efficiency versus taper length for different III-V and silicon end widths (h_{BCB} = 60 nm); (e) Influence of the DVS-BCB thickness assuming a perfect adiabatic taper ($w_{\text{Si, end}}$ = 1.5 μm and $w_{\text{III-V, end}}$ = 500 nm); (f) Taper coupling efficiency versus taper length for DVS-BCB thicknesses ($w_{\text{Si, end}}$ = 1.5 μm and $w_{\text{III-V, end}}$ = 500 nm).

3.1.2 Misalignment tolerance

Figure 3.3 shows the coupling efficiency versus taper length for a 0 nm (full line) and a 500 nm (dashed line) offset of the silicon waveguide with respect to the III-V waveguide for different III-V taper tips. The smaller the taper tip, the longer the taper should be to reach a certain coupling efficiency. So although a very narrow taper tip is best in an ideal situation, in reality a slightly broader taper tip can be more robust since it allows for more efficient coupling with shorter tapers when the alignment is not perfect.

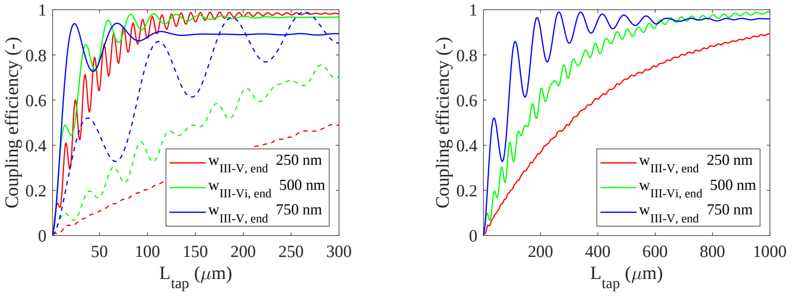

(a) The full lines have no offset, the dashed lines have an offset of 500 nm.

(b) Very long tapers needed to achieve good coupling for an offset of 500 nm.

Figure 3.3: Coupling efficiency versus taper length for different alignment offsets ($w_{\text{Si, end}}$ = 1.5 μm and h_{BCB} = 60 nm) .

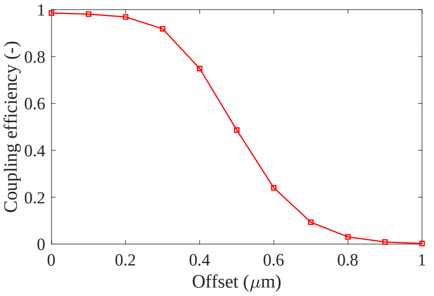

Figure 3.4: Coupling efficiency as a function of alignment offset for $w_{\text{III-V, end}}$ = 500 nm and L_{Tap} = 150 μm ($w_{\text{Si, end}}$ = 1.5 μm and h_{BCB} = 60 nm) .

As a rule of thumb, the taper tip needs to be as broad as it should be. In the spotsize converter presented here we see that in the ideal case there is hardly any difference between a tip width of 250 nm and a tip width of 500 nm, however a tip of 750 nm introduces considerable losses. So for robustness we can increase the tip width up to 500 nm, but increasing it further is not desirable. In figure 3.4 the coupling efficiency is shown as a function of lateral alignment offset for a fixed taper length of 150 μm. We can clearly see that this structure is not very tolerant for misalignment. The coupling efficiency is already halved for a misalignment of 500 nm.

The required tolerance for misalignment depends on the integration technique used. When transfer printing pre-processed gain coupons, the positioning during printing is the most critical step. With the printer used in this work the coupons can be printed with an alignment accuracy of 1.5 μm (3σ). Although there is still room for improvement, the accuracy of this integration technique will always be limited to the same accuracy as proximity lithography. Wafer bonding is a different story. In this case, the defining step is the litho step that defines the III-V tapers. In this work, contact lithography is used with an accuracy around 500 nm. However nothing in this integration technique prevents us to use an i-line stepper (accuracy around 200 nm) or a deep-UV stepper (accuracy of a few tens of nanometers). This is something to keep in mind when designing a coupling structure.

3.1.3 Overall coupling structure

Finally figure 3.5 shows the wavelength dependence of the coupling structure for no offset and a 500 nm-offset. We see that the efficiency decreases with decreasing wavelength. When the wavelength is smaller, the width of the taper tip and the offset appear wider for the propagating light and therefore their impact is bigger.

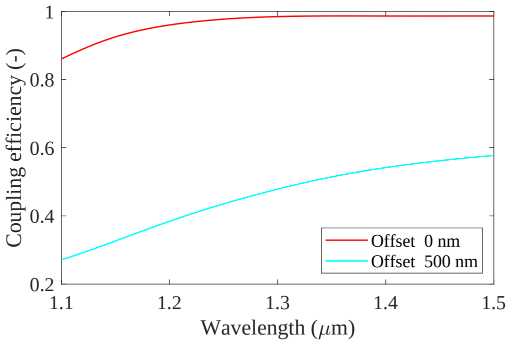

Figure 3.5: Wavelength dependence of the coupler efficiency for the overall optimized coupling structure.

The standard adiabatic taper coupler is a low loss coupling mechanism provided that the misalignment is small. On top of that the III-V tapers are relatively long (150 μm) to achieve good coupling. Because of that, this coupling structure is not well suited for transfer-printing. The alignment accuracy of high-throughput transfer printing (between 500 nm and 1 μm) is not good enough to ensure good coupling. However for wafer bonded lasers this coupling structure is very well-suited and used extensively [11, 15, 16]. DFB lasers and different types of mode-locked lasers are fabricated using the adiabatic taper coupler. They are described in much more detail in chapters 4, 5 and 6.

In reality the mesa width is of course not uniform over the cross-section due to the undercut in the mesa as explained extensively in section 2.3.3. In the above simulations the mesa width $w_{\text{III-V}}$ is actually the width of the QD section. For ease of simulation, we have assumed that the p-cladding has the same width instead of having an inverted triangular shape. In figure 3.6 the mode profile of the fundamental mode is plotted at the start of the taper ($w_{\text{III-V}}$ = 1.0 μm and $w_{\text{Si, start}}$ = 150 nm) where the mode is still mostly confined in the III-V. We see that the two mode profiles are almost identical, this is also reflected in their effective indices: $n_{\text{eff, rectangle}}$ = 3.246 and $n_{\text{eff, triangle}}$ = 3.247. So the above simulation results stay valid for the real taper structure.

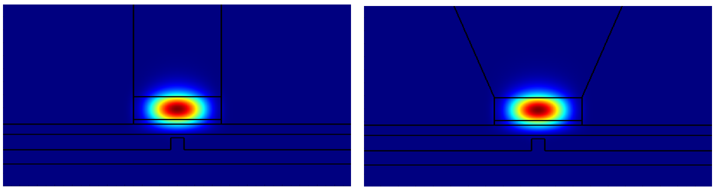
(a) (b)

Figure 3.6: Mode profile of the fundamental mode in case of (a) a uniform mesa width or (b) an inverted triangular p-cladding.

3.2 Adiabatic taper coupler with polymer intermediate waveguide

Currently the alignment accuracy in high-throughput transfer printing lies between 500 nm and 1 μm such that conventional coupling structures as described above are not suited for transfer printing. Therefore we propose a novel adiabatic tapered coupler that enables alignment-tolerant coupling for active III-V/SOI devices.

To keep the III-V processing to a minimum, we propose a coupling structure that does not require tapers to be etched in the III-V waveguide. A schematic of the coupling structure is shown in Figure 3.7. The III-V device is transfer printed onto the SOI chip using a 50 nm thick DVS-BCB adhesive bonding layer. To couple the light from the III-V waveguide into the silicon circuit layer, first, a butt-coupling approach is used to couple from the III-V waveguide into a polymer waveguide (n = 1.69). This polymer waveguide structure is post-processed after device transfer. The mode in the polymer waveguide structure is then coupled to the underlying 220 nm thick silicon waveguide using an inverted taper structure. A DVS-BCB (n = 1.53) cladding layer of the whole structure is assumed. By this coupling technique the length of the structures that need to be transfer printed is greatly reduced.

The design of this coupling structure consist of two parts: the optimization of the butt-coupling at the interface between the III-V waveguide and the polymer waveguide and the design of the adiabatic taper.

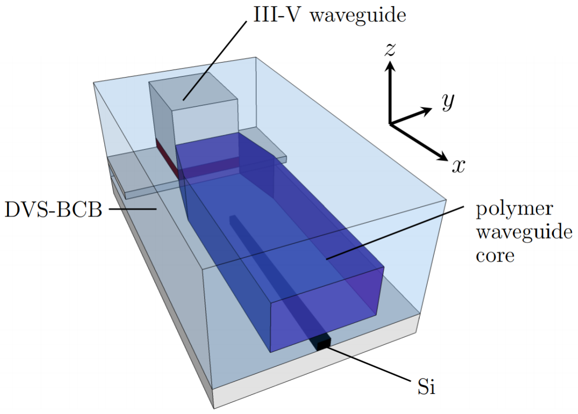

Figure 3.7: Schematic of the adiabatic-taper-based coupling scheme using an intermediate polymer waveguide.

For the simulations we consider a 220 nm thick silicon waveguide layer (available on imec's Si-Photonics passives+ platform and imec's Si-Photonics iSiPP50G platform [21]). The silicon substrate and silicon device layer are separated by a 2 μm-thick BOX layer. The III-V layer stack is adhesively bonded to the planarized silicon-on-insulator (SOI) using a 50 nm-thick DVS-BCB bonding layer. For the III-V material an epitaxial stack is assumed that matches a typical 1550 nm optical amplifier epitaxial layer stack. The stack consists of an n-InP bottom cladding layer (thickness to be optimized), a 300 nm-thick AlGaInAs core layer and a 1.6 μm-thick InP top cladding. The Eigenmode Expansion (EME) method of Fimmwave is used to simulate the light propagation in the proposed coupling structures. Simulations are carried out for transverse electric (TE)-polarized light at a wavelength of 1550 nm, but the results are also valid at 1310 nm.

3.2.1 Optimization of the butt-coupling at the III-V/polymer interface

In a first stage, the interface between the III-V waveguide and the polymer waveguide structure is assessed. To avoid unwanted Fresnel reflections at the III-V/polymer interface, the facet of the III-V waveguide is anti-reflection (AR) coated. A standard quarter wavelength AR coating is assumed. Figure 3.8 shows the coupling efficiency of the interface as a function of the polymer (n = 1.69) waveguide core thickness and the n-InP layer thickness. Polymer waveguides were assumed to be the same width as the III-V material (here 5 μm wide). The optimal coupling efficiency is about 92 % and is slowly decreasing with increasing n-InP thickness. The optimal polymer waveguide thickness increases with increasing n-InP thickness.

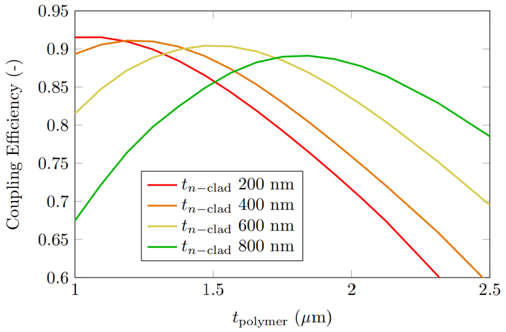

Figure 3.8: Butt-coupling efficiency at the III-V/polymer interface as a function of polymer waveguide thickness for different thicknesses of the n-InP bottom cladding. The III-V and polymer waveguide are assumed to be 5 μm wide.

3.2.2 Optimization of the SOI taper coupling section

The details of the SOI taper coupling section are shown in figure 3.9a and 3.9b. The optical mode initially resides in the polymer waveguide, which is assumed to be 5 μm wide. While no tapering occurs in the polymer waveguide structure, the SOI waveguide structure tapers down to a narrow tip to achieve good coupling efficiency at the taper tip/polymer waveguide interface. The coupling efficiency strongly depends on the polymer thickness ($t_{polymer}$) and the width of the silicon taper tip ($w_{silicontip}$).

In figures 3.9c and 3.9d the taper coupling efficiency is plotted as a function of the taper length for a taper tip width of 120 nm and 150 nm, respectively. In both cases, the thicker the polymer waveguide, the longer the taper should be before adiabatic taper coupling is achieved. Furthermore, an increase in taper tip width,

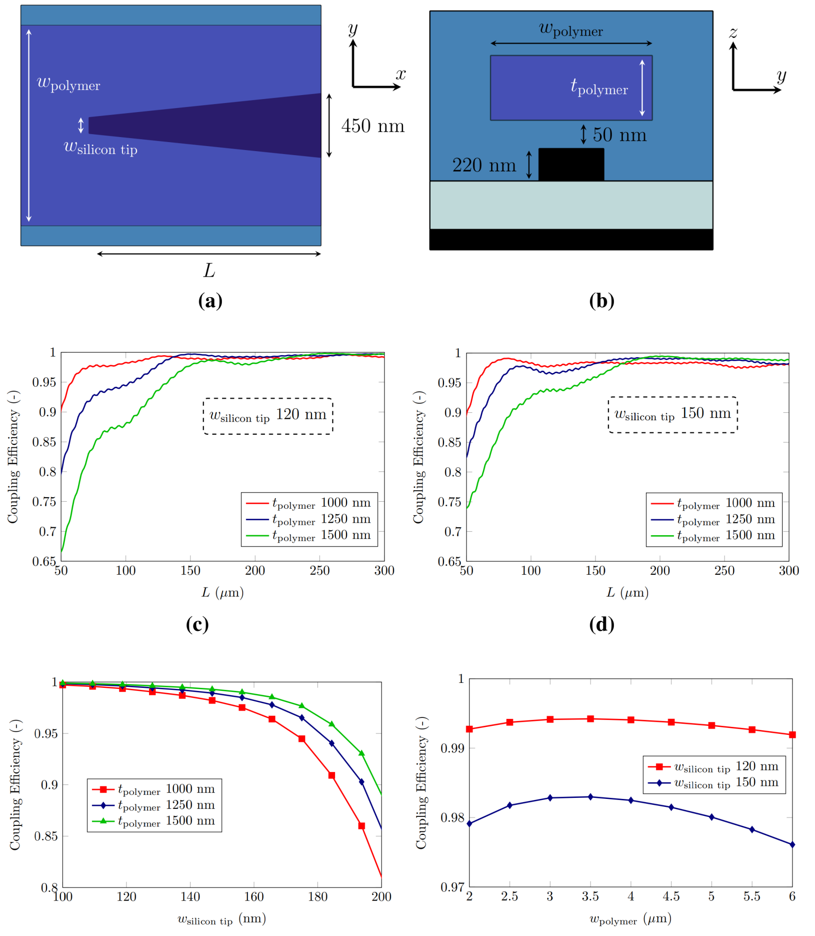

(a) **(b)**

(c) **(d)**

(e) **(f)**

Figure 3.9: Optimization of the SOI taper coupling section. (a) Top view of the taper coupling section; (b) Cross-sectional view along the taper; (c) Taper coupling efficiency versus taper length for different polymer thicknesses, $w_{polymer}$ = 5 μm and $w_{silicontip}$ = 120 nm; (d) Taper coupling efficiency versus taper length for different polymer thicknesses, $w_{polymer}$ = 5 μm and $w_{silicontip}$ = 150 nm; (e) Influence of the SOI taper tip width on the coupling efficiency for different polymer thicknesses, $w_{polymer}$ = 5 μm; (f) Taper coupling efficiency versus polymer width for different taper tips, $t_{polymer}$ = 1 μm.

results in an increase of the coupling efficiency for short tapers since the mode is pulled more strongly from the polymer to the silicon waveguide. However, a wider tip also results in higher losses at the coupling interface, thus the overall coupling efficiency for adiabatic coupling is lower for wider taper tips. This is also illustrated in figure 3.9e. Moreover, increasing the polymer waveguide thickness slightly reduces the coupling sensitivity for taper tip width.

Since the influence of the polymer thickness on the SOI taper coupling section is rather small for taper tips of 150 nm or smaller, the polymer thickness should be chosen to accommodate optimal III-V to polymer coupling. To allow the possibility of using the silicon to create for example a grating underneath the III-V waveguide to make distributed feedback lasers, an n-InP thickness of 200 nm is used for the remainder of the simulations. This results in an optimal polymer thickness of 1 μm.

Figure 3.9f shows that the width of the polymer waveguide has only a small influence on the coupling efficiency from polymer to silicon.

3.2.3 Overall coupling structure - lateral misalignment tolerance

Figure 3.10a shows the coupling efficiency versus taper length for different lateral alignment offsets (y-direction) of the silicon waveguide with respect to the III-V waveguide, both for silicon taper tip widths of 120 nm and 150 nm. A polymer thickness of 1 μm and a polymer width of 5 μm are assumed. The larger the lateral alignment offset, the longer the taper should be to reach a certain coupling efficiency. In figure 3.10b the coupling efficiency is shown as a function of lateral alignment offset for a fixed taper length of 200 μm and of 500 μm. At a length of 200 μm, fluctuations can be observed in the curve, meaning that the taper is not perfectly adiabatic yet. As expected, the fluctuations are larger for smaller taper tips for a fixed length, since the taper width changes more rapidly and the taper is thus less adiabatic. By increasing the length to 500 μm, adiabatic coupling is achieved. Since the taper is no part of the transfer printed structure, the length can be chosen freely. However, since the fluctuations are small, very long tapers are not necessary. As more than 90% of the light is coupled into the fundamental mode, only a small fraction of the light couples to higher order modes. Moreover, at the end of the coupling structure, light is coupled into a single mode waveguide, which means that the higher order modes will not be present in the remaining optical circuit. The coupling efficiency varies only a few percent with increasing lateral alignment offset, resulting in a very robust coupling performance.

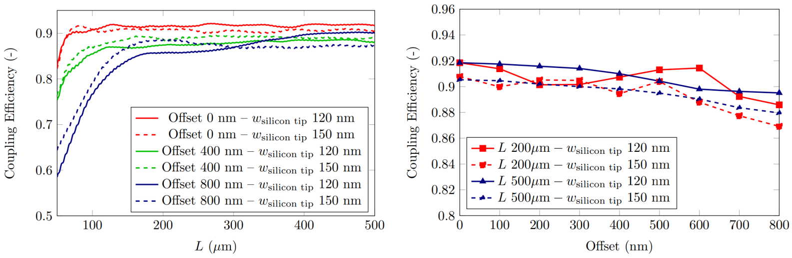

(a) Coupling efficiency versus taper length for different alignment offsets

(b) Coupling efficiency versus alignment offset.

Figure 3.10: Overall coupling structure.

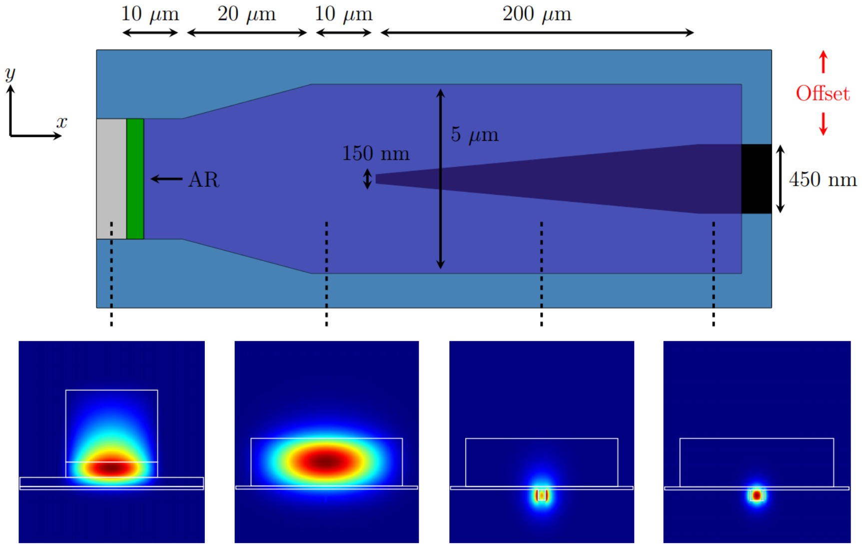

Figure 3.11: Overall coupling structure. Light propagation from the III-V waveguide to the SOI waveguide in the overall coupling structure. Mode profiles along the coupler are indicated as well.

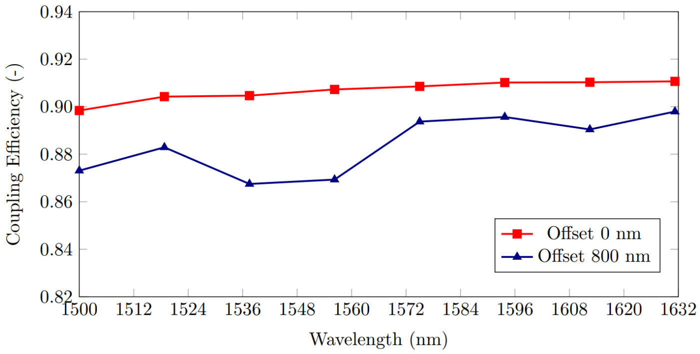

Figure 3.12: Wavelength dependence of the coupler efficiency for the overall optimized coupling structure with polymer intermediate waveguide.

Figure 3.11 shows the overall optimized coupling structure. Mode profiles along the coupler show the adiabatic mode transformation from the III-V to the SOI waveguide. As long as the polymer width is kept between 3 μm and 6 μm, it will not have a big impact on the coupler efficiency. However, otherwise a pure polymer taper can be used to convert the mesa mode to a polymer mode more suited to couple into the silicon waveguide. To illustrate this, one can see a 20 μm-long polymer taper is added between the mesa and the start of the polymer-silicon taper structure. This taper is used to gradually change the polymer width from the mesa width (3 μm in this simulation) to the 5 μm-wide polymer waveguide above the silicon taper. The length of the taper is chosen such that the transition is completely adiabatic and can be adapted for other mesa widths. Finally figure 3.12 shows the wavelength dependence of the coupling structure, both at 0 nm and 800 nm lateral alignment offset. Simulations indicate that this structure will work efficiently in the complete C and L band.

3.3 Intracavity coupling

The fabrication of tapers and especially narrow taper tips in the III-V is not straightforward. Furthermore, the spotsize converter described in section 3.1 is very sensitive to misalignment. Therefore we investigate another approach to realize a III-V-on-silicon laser. This approach was first suggested in [22]. The laser consists of two active DBR gratings providing nearly 100% reflection. In the center of the laser cavity the light is coupled evanescently into a silicon waveguide underneath. The laser is depicted in figure 3.13.

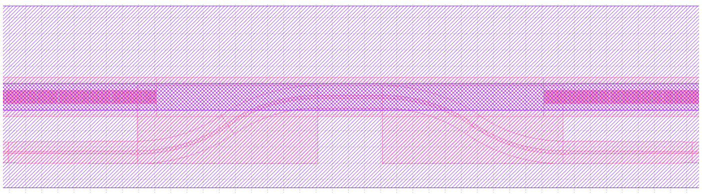

Figure 3.13: Schematic of the intracavity coupling scheme.

For the simulations we consider a 400 nm thick silicon waveguide layer with a 180 nm etch depth. The silicon substrate and silicon device layer are separated by a 2 μm-thick BOX layer. The GaAs quantum dot epitaxial layer stack is adhesively bonded to the planarized silicon-on-insulator (SOI) using a 60 nm-thick DVS-BCB bonding layer (n = 1.53). The III-V active region is the same as described in section 3.1. The details of the assumed epitaxial layer stack are shown in Table 2.1. The commercially available software Lumerical FDTD [23] is used to simulate the light propagation in the proposed coupling structures. The Finite-Difference Time-Domain (FDTD) method is a state-of-the-art method for solving Maxwell's equations in complex geometries. Simulations are carried out for transverse electric (TE)-polarized light at a wavelength of 1310 nm.

In figure 3.14 the E-field profiles of the FDTD simulation of the coupling section are plotted. The light is coming from the left side. We can clearly see that part of the light is coupled into the silicon waveguide. But if we look at the E-field in the III-V mesa after the coupling section, we see that higher order modes are introduced, which is highly undesirable. The total transmission of the light into the silicon waveguide can be quite high, depending on the length of the coupling section. However a large part of the coupled light is caused by the coupling of higher order modes.

The laser was fabricated using the process described in 2.3. It has a second order DFB grating with grating periods of 400 nm, which corresponds with a Bragg wavelength of 1320 nm. Due to fabrication limitations, we opted for a second order grating with a duty cycle of 70%. The III-V gain section is 920 μm: 2×400 μm long gratings, a 20 μm long coupling section in the center and 2×50 μm III-V mesa were the silicon waveguide is routed away from underneath the III-V mesa. Underneath a 1 μm wide silicon waveguide bend is present with a 50 μm bend radius as shown in figure 3.13.

The continuous wave (CW) light-current-voltage (LIV) characteristic of the intracavity laser is shown in figure 3.15a, as a function of temperature. It shows CW lasing is observed up to 90°C. We measure output powers up to 2.0 mW in the waveguide at room temperature.

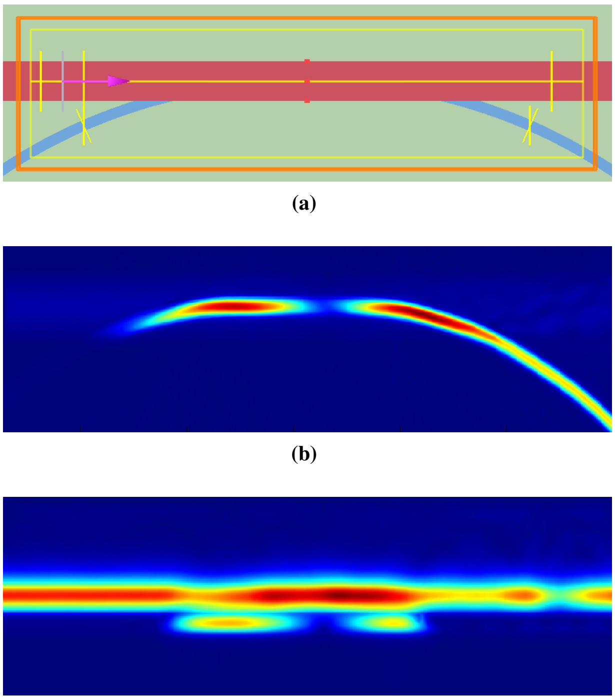

(a)

(b)

(c)

Figure 3.14: Illustration of the FDTD simulation. (a) The arrow indicates the source of the fundamental TE mode. At the yellow stripes the light is measured and overlapped with the fundamental mode profile. (b) E-field in the silicon waveguide plane. (c) E-field perpendicular on the chip through the III-V mesa and the silicon waveguide at the coupling section.

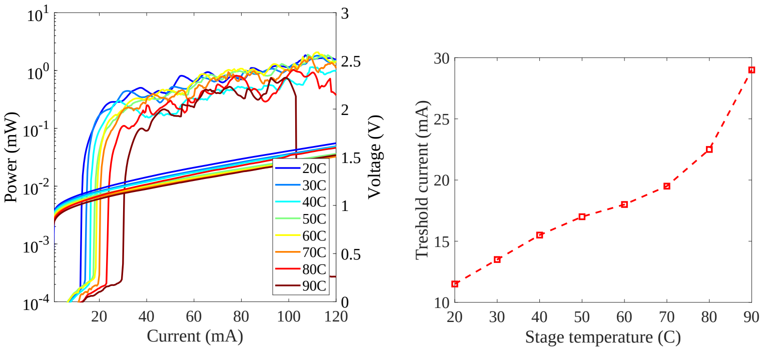

(a) **(b)**

Figure 3.15: (a) LIV curve as a function of temperature. The power in the waveguide is plotted. (b) Threshold current data as a function of stage temperature.

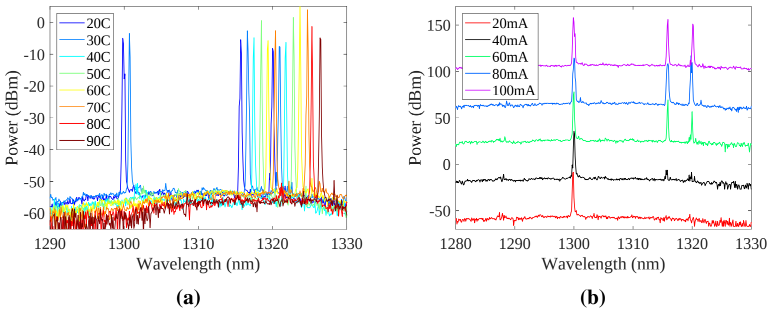

Figure 3.16: (a) Optical spectrum for a drive current of 100 mA as a function of temperature. (b) Optical spectra for different drive currents at room temperature. The different spectra are shifted 40 dB apart for clarity (OSA resolution: 0.06 nm).

In figure 3.16 the optical spectra are plotted as a function of temperature and of drive current. We see that this type of laser is multimode, as we could expect from simulations. We know that multiple modes are present in the laser cavity. In addition, the coupling mechanism doesn't provide a selection mechanism to filter out higher order modes, hence we see them in the laser spectrum. We suspect that the higher order modes start lasing first, since they are better aligned with the gain peak of the QD material.

Although this coupling mechanism eases the processing requirements, it fails to deliver single mode lasers. Therefore, it was not further investigated.

3.4 Edge couplers in silicon photonic ICs

When integrating III-V devices on full platform silicon photonic ICs, sparse integration and a thick back-end stack make wafer bonding an unsuitable technology. Instead, it is more preferable to first pre-process the lasers on their original substrate (see figure 3.17a). This way the III-V material is used optimally and the lasers can be tested before integration on an active platform. Then some of the devices are removed from their native substrate, depicted in figure 3.17b and transferred to an active silicon substrate through transfer printing (see figure 3.17c). In this way, minimal post-processing on the full platform is required.

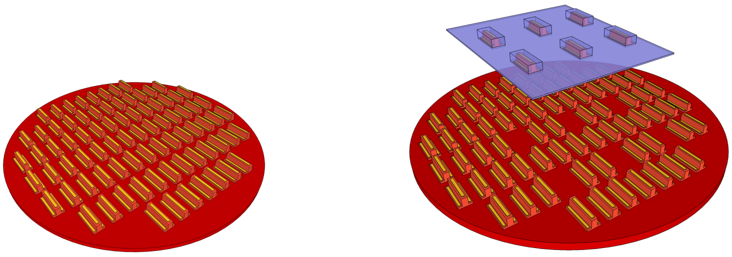

(a) Lasers processed on III-V substrate

(b) Pick-up for transfer printing

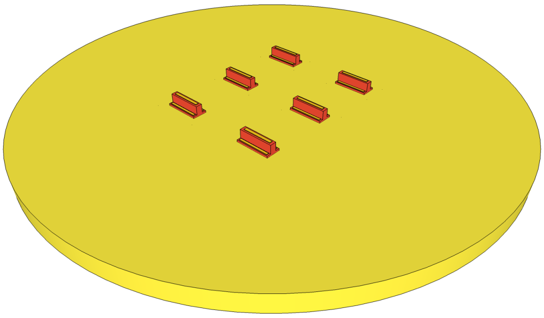

(c) Printed on a full silicon platform

Figure 3.17: Transfer-printing from a III-V source substrate to a full platform SOI target wafer.

In an active silicon platform, there is a back-end stack of considerable thickness covering the waveguides, which contains the metal interconnects. To be able to interface the laser with the waveguide circuit, we will etch a well in the back-end stack in which the GaAs-coupon will be printed, as is illustrated in figure 3.18. The well is etched through both the back-end stack and the 2 μm-thick BOX layer. In this way the laser is connected directly to the silicon substrate which acts as a very efficient heat sink. By careful design of the epitaxial layerstack of the laser, the active layer is at the same height as the silicon waveguide layer and the laser output can be directly butt coupled into the silicon waveguide. The butt-coupling scheme enables the the silicon photonics platform and the III-V laser to be individually optimized to obtain maximum performance without mutual constraints. Different coupling mechanisms are discussed below.

In this section imec's active silicon photonic integration platform [24] is considered as the target wafer for the transfer printed devices. The silicon waveguides used in the simulations are 220 nm thick and are fully etched. The silicon substrate and silicon device layer are separated by a 2 μm-thick BOX layer. The III-V active region consists of an n-GaAs bottom contact layer, an n-$\mathrm{Al}_{0.4}\mathrm{Ga}_{0.6}\mathrm{As}$ bottom

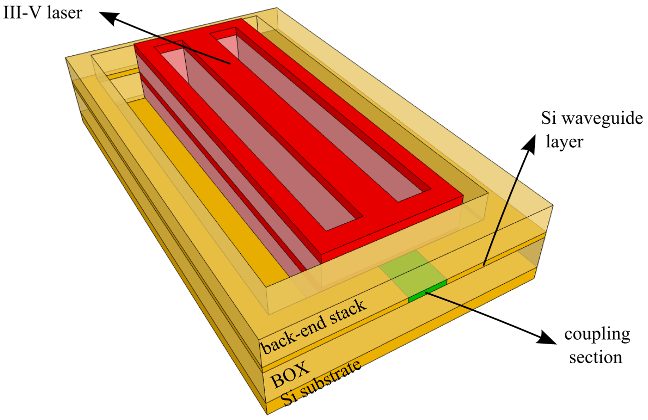

Figure 3.18: Schematic drawing of butt coupling in a well. The well is etched through the back-end stack, silicon waveguide layer and BOX layer and stops on the silicon substrate. Typical dimensions are 100 μm × 800 μm.

cladding layer (1.5 μm thick, thickness chosen such that the active layer comes at the same height as the Si waveguide layer), an InAs/GaAs QD active layer with a total thickness of 800 nm, a p-type $\mathrm{Al}_{0.4}\mathrm{Ga}_{0.6}\mathrm{As}$ cladding layer (1.5 μm thick) and a p^{++}-GaAs top contact layer (300 nm thick). The width of the laser mesa is 4 μm.

Extensive use is made of Lumerical FDTD to simulate the coupling between the III-V mesa and the silicon spotsize converter. When the coupling is not perfect, the light will diffract before it is collected into the waveguide, so for this simulation FDTD is the best approach. To simulate the propagation after coupling into the waveguide we can use the optical mode solver Fimmwave. Simulations are carried out for transverse electric (TE)-polarized light at a wavelength of 1310 nm.

3.4.1 Inverted taper

The first butt-coupling scheme we investigate is the conventional inverted taper. The height of the silicon is fixed at 220 nm, so the only parameter to play with is the width of the waveguide. This structure is depicted in figure 3.19.

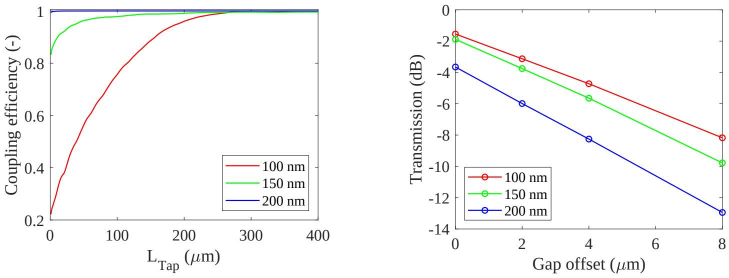

(a) **(b)**

Figure 3.20: (a) Transmission as a function of taper length (assuming perfect coupling) for different taper tip widths. (b) Transmission as a function of gap length for different taper tip widths.

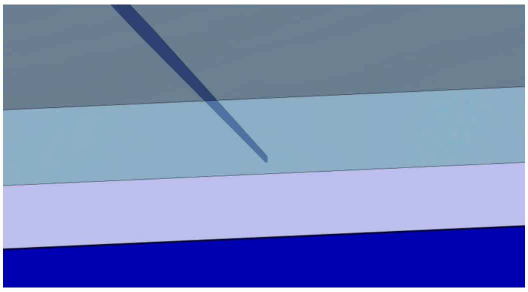

Figure 3.19: Schematic of butt-coupling in a well by means of an inverted taper.

Firstly we used Fimmwave to estimate the required length of the tapers as a function of taper tip width as depicted in figure 3.20a. The waveguide is coupling to a standard 350 nm-wide waveguide. As expected, the smaller the tip the longer the taper should be to achieve adiabatic coupling.

In figure 3.20b the coupling between the III-V mesa and the silicon taper is plotted as a function of offset between both of them for different tip widths. The taper itself is assumed to be perfect. For this simulation we used Lumerical FDTD. As we can see, the coupling decreases with increasing tip width. For a taper tip of 100 nm we have a coupling of -1.55 dB in case of perfect alignment. We loose 3 dB of the light for a gap of 3.8 μm. The length of the actual gap depends on multiple factors: the accuracy of the transfer-printing (1.5 μm (3σ)), the thickness of the AR coating (around 300 nm), the distance between the silicon taper and the edge of the well (between 1 and 2 μm) and a possible slope in the well. So a 3 μm

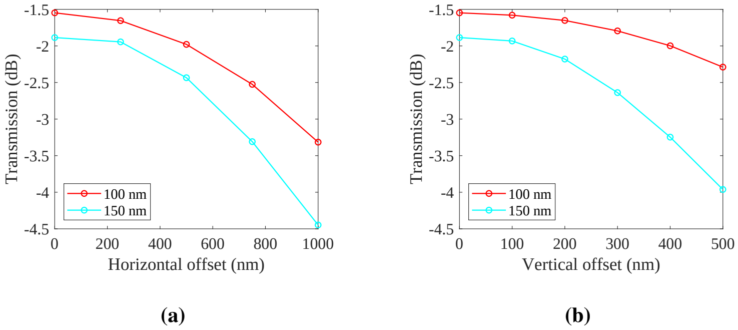

Figure 3.21: Influence of misalignment for different taper tip widths (gap offset: 0 μm). (a) Horizontal; (b) Vertical.

long gap is very normal.

In figure 3.21 the influence of horizontal and vertical misalignment is plotted. The horizontal misalignment is defined by the printing accuracy. The vertical misalignment depends on deviations in the thickness of the III-V layers, the BOX layer and the etch stop precision when defining the wells.

To measure the losses of the inverted tapers, we formed chains with various numbers of inverted tapers for different lengths and tip widths as is shown in figure 3.22. Different loss mechanisms are at work: mode conversion loss when the taper is not adiabatic, leakage to the substrate because the mode is very big and normal Si waveguide losses. The losses vary between 1 to 2.5 dB/taper for a 100 nm tip width to 0.2 dB/taper for a 175 nm tip width, for a taper length of 150 μm.

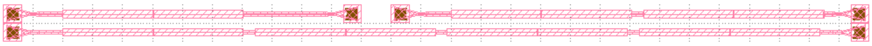

Figure 3.22: Series of inverted tapers in order to estimate the losses.

3.4.2 SiON waveguide

A second method is to match the III-V output mode with the help of a large silicon oxi-nitride (SiON) waveguide [25]. The refractive index of the SiON can be determined by varying its composition. For these simulations we used n = 1.594. Next, the light is coupled from the big SiON waveguide into a 220 nm silicon waveguide by means of an inverted taper, very similar to the polymer waveguide approach described in section 3.2. A schematic picture of this coupling method is shown in figure 3.23.

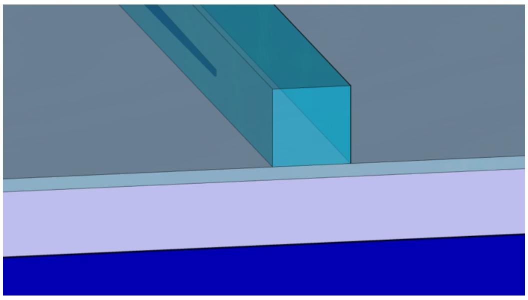

Figure 3.23: Schematic representation of the SiON waveguide coupler for butt-coupling III-V to silicon in a well.

In figure 3.24 the coupling of the III-V mesa to the SiON waveguide as a function of gap offset is plotted for different SiON dimensions. Regardless of the height, it is better to use a wider SiON waveguide (dashed line). However, it depends on the printing accuracy which SiON height is most desirable. A 3μm high SiON waveguide has almost 3 dB coupling loss for a zero gap offset, but less than 0.5 dB extra light is lost when the offset increases to 4 μm. Whereas a 1μm high SiON waveguide has around 1 dB coupling loss for a zero gap offset, but more than 3 dB extra light is lost when the offset increases to 4 μm.

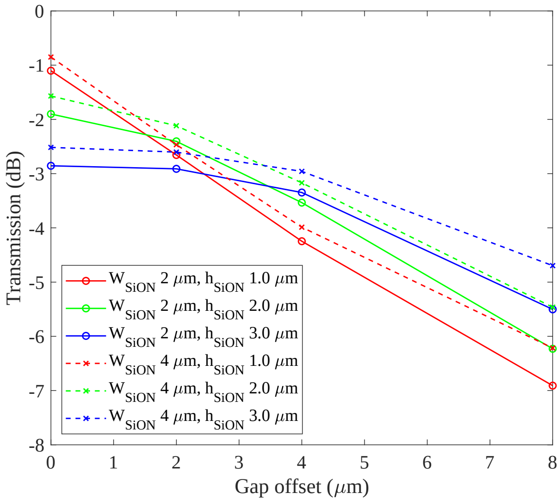

Figure 3.24: Transmission as a function of gap offset for different SiON heigths and widths.

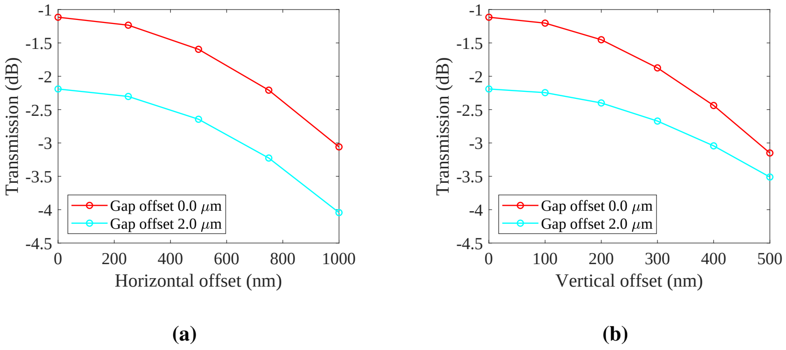

(a) (b)

Figure 3.25: Influence of misalignment for different gap offsets (W_{SiON} = 4.0 μm and h_{SiON} = 2.0 μm). (a) Horizontal; (b) vertical.

In figure 3.25 the horizontal and vertical misalignment are plotted.

3.4.3 Trident spotsize converter

Finally, we investigated a trident spotsize converter similar to the one proposed in [26]. It consists of three tapered silicon waveguides (height 220 nm) as depicted in figure 3.26. The inverted taper coupling structure proposed in section 3.4.1 is quite sensitive to the width of the taper tip. By adding an extra degree of freedom, the spotsize of the trident structure not only depends on the tip width but also on the spacing between the two tapers. This reduces the sensitivity for the tip width and makes this structure more robust against manufacturing variations.

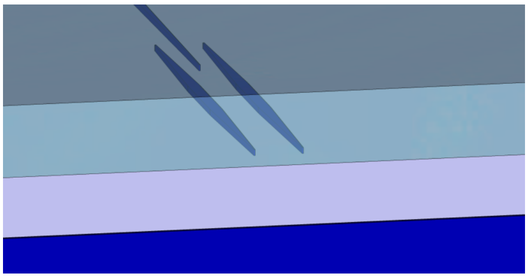

Figure 3.26: Structure of the trident SSC on SOI wafer.

First, the silicon trident is simulated in Fimmwave assuming perfect optical coupling from the III-V to the silicon. The exact dimensions of the spotsize converter are shown in figures 3.27a and 3.27b.

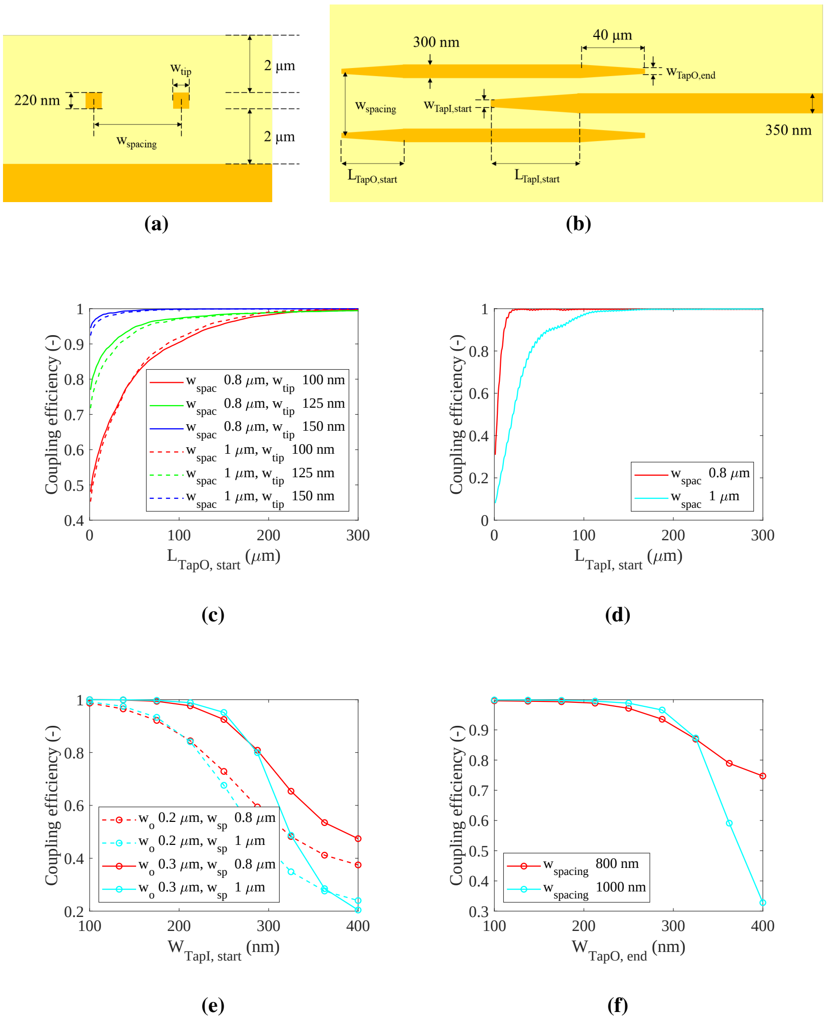

Figure 3.27: Optimization of the trident coupling section. (a) Cross-sectional view of the taper coupling section; (b) Top view along the taper; (c) Coupling efficiency as a function of outer taper length ($L_{\text{TapO, start}}$) for different outer waveguide spacings (w_{spacing}) and taper tip widths (w_{tip}); (d) Coupling efficiency as a function of inner taper length ($L_{\text{TapI, start}}$) for different outer waveguide spacings; (e) Influence of the tip width of the inner waveguide ($w_{\text{TapI, start}}$); (f) Influence of the tip width of the outer waveguide at the end ($w_{\text{TapO, end}}$).

Figure 3.27c shows the coupling efficiency as a function of taper length $L_{\text{TapO, start}}$ for different tip widths and spacings. The smaller the taper tip, the longer it takes to have a perfect adiabatic taper, regardless the spacing. Next, we look at the impact of the middle taper tip (assuming perfect adiabatic coupling) for different spacings and different widths of the outer waveguides (w_o). This is plotted in figure 3.27e. As expected, the influence of the tip is greater if the width of the outer waveguides is smaller. The spacing only starts to matter when the taper tip becomes really broad. For the rest of the simulations we use an outer waveguide width of 300 nm, such that the losses and reflections inside the trident are minimal and not oversensitive to the taper tip width. Next, we plotted the influence of the taper length of the inner waveguide $L_{\text{TapI, start}}$ assuming an inner waveguide tip of 100 nm. Finally, we also look at the influence of the taper tip width of the end tapers of the outer waveguides. This is plotted in figure 3.27f. We see that the trident spotsize converter is robust enough to handle width variations.

In a second step Lumerical FDTD is used to simulate the coupling between the III-V and the trident, assuming the trident itself to be perfect. In figure 3.28 the coupling efficiency is plotted as a function of gap offset for different spacings and tip widths. When the alignment is perfect the losses are all very similar around 1.2 dB. When the gap offset increases, the losses increase a bit faster for the 150 nm wide taper tips compared to the 100 nm wide tip.

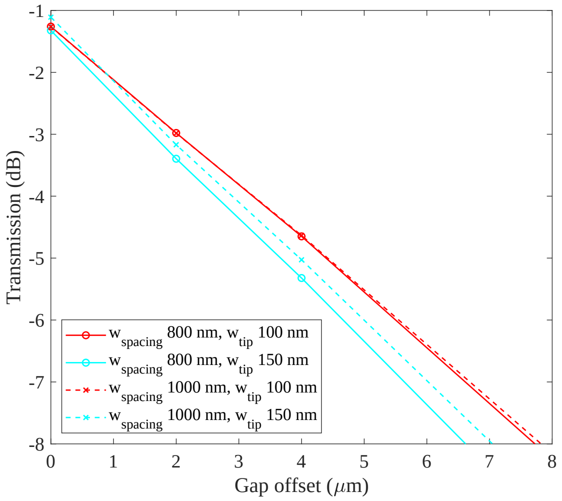

Figure 3.28: Optimization of the III-V–trident interface for different gap lengths as a function of taper tip width and spacing (FDTD).

In figure 3.29 the influence of horizontal and vertical misalignment is plotted.

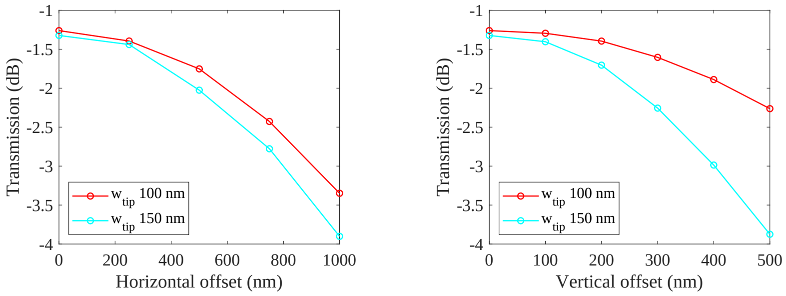

(a) **(b)**

Figure 3.29: Influence of misalignment for different taper tip widths (w_{spacing} = 800 nm and gap offset is 0 μm). (a) Horizontal; (b) Vertical.

3.4.4 Comparison of the different coupling structures

In table 3.1 some numbers for the different edge couplers are displayed. When the laser is perfectly aligned the coupling losses are very similar between -1.12 dB for the SiON, the best and -1.55 dB for the standard taper, the worst. An extra 3 dB is lost for a 5 μm gap for the SiON, making this edge coupler the most resistant to an offset, compared with the 3.5 μm and 3.8 μm gap for the trident and inverted taper, respectively. A horizontal misalignment of around 500 nm results for all couplers in a 0.5 dB transmission penalty. When a vertical offset occurs the SiON transmission decreases faster than that of the silicon taper and trident. But overall, we can say that the 3 options resemble each other very much. Since the trident losses are very variable due to a combination of different loss mechanisms, it might be better to opt for the straightforward inverted taper instead. The SiON waveguide also seems promising but this technology is not always available to the designer.

	Taper	**SiON**	**Trident**
Transmission gap: 0 μm	-1.55 dB	-1.12 dB	-1.26 dB
1 dB gap offset	1.3 μm	2 μm	1.2 μm
3 dB gap offset	3.8 μm	5 μm	3.5 μm
0.5 dB gap horizontal offset	532 nm	510 nm	505 nm
3 dB gap horizontal offset	> 1 μm	> 1 μm	> 1 μm
0.5 dB gap vertical offset	417 nm	240 nm	355 nm

Table 3.1: Overview of the different couplers. Inverted taper: tip width: 100 nm, SiON waveguide: width: 4 μm and height: 1.5 μm, trident spotsize converter: tip width: 100 nm and spacing 800 nm.

A mask was designed to test the inverted tapers and trident spotsize converters, as shown in figure 3.30. Each etched trench can be used both in the O-band (coupons should couple to the left) and C-band (coupons should couple to the right). Each trench has a different spotsize converter: taper tips and taper length are swept for the inverted taper and tips and spacing are swept for the tridents. Some coupling structures are angled to avoid reflections.

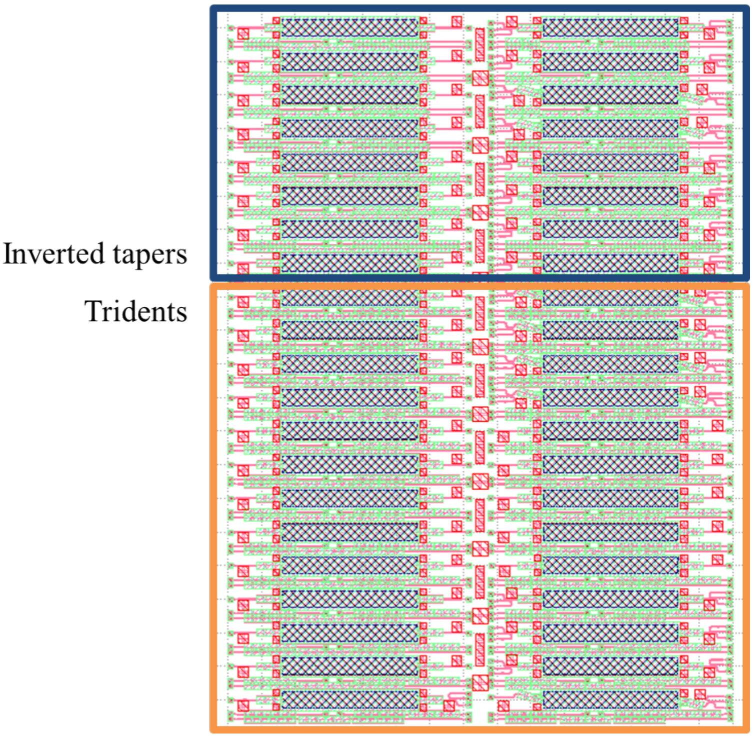

Figure 3.30: Mask design to test the different edge coupler structures both for the O-band and the C-band.

C-band, etched facet Fabry-Pérot (FP) lasers are transfer-printed in the etched wells as shown in figure 3.31 by dr. Joan Juvert. Output powers as high as 1 mW were measured in the silicon waveguide. However, due to the low uniformity in the quality of the contacts across different coupons it is difficult to compare the performance of the different coupling structures. Furthermore, it was impossible to measure the emission of the laser before and after transfer-printing, making it difficult to estimate the coupling loss of the edge couplers. [27]

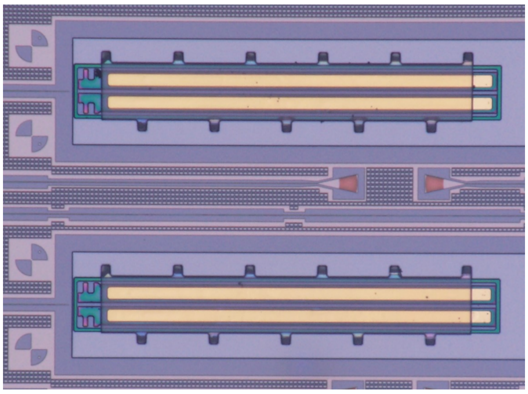

Figure 3.31: Coupons transfer printed in the BOX trench. The bowtie features are used for pattern recognition during transfer printing. The coupling structures can be seen immediately to the left of the coupons. Picture from [27]

Since the laser is made independently from the silicon chip, better coupling can be achieved by using a laser with a spotsize converter as well.

3.5 SiN - aSi -III-V coupler

In recent years silicon-nitride-on-insulator is emerging as a promising material platform, which is transparent in the 400-5000 nm wavelength range [28]. Owing to a lower refractive index contrast than silicon, much lower losses can be achieved in silicon nitride (Si_3N_4) waveguides. Moreover, Si_3N_4 has a lower thermo-optic coefficient than silicon. Since silicon nitride circuits can also be fabricated in a CMOS fab, they inherit the same advantages as the silicon-on-insulator waveguide platform.

However, heterogeneous integration of III-V materials on the silicon nitride platform leads to a more complicated design, making it more susceptible to fabrication intolerance [29]. The fundamental issue is the low refractive index of silicon nitride compared with silicon, which prevents easy coupling of light from the III-V material into the silicon nitride waveguides.

Therefore we investigated a new coupling approach from III-V to silicon nitride, based on a spotsize converter that uses amorphous silicon (aSi) as an intermediate coupling layer. Since the proposed method can be done completely in a CMOS fab, we can leverage from the supreme fabrication technology inherent to silicon. However, since we will do the aSi processing in the UGent cleanroom with a SUSS MA/BA6 mask aligner [30], contact masks are used. As a result the resolution does not get better than 600 nm, something we have taken into account in the design.

3.5.1 Two taper designs

Because the refractive index of Si_3N_4 is too low, we cannot achieve phase matching between the silicon nitride waveguide and the III-V mode, so no light will couple from the III-V to the silicon nitride, unless extremely narrow III-V structures are used. In order to solve this problem, we will first couple from the III-V into an intermediate amorphous silicon (aSi) layer and only then the light will be coupled to the silicon nitride waveguide. We will look at two different spotsize converter designs, depicted in figures 3.32 and 3.33.

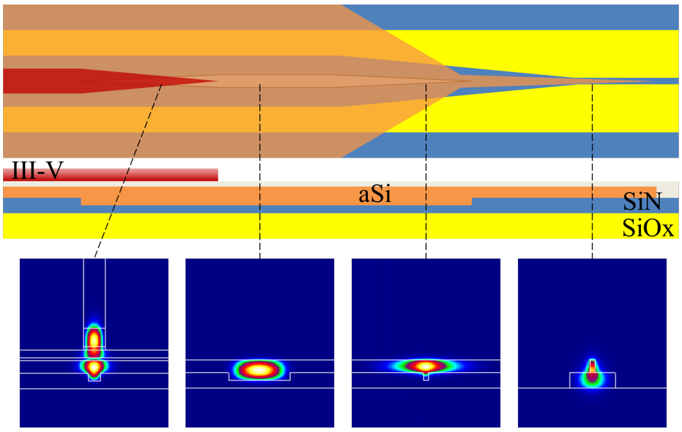

Figure 3.32: Shallow etched spotsize converter design to couple light from the III-V into the silicon nitride waveguide by means of an intermediate aSi layer. Mode profiles along the couplers are indicated as well. (red: III-V, grey: DVS-BCB, orange: amorphous silicon, blue: silicon nitride, yellow: silicon oxide)

First, the laser light is coupled from the III-V into the aSi layer by means of an adiabatic spotsize converter as described in section 3.1: the III-V tapers down to a narrow taper tip, while the width of the amorphous silicon increases. In the coupler design depicted in figure 3.32, the aSi taper is formed by filling a shallowly etched taper-shaped hole in the silicon nitride. In the second design shown in figure 3.33,

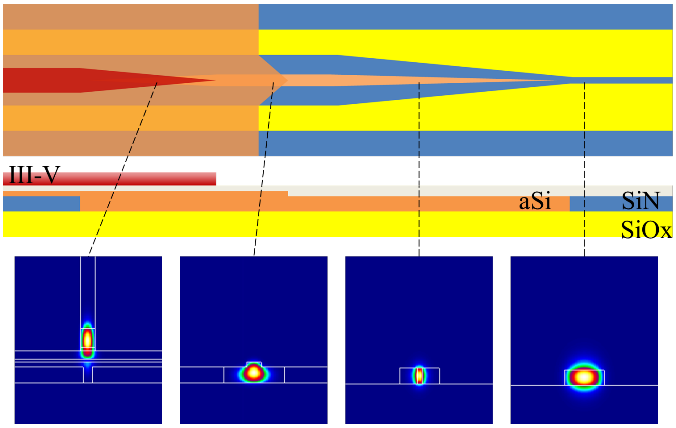

Figure 3.33: Fully etched spotsize converter design to couple light from the III-V into the silicon nitride waveguide by means of an intermediate aSi layer. Mode profiles along the couplers are indicated as well. (red: III-V, grey: DVS-BCB, orange: amorphous silicon, blue: silicon nitride, yellow: silicon oxide)

the taper is fully etched into the silicon nitride. The aSi layer thickness needs to be adapted to allow for easy coupling between the III-V and the silicon in both cases. This means that the aSi layer on top of the silicon nitride waveguide will be thicker for the case of the shallowly etched taper than for the fully etched taper.

In a next step, the light propagates from the aSi layer into the Si_3N_4 waveguide. When the taper is fully etched, only a thin layer of aSi is present on top of the Si_3N_4 waveguide. First, an aSi taper with a broad taper tip is used to couple the light completely in the etched taper. This is shown in the second mode profile in figure 3.33. Next, the etched taper couples to the silicon nitride waveguide, as illustrated in the third and fourth mode profile of figure 3.33. On the other hand in the shallow etched taper, the light will first couple from the shallow etched taper into an aSi waveguide on top of a silicon nitride waveguide (mode profile 2 and 3 in figure 3.32). Subsequently, the aSi waveguide will taper down to couple the light in the Si_3N_4 waveguide. Because all this can be done before bonding or transfer-printing, no complex post-processing is necessary.

3.5.2 Simulation results

In order to evaluate the operation of the two taper designs, simulations were carried out with FIMMWAVE. We assumed a silicon nitride waveguide thickness of 300 nm and a shallow etch step of 150 nm. The simulation results shown here are all for a wavelength of 1310 nm, but we can see the same trends when using 1550 nm light.

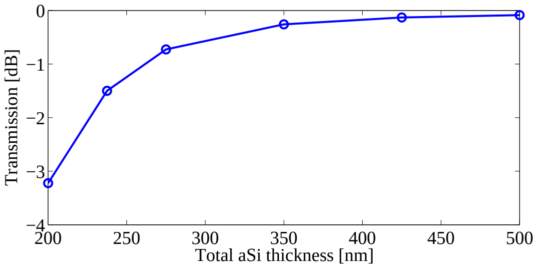

Figure 3.34: Transmission from the III-V mode to the amorphous silicon as a function of total aSi thickness.

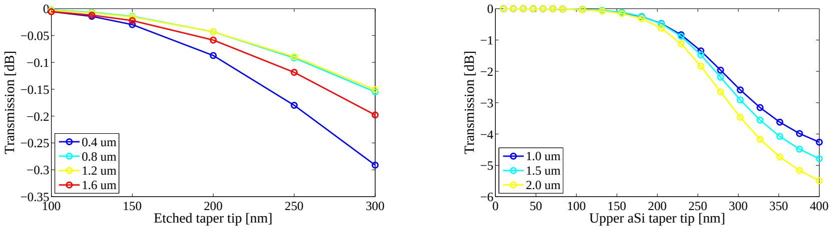

(a) Coupling from the etched taper to the upper aSi waveguide as a function of etched taper tip for different upper-waveguide widths.

(b) Coupling from the aSi into the silicon nitride waveguide as a function of aSi taper tip for different Si_3N_4 waveguide widths.

Figure 3.35: Simulation of the shallowly etched taper.

In figure 3.34 one can see that a minimal amorphous silicon thickness is needed for good coupling from the III-V mode into the silicon taper. We assumed a III-V taper tip width of 500 nm and a DVS-BCB thickness of 50 nm. For the simulations a layerstack similar as in [17] is used. For the rest of the simulations a total aSi thickness of 400 nm is used.

In figure 3.35, the shallowly etched taper (pictured in figure 3.32), is simulated. For an etch depth of 150 nm, this means we assume 250 nm of aSi to be deposited on top of the silicon nitride waveguide. In figure 3.35a we plotted the influence of the taper tip etched in the silicon nitride and filled with amorphous silicon for various widths of the aSi waveguide on top. Figure 3.35b shows the coupling between the upper aSi layer and the underlying silicon nitride waveguide as a function of aSi taper tip width. A narrow upper amorphous silicon taper tip is of key importance for good coupling between the aSi layer and the silicon nitride waveguide. Less crucial is the width of the shallowly etched aSi taper.

In figure 3.36 the transmission characteristics of the fully etched taper design are plotted as a function of taper dimensions. First, the coupling from the upper aSi waveguide into the fully etched taper is simulated. The width of the fully etched

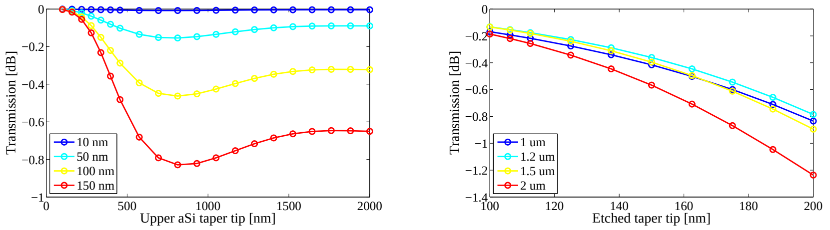

(a) Coupling from the upper aSi into the etched aSi taper as a function of upper aSi taper tip for different aSi upper layer heights.

(b) Coupling from the etched taper to the silicon nitride waveguide as a function of etched taper tip for different Si_3N_4 waveguide widths.

Figure 3.36: Simulation of the fully etched taper.

aSi taper at that point is 2 μm. The thinner the aSi layer on top of the silicon nitride, the less sensitive the coupling is to the tip width of the upper taper, as shown in figure 3.36a. Figure 3.36b shows the importance of a narrow fully etched taper to allow for good coupling between the aSi and the Si_3N_4 waveguide.

In the shallow etched coupler the taper transmission is most sensitive to the width of the upper taper tip, where in case of the fully etched taper the width of the etched taper tip proves to be the most crucial. Depending on which process proves to be the least trivial, either approach can be used.

3.5.3 Fabrication of the aSi tapers

The SiN chips are processed in imec where they can make taper tips as small as 150 nm. According to the above simulations both proposed designs can work with this minimum dimension. A taper is etched in the middle of a broad silicon nitride waveguide in the same etch step as the silicon nitride waveguide definition and is therefore self-aligned. In the first design, only part of the silicon nitride is etched as is shown in figure 3.37a. In the second design, the silicon nitride is fully etched as shown in 3.37c. The rest of the processing is done in our own UGent cleanroom.

In a first step the whole chip, including the tapers etched in the silicon nitride waveguide, is covered with aSi in the PECVD. Of course topography is introduced because of this. Chemical mechanical polishing (CMP) is used to thin down to aSi to the SiN level. On the now flat chip, a second aSi deposition is carried out while controlling the height very carefully to reach the wanted aSi thickness.

Next, the aSi is patterned in order to couple the light from the aSi to the Si_3N_4. For the shallow etched taper, a resist mask is put to protect the aSi we want to keep (this can be seen in figure 3.37b). In between the lasers, the aSi can stay as a heatsink, but in the trenches of the waveguides the aSi should be removed completely. Therefore wet etching is preferred and a considerable over-etch is

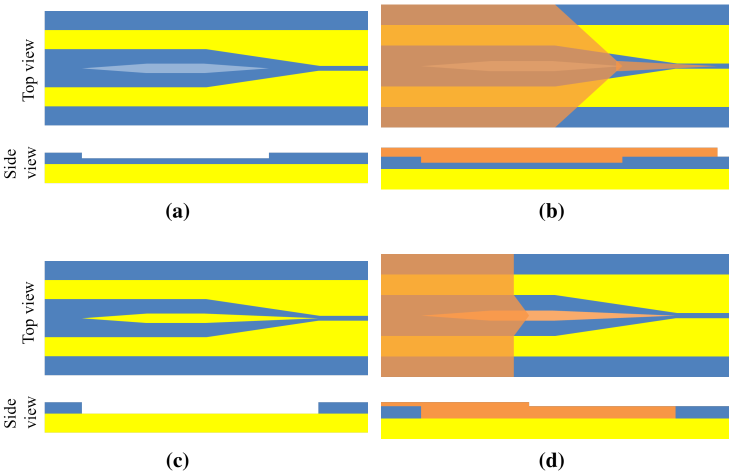

Figure 3.37: Creating the intermediate aSi taper for the two spotsize converter designs to couple light from the III-V into the silicon nitride waveguide: (a-b) shallowly etched taper, (d-e) fully etched taper. (orange: amorphous silicon, blue: silicon nitride, yellow: silicon oxide)

necessary. This will also reduce the upper aSi taper tip width, since the etchant works not only vertically but also horizontally.

For the fully etched taper, two more etch steps are needed. In the first step a resist mask protects the complete taper structure and the location of the lasers. A wet etch is done to make sure all aSi is removed from the trenches. In a second step, the aSi taper on top of the fully etched taper is formed. Dry etching is used in order to monitor the etch speed very precisely to avoid etching into the underlying taper.

Figure 3.38 shows SEM pictures of a FIB cross-section after the deposition of the amorphous silicon in the fully etched taper (figure 3.38a) and the shallow etched taper (figure 3.38b). We see that a problem arises for the fully etched taper: since the width of the taper is smaller than the height of the gap we have to fill, it is not completely filled. An extra CMP and deposition step might help, but this will make an already complex process even more complicated.

However, the biggest problem was with the CMP process. Stopping at or close to the silicon nitride layer without damaging part of the chip was difficult and not robust. In order for it to work, the chips should be redesigned to have a similar SiN waveguide density over the whole chip. So although the new coupling techniques look promising and should allow for easy heterogeneous integration of III-V materials on the silicon-nitride-on-insulator platform, the processing is not straight-forward.

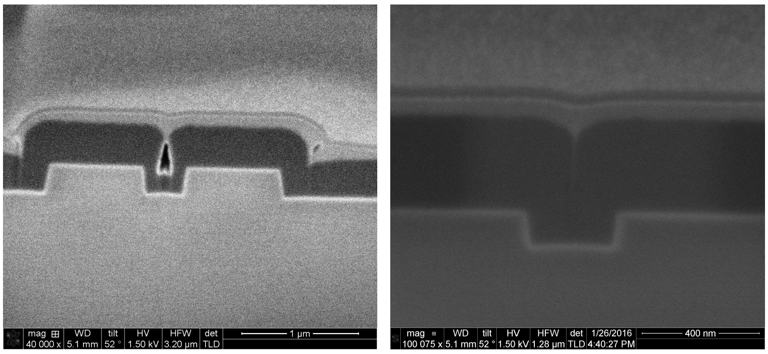

(a) Fully etched waveguide **(b)** Shallow etched waveguide

Figure 3.38: SEM picture of a FIB cross-section after amorphous silicon deposition.

A possible solution is to use e-beam lithography, so very sharp tapers can be defined in the amorphous silicon. When this is possible, there is no need anymore to define the tapers by filling taper-shaped trenches in the SiN layer with a-Si. The SiN chip can be planarized and CMP is no longer necessary, simplifying the processing considerably. This process was developed by Camiel Op de Beeck in our UGent cleanroom and in [31] and [32] a heterogeneously integrated laser around 1550 nm on a silicon-nitride-on-insulator chip is demonstrated. An intermediate amorphous silicon layer is used to bridge the index contrast between the nitride and the active device as is shown in figure 3.39.

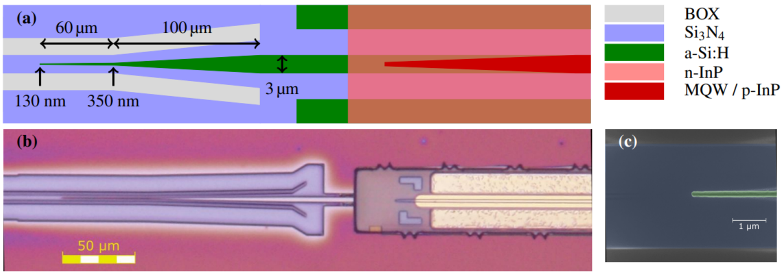

Figure 3.39: (a) Schematic top view of the taper from the silicon nitride waveguide to the amplifier. (b) Microscope image of a fabricated device. (c) False color SEM image of the a-Si taper tip on the SiN waveguide. [31]

3.6 Comparison of optical coupling schemes

As is clear from the previous discussion, the different coupling schemes all have their own advantages and disadvantages. An overview of the coupler methods is presented in table 3.2.

First, we compare the different technologies in relation to the coupling method. Besides the edge couplers in a well, every coupling scheme can be used in combination with wafer bonding. The transfer-printing of unprocessed coupons is possible for all coupling methods. The low misalignment tolerance of the adiabatic tapers is not a problem here, since the critical alignment step only happens during the post-processing of the laser and not while printing. Although we can post-process the laser after printing in a well on the active platform, this leads to numerous problems and should be avoided as much as possible. Pre-processed lasers can be printed when no III-V taper is needed for coupling. The alignment tolerance of the current coupling structure is too low to allow for printing of pre-processed devices. However, the spotsize converter design can be adapted in order to realize an alignment tolerant adiabatic taper structure. In [33] a misalignment-tolerant taper for the evanescent coupling of light from preprocessed III-V SOAs into Si photonic integrated circuit is proposed. The adiabatic taper structure has an alignment tolerance of 1 μm and is 225 μm long.

We also listed the footprint of the III-V tapers, since III-V tapers induce extra losses both due to sidewall recombination and insufficient electrical pumping [16, 34, 35].

All coupling mechanisms allow for single mode coupling except the intracavity coupling. Although this coupling mechanism has a lot of advantages like easy processing, this shortcoming makes it unsuitable for most applications.

Finally we compare the possibility to use the coupling schemes to make hybrid lasers like for example the mode-locked lasers described in chapters 5 and 6 where part of the cavity is made in the silicon. In case of the intracavity scheme, the cavity is made completely in the III-V making a hybrid laser impossible. The edge couplers will introduce some reflections in the cavity. This will make the realization of hybrid lasers more difficult.

In the end there is no one coupling technology that fits all and depending on the application one or the other will be the better choice.

	Adiabatic taper	**Polymer waveguide**	**Intracavity**	**Edge coupling in a well**	**SiN–aSi–III-V coupler**
Wafer bonding	Yes	Yes	Yes	No	Yes
Transfer-printing of unprocessed coupons	Yes	Yes	Yes	Difficult	Yes
Transfer-printing of preprocessed coupons	Difficult	Yes	Yes	Yes	Difficult
Challenging step III-V processing	Narrow taper tip	Clean lasing facet	–	Clean lasing facet	Narrow taper tip
Challenging step Si processing	–	–	–	Etched well with vertical facet	aSi tapers
III-V footprint coupler section	150 μm	0 μm	0 μm	0 μm	150 μm
Misalignment tolerance	Bad	Good	Medium	Medium	Bad
Single mode	Yes	Yes	No	Yes	Yes
Hybrid laser possible	Yes	Yes	No	Limited	Yes

Table 3.2: Comparison of the different coupling schemes.

References

[1] David AB Miller. *Rationale and challenges for optical interconnects to electronic chips*. Proceedings of the IEEE, 88(6):728–749, 2000.

[2] Graham T Reed, G Mashanovich, FY Gardes, and DJ Thomson. *Silicon optical modulators*. Nature Photonics, 4(8):518–526, 2010.

[3] Jurgen Michel, Jifeng Liu, and Lionel C Kimerling. *High-performance Ge-on-Si photodetectors*. Nature Photonics, 4(8):527–534, 2010.

[4] Zhiping Zhou, Bing Yin, and Jurgen Michel. *On-chip light sources for silicon photonics*. Light: Science & Applications, 4(11):e358, 2015.

[5] Fuad E Doany, Benjamin G Lee, Solomon Assefa, William MJ Green, Min Yang, Clint L Schow, Christopher V Jahnes, Sheng Zhang, Jonathan Singer, Victor I Kopp, et al. *Multichannel high-bandwidth coupling of ultradense silicon photonic waveguide array to standard-pitch fiber array*. Lightwave Technology, Journal of, 29(4):475–482, 2011.

[6] Bradley Snyder, Brian Corbett, and Peter O Brien. *Hybrid Integration of the Wavelength-Tunable Laser With a Silicon Photonic Integrated Circuit*. Journal of Lightwave Technology, 31(24):3934–3942, 2013.

[7] Peter De Dobbelaere, Ali Ayazi, Yuemeng Chi, Anders Dahl, Scott Denton, Steffen Gloeckner, Kam-Yan Hon, Steve Hovey, Yi Liang, Michael Mack, et al. *Packaging of Silicon Photonics Systems*. In Optical Fiber Communication Conference, pages W3I–2. Optical Society of America, 2014.

[8] MJ Heck, Jared F Bauters, Michael L Davenport, Jonathan K Doylend, Siddharth Jain, Geza Kurczveil, Sudharsanan Srinivasan, Yongbo Tang, and John E Bowers. *Hybrid silicon photonic integrated circuit technology*. IEEE Journal of Selected Topics in Quantum Electronics, 19(4), 2013.

[9] ML Davenport, Sudharsanan Srinivasan, Martijn Heck, and JE Bowers. *A Hybrid Silicon/InP Integrated Feedback Stabilized Mode-Locked Laser*. In National Fiber Optic Engineers Conference.

[10] Stevan Stankovic, Richard Jones, Matthew N Sysak, John M Heck, Günther Roelkens, and Dries Van Thourhout. *Hybrid III–V/Si Distributed-Feedback Laser Based on Adhesive Bonding*. IEEE PHOTONICS TECHNOLOGY LETTERS, 24(23):2155, 2012.

[11] Shahram Keyvaninia, Gunther Roelkens, Dries Van Thourhout, Christophe Jany, Marco Lamponi, Alban Le Liepvre, Francois Lelarge, Dalila Make, Guang-Hua Duan, Damien Bordel, et al. *Demonstration of a heterogeneously integrated III-V/SOI single wavelength tunable laser*. Opt. Express, 21(3):3784–3792, 2013.

[12] Günther Roelkens, Liu Liu, Di Liang, Richard Jones, Alexander Fang, Brian Koch, and John Bowers. *III-V/silicon photonics for on-chip and intra-chip optical interconnects*. Laser & Photonics Reviews, 4(6):751–779, 2010.

[13] John Justice, Chris Bower, Matthew Meitl, Marcus B Mooney, Mark A Gubbins, and Brian Corbett. *Wafer-scale integration of group III-V lasers on silicon using transfer printing of epitaxial layers*. Nature Photonics, 6(9):610–614, 2012.

[14] Xiankai Sun, Hsi-Chun Liu, and Amnon Yariv. *Adiabaticity criterion and the shortest adiabatic mode transformer in a coupled-waveguide system*. Optics letters, 34(3):280–282, 2009.

[15] M Lamponi, Shahram Keyvaninia, C Jany, F Poingt, F Lelarge, G De Valicourt, Günther Roelkens, Dries Van Thourhout, S Messaoudene, J-M Fedeli, et al. *Low-threshold heterogeneously integrated InP/SOI lasers with a double adiabatic taper coupler*. Photonics Technology Letters, IEEE, 24(1):76–78, 2012.

[16] Geza Kurczveil, Paolo Pintus, Martijn JR Heck, Jonathan D Peters, and John E Bowers. *Characterization of insertion loss and back reflection in passive hybrid silicon tapers*. IEEE Photonics Journal, 5(2):6600410–6600410, 2013.

[17] Gunther Roelkens, Amin Abassi, Paolo Cardile, Utsav Dave, Andreas De Groote, Yannick De Koninck, Sören Dhoore, Xin Fu, Alban Gassenq, Nannicha Hattasan, Q Huang, S Kumari, S Keyvaninia, B Kuyken, L Li, P Mechet, M Muneeb, D Sanchez, H Shao, T Spuesens, A Subramanian, S Uvin, M Tassaert, K Van Gasse, J Verbist, R Wang, Z Wang, J Zhang, et al. *III-V-on-Silicon Photonic Devices for Optical Communication and Sensing*. In Photonics, volume 2, pages 969–1004. Multidisciplinary Digital Publishing Institute, 2015.

[18] Photon Design, 2019. `www.photond.com/products/fimmwave.htm`.

[19] Dominic FG Gallagher and Thomas P Felici. *Eigenmode expansion methods for simulation of optical propagation in photonics: pros and cons*. In Integrated Optics: Devices, Materials, and Technologies VII, volume 4987, pages 69–82. International Society for Optics and Photonics, 2003.

[20] Lumerical, 2019. `www.lumerical.com/products/mode/`.

[21] Europractice, 2019. `http://europractice-ic.com/mpw-prototyping/siphotonics/imec/`.

[22] Shahram Keyvaninia, Yannick De Koninck, Dries Van Thourhout, Roel Baets, and Günther Roelkens. *A novel III-V-on-Si distributed feedback laser design*. In 16th European Conference on Integrated Optics (ECIO-2012), 2012.

[23] Lumerical, 2019. `www.lumerical.com/products/fdtd/`.

[24] Philippe P Absil, Peter Verheyen, Peter De Heyn, Marianna Pantouvaki, Guy Lepage, Jeroen De Coster, and Joris Van Campenhout. *Silicon photonics integrated circuits: a manufacturing platform for high density, low power optical I/O's*. Optics express, 23(7):9369–9378, 2015.

[25] Takanori Shimizu, Nobuaki Hatori, Makoto Okano, Masashige Ishizaka, Yutaka Urino, Tsuyoshi Yamamoto, Masahiko Mori, Takahiro Nakamura, and Yasuhiko Arakawa. *High density hybrid integrated light source with a laser diode array on a silicon optical waveguide platform for inter-chip optical interconnection*. In 8th IEEE International Conference on Group IV Photonics, pages 181–183. IEEE, 2011.

[26] Nobuaki Hatori, Takanori Shimizu, Makoto Okano, Masashige Ishizaka, Tsuyoshi Yamamoto, Yutaka Urino, Masahiko Mori, Takahiro Nakamura, and Yasuhiko Arakawa. *A hybrid integrated light source on a silicon platform using a trident spot-size converter*. Journal of Lightwave Technology, 32(7):1329–1336, 2014.

[27] Joan Juvert, Tommaso Cassese, Sarah Uvin, Andreas De Groote, Brad Snyder, Lieve Bogaerts, Geraldine Jamieson, Joris Van Campenhout, Günther Roelkens, and Dries Van Thourhout. *Integration of etched facet, electrically pumped, C-band Fabry-Pérot lasers on a silicon photonic integrated circuit by transfer printing*. Optics express, 26(17):21443–21454, 2018.

[28] Daniel J Blumenthal, Rene Heideman, Douwe Geuzebroek, Arne Leinse, and Chris Roeloffzen. *Silicon nitride in silicon photonics*. Proceedings of the IEEE, 106(12):2209–2231, 2018.

[29] Sulakshna Kumari et al. *Integration of GaAs-based VCSEL array on SiN platform with HCG reflectors for WDM applications*. In SPIE OPTO, pages 93720U–93720U. International Society for Optics and Photonics, 2015.

[30] SUSS MicroTec, 2019. `www.suss.com/brochures-datasheets/mask-aligner-ma-ba-6.pdf`.

[31] Camiel Op de Beeck, Lukas Elsinger, Bahawal Haq, Günther Roelkens, and Bart Kuyken. *Towards the Integration of C-band Amplifiers on Silicon Nitride Waveguides via Transfer Printing*. In Frontiers in Optics, pages FTu5C–6. Optical Society of America, 2019.

[32] Camiel Op de Beeck, Lukas Elsinger, Bahawal Haq, Günther Roelkens, and Bart Kuyken. *Heterogeneously Integrated Laser on a Silicon Nitride Platform via Micro-Transfer Printing*. In Frontiers in Optics, pages FTu6B–1. Optical Society of America, 2019.

[33] Bahawal Haq and Günther Roelkens. *Alignment-tolerant taper design for transfer printed III-V-on-Si devices*. In 21st European Conference on Integratred Optics (ECIO 2019), pages 1–3, 2019.

[34] Kasper Van Gasse, Ruijun Wang, and Gunther Roelkens. *27 dB gain III–V-on-silicon semiconductor optical amplifier with¿ 17 dBm output power*. Optics express, 27(1):293–302, 2019.

[35] Michael Davenport. *The heterogeneous transition*. In Heterogeneous Silicon III-V Mode-Locked Lasers. University of California, Santa Barbara, 2017.

4

InAs/GaAs quantum dot DFB lasers on silicon

In the present Big Data era, the demand for higher bandwidths in datacenters is increasing at an unprecedented pace. This trend requires high-performance interconnects that can sustain this high bandwidth without consuming exorbitant amounts of energy. Silicon photonics is emerging as an important platform for the realization of power-efficient, high-speed optical transceivers [1]. However, currently the lack of cost-effective integration of the light source limits silicon-based photonic integrated circuits (PIC) deployment in these fields. In order to become a competitive technology, on-chip lasers operating at high ambient temperature and with low-loss coupling to the silicon waveguide circuits are very important [2].

Due to the three dimensional confinement of carriers, InAs/GaAs quantum dot (QD) lasers inherently have a more stable performance over the 20°C-100°C temperature range compared to quantum well lasers [3]. Furthermore, they can achieve very low threshold current densities [4] and because of the way QDs are grown they have a wider gain spectrum compared to conventional quantum well lasers making this material system an excellent candidate for creating multi-wavelength transmitters.

The integration of QD lasers directly on the silicon photonics platform, leveraging the well-developed CMOS fabrication infrastructure and its economies of scale, can provide a distinct cost advantage over other optical technologies. At the same time it would reduce coupling losses and packaging costs inherent in multi-chip solutions. Furthermore, the integration of the laser source directly on silicon enables the scaling of the aggregate bandwidth of transceivers to the Terabit/s range. [5]

Multiple ways to integrate InAs/GaAs quantum dot lasers with silicon photonic circuits are already demonstrated. Typical integration schemes include heteroepitaxy of III-V materials [6, 7], flip-chip bonding [8] and wafer bonding [9]. Some wafer-bonding approaches use a metal layer between the silicon and the GaAs wafers to facilitate bonding [10], which complicates the coupling to an underlying silicon waveguide circuit. Wafer-bonded QD lasers without a metal layer have recently been demonstrated [11, 12]. Since both electrical contacts are now laterally formed on the III-V, low-loss coupling of the laser light to a silicon waveguide is possible. This allows for the integration of heterogeneous III-V-on-Si quantum dot lasers with high-quality Si photonic components.

Distributed-feedback (DFB) lasers are important optical sources, providing longitudinal single-mode emission with a relatively narrow line width. They are essential for wavelength division multiplexing (WDM) systems [13, 14]. This was also recognized in [7] where the first single-mode InAs/GaAs QD DFB laser epitaxially grown on silicon is demonstrated.

Here we describe single mode InAs/GaAs quantum dot DFB lasers bonded on SOI with coupling to a silicon waveguide. When these lasers were fabricated and characterized, they were the first of their kind [15]. Continuous wave (CW) laser operation up to 100°C is shown. The DFB laser structures demonstrated here are based on second order gratings defined in the silicon circuit with Bragg wavelengths around 1300 nm and 1320 nm. This research formed the starting point for the European CALADAN project [16] which focuses upon the micro-transfer-printing technology to integrate GaAs quantum dot lasers in order to demonstrate Terabit/s capable optical transceivers for the datacom market segment.

4.1 Design of III-V-on-silicon DFB laser diodes

4.1.1 Distributed-feedback laser basics

Just like in Fabry-Pérot lasers, there are two fundamental conditions for lasing in a DFB laser:

1. The cavity round trip gain is unity. This means that when the optical field makes a back and forth roundtrip through the cavity, the gain needs to compensate all losses. The gain condition can be expressed as [17]:

   $$\Gamma_A g_A(\lambda) = \alpha_i + \alpha_m(\lambda) \tag{4.1}$$

   where α_i and α_m are the internal and mirror losses, g_A is the gain of the active medium and Γ_A the confinement factor of the optical mode in the active layer.

2. The round trip phase $\phi(\lambda)$ is an integer multiple of 2π. The phase condition can be written as:

$$\phi(\lambda) = 2k_0 n_{eff} L = \frac{4\pi n_{eff} L}{\lambda_m} = 2\pi m \tag{4.2}$$

$$\lambda_m = \frac{2n_{eff} L}{m} \tag{4.3}$$

   where L is the cavity length, n_{eff} the effective index of the optical mode, $k_0 = 2\pi/\lambda_0$ the free-space propagation constant (λ_0 the free-space wavelength) and m the order of the cavity mode. The phase condition is fulfilled by a number of wavelengths, the longitudinal modes of the laser cavity. The spacing between two adjacent longitudinal modes is given by:

$$\Delta\lambda = \frac{\lambda^2}{2n_{eff} L} \tag{4.4}$$

Laser operation will start when one of the longitudinal modes reaches the gain condition (4.1). This is the mode that experiences the largest gain and/or the lowest mirror losses. The carrier pumping level at which this happens is called the threshold current. When the carrier density is further increased, the roundtrip gain will remain clamped to 1 and the excess carriers are used to generate light through stimulated emission.

Because the roundtrip gain is clamped, one would expect single mode operation of the laser. However this is not correct. Since the gain of the active medium is much more broadband than the spacing between two longitudinal modes (e.g. $\Delta\lambda$ = 0.26 nm in a GaAs QD laser with a 1 mm long cavity at 1310 nm), quite a few longitudinal modes feel more or less the same gain. Because of spontaneous emission and non-linear gain mechanisms, a number of side modes will also appear in the power spectrum as is illustrated on the left side of figure 4.1.

In DFB lasers a narrow-band wavelength dependent mirror, a Bragg grating, is used to make sure only one longitudinal mode can reach the gain condition as is illustrated on the right side of figure 4.1. A Bragg grating is a structure whose refractive index changes periodically along the direction of the light propagation. This means that the effective index of the optical mode present in the cavity changes periodically. Gratings have been extensively studied and detailed models of distributed reflections are obtained from the transfer matrix method and the coupled mode theory [17–19]. However in this work, we will set the thoughts with simple, intuitive reasoning.

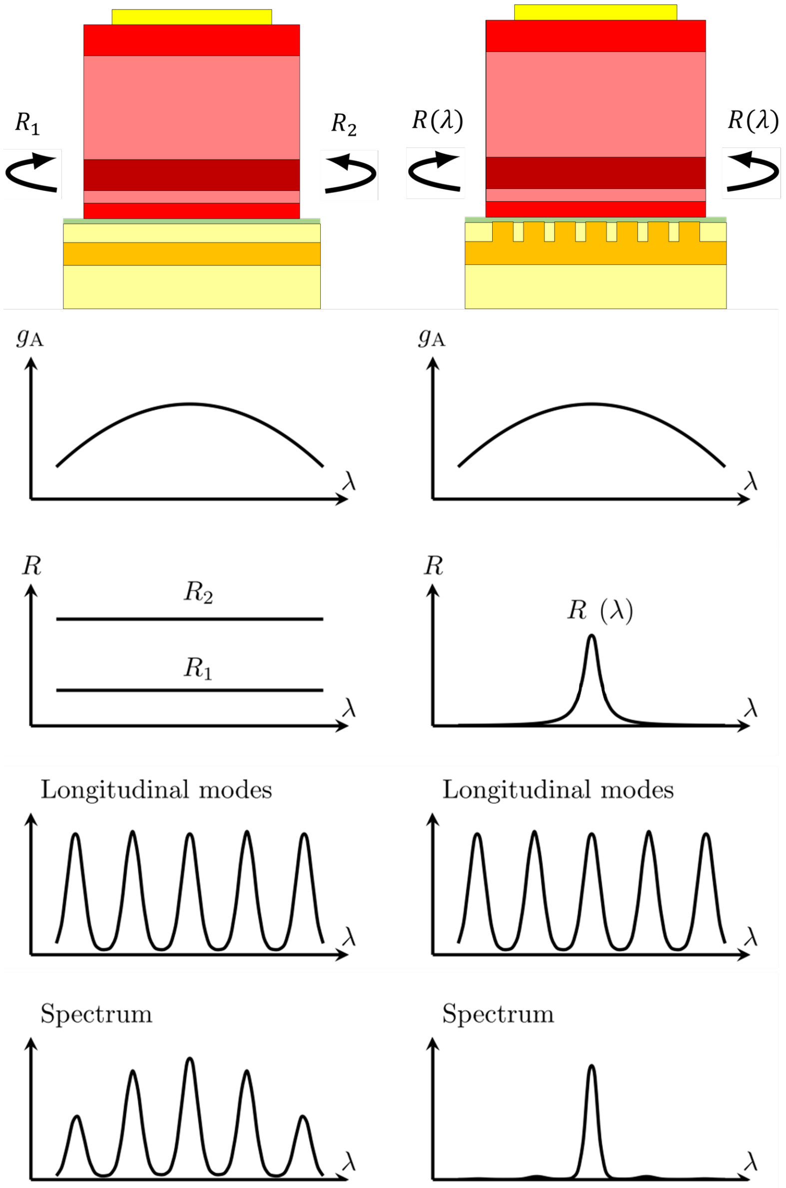

Figure 4.1: Laser operation. Left: heterogeneously integrated Fabry-Perot laser; right: heterogeneously integrated DFB laser.

While the mode propagates along the structure, reflections occur at the interface between regions with lower and higher refractive indices. The reflection coefficient is given by:

$$r = \frac{n_{eff,h} - n_{eff,l}}{n_{eff,h} + n_{eff,l}} \approx \frac{\Delta n_{eff}}{2n_{eff}} \tag{4.5}$$

assuming the difference between the effective indices to be small. For a first order grating with a 50% duty cycle the total reflection r_{tot} is then given by:

$$r_{tot} = r - re^{-2jk_0 n_{eff}\frac{\Lambda}{2}} + re^{-2jk_0 n_{eff}\Lambda} - re^{-2jk_0 n_{eff}\frac{3\Lambda}{2}} + \cdots \tag{4.6}$$

The back-reflecting waves will interfere constructively and the grating reflectance will reach its maximum when:

$$k_B n_{eff}\Lambda = m\pi \Rightarrow \Lambda = m\frac{\lambda_B}{2n_{eff}} \tag{4.7}$$

where λ_B is the called the Bragg wavelength and m is a positive integer which represents the order of the grating. This is called the Bragg condition. In the case of m = 1, we speak of a first-order grating, for m = 2, we have a second-order grating and so on.

A very important parameter is the coupling coefficient κ. This is the fraction of wave amplitude reflected per unit length:

$$\kappa \sim \frac{r}{\frac{\Lambda}{2}} \approx \frac{\Delta n_{eff}}{n_{eff}\Lambda} \tag{4.8}$$

In the case of a square profile of the grating and using a small perturbation approximation, the coupling coefficient κ can be calculated using the expression:

$$\kappa = \frac{2(n_{eff,h} - n_{eff,l})}{\lambda_B} sin(m \cdot \pi\frac{l_h}{\Lambda}) \tag{4.9}$$

where l_h is the length of the unetched region (with a higher effective refractive index). The ratio l_h/Λ is called the duty cycle of the grating. For a first-order grating, the maximum coupling is achieved for a duty cycle of 50%, while for a second-order grating, the maxima occur for duty cycles of 25% and 75%.

From exact mathematical descriptions based on coupled wave equations [18, 19], one can derive that for a lossless grating (i.e. no absorption in the material) with length L, the power reflection $R = |r|^2$ at the Bragg wavelength is given by

$$R = \tanh^2(\kappa \cdot L) \tag{4.10}$$

4.1.2 General structure of the laser

The three-dimensional layout of the DFB laser is shown in Fig. 4.2a. The laser cavity consists of a DFB grating defined in the silicon waveguide layer with the

III-V gain region bonded on top. As our goal is to fabricate a laser emitting at 1310 nm, the QD region is designed to provide a photo-luminescence peak near that wavelength. Tapered spotsize converters are used to couple the light from the hybrid gain section into the passive silicon waveguides.

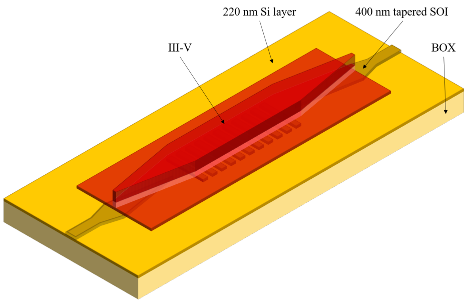

(a) 3D view of the III-V-on-silicon DFB laser

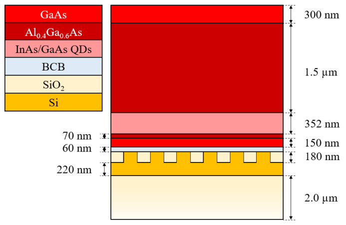

(b) Cross-sectional diagram of the laser structure

Figure 4.2: III-V/Si distributed feedback laser design.

A schematic cross-section of the III-V-on-silicon waveguide structure is depicted in Fig. 4.2b. The laser consists of a planarized SOI wafer containing the silicon waveguides and gratings defined in a 400 nm-thick silicon waveguide layer using 193 nm deep UV lithography (180 nm etch depth) fabricated in a CMOS pilotline at imec. The GaAs quantum dot epitaxial layer stack is adhesively bonded to the planarized silicon-on-insulator (SOI) using a 60 nm-thick divinylsiloxane-bisbenzocyclobutene (DVS-BCB) bonding layer. Top to bottom, the III-V layers comprise a highly-doped p-type GaAs ohmic contact and a p-type AlGaAs top cladding layer, followed by the quantum dot region. This QD active region consists of nine dot-in-a-well (DWELL) layers (InAs/InGaAs) separated by GaAs barriers. Finally, there is an n-type AlGaAs bottom cladding layer and a n-type GaAs contact. The epitaxial layer stack is described in detail in section 2.1. An electric p-type contact (anode) is located on the top of the mesa, while the cathodes are located on top of the n-contact layer, symmetrically on both sides of the mesa.

4.1.3 400 nm platform for O-band lasers

Single mode waveguide

The waveguide geometry is shown in figure 4.3a. The waveguides are defined in a 400 nm-thick silicon waveguide layer using 193 nm deep UV lithography (180 nm etch depth) fabricated at imec. The wafer is planarized with silicon oxide to ensure high quality bonding when integrating the lasers. After the laser integration, the whole chip is covered in DVS-BCB to ensure that the metal laser contacts are far away from the silicon waveguides.

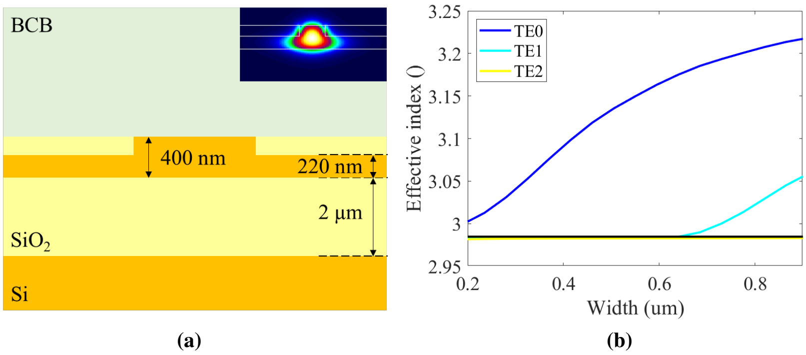

(a) (b)

Figure 4.3: (a) Cross-sectional geometry of the Si waveguide. The thickness of the buried oxide (BOX) and the Si device layer are 2 μm and 400 nm, respectively. The 180 nm tall Si rib is formed by dry-etching, leaving a 220 nm thick Si slab. Inset: Electric field profile of the fundamental mode in a 500 nm wide waveguide. (b) Effective index versus waveguide width in the 180 nm rib Si waveguide.

The effective index of the TE modes as a function of waveguide width is plotted in figure 4.3b for a wavelength of 1310 nm. The horizontal black line represents the effective index of the slab mode. We see that the waveguide is single mode, as long as the width is smaller than 640 nm. In the inset of figure 4.3a the electrical field profile of the fundamental mode for a 500 nm wide waveguide is shown. We experimentally determined a waveguide loss of 1.3 dB/cm for a 500 nm wide waveguide at 1310 nm.

4.1.4 III-V-on-Si mesa design

The design of the III-V-on-Si mesa is the core of the laser design. This will define the laser characteristics like output power, threshold current, speed, etc., as it contains the gain material, the optical confinement, the electrical contacts and the carrier confinement.

For the design of the epitaxial layerstack, many elements can be copied from monolithic III-V gain stacks. The design of the active layer, containing the quantum dots and barriers is unaffected by heterogeneous integration [20] and therefore we based our design on layer stacks reported in literature [21, 22] and the knowledge of the epi-vendor. We included 9 layers of quantum dots to ensure a high enough modal gain. It was reported in [23] that increasing the number of quantum dot layers even further did not result in considerably higher modal gain. A large number of quantum dot layers may lead to non-uniform carrier injection and the optical confinement factor for the top and bottom QD layers decreases. A cross section of the heterogeneous laser waveguide is shown in figure 4.2b and more details on the epitaxial layerstack can be found in table 2.1.

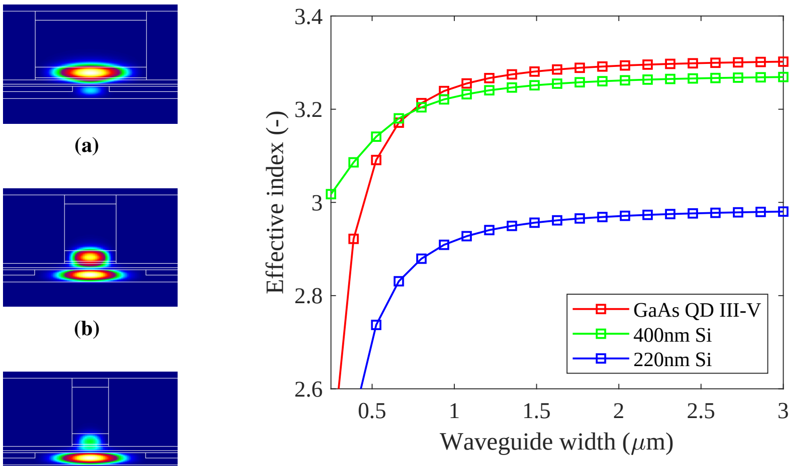

(a)

(b)

(c)

(d)

Figure 4.4: Optical mode profiles of the heterogeneous (Si/III-V) waveguide with 400 nm thick silicon: (a) $n_{\text{eff, IIIV}} > n_{\text{eff, Si}}$: mode is mainly confined in the active medium; (b) $n_{\text{eff, IIIV}} \approx n_{\text{eff, Si}}$; (c) $n_{\text{eff, IIIV}} < n_{\text{eff, Si}}$: higher confinement in the silicon. (d) Effective indices of 220 nm and 400 nm silicon waveguides and of the III-V layerstack used to make the lasers (details in table 2.1) as a function of width. All simulations are done at a wavelength of 1310 nm.

By adding a silicon waveguide underneath the III-V, we can control the optical confinement factor in the active and passive layer by varying the waveguide widths of both the silicon and the III-V mesa. When the effective index of the III-V is higher than that of the silicon, the optical mode is pulled up in the III-V mesa, as is

Layer	**Material**	**Refractive index**
p-contact	GaAs	3.411
Graded SCH	$\mathrm{Al}_{0-0.4}\mathrm{Ga}_{1.0-0.6}\mathrm{As}$	3.306
p-cladding	$\mathrm{Al}_{0.4}\mathrm{Ga}_{0.6}\mathrm{As}$	3.2
Graded SCH	$\mathrm{Al}_{0.4-0}\mathrm{Ga}_{0.6-1.0}\mathrm{As}$	3.306
Barrier ×8	GaAs	3.411
DWELL ×9	$\mathrm{InAs/In}_{0.15}\mathrm{Ga}_{0.85}\mathrm{As}$	3.463
Graded SCH	$\mathrm{Al}_{0-0.4}\mathrm{Ga}_{1-0.6}\mathrm{As}$	3.306
n-cladding	$\mathrm{Al}_{0.4}\mathrm{Ga}_{0.6}\mathrm{As}$	3.2
Graded SCH	$\mathrm{Al}_{0.4-0}\mathrm{Ga}_{0.6-1.0}\mathrm{As}$	3.306
n-contact	GaAs	3.411
Bonding layer	DVS-BCB	1.537
Waveguide	Si	3.497
Burried oxide	SiO_2	1.45

Table 4.1: Refractive indices of the III-V-on-Si mesa layers used in the simulations for a wavelength of 1310 nm.

shown in figure 4.4a. By adapting the waveguide widths, the optical mode can be pushed more and more into the silicon waveguide, as is shown in figure 4.4b and 4.4c. To be able to carefully engineer the optical mode, the effective indices of the silicon waveguide and the III-V mesa should be well matched. So the thickness of the silicon should be chosen accordingly. [24] As we can see in figure 4.4d, the standard 220 nm SOI waveguides [25] are too thin to achieve index matching. However, the effective index of a silicon layer with a thickness of 400 nm is well matched to the III-V layer. The lasers will be integrated on a 400 nm thick silicon on 2 μm burried oxide on silicon substrates. By varying the widths of the silicon waveguide and the III-V mesa we can integrate low and high confinement amplifier waveguide sections on the same chip.

To design the III-V-on-Si mesa, we carried out simulations of the optical mode in Fimmwave. The refractive indices used in the simulations are summarized in table 4.1.

We have calculated the optical confinement factor $\Gamma_{\text{III-V}}$ as a function of the III-V and silicon widths. The optical confinement factor can be used to estimate the net modal gain coefficient g_{net}:

$$g_{\text{net}}(w) = \Gamma_{\text{III-V}}(w) g_A - \alpha_i(w) \tag{4.11}$$

where g_A is the material gain and α_i is the mode's internal loss. The latter is also dependent on the mesa width. Different loss mechanisms are at work in the laser mesa. First, the optical mode experiences doping losses mainly in the p-cladding layer. Secondly, there are propagation losses mainly due to side-wall roughness. The propagation losses in silicon are negligible compared with the III-

V losses and depend on the III-V widths. Third, absorption in the active layer due to incomplete pumping may occur for example when the optical mode is wider than the pumped region.

Introducing a silicon waveguide underneath the III-V region will impact all these internal losses. First of all, the mode is pulled down from the III-V into the silicon. Therefore both the doping losses and propagation losses will decrease. Since $\Gamma_{\text{III-V}}$ will also decrease, the gain $\Gamma_{\text{III-V}}(w)g_A$ felt by the optical mode will decrease too. Because of this, also the absorption loss will decrease. Moreover, the introduction of the silicon waveguide may lead to more lateral confinement of the optical mode. If this is the case, the propagation and absorption losses decrease even more. As a result the net modal gain $g_{\text{net}}(w)$ can both increase and decrease depending on the actual values.

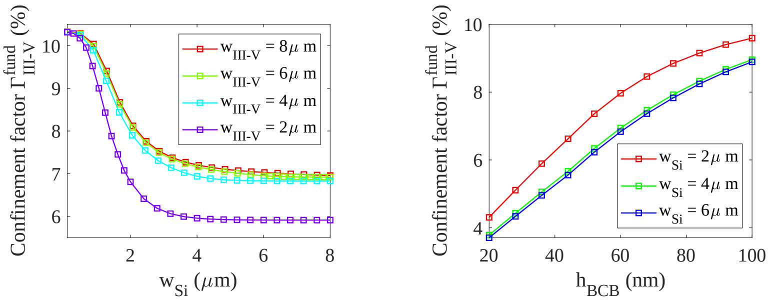

(a) (b)

Figure 4.5: The confinement factor $\Gamma_{\text{III-V}}^{\text{fund}}$ of the fundamental mode in the InAs/InGaAs quantum dot active layers (a) as a function of the silicon waveguide width w_{Si} for various III-V widths $w_{\text{III-V}}$ (h_{BCB} = 60 nm); (b) as a function of DVS-BCB thickness (h_{BCB}) for various silicon waveguide widths ($w_{\text{III-V}}$ = 4 μm).

In figure 4.5 the confinement factor $\Gamma_{\text{III-V}}^{\text{fund}}$ of the fundamental mode in the InAs/InGaAs quantum dot active layers is plotted as function of the silicon waveguide width and DVS-BCB thickness. When increasing w_{Si} the optical mode is pulled down and so $\Gamma_{\text{III-V}}^{\text{fund}}$ decreases, as can be seen in figure 4.5a. Since the effective index of the silicon is in all these cases a little bit lower than the effective index of the QD-based mesa (as can be seen in figure 4.4d), no very drastic change in confinement factor can be achieved as the mode will always reside partially in the III-V. In the case of very narrow silicon waveguides, the mode resides almost completely in the III-V region. Note that the value of $\Gamma_{\text{III-V}}^{\text{fund}}$ in the plots is the confinement in the InAs/InGaAs quantum dot active layers. Since these layers comprise only 15% of the active area, the number might seem lower than expected.

When increasing the silicon waveguide width the mode is pulled down. However, the slope of the effective index change decreases with increasing width, so very wide silicon waveguides will not impact the optical confinement factor. Furthermore, we see a similar story when increasing the III-V width: changing an already wide III-V waveguide will not have a huge impact on the confinement factor. In figure 4.5b the influence of the DVS-BCB thickness is plotted. Since the mode mainly resides in the III-V, thicker DVS-BCB makes it even harder to feel the pull of the silicon. So increasing DVS-BCB thickness will increase the confinement of the optical mode in the III-V.

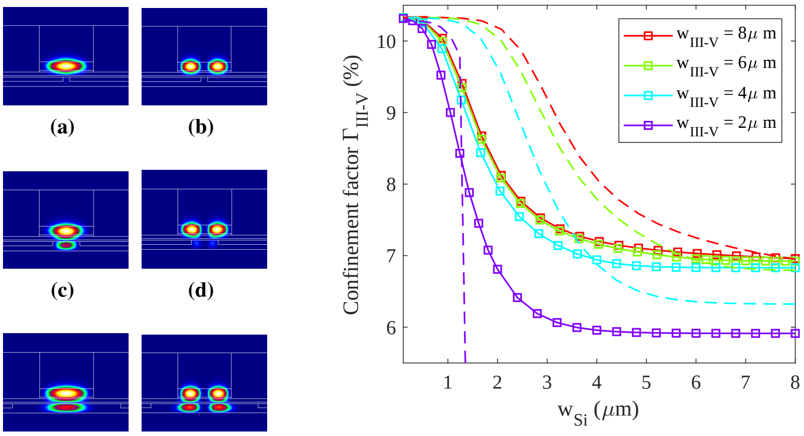

(a) **(b)**

(c) **(d)**

(e) **(f)** **(g)**

Figure 4.6: Optical mode profiles of the fundamental and second order mode of the heterogeneous (Si/III-V) waveguide for $w_{\text{III-V}}$ = 4 μm: (a-b) w_{Si} = 500 nm; (c-d) w_{Si} = 2 μm; (e-f) w_{Si} = 8 μm. (g) The confinement factor $\Gamma_{\text{III-V}}$ of the fundamental mode (full line) and second order mode (dotted line) as a function of w_{Si} for various $w_{\text{III-V}}$ (h_{BCB} = 60 nm).

Up till now, only the fundamental optical mode was taken into account. However, since the subsequent passive circuits are usually designed to work only for the fundamental mode, we should make sure only this mode lases. In figure 4.6 the mode profiles and confinement factors of the fundamental and the second order mode are plotted for different silicon widths. We see that the second order mode can have an optical confinement factor $\Gamma^{\text{2nd}}_{\text{III-V}}$ that is higher than that of the fundamental mode. Although its internal losses will be higher too, this can impede lasing solely in the fundamental mode. This is something we experienced in our fabricated lasers and will be described in section 4.2.

To get rid of this problem, other mesa designs should be considered. The mode profiles of the fundamental and second order mode of different mesa designs are displayed in figure 4.7. Figures 4.7a and 4.7e represent the mesa discussed above. In figures 4.7b, 4.7c, 4.7f and 4.7g, the quantum dot area is widened, but the p-cladding is not, to ensure enough carrier confinement. Although slight changes can be observed in the confinement factors and internal losses, the second order mode is still guided and thus a reason for concern. A much smaller waveguide trench, so that the unetched silicon slab is brought underneath the III-V mesa, can be the solution. As is shown in figures 4.7d and 4.7h the second order mode is coupled into a radiation mode in the waveguide slab, while the fundamental mode is unchanged. This approach is also used by [26].

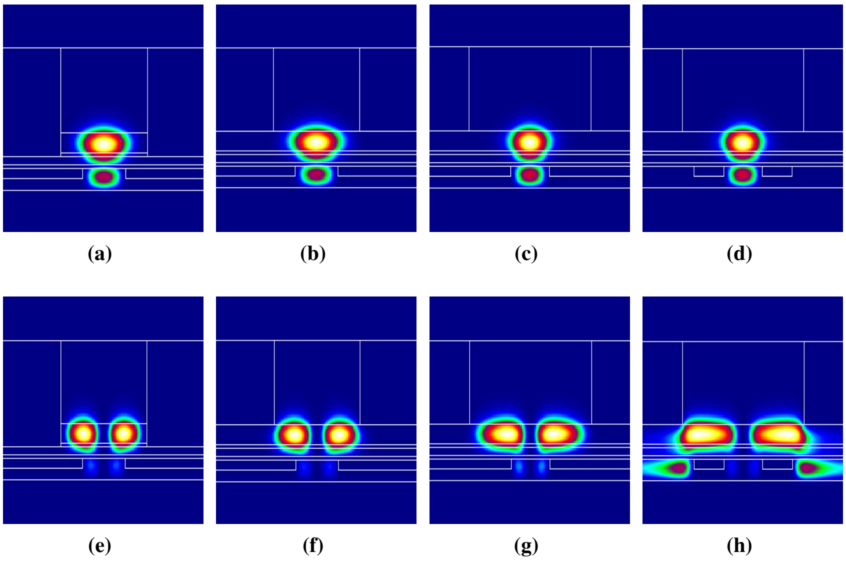
(a) **(b)** **(c)** **(d)**

(e) **(f)** **(g)** **(h)**

Figure 4.7: Optical mode profiles of the fundamental and second order mode of the heterogeneous (Si/III-V) waveguide for different mesa designs: (a)(e) $w_{\text{III-V}} = 4\ \mu$m; (b)(f) $w_{\text{p-clad}} = 4\ \mu$m; (c)(g) $w_{\text{p-clad}} = 8\ \mu$m; (d)(h) $w_{\text{p-clad}} = 8\ \mu$m and $w_{\text{Si, trenches}} = 2\ \mu$m; ($h_{\text{BCB}}$ = 60 nm and $w_{Si} = 2\ \mu$m).

Another important part of the mesa design deals with the electrical contacts and carrier confinement. In order to reduce the electrical resistance of the p-contact, we want its surface to be as large as possible. On the other hand, a wide mesa will increase the transparency current because the volume of gain material that needs to be pumped, increases. One way to address this, is the use of a proton implantation as described in [27, 28]. In our design we can make use of a property of the wet etching process used to define the laser mesas. As described in chapter 2, the reaction rate limited wet etching of the p-AlGaAs cladding layer in $KI:I_2:H_2O$ results in a V-shaped structure dependent on the crystal orientation as is shown in figure 4.8. Thanks to this V-shape, the electrical p-contact is wide, while the carriers are guided to a much smaller volume of quantum dot material.

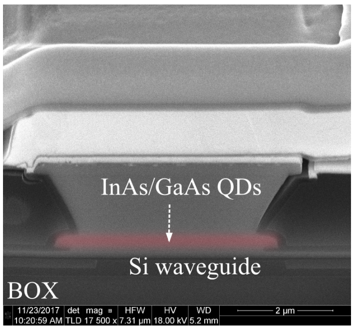

Figure 4.8: SEM picture of a FIB cross-section of the laser mesa.

4.1.5 Design of the Bragg grating

An important part of the DFB laser design, is the design of the Bragg grating that forms the laser mirror. Using formula 4.7, we can calculate that at 1300 nm, for our QD epitaxial layerstack, the first order grating period is equal to 196 nm. Since this is too small to be fabricated with 193 nm deep UV lithography at imec, we chose a second order Bragg grating with a period Λ equal to 392 nm and a 70% duty cycle. Using Fimmwave, the effective indices $n_{\text{eff,h}}$ and $n_{\text{eff,l}}$ of the fundamental mode are simulated. Based on formula 4.9, the coupling coefficient κ is calculated assuming a second order grating with a 70% duty cycle. In figure 4.9a, κ is plotted as a function of the DVS-BCB thickness for various grating widths. The III-V mesa is 4 μm wide. The smaller the silicon waveguide width and the thicker the DVS-BCB layer, the more the mode is pulled into the III-V, resulting in lower coupling. In figure 4.9b we compare the coupling coefficients of the different mesa designs suggested in figure 4.7. Since these design were mainly chosen to affect the second order mode and not the fundamental mode, they show similar coupling coefficients.

A common figure of merit to describe a DFB laser, is the $\kappa \cdot L$ product, with L the length of the grating. Typically this product is chosen between 1 and 3. According to equation 4.10, a $\kappa \cdot L$ product equal to 1 corresponds with a reflectance of 58% and $\kappa \cdot L$ equals 3 corresponds with a 99% reflectance. If $\kappa \cdot L$ is lower than 1, it becomes hard for the laser device to start lasing. If $\kappa \cdot L$ is higher than 3, it can lead to spatial-hole burning [19]. However, devices with a much higher $\kappa \cdot L$ are reported to exhibit successful laser operation [29]. This can be interesting for

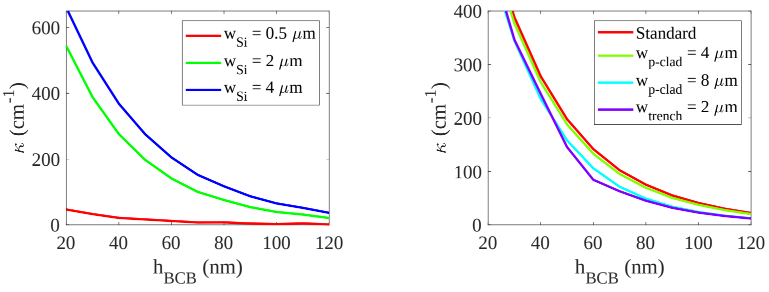

(a) **(b)**

Figure 4.9: Coupling coefficient κ as a function of DVS-BCB thickness for (a) the standard mesa ($w_{\text{III-V}}$ = 4 μm) for various grating widths; (b) different mesa designs (w_{Si} = 2 μm): the 4 designs displayed in figure 4.7.

high speed devices since a large κ results in a low threshold current, which enables a large direct modulation bandwidth [19].

In figure 4.10, the $\kappa \cdot L$ product and corresponding reflectance R is plotted as a function of grating length for several silicon widths and DVS-BCB thicknesses. Very short grating lengths should be avoided since this increases the thermal resistance and thus decreases the maximum output power. By varying the silicon width and DVS-BCB thickness, one can adjust the $\kappa \cdot L$ product of the grating without needing to go to very short gratings.

The impact of the bonding layer thickness on the reflectance spectra of the gratings is simulated with a full vectorial Maxwell solver tool (CAMFR). The results are plotted in figure 4.11. We see a red-shift of the spectrum with several nanometers for decreasing DVS-BCB thickness. Furthermore, a wider full-width at half maximum (FWHM) reflectance spectrum is observed for thinner DVS-BCB.

4.1.6 Taper design

The design of the spotsize converter was discussed at length in section 3.1.

4.2 Characterization

The lasers discussed here have second order DFB gratings with a phase-shift in the middle with grating periods of 392 nm and 400 nm, which corresponds with Bragg wavelengths of 1300 nm and 1320 nm, respectively. Due to fabrication limitations, we opted for a second order grating with a duty cycle of 70%. The grating κ is estimated to be around 77 cm^{-1} for both grating periods. The III-V gain section is

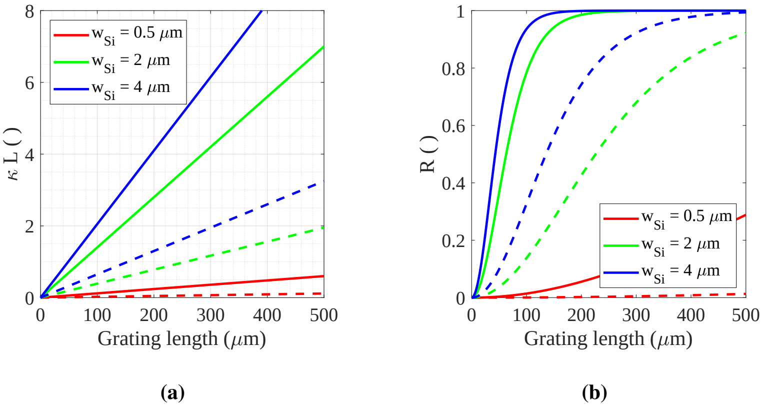

Figure 4.10: (a) Plots of the κ L product vs. grating length; (b) The reflectance R as a function of grating length. The full lines have a DVS-BCB thickness of 60 nm, the dotted lines have a DVS-BCB thickness of 100 nm.

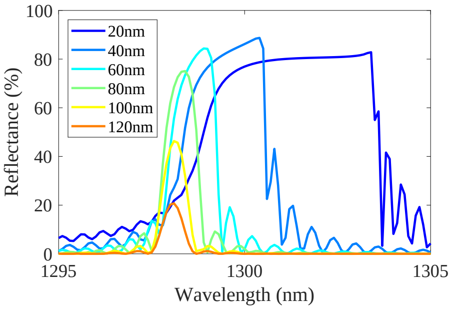

Figure 4.11: The impact of the bonding layer thickness on the reflectance spectra of the gratings. Second order gratings with a period of 392 nm, a duty cycle of 70 %. The grating length is equal to 1000 periods Λ.

800 μm (period: 392 nm) and 1000 μm (period: 400 nm) long (not including the 215 μm-long spotsize converters on each side). A 215 μm-long tapered spotsize converter is used to couple the light from the gain section into the passive silicon waveguides. The III-V taper is a piecewise linear taper that quickly tapers (L = 35 μm) from a 3.7 μm mesa width to an 1.7 μm wide waveguide width after which a slower adiabatic taper (L = 180 μm) is implemented by tapering both the III-V and silicon waveguide structure.

Two DFB lasers with grating periods of 392 nm and 400 nm and Bragg wavelengths of 1300 nm and 1320 nm, respectively were investigated. The laser characterization is carried out by coupling the output of the DFB laser to a cleaved standard single mode fiber through a fiber-to-chip grating coupler. The loss of the grating coupler was measured to be around 8 dB. The measurements were carried out with the device on a thermo-electric heater set at temperatures ranging from 20°C to 100°C. A schematic drawing of the set-up is shown in figure 4.12.

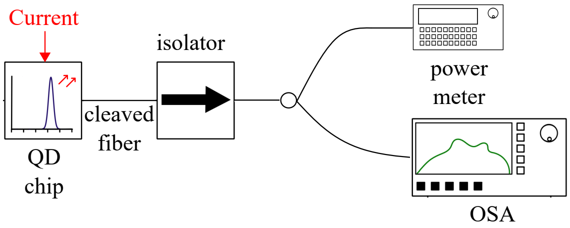

Figure 4.12: Schematic drawing of the measurement set-up.

The continuous wave (CW) light-current-voltage (LIV) characteristic of the DFB lasers is shown in Fig. 4.13, as a function of temperature. Figure 4.13b shows CW lasing is observed up to 100°C for the DFB laser lasing around 1320 nm. We measure output powers up to 2.5 mW in the waveguide at room temperature for both lasers. The ripple observed in the LI characteristics is attributed to parasitic reflections from the grating coupler used for fiber coupling and reflections at the taper tip of the III-V material. This could be improved by using low reflection grating couplers [30] and a better taper tip definition. The differential resistance at 70 mA is 4.1 Ω for the 1300 nm laser and 3.6 Ω for the 1320 nm laser. The wall-plug efficiency of the laser diode is 1.4 % for the 1300 nm laser at 120 mA and 1.7 % at 100 mA for the 1320 nm laser.

The CW threshold current as a function of stage temperature is shown in Fig. 4.14. The lowest threshold currents are 9.5 mA, reached at 20°C (shown in Fig. 4.14a) and 19 mA, reached at 50°C (shown in Fig. 4.14b) for the 1300 nm and 1320 nm DFB lasers, respectively. These correspond with state-of-the-art threshold current densities of 205 A/cm^2 (mesa width: 3.7 μm and laser length: 1250 μm) and 353 A/cm^2 (mesa width: 3.7 μm and laser length: 1450 μm), respectively. The total coupling strength κL for both devices was estimated by the band gap width to be around 6 for the 1300 nm laser and around 7.7 for the 1320 nm laser. This relatively strong coupling strength results in a low threshold modal gain as described in [31] and thus a low threshold current.

To understand the behavior of the threshold current as a function of temperature, we have to take into account that in a DFB laser the threshold current depends on the position of the gain peak relatively to the Bragg wavelength, which is determined by the grating period. In the 1320 nm DFB laser, the threshold current

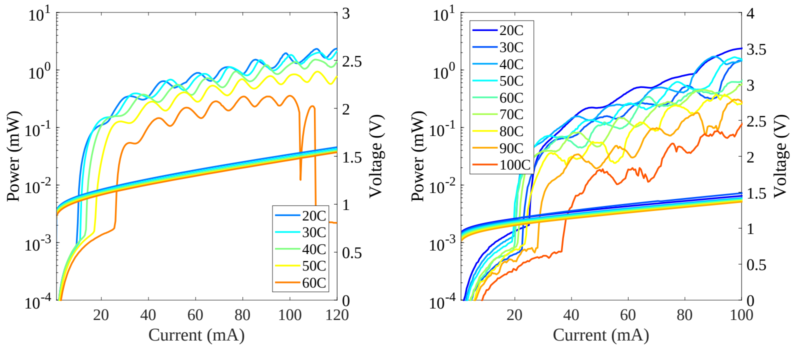

(a) 1300 nm **(b)** 1320 nm

Figure 4.13: LIV curve as a function of temperature. The power in the waveguide is plotted.

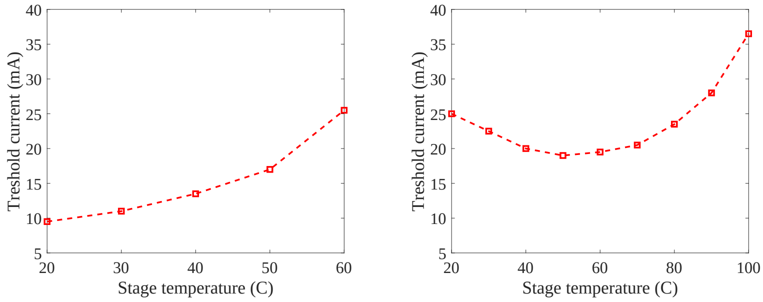

(a) 1300 nm **(b)** 1320 nm

Figure 4.14: Threshold current data as a function of stage temperature.

decreases with increasing temperature up to 50°C. This is due to the red detuning of the Bragg wavelength with respect to the gain peak at room temperature: when increasing the temperature, the gain shifts to longer wavelengths at a rate approximately five times faster than the Bragg wavelength and thus aligns better with the Bragg wavelength of the grating. At temperatures above 55°C, the threshold current starts increasing with increasing temperature. In the 1300 nm DFB laser, when increasing the temperature the gain peak shifts away from the Bragg wavelength, resulting in an increasing threshold current. At high temperatures the detuning between the Bragg wavelength and the gain peak becomes that big that it prevents CW lasing above 60°C. To improve the intrinsic temperature stability of the GaAs quantum dot material, the undoped quantum dots could be replaced with p-type modulation-doped quantum dots [32]. Furthermore, all improvements of the thermal sinking, like thicker metal on top and thermal vias will benefit the performance of the laser.

For both DFB lasers, the optical spectrum as a function of temperature for a drive current of 60 mA is plotted in Fig. 4.15. Laser emission at 20°C is observed around 1298 nm for a grating period of 392 nm, plotted in Fig. 4.15a and around 1322 nm for a grating period of 400 nm, plotted in Fig. 4.15b. With increasing temperature the laser output wavelength shifts to longer wavelengths with a temperature coefficient of 0.1nm/°C. We see single mode operation and a side-mode suppression ratio (SMSR) of 47 dB (1298 nm) and 40 dB (1322 nm). The SMSR is not affected by the ripple observed in the LI curve.

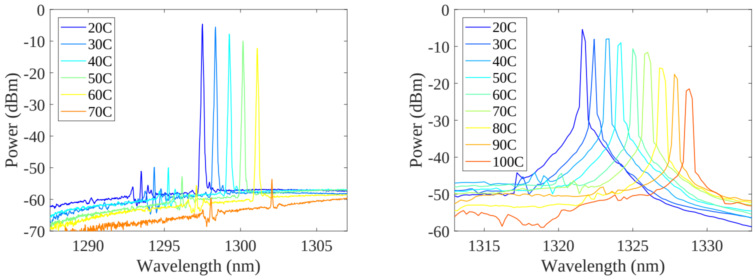

(a) **(b)**

Figure 4.15: (a) Optical spectrum for a drive current of 60 mA as a function of temperature: single mode operation with a SMSR of 47 dB. The DFB laser has a grating period of 392 nm. (OSA resolution: 0.06 nm) (b) Optical spectrum for a drive current of 60 mA as a function of temperature: single mode operation with a SMSR of 40 dB for a DFB laser with a grating period of 400 nm. (OSA resolution: 0.1 nm) Note that the difference in shape between the lasing peaks of (a) and (b) is due to the fact that different optical spectrum analyzers (OSA) were used to measure both lasers.

Figure 4.16 shows the optical spectra as a function of drive current at room temperature. At higher drive currents (e.g. from 90 mA at 20°C) higher order modes appear for the 1320 nm DFB laser, as is shown in Fig. 4.16b. This is due to lateral higher order modes that exist in the laser mesa as can be seen in Fig. 4.17. These modes have a similar optical confinement in the active region (8.9% for the fundamental mode and 8.8% for the first order mode) and therefore experience a similar level of gain. They have a slightly lower effective index ($n_{eff,0}$ = 3.31 and $n_{eff,1}$ = 3.29) and thus a lower Bragg wavelength than the fundamental mode ($\lambda_{B,0}$ = 1322 nm and $\lambda_{B,1}$ = 1318 nm). Normally, when an adiabatic taper is present, this taper will act as a mode filter and only the fundamental mode will couple into the silicon waveguide. However, a small misalignment (300 nm)

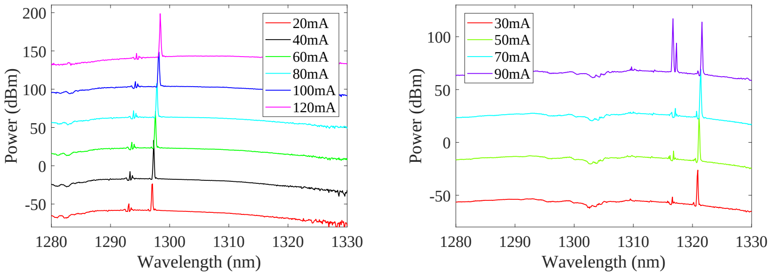

(a) Grating period: 392 nm **(b)** Grating period: 400 nm

Figure 4.16: Optical spectra for different drive currents at room temperature. The different spectra are shifted 40 dB apart for clarity (OSA resolution: 0.06 nm).

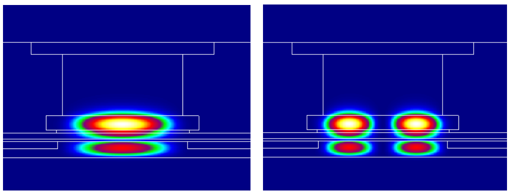

(a) Fundamental mode **(b)** Second order mode

Figure 4.17: Mode profiles of the hybrid modes present in the laser cavity.

allowed the second order mode to also couple to the silicon waveguide's fundamental mode at higher drive currents in case of the 1320 nm DFB laser. We didn't have the same problem with the 1300 nm laser, since in this case the first order mode is further removed from the gain peak than the fundamental mode and never reaches the lasing threshold.

Furthermore, due to imperfect fabrication of the laser mesa the taper tip was too broad, such that the laser suffered from back-reflections from the III-V taper tip and higher coupling losses. We tried to improve the tapers in new laser fabrication runs by putting them longer in the KI:I_2:H_2O etch solution. As described in chapter 2, the 1.5 μm thick p-$Al_{0.4}Ga_{0.6}As$ cladding layer is wet etched in KI:I_2:H_2O and this gives the mesa its characteristic reverse triangle shape. However, when we make the tapers narrower, many of them are taken out by defects. Examples of this are shown in figure 4.18. In figure 4.18a we see a microscope image of a taper right after the mesa etch. We can clearly see that the mesa is damaged during this etch step and this will in turn prevent efficient coupling from the III-V into the silicon waveguides. Not all of the defects are visible from above. In figure 4.18b we see an SEM picture of a FIB cross-section of the taper. We see that their is some sort of hole in the sidewall of the p-$Al_{0.4}Ga_{0.6}As$ cladding layer, again resulting in major taper losses. In a last SEM picture, shown in figure 4.18c we see that at the taper tip the laser mesa broke loose from the SOI, due to some strain present in the epitaxial layer, preventing all coupling. Improving the laser working will go hand in hand with improving the epitaxial material.

4.3 Conclusion

We demonstrated a single mode quantum dot DFB laser on a silicon photonic integrated circuit with efficient coupling of light to a silicon waveguide. We demonstrated high temperature operation with CW lasing up to 100°C. Threshold current densities as low as 205 A/cm^2 were measured. The laser showed single mode behavior with a side-mode suppression ratio of 47 dB. The device performance is currently limited by the suboptimal III-V tapers, resulting in residual reflections, extra losses and the existence of higher order modes. We expect significant improvement with better III-V taper structures. These devices are attractive candidates for uncooled transceivers in data centers.

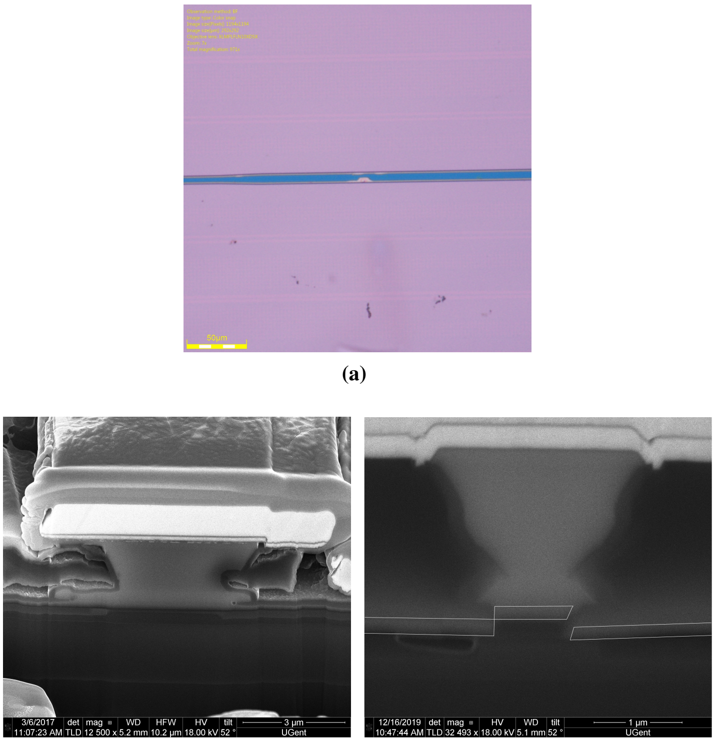

(a)

(b)

(c)

Figure 4.18: Processing of narrow taper tips in order to improve the coupling efficiency gives rise to defects. (a) Microscope image of a taper right after etching of the quantum dot layer: the mesa edge became uneven due to defects present in the material. The 300 nm SiN hard mask on top of the mesa is underetched. We can still see its original shape, but underneath we see the III-V mesa in blue. (b) SEM picture of a FIB cross-section of the taper: although this taper seemed fine from the top, the side-walls became wobbly during etching. (c) SEM picture of a FIB cross-section of the taper: the taper tip broke loose from the SOI. The n-GaAs contact layer stayed bonded to the SOI where no mesa was present.

References

[1] David AB Miller. *Rationale and challenges for optical interconnects to electronic chips*. Proceedings of the IEEE, 88(6):728–749, 2000.

[2] Zhiping Zhou, Bing Yin, and Jurgen Michel. *On-chip light sources for silicon photonics*. Light: Science & Applications, 4(11):e358, 2015.

[3] Mitsuru Sugawara and Michael Usami. *Quantum dot devices: Handling the heat*. Nature Photonics, 3(1):30–31, 2009.

[4] HY Liu, DT Childs, TJ Badcock, KM Groom, IR Sellers, M Hopkinson, RA Hogg, DJ Robbins, DJ Mowbray, and MS Skolnick. *High-performance three-layer 1.3-μm InAs-GaAs quantum-dot lasers with very low continuous-wave room-temperature threshold currents*. Photonics Technology Letters, IEEE, 17(6):1139–1141, 2005.

[5] Di Liang, Geza Kurczveil, Xue Huang, Chong Zhang, Sudharsanan Srinivasan, Zhihong Huang, M Ashkan Seyedi, Kate Norris, Marco Fiorentino, John E Bowers, and Raymond G Beausoleil. *Heterogeneous silicon light sources for datacom applications*. Optical Fiber Technology, 2017.

[6] Daehwan Jung, Zeyu Zhang, Justin Norman, Robert Herrick, MJ Kennedy, Pari Patel, Katherine Turnlund, Catherine Jan, Yating Wan, Arthur Gossard, and John Bowers. *Highly reliable low threshold InAs quantum dot lasers on on-axis (001) Si with 87% injection efficiency*. ACS Photonics, 2017.

[7] Yi Wang, Siming Chen, Ying Yu, Lidan Zhou, Lin Liu, Chunchuan Yang, Mengya Liao, Mingchu Tang, Zizhuo Liu, Jiang Wu, et al. *Monolithic quantum-dot distributed feedback laser array on silicon*. Optica, 5(5):528–533, 2018.

[8] Nobuaki Hatori, Yutaka Urino, Takanori Shimizu, Makoto Okano, Tsuyoshi Yamamoto, Masahiko Mori, Takahiro Nakamura, and Yasuhiko Arakawa. *Quantum Dot Laser for a Light Source of an Athermal Silicon Optical Interposer*. In Photonics, volume 2, pages 355–364. Multidisciplinary Digital Publishing Institute, 2015.

[9] Katsuaki Tanabe, Katsuyuki Watanabe, and Yasuhiko Arakawa. *III-V/Si hybrid photonic devices by direct fusion bonding*. Scientific reports, 2, 2012.

[10] Yuan-Hsuan Jhang, Katsuaki Tanabe, Satoshi Iwamoto, and Yasuhiko Arakawa. *InAs/GaAs Quantum Dot Lasers on Silicon-on-Insulator Substrates by Metal-Stripe Wafer Bonding*. Photonics Technology Letters, IEEE, 27(8):875–878, 2015.

[11] Géza Kurczveil, Di Liang, Marco Fiorentino, and Raymond G Beausoleil. *Robust hybrid quantum dot laser for integrated silicon photonics*. Optics Express, 24(14):16167–16174, 2016.

[12] Bongyong Jang, Katsuaki Tanabe, Satoshi Kako, Satoshi Iwamoto, Tai Tsuchizawa, Hidetaka Nishi, Nobuaki Hatori, Masataka Noguchi, Takahiro Nakamura, Keizo Takemasa, et al. *A hybrid silicon evanescent quantum dot laser*. Applied Physics Express, 9(9):092102, 2016.

[13] Alexander W Fang, Erica Lively, Ying-Hao Kuo, Di Liang, and John E Bowers. *A distributed feedback silicon evanescent laser*. Optics Express, 16(7):4413–4419, 2008.

[14] Shahram Keyvaninia, Steven Verstuyft, Liesbet Van Landschoot, F Lelarge, G-H Duan, S Messaoudene, JM Fedeli, T De Vries, B Smalbrugge, EJ Geluk, et al. *Heterogeneously integrated III-V/silicon distributed feedback lasers*. Optics letters, 38(24):5434–5437, 2013.

[15] Sarah Uvin, Sulakshna Kumari, Andreas De Groote, Steven Verstuyft, Guy Lepage, Peter Verheyen, Joris Van Campenhout, Geert Morthier, Dries Van Thourhout, and Gunther Roelkens. *1.3 μm InAs/GaAs quantum dot DFB laser integrated on a Si waveguide circuit by means of adhesive die-to-wafer bonding*. Optics express, 26(14):18302–18309, 2018.

[16] 2020. `http://www.ict-caladan.eu/`.

[17] Larry A Coldren, Scott W Corzine, and Milan L Mashanovitch. *Diode lasers and photonic integrated circuits*, volume 218. Wiley. com, 2012.

[18] H Ghafouri-Shiraz. *Distributed feedback laser diodes and optical tunable filters*. John Wiley & Sons, 2004.

[19] Geert Morthier and Patrick Vankwikelberge. *Handbook of distributed feedback laser diodes*. Artech House, 2013.

[20] Michael L Davenport, Sandra Skendžić, Nicolas Volet, Jared C Hulme, Martijn JR Heck, and John E Bowers. *Heterogeneous silicon/III–V semiconductor optical amplifiers*. IEEE Journal of Selected Topics in Quantum Electronics, 22(6):78–88, 2016.

[21] Alan Y Liu, Chong Zhang, Justin Norman, Andrew Snyder, Dmitri Lubyshev, Joel M Fastenau, Amy WK Liu, Arthur C Gossard, and John E Bowers. *High performance continuous wave 1.3 μm quantum dot lasers on silicon*. Applied Physics Letters, 104(4):041104, 2014.

[22] Dieter Bimberg, M Grundmann, F Heinrichsdorff, NN Ledentsov, VM Ustinov, AE Zhukov, AR Kovsh, MV Maximov, YM Shernyakov, BV Volovik, et al. *Quantum dot lasers: breakthrough in optoelectronics*. Thin Solid Films, 367(1):235–249, 2000.

[23] A Kovsh, A Gubenko, I Krestnikov, D Livshits, S Mikhrin, J Weimert, L West, G Wojcik, D Yin, C Bornholdt, et al. *Quantum dot comb-laser as efficient light source for silicon photonics*. In Photonics Europe, pages 69960V–69960V. International Society for Optics and Photonics, 2008.

[24] Minh A Tran, Duanni Huang, Tin Komljenovic, Jonathan Peters, Aditya Malik, and John E Bowers. *Ultra-low-loss silicon waveguides for heterogeneously integrated silicon/III-V photonics*. Applied Sciences, 8(7):1139, 2018.

[25] Philippe P Absil, Peter De Heyn, Hongtao Chen, Peter Verheyen, Guy Lepage, Marianna Pantouvaki, Jeroen De Coster, Amit Khanna, Youssef Drissi, Dries Van Thourhout, et al. *Imec iSiPP25G silicon photonics: a robust CMOS-based photonics technology platform*. In Silicon Photonics X, volume 9367, page 93670V. International Society for Optics and Photonics, 2015.

[26] Michael Davenport. *Heterogeneous Silicon III-V Mode-Locked Lasers*. PhD thesis, University of California, Santa Barbara, 2017.

[27] H Boudinov, Hoe H Tan, and Chenupati Jagadish. *Electrical isolation of n-type and p-type InP layers by proton bombardment*. Journal of Applied Physics, 89(10):5343–5347, 2001.

[28] Alexander W Fang, Hyundai Park, Oded Cohen, Richard Jones, Mario J Paniccia, and John E Bowers. *Electrically pumped hybrid AlGaInAs-silicon evanescent laser*. Optics express, 14(20):9203–9210, 2006.

[29] Shinji Matsuo and Takaaki Kakitsuka. *Low-operating-energy directly modulated lasers for short-distance optical interconnects*. Advances in Optics and Photonics, 10(3):567–643, 2018.

[30] Diedrik Vermeulen, Yannick De Koninck, Yanlu Li, Emmanuel Lambert, Wim Bogaerts, Roel Baets, and Günther Roelkens. *Reflectionless grating couplers for Silicon-on-Insulator photonic integrated circuits*. Optics express, 20(20):22278–22283, 2012.

[31] Chong Zhang, Sudharsanan Srinivasan, Yongbo Tang, Martijn JR Heck, Michael L Davenport, and John E Bowers. *Low threshold and high speed short cavity distributed feedback hybrid silicon lasers*. Optics Express, 22(9):10202–10209, 2014.

[32] Qizhu Li, Xu Wang, Hongmei Chen, Yuanqing Huang, Chuncai Hou, Jie Wang, Ruiying Zhang, Jiqiang Ning, Jiahua Min, and Changcheng Zheng. *Development of Modulation P-Doped 1310 nm InAs/GaAs Quantum Dot Laser Materials, and Ultra-Short Cavity Fabry-Perot and Distributed-Feedback Laser Diodes*. ACS Photonics, 2017.

5

InP quantum well mode-locked lasers integrated on silicon

Mode-locked lasers are an attractive source of short (femto- and picosecond) optical pulses at radio frequencies. Moreover, the emission of short pulses in the time domain generates a broad optical comb in the frequency domain. Because of their excellent characteristics mode-locked laser are of interest in a range of applications. Their short pulses combined with very high peak powers make them excellent light sources for precision medical cutting applications [1] for example corneal surgeries [2]. Due to the stable timing between pulses they are well suited to create photonic analog-to-digital converters [3]. Since mode-locked lasers produce a broad comb of optical frequency tones, they can be used for broadband spectroscopy [4], high-speed gas spectroscopy [5] and in wavelength division multiplexing (WDM) systems [6]. In the electrical domain a harmonic series of tones at different microwave frequencies is generated. Therefore the mode-locked laser is gaining interest as a compact microwave signal source [7–9] for example for the signal generation in photonic radar [10].

The gain medium of mode-locked lasers comes in all shapes and sizes, from bulk crystals like Nd:YAG and Ti:sapphire over doped glass fibers such as the erbium-doped fiber amplifier (EDFA) to semiconductors. The latter results in mode-locked laser diodes. They can be made very small and can be electrically pumped unlike the bulk crystal and fiber lasers which should be pumped optically. This significantly reduces the cost and complexity of the laser systems. Moreover all advantages of semiconductor manufacturing can be leveraged. The lasers can be produced in large numbers on wafer scale. Also they can be part of larger integrated circuits opening up a whole new range of applications [11, 12].

Two material platforms are widely used to produce integrated mode-locked lasers. The most mature platform is the monolithic indium phosphide (InP) platform. It consists of an active-passive integration technology to integrate optical amplifiers and passive waveguides on the same chip [11, 13]. More recently, the heterogeneous III-V-on-silicon platform has emerged as an attractive technology to make integrated (mode-locked) lasers. Silicon-on-insulator (SOI) is used to realize all the passive components. III-V material, InP-based (chapter 5) or GaAs-based (chapter 4 and 6), is bonded or transfer-printed in order to provide optical amplification [14, 15].

Low-noise performance is of paramount importance in most mode-locked laser applications. Fundamentally, the noise performance is determined by the spontaneous emission generated in the amplifier section of the mode-locked laser. Therefore, limiting the length of the semiconductor optical amplifier and realizing a low-loss optical cavity, consisting for a large part out of passive waveguides is crucial. Thanks to lower optical losses in SOI waveguides compared with InP waveguides and provided the III-V to silicon coupling structure is low loss, the cavity loss can be reduced significantly when replacing the III-V passive waveguide circuit by a silicon photonic integrated circuit. Furthermore, at telecom wavelengths also the two-photon absorption losses are substantially lower in silicon compared to InP-based waveguides, thereby creating less excess loss related to the high peak power nature of the optical pulses traveling in the mode-locked laser cavity. Moreover, silicon photonics, leveraging the well-developed CMOS fabrication infrastructure and its economy of scale, provides a distinct cost advantage over other optical technologies for transceiver applications. At the same time it allows lower power consumption and enables the scaling of the aggregate bandwidth of transceivers to the Terabit/s range. [16, 17]

The ultimate goal in this work is the realization of InAs/GaAs quantum dot mode-locked lasers integrated on silicon (see chapter 6). However, before we started doing that, we first did extensive research on InP-on-SOI mode-locked lasers, since this material platform is much better known. We will start this chapter with a brief introduction to the working principles of mode-locked lasers. In section 5.2 the fabrication of InP-on-SOI mode-locked lasers is discussed. On this platform three different mode-locked laser designs were fabricated: the linear colliding pulse MLL (section 5.3), the ring MLL (section 5.4) and the linear anti-colliding MLL (section 5.5). Next, we used the linear colliding pulse MLL to create a narrow line width frequency comb source based on an injection-locking of the MLL for OFDM applications (section 5.6).

5.1 Fundamentals of mode-locked lasers

In a standard laser cavity multiple longitudinal modes are present. Each mode is defined by its amplitude, its phase and its carrier frequency. The distance between two modes depends on the length of the cavity:

$$\Delta f = \frac{c}{2n_g L} \tag{5.1}$$

with n_g the group index and L the length of the cavity. The total signal is a superposition of all modes present in the cavity. This is illustrated in figure 5.1. In the top row, the modes present in the cavity are plotted (from left to right, the number of modes is equal to 1, 2, 5 and 10). In the bottom row, the modes are added together. We can clearly see that a pulse is created.

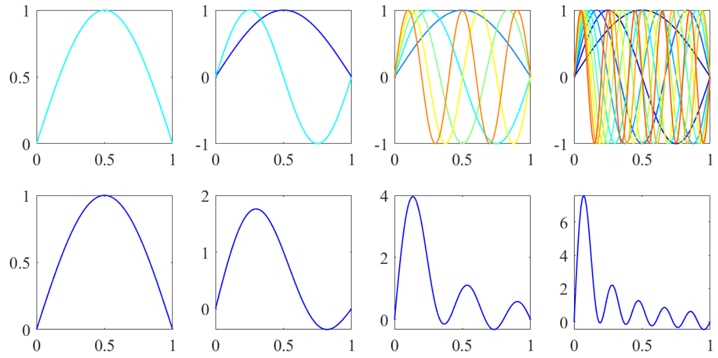

Figure 5.1: Generation of a pulse in a multi-mode laser. From left to right there are 1, 2, 5 and 10 modes present.

However, in normal multi-mode lasers all modes behave independently from each other (they are incoherent), resulting in a fluctuating output. Only when the modes have a constant phase relation in the laser cavity, an optical pulse train is generated. This is made clear in figure 5.2. The phases are locked and at fixed time intervals all modes interfere constructively, generating an optical pulse train. The distance between pulses T is equal to

$$T = \frac{1}{\Delta f} = \frac{2n_g L}{c} \tag{5.2}$$

So the pulse repetition rate is defined by the length of the cavity. A multi-mode laser with locked modes is called a mode-locked laser.

In the optical domain, the different modes result in a frequency comb. If the phases are perfectly locked, the pulse width is inversely proportional to the width

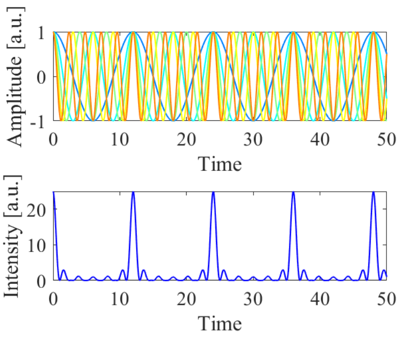

Figure 5.2: The modes should be locked in order to generate a pulse train. Example with 10 modes.

of the optical frequency comb: the more modes contribute to the pulse the shorter it becomes. This is also clear from figure 5.1.

However, in reality multiple noise sources like gain fluctuations, variation of the cavity length, refractive index variations, temperature variations, spontaneous emission, intracavity- and back-reflections and noise from the power source to bias the laser are present [18]. This results in fluctuations in the phase relationship between modes and of the amplitude of the modes. Amplitude and timing fluctuations appear in the pulse train.

To measure these fluctuations, it is interesting to look at the electrical domain in addition to the optical and time domain. By sending the signal to a photodetector, we can measure the signal generated by the beating between the modes [19]. A variation in the phase relation between the modes can be seen in the broadening of the radio-frequency (RF) beat tone. This beat tone represents the distance between adjacent modes Δf and thus also the time T between pulses. A fluctuation of T is also called timing jitter. Amplitude variation on the other hand causes the appearance of frequencies much lower than the repetition rate. These frequencies also appear around the RF tone and its harmonics.

In case the timing and amplitude variation are not related, the effect of the amplitude variation on the shape of the RF beat notes is the same for every harmonic. The effect of the timing jitter increases quadratically with the harmonic number. In reality however, in semiconductor mode-locked lasers the timing and amplitude jitter are usually linked to each other [20]. So a strong and narrow RF beat tone is an important indication of good mode-locking. [21]

There are different ways to lock the modes of a laser [22]. In case of active mode-locking, a sinusoidal signal with a frequency equal to Δf, the repetition rate of the laser cavity, is sent to an optical loss modulator inside the cavity. As illustrated in figure 5.3, net-amplification of the signal only occurs around minimal loss creating a pulse train.

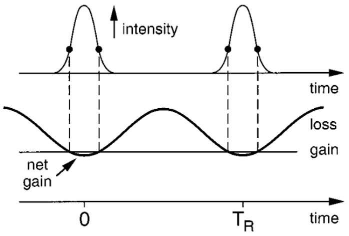

Figure 5.3: Schematic of the laser actively mode-locked and the time dependence of the net gain [22].

Secondly, the modes can also be locked through passive mode-locking. No external RF modulation source is needed, instead a saturable absorber is used. In semiconductor lasers this saturable absorber is made by electrically isolating part of the gain section and reverse biasing it. On start up of the laser emission, noisy bursts of light start to oscillate in the cavity since the phases are still random. The saturable absorber absorbs all low power light, but at some point a burst can be energetic enough to bleach the absorber. Around the intensity peak the losses are lower, however the low power wings are still absorbed. By traveling back and forth in the cavity, only the peak is amplified and the pulse grows stronger and more narrow. At steady state this results in a train of mode-locked pulses. To understand the mode-locking process better, the dynamics of the absorption and the gain are important. This is shown in figure 5.4. At steady state, when the pulse reaches the absorber, the loss saturates more quickly than the gain. This results in a net gain window. The leading edge of the pulse is absorbed and thus becomes steeper. Next, the saturable absorber is saturated, so the peak experiences a high net gain. Subsequently, the gain saturates, but the loss is not saturated anymore, so the trailing edge of the pulse experiences a net loss. The shorter the net gain window, the shorter the pulses. [23]

5.2 Fabrication process

Three different integrated mode-locked laser cavity designs, the linear colliding pulse MLL (section 5.3), the ring MLL (section 5.4) and the linear anti-colliding MLL (section 5.5) were fabricated on one chip sharing the same epitaxial material and fabrication process. The device processing was carried out by Shahram Keyvaninia, while the author took the lead in the characterization of the devices.

The mode-locked lasers consist of a planarized SOI waveguide circuit and gratings defined in a 400 nm thick silicon waveguide layer using 193 nm deep UV lithography (180 nm etch depth) fabricated in a CMOS pilot-line at imec. The

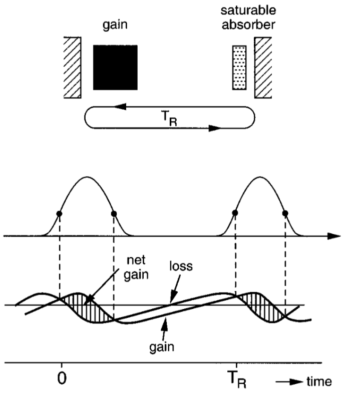

Figure 5.4: Schematic of passive mode-locking and the time dependence of the pulse train, gain and loss [22].

InGaAsP quantum well epitaxial layer stack is adhesively bonded to the planarized silicon-on-insulator (SOI) using a 75 nm-thick divinylsiloxane-bisbenzocyclobutene (DVS-BCB) bonding layer. The epitaxial layer stack consists of 6 InGaAsP quantum wells (6 nm thick, emission wavelength 1550 nm) surrounded by InGaAsP barriers sandwiched between two 100 nm thick InGaAsP separate confinement heterostructure (SCH) layers. The layer stack is described in detail in [17]. The confinement factor of the optical mode is 7.5% in the quantum well layers both in the gain section and in the saturable absorber.

A 210 μm-long tapered spotsize converter is used to couple the light from the gain section into the passive silicon waveguides. The III-V taper is a piecewise linear taper that quickly tapers (L = 50 μm) from a 3.0 μm mesa width to an 1.2 μm wide waveguide width after which a slower adiabatic taper (L = 160 μm) is implemented by tapering both the III-V and silicon waveguide structure, similar to the spotsize converter described in section 3.1.

The fabrication process of the laser is broadly similar to the process described in section 2.3.3, however different etchants were used since the III-V material is InP-based instead of GaAs. More details about the device fabrication can be found in [17].

5.3 Linear colliding pulse mode-locked laser

First, we look at a linear mode-locked laser realized in a colliding pulse configuration. The structure of the laser comprises a saturable absorber (SA) section located in the middle of the resonator cavity between two semiconductor optical amplifier (SOA) sections, as is illustrated in figure 5.5. Two counter-propagating pulses circulate in the cavity and only interact in the saturable absorber. This leads to a doubling of the repetition frequency and thus a halving of the pulse period. Due to its geometry, this design is very sensitive to any mismatch in the saturable absorber position. When the symmetry is not perfect, the harmonic mode-locking can fail and tones at half the repetition frequency can appear. [24]

Their are different ways to form the cavity. The silicon waveguides can be polished in order to create flat facet mirrors [25] and loop mirrors can be created in the silicon. The latter resulted in a 20 GHz MLL with a peak power of 98 mW, the highest of any fully integrated laser at 20 GHz, a 1.1 kHz RF-linewidth and a 900 fs pulse [12]. In this work we used a distributed Bragg reflector (DBR) to form the cavity.

5.3.1 Implementation

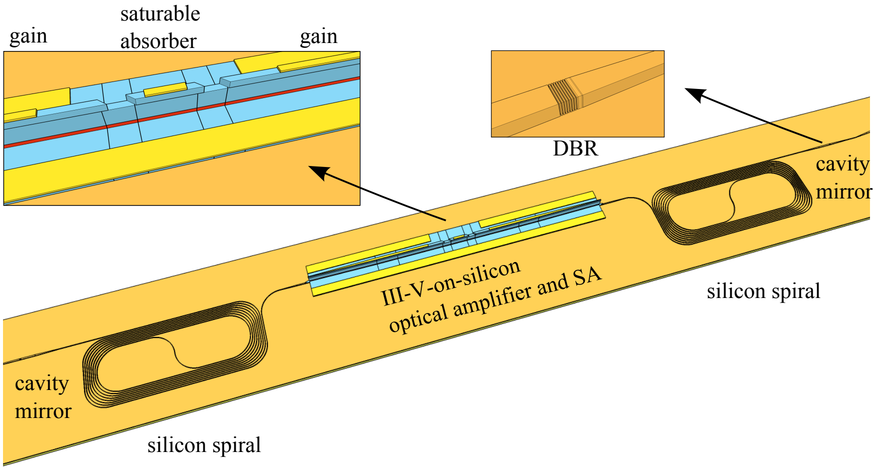

Figure 5.5: Illustration of the linear cavity colliding pulse mode-locked laser.

The three-dimensional layout of the linear colliding pulse mode-locked (CPML) laser is shown in Fig. 5.5. The optical amplifier and the saturable absorber are implemented in the III-V-on-silicon waveguide section. The III-V gain section is 2×380 μm long (not including the 210 μm long spotsize converters), while the III-V saturable absorber, placed in the center of the laser cavity is 100 μm long. The main part of the cavity length is formed by two silicon spiral waveguides of 0.7 cm length each in order to reach a pulse repetition rate of about 5 GHz (4.69 GHz in the experiment) in colliding pulse mode. The propagating loss in the silicon waveguide is measured to be 0.7 dB/cm. The laser cavity mirrors are also fabricated in the silicon waveguide layer. Two first order silicon distributed Bragg reflector (DBR) mirrors (period 255 nm, 50 % duty cycle, 7 periods) providing close to 50 % reflectivity are placed at both ends of the laser cavity.

5.3.2 Characterization

The measurements are carried out with the device on a thermo-electric cooler set at 20 °C. Figure 5.6 shows the schematic of the measurement set-up. The output of the mode-locked laser is coupled to an optical fiber through a fiber-to-chip grating coupler. The coupling efficiency is measured to be -12 dB. An optical isolator is used to prevent back-reflections into the laser. The performance of the laser is investigated by connecting the laser to a high-resolution optical spectrum analyzer (OSA) (20 MHz resolution), to a high-speed photodiode (50 GHz bandwidth) that is connected to a 50 GHz electrical spectrum analyzer (ESA) or to a second harmonic generation based intensity autocorrelator (SHG-AC), after passing through an EDFA.

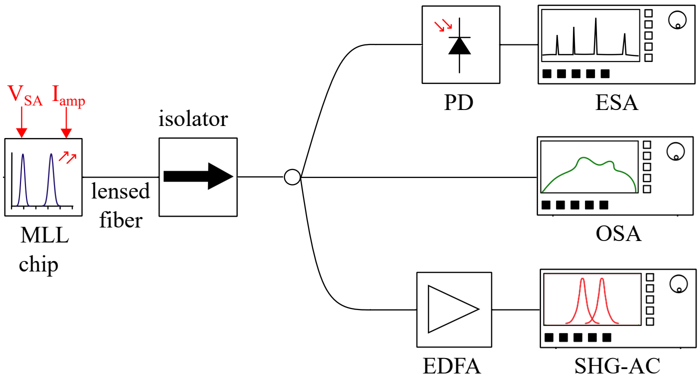

Figure 5.6: Schematic of the experimental set-up used for the characterization of the mode-locked laser.

The light-current characteristic of the realized device is shown in figure 5.7, as a function of saturable absorber reverse bias. The dips observed in the light-current characteristics are attributed to parasitic reflections from the grating coupler used for fiber coupling.

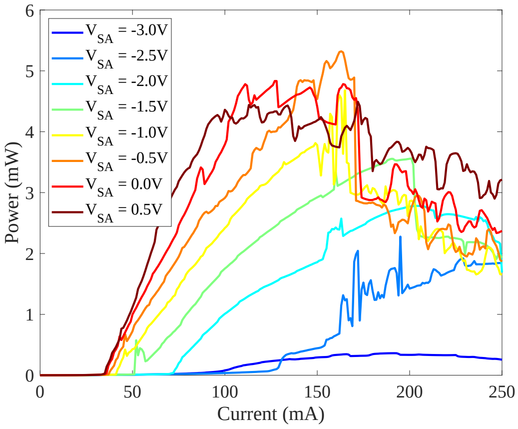

Figure 5.7: LI curve as a function of saturable absorber voltage. The power in the waveguide is plotted.

For the passive mode-locking experiments, a reverse bias voltage of -1.2 V was applied to the saturable absorber and 160 mA current is injected in the spot-size converters and semiconductor optical amplifier as these settings resulted in the most flat RF spectrum of the generated pulse train. Figure 5.8 shows a high-resolution optical spectrum generated by the mode-locked laser. A 9 nm 3 dB optical bandwidth is obtained.

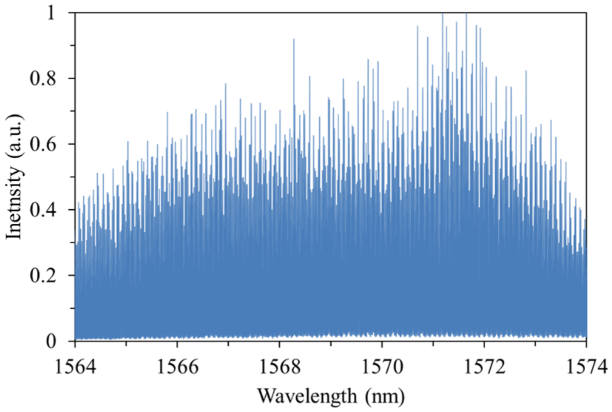

Figure 5.8: High resolution optical spectrum (resolution bandwidth: 20 MHz). The laser gain section is biased at 160 mA, while the saturable absorber has a reverse bias of -1.2 V.

Using a second harmonic generation autocorrelator (SHG-AC) the pulse duration was determined to be 1.5 ps assuming a sech^2 pulse shape as shown in figure

5.9, using a correction factor of 1.54 between the full width at half maximum (FWHM) of the SHG-AC trace and the actual pulse width. The shortest pulse came at 160 mA bias current and a -1.2 V reverse bias voltage, when the CW power was 3.2 mW. This corresponds to a 450 mW peak power in the waveguide.

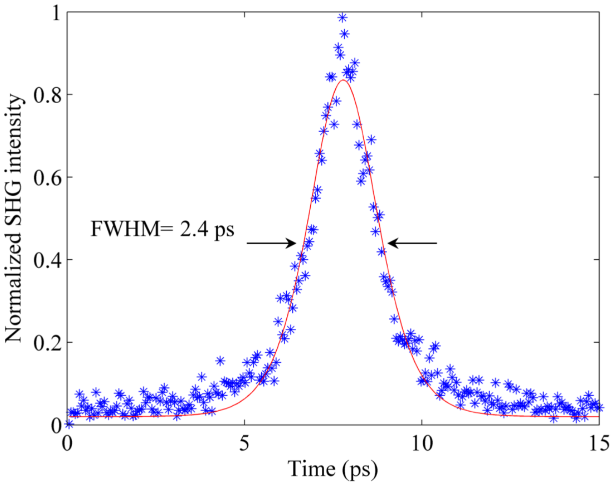

Figure 5.9: Intensity autocorrelation trace of the pulse train. The laser gain section is biased at 160 mA, while the saturable absorber has a reverse bias of -1.2 V.

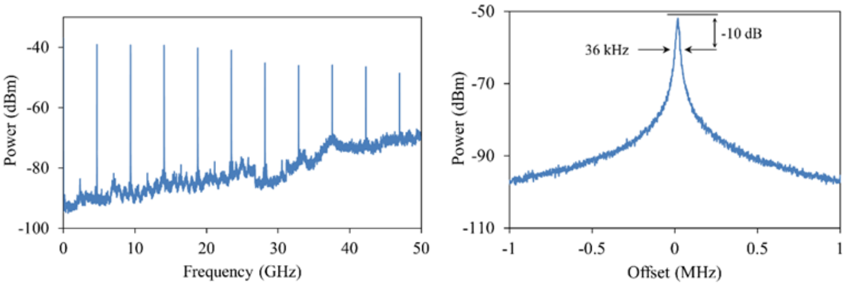

(a) (b)

Figure 5.10: (a) Wide span electrical spectrum of the generated pulse train (Resolution bandwidth (RBW): 500 kHz and video bandwidth (VBW): 50 kHz). (b) Linewidth of the fundamental RF tone at 4.69 GHz (RBW and VBW used to obtain the RF spectrum were 2 kHz and 20 Hz). The laser gain section was biased at 160 mA, while the saturable absorber had a reverse bias of -1.2 V.

Next, RF spectra are recorded at the same operation point as is used for the optical spectrum measurement. Figure 5.10a shows a wide frequency span electrical spectrum. We can see a residual component at half the repetition rate due to the fact that in the linear CPML design two pulses travel in the laser cavity and couple to the same output. If these two pulses are not identical, a spurious tone occurs. However, the unwanted residual component is more than 40 dB below the main RF tone, indicating good colliding pulse operation of the device.

Figure 5.10b shows the fundamental RF tone (at 4.69 GHz) with a 36 kHz 10 dB linewidth.

5.4 Ring mode-locked laser

An alternative manner to realize mode-locked lasers in a colliding pulse configuration is the ring or racetrack laser as is shown in figure 5.11. Two pulses propagate in the ring cavity in opposite directions and collide in the SA. Since the two pulses couple to different output waveguides, the frequency is not doubled as is the case in linear colliding pulse configurations (explained in section 5.3). This means that in the ring mode-locked laser no spurious tones appear when the SA is not placed exactly in the middle.

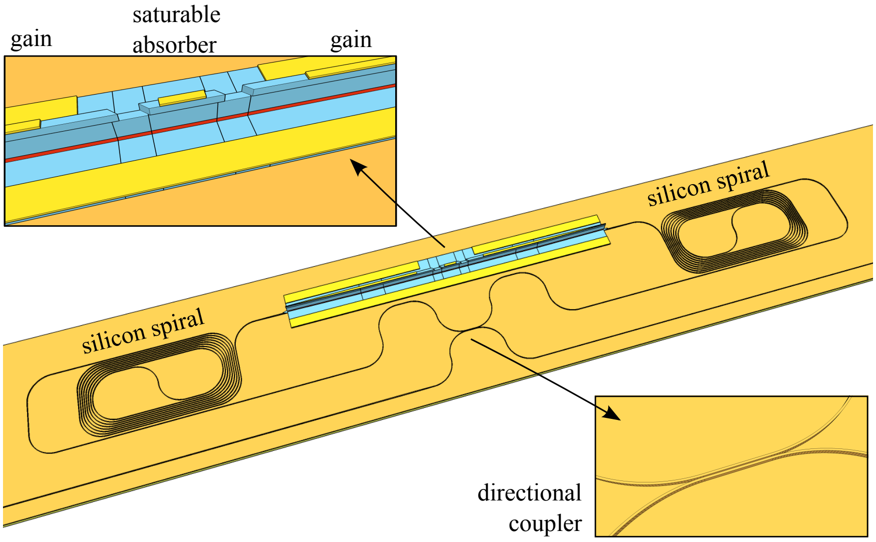

Figure 5.11: Illustration of the ring cavity colliding pulse mode-locked laser.

5.4.1 Implementation

The three-dimensional layout of the ring mode-locked laser is shown in Fig. 5.11. The optical amplifier and the saturable absorber are implemented in the III-V-on-silicon waveguide section. The III-V gain section is 2×740 μm long (not including the 210 μm long spotsize converters), while the III-V saturable absorber, placed symmetrically in the laser cavity is 180 μm long. The main part of the cavity length is formed by two silicon spiral waveguides of around 0.65 cm length each in order to reach a pulse repetition rate of about 5 GHz (4.72 GHz in the experiment). A directional coupler (coupling around 35%) is used for the optical coupling between the laser cavity and the silicon output waveguide.

5.4.2 Characterization

The measurements are carried out on the same set-up as shown in figure 5.6 and described in section 5.3.2.

The light-current characteristic of the realized device is shown in figure 5.12, as a function of saturable absorber reverse bias. The dips observed in the light-current characteristics are attributed to parasitic reflections from the grating coupler used for fiber coupling.

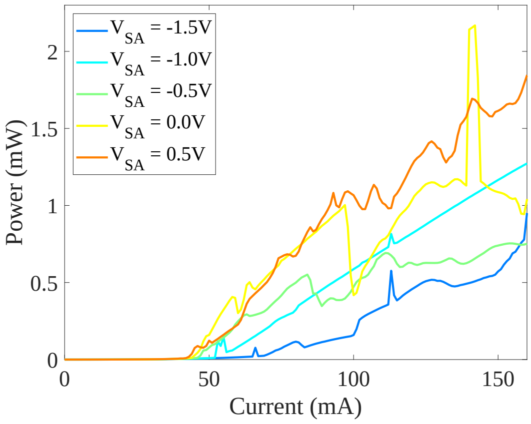

Figure 5.12: LI curve as a function of saturable absorber voltage. The power coupled in the silicon waveguide is plotted.

For the passive mode-locking experiments, a reverse bias voltage of -1.3 V was applied to the saturable absorber and 179 mA current is injected in the spot-size converters and semiconductor optical amplifiers. Figure 5.13 shows a high-resolution optical spectrum generated by the mode-locked laser. A 2.5 nm 3 dB optical bandwidth and a 7 nm 10 dB optical bandwidth is obtained.

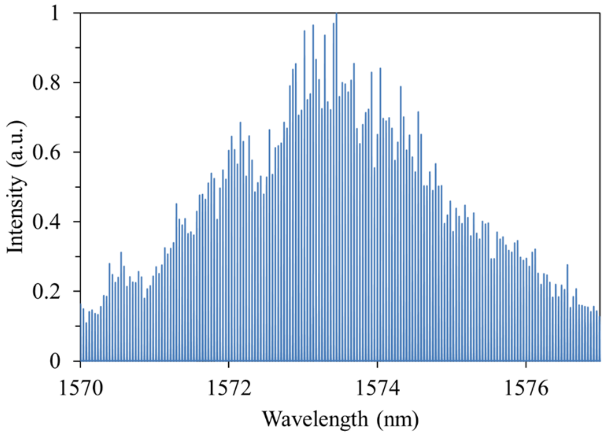

Figure 5.13: High resolution optical spectrum (resolution bandwidth: 20 MHz). The laser gain section is biased at 179 mA, while the saturable absorber has a reverse bias of -1.3 V.

Figure 5.14 shows the intensity autocorrelator trace. The pulse shape is not bell-shaped as in the linear cavity arrangement. This is attributed to the existence of additional features around the main pulse such as leading or trailing satellite peaks, attributed to partial incoherence of the laser comb spectrum, the source of which is not fully understood

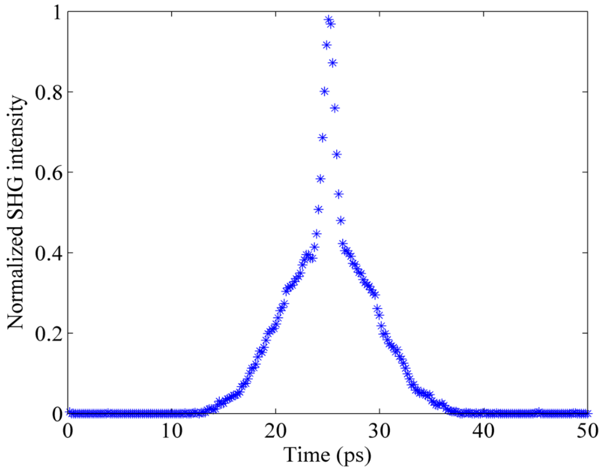

Figure 5.14: Intensity autocorrelation trace of the pulse train. The laser gain section is biased at 179 mA, while the saturable absorber has a reverse bias of -1.3 V.

Next, RF spectra are recorded at the same operation point as is used for the optical spectrum measurement. Figure 5.15a shows a wide frequency span electrical spectrum. Figure 5.15b shows the fundamental RF tone (at 4.72 GHz) with a 49 kHz 10 dB linewidth.

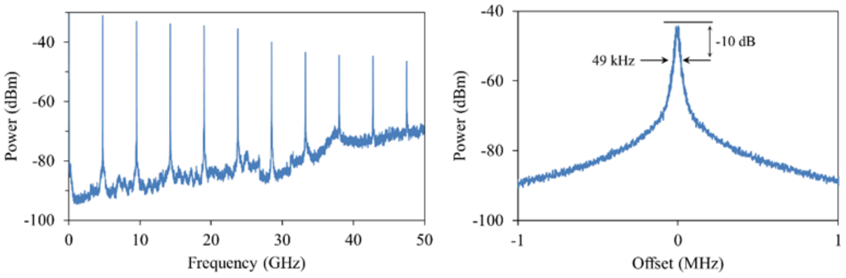

(a) **(b)**

Figure 5.15: (a) Wide span electrical spectrum of the generated pulse train (Resolution bandwidth (RBW): 500 kHz and video bandwidth (VBW): 50 kHz). (b) Linewidth of the fundamental RF tone at 4.72 GHz (RBW and VBW used to obtain the RF spectrum were 2 kHz and 20 Hz). The laser gain section was biased at 179 mA, while the saturable absorber had a reverse bias of -1.3 V.

5.5 Anti-colliding mode-locked laser

Next to a colliding pulse mode-locking scheme, one can also place the saturable absorber close to one of the mirrors. Traditionally, the SA is placed close to the high reflectivity mirror, the so-called self-colliding pulse mode-locking scheme (SCPM), where the pulse interacts with itself in the SA [26–28]. A deeper SA saturation and thus better mode-locking is assumed due to the strong interaction between the forward and backward propagating pulses.

However in [29] a theoretical analysis predicts an increase in output power and a reduction in amplitude and timing jitter compared with the self-colliding pulse designs when putting the SA next to the low reflectivity mirror. This is called anti-colliding pulse mode-locking (ACPML), since the interaction between the forward and backward propagating pulses is strongly reduced. In the optical amplifier, the resulting intensity profile leads to more population inversion, causing more gain and thus higher output powers. The high intensities in the SA result in strong modulation, causing narrow RF linewidths. This theory was first proven in [30] and resulted in a 1 GHz III-V-on-Si mode-locked laser with a 900 Hz 10 dB RF linewidth [31].

5.5.1 Implementation

The device geometry is shown in figure 5.16. The optical amplifier and the saturable absorber are implemented in the III-V-on-silicon waveguide section. The III-V gain section is 650 μm long (not including the 150 μm long spotsize converters), while the III-V saturable absorber is 65 μm long. The confinement factor of the optical mode in the quantum wells is 7.5 % both in the gain section and in the saturable absorber.

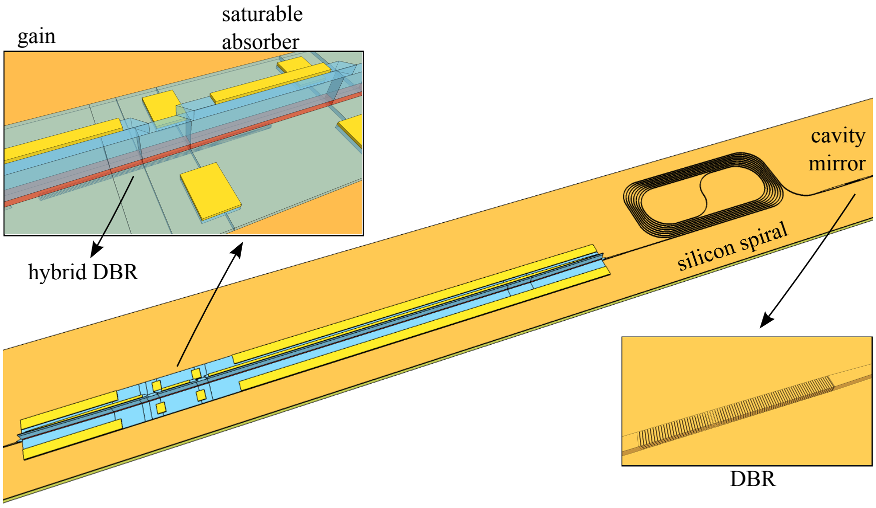

Figure 5.16: Illustration of the DBR cavity anti-colliding pulse mode-locked laser.

The main part of the cavity length is formed by a silicon spiral waveguide of 0.7 cm length in order to reach a pulse repetition rate of about 5 GHz (4.83 GHz in the experiment). The laser cavity mirrors are also fabricated in the silicon waveguide layer. A high reflectivity cavity mirror is created by a broadband silicon distributed Bragg reflector (DBR) mirror (period 505 nm, 75 % duty cycle, 40 μm long) providing close to 100 % reflectivity at the right end of the laser cavity. The second cavity mirror is formed by a silicon DBR grating implemented partly underneath the saturable absorber, as is shown in figure 5.18. This grating has a 490 nm period, 75 % duty cycle, a total length of 100 μm and extends 40 μm under the output III-V spotsize converter. According to simulations the peak reflectivity and bandwidth of this grating depend on the thickness of the DVS-BCB bonding layer, as can be seen in figure 5.17. Qualitatively, a thinner bonding layer results in a wider bandwidth reflectance spectrum, with a red-shift of the spectrum peak. For a 75 nm thick DVS-BCB bonding layer as used in the experiment, see figure 5.18, this yields a peak reflectivity of 60% and a 3 dB bandwidth of 4 nm.

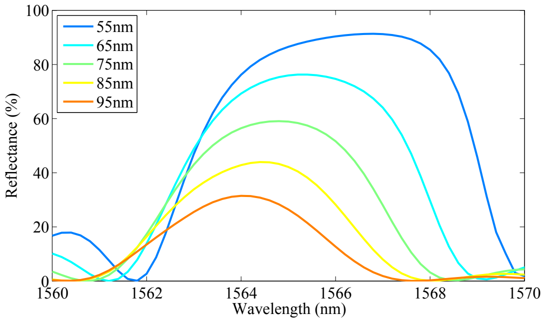

Figure 5.17: The impact of bonding layer thickness on the reflectance spectra of the gratings simulated with a full vectorial Maxwell solver tool (CAMFR).

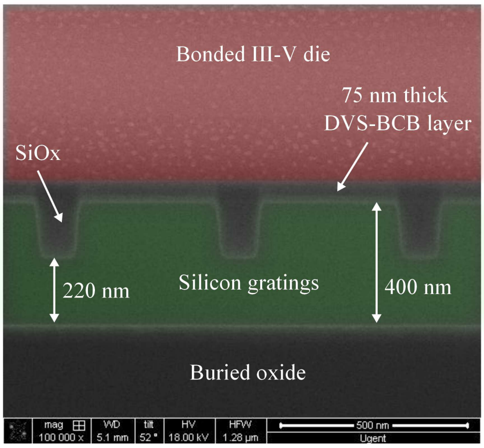

Figure 5.18: SEM picture of the bonding interface at the saturable absorber.

5.5.2 Characterization

The measurements are carried out on the same set-up as shown in figure 5.6 and described in section 5.3.2.

The light-current characteristic of the realized device is shown in figure 5.19, as a function of saturable absorber reverse bias. At thermal roll-over the waveguide coupled output power is over 9 mW for a -0.7 V reverse bias voltage on the saturable absorber, substantially higher than the ring cavity and linear cavity colliding pulse lasers with similar dimensions implemented using the same technology. The dips observed in the light-current characteristics are attributed to parasitic reflections from the grating coupler used for fiber coupling.

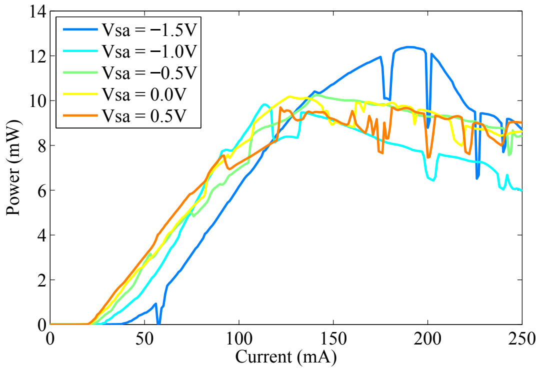

Figure 5.19: Power versus current plot of the anti-colliding mode-locked laser as a function of saturable absorber reverse bias voltage.

For the passive mode-locking experiments, a reverse bias voltage of -0.7 V was applied to the saturable absorber and 61 mA current is injected in the spotsize converters and semiconductor optical amplifier as these settings resulted in the most flat RF spectrum of the generated pulse train. Figure 5.20 shows a high-resolution optical spectrum generated by the mode-locked laser. A 3.5 nm 10 dB optical bandwidth is obtained. Using a second harmonic generation autocorrelator (SHG-AC) the pulse duration was determined to be 3 ps. An intensity autocorrelator trace is plotted in figure 5.21.

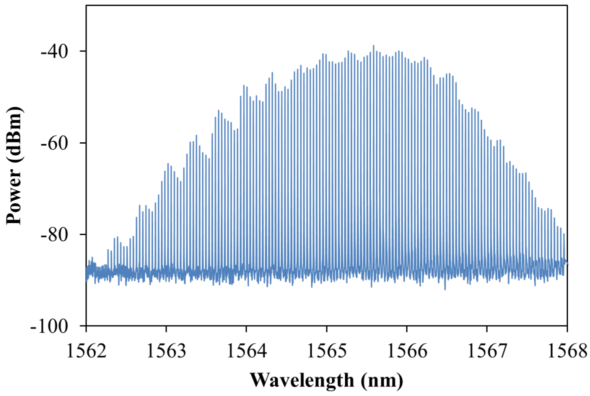

Figure 5.20: High resolution optical spectrum at 61 mA drive current and -0.7 V reverse bias on the saturable absorber showing the 40 pm spaced longitudinal modes (20 MHz spectral resolution). A 10 dB optical bandwidth of 3.5 nm is obtained.

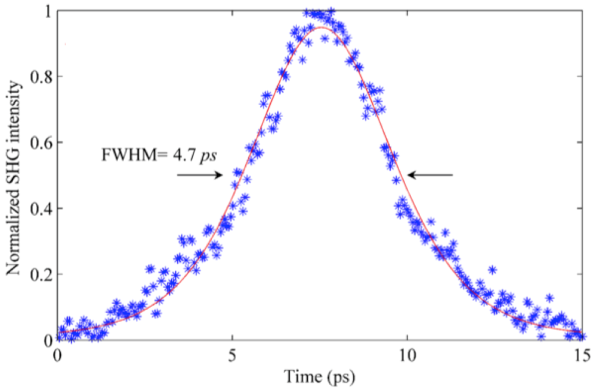

Figure 5.21: Intensity autocorrelator trace (blue: experimental, red: theoretical fitting). The 4.7 ps FWHM of the trace corresponds to a 3 ps pulse width assuming its sech^2 amplitude profile. The laser gain section is biased at 61 mA, while the saturable absorber has a reverse bias of -0.7 V.

Next, RF spectra are recorded at the same operation point as is used for the optical spectrum measurement. Figure 5.22a shows a wide frequency span electrical spectrum. The linewidth of the fundamental RF tone (at 4.83 GHz) is very narrow: a 1.7 kHz 3 dB linewidth (5 kHz 10 dB linewidth) is observed, as shown in figure 5.22b. This linewidth is state-of-the art for fully integrated heterogeneous Si lasers and considerably lower than those of the majority of fully integrated devices [12].

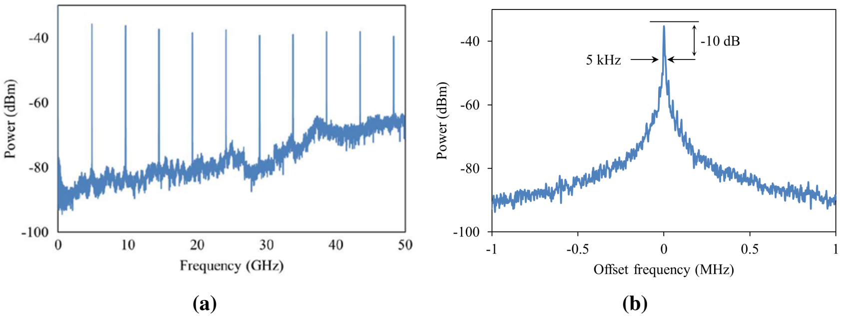

Figure 5.22: (a) Wide span electrical spectrum of the generated pulse train (Resolution bandwidth (RBW): 500 kHz and video bandwidth (VBW): 50 kHz). (b) Linewidth of the fundamental RF tone (resolution bandwidth and video bandwidth used to obtain the RF spectrum were 1.5 kHz and 150 Hz). The laser gain section was biased at 61 mA, while the saturable absorber had a reverse bias of -0.7 V.

5.6 Narrow line width frequency comb source based on an injection-locked mode-locked laser

The global Internet traffic has grown dramatically in the past two decades. Advanced transceiver technology is indispensable to handle the massive amount of information that needs to be transported over the optical network. The spectral efficiency of these transceivers is of paramount importance for the effective use of the available optical fiber bandwidth. The conventional solution is to use highly parallel wavelength division multiplexing (WDM) with several tens of channels. The spectral efficiency of such a system is however far below the theoretical limit, due to the guard bands inserted in between the wavelength channels. Moreover, the management of large arrays of single wavelength lasers is far from trivial. Coherent optical orthogonal frequency division multiplexing (OFDM) systems can provide a solution to these problems. Tbps optical OFDM communication systems with high spectral efficiency have been demonstrated [32]. Such a system requires an optical frequency comb source to generate an array of narrow line width lines with a fixed phase relation and fixed frequency spacing.

The frequency comb can be generated by a mode-locked laser. Because of the mode-locking, the laser lines have inherently a distinct phase relation, while the frequency spacing is determined by the repetition rate of the laser. It has been shown that (stabilized) mode-locked fiber lasers can serve as a frequency comb source, however, these lasers have typically a low repetition rate (and hence too small frequency spacings for optical communication) because of the long laser cavity length [33]. Integrating mode-locked lasers on chip could overcome this problem, and has additionally a clear advantage in volume factor and power consumption. However the line width of the longitudinal modes of such lasers is typically in the MHz-range, which is too broad for advanced coherent communication schemes [34]. To overcome the line width problem Kerr combs have been suggested as alternative. This approach uses the strong Kerr-nonlinearity in integrated microring resonators to generate combs. Although it has been challenging to generate coherent microresonator frequency combs, their wide bandwidth and frequency spacing compared to fiber lasers allow high data rate communication links [35]. However, the relatively low power efficiency in converting the laser light into the sidebands and high optical pump power needed, complicate the co-integration of the pump laser and resonator on a chip. Recently, a laser-integrated Kerr frequency comb generator was demonstrated through the use of extremely low loss silicon nitride waveguides that form both the microresonator and an integrated laser cavity [36]. Alternatively, cascaded phase and amplitude modulation of a narrow line width CW source can be used to create a frequency comb [37, 38]. However, this approach suffers from the high power consumption for driving the modulators and the high insertion loss of the cascade of modulators. We propose a solution based on the injection locking of an integrated mode-locked laser with a narrow line width continuous wave (CW) source. We show that the laser lines generated by the mode-locked laser are coherent with the narrow line width CW source. Due to the low optical power that is needed to lock the mode-locked laser, the system could be completely integrated on a single chip.

To meet the demanding requirements of coherent communications, the mode-locked laser needs to have a narrow optical line width. At 40 Gbit/s for example, the laser line widths must be in the range of 1 kHz to 240 kHz, depending on the modulation format [34]. However, the optical line width of the individual lines of the mode-locked lasers described in the previous sections still lie in the MHz range, insufficient for coherent communication. By injection of a narrow line width CW tone in the mode-locked laser, the optical line width can be reduced ideally to the line width of the CW source [39, 40]. We reduced the optical laser line width to 50 kHz for a 4.71 GHz repetition rate mode-locked laser. This line width is narrow enough to enable coherent data transmission with advanced modulation formats.

Furthermore, the mode-locked lasers need to have also a low timing jitter. To improve the timing jitter, hybrid mode-locking can be used to synchronize the repetition rate of the laser to that of an external RF source.

Two locking techniques are explored. Both methods address the need for low timing jitter and a narrow optical line width at the same time. In a first approach a hybrid mode-locked III-V-on-silicon laser is injection locked with a CW source. In a second approach, hybrid mode-locking can be avoided, by injecting light from a modulated CW source in the passively mode-locked laser cavity. Coherence between more than 50 longitudinal modes and the CW source is experimentally confirmed.

5.6.1 Design and fabrication

The injection locking experiments were carried out on a linear cavity colliding pulse III-V-on-silicon mode-locked laser as described in section 5.3. The III-V gain section is 2×380 μm long (not including the 210 μm long spotsize converters), while the III-V saturable absorber is 100 μm long. A 210 μm-long tapered spotsize converter is used to couple between the hybrid gain section and the passive waveguide section as described in section 5.2. The main part of the cavity length is formed by two silicon spiral waveguides of each 0.7 cm length in order to reach a pulse repetition rate around 5 GHz (4.71 GHz in the experiment). The cavity mirrors are formed by first order distributed Bragg reflectors (DBR) (255 nm grating period, 50 % duty cycle, 180 nm etch depth), corresponding to a mirror reflectivity around 50 % in the wavelength range of interest. The laser emits in the L-band (around 1580 nm), the exact wavelength coverage depending on the laser drive conditions.

The measurements were carried out with the device on a thermo-electric cooler keeping the device at 20 °C. For the injection locking experiments, the saturable absorber is reverse biased at -1.3 V and 100 mA current is injected in the spotsize converters and semiconductor optical amplifiers as these settings resulted in the widest injection locking range. For these bias settings, the waveguide coupled laser output power is 6 mW. Although in free-running operation these settings are suboptimal, we noticed that less stable free-running mode-locked operation seems to lead to more stable locking operation under CW injection. This was also reported in [39].

In case of passive mode-locking, the 3 dB optical line width of the longitudinal modes of the mode-locked laser is several MHz and the RF line width was found to be 55 kHz when fitting a Lorentzian curve to the RF spectrum. Hybrid mode-locking and injection locking techniques are therefore needed to meet the stringent requirements of terabits per second coherent communications in terms of line width and phase stability.

5.6.2 Verifying the coherence of the laser lines spectrally close to the seed laser

Optical injection locking with a narrow line width CW tone has been shown to be an effective technique to reduce the longitudinal modes' phase and frequency noise [40]. By locking the comb generated by the MLL to a narrow line width source, the line width of the longitudinal modes can be reduced, ideally to the line width of the seed.

In a first experiment, a narrow line width fiber-coupled CW source, acting as the seed, is injected in the mode-locked laser through a fiber-to-chip grating coupler. A continuous wave optical parametric oscillator (OPO)-based source with a 50 kHz optical line width was used in the experiment. The wavelength of the narrow line width seed is tuned such that it coincides with the center of the mode-locked laser spectrum. The on-chip CW seed power is 0.6 mW. The position of the longitudinal mode closest to the seed will be pulled toward the seed wavelength, locking both its frequency and phase.

The injection-locking measurement set-up is depicted in Fig. 5.23. To verify the line width of the comb teeth, a frequency shifted copy of the seed source (by sending it through an acousto-optic modulator (AOM) inducing a 200 MHz frequency shift) is combined with the MLL emission and sent to a high speed photodetector connected to an RF spectrum analyzer recording the beat notes. An optical circulator is used to ensure that only the MLL output beam is combined with the shifted copy of the seed.

With this experiment, we can already verify that the lines with an optical frequency in the vicinity of the seed source are coherent with the seed source. Indeed,

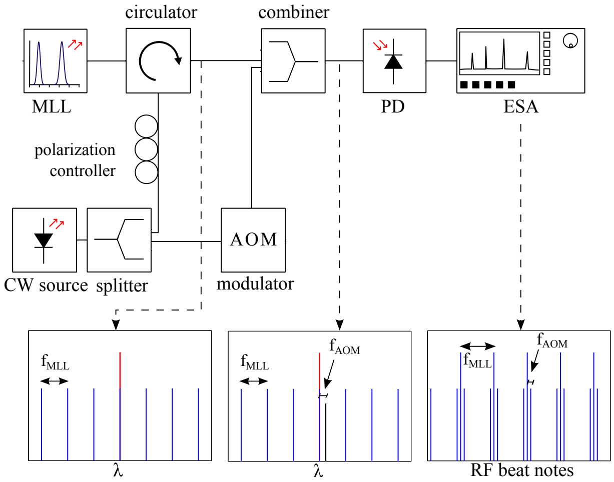

Figure 5.23: (a) Measurement set-up to verify the injection locking of the mode-locked laser. The mode-locked laser (blue) is locked to the CW laser (red) (b), combined with a frequency shifted version of the first laser (black) (c) and sent to a photodetector in order to measure the beat notes (d).

the six most adjacent lines to the seed frequency result in a sub-hertz RF beat note when interfered with the frequency shifted seed. This confirms the injection locking and the coherence of these lines. The optical line width of the MLL longitudinal modes is thus reduced down to the line width of the seed source, 50 kHz. Figure 5.24a shows the beat note of the first adjacent line. The 200 MHz shifted copy of the seed will beat with the line, which is spaced by the repetition rate f_{MLL} from the original seed source. This leads to beat notes at $f_{\mathrm{MLL}} - 200\mathrm{MHz}$ and at $f_{\mathrm{MLL}} + 200\mathrm{MHz}$, as is shown in Fig. 5.23. Of course also the repetition rate of the MLL itself is present in the RF spectrum. Figure 5.24b shows a zoom in on the beat note situated around $f_{\mathrm{MLL}} + 200\mathrm{MHz}$ or 4.909 GHz.

5.6.3 Verifying the coherence of the comb source over its whole spectrum

To assess the lines spectrally further away from the seed laser, the measurement set-up depicted in Fig. 5.25 is used. In this experiment a commercial fiber frequency comb source (Menlo Systems) is used to interfere with the III-V-on-silicon MLL. The commercial frequency comb lines are spaced f_{probe} = 100 MHz. The beat notes of the CW seed source with the commercial fiber comb source have a line width of around 100 kHz. The output of the comb laser is first sent through a filter with a 3 dB bandwidth of 0.1 nm and a tunable center wavelength, such that one can scan over the different lines of the mode-locked laser (spaced 40 pm apart)

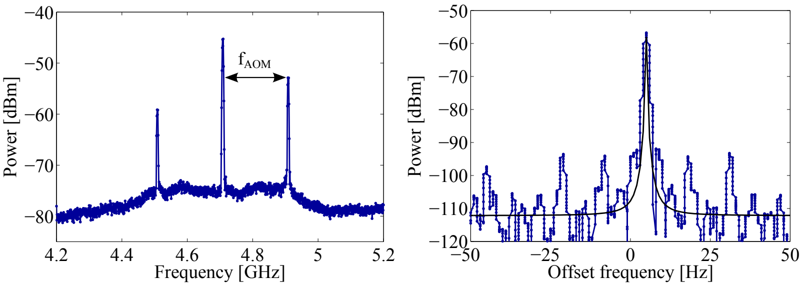

(a) (b)

Figure 5.24: (a) Lines in the vicinity of the seed are coherent with the seed source (Resolution bandwidth (RBW): 3 MHz), (b) A zoom in on one of the beat notes (situated at 4.909 GHz) shows the beat note has a sub-hertz RF line width (blue: experimental data, black: Lorentzian fit) (RBW: 1 Hz).

without probing them all at the same time. Next, the combined output is sent to a photodetector connected to an RF spectrum analyzer to record the beat notes, as indicated in Fig. 5.25.

Many different beat notes will be generated. With f_a being the distance between a mode-locked laser longitudinal mode and the nearest neighbour comb line, f_{MLL} the repetition rate of the mode-locked laser and f_{probe} the repetition rate of probe comb source, we can find beat notes at:

$$\pm f_a + m f_{\text{MLL}} + l f_{\text{probe}} \qquad m, l \in \mathbb{Z} \tag{5.3}$$

the line width of which is determined by the line width of the MLL longitudinal modes and that of the reference comb source. To minimize both the line width of the longitudinal modes of the MLL (measure of the stability of the total comb position) and the RF line width (measure of the stability of the repetition rate), two approaches are considered. In a first approach, the MLL is first hybrid mode-locked with an external RF source and then injection-locked to a narrow seed laser. In a second approach, a passively mode-locked laser is injection-locked to a modulated narrow seed laser.

5.6.3.1 Injection locking of a hybrid mode-locked laser with a CW source.

Hybrid mode-locking was obtained by delivering a local oscillator signal at 4.71 GHz (5 dBm RF power at the RF generator) to the saturable absorber using a bias-T. This results in a sub-hertz RF line width of the repetition rate, but the optical line width of the individual lines did not improve compared to passive mode-locking.

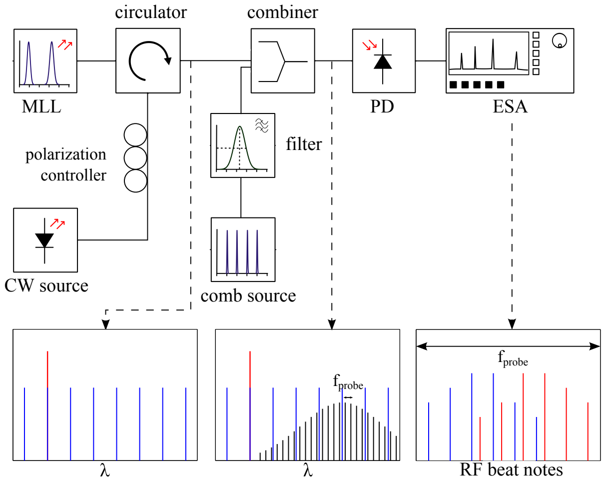

Figure 5.25: (a) Measurement set-up to verify the locking of a broad frequency comb. (b) The mode-locked laser (blue) is locked to the CW laser (red). (c) The output signal is combined with a filtered commercial comb laser (black) with a comb line spacing of f_{probe} = 100 MHz. (d) The beat notes are recorded on an electrical spectrum analyzer.

In order to reduce the optical line width, the hybrid mode-locking needs to be combined with optical injection locking with a narrow line width seed laser.

In Fig. 5.26, the optical spectrum before (blue) and after (red) injection locking is depicted. The injection power was measured to be 0.6 mW on chip. The optical spectrum becomes narrower compared to the non-injection locked state. This has been reported both in [39] and [40]. Before injection locking a 6.5 nm 3 dB optical bandwidth was measured. When the mode-locked laser is injection locked to the seed, a red shift of the spectrum occurs and the optical bandwidth reduces, as also discussed in [41].

In Fig. 5.27, the beat notes of the mode-locked laser longitudinal modes with the filtered probe comb lines are plotted. The center of the filter was positioned at 1579.2 nm. We can distinguish 12 different lines that correspond to the aforementioned equation 5.3 (the peak around 50 MHz actually corresponds to 2 lines very close together, as is shown in Fig. 5.27b). Line 1a and 1b result from two fiber frequency comb lines spaced f_a and $f_{\text{probe}} - f_a$ from the same MLL comb line. Line 2a and 2b result from the beating of the probe comb with the neighbouring MLL comb line and so on, meaning 6 mode-locked laser longitudinal modes are probed. From the Lorentzian fit of any of the beat notes, a beat note 3 dB line width < 100 kHz is obtained, which is the limit of the measurement system. This proves that the probed mode-locked laser lines are coherent with the seed source.

To determine the total number of comb lines that is coherent with the seed,

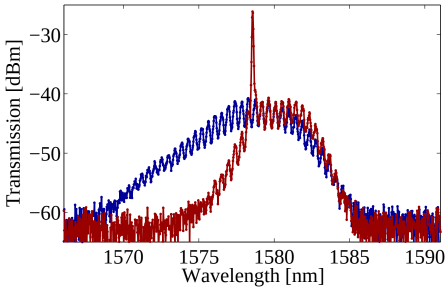

Figure 5.26: Optical spectrum of the mode-locked laser without injection locking (blue) and with injection locking (P_{CW} = 0.6 mW in the waveguide)(red) (60 pm spectral resolution).

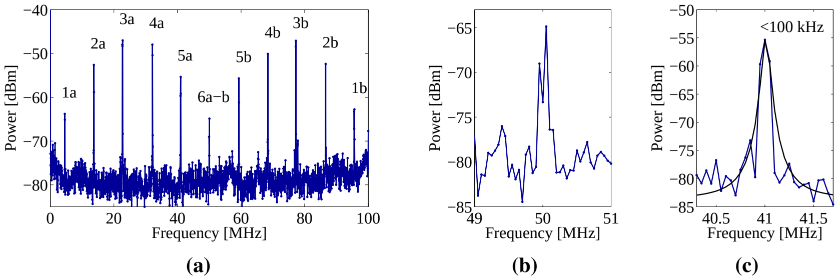

(a) **(b)** **(c)**

Figure 5.27: (a) Beat notes recorded on the electrical spectrum analyzer, (b) Zoom in on peak 6a and b, (c) Lorentzian fit of one of the beat notes with a 3 dB line width $<$ 100 kHz (blue: experimental data, black: Lorentzian fit) (RBW: 50 kHz).

the probe comb is swept over the different mode-locked laser lines by tuning the center of the filter. Narrow beat notes can be measured from a center wavelength of 1578.4 nm to 1579.5 nm for an injection power of 0.6 mW on chip, indicating that 30 mode-locked laser lines are coherent with the seed.

When decreasing the optical injection power, the number of coherent lines will decrease. This is illustrated in Fig. 5.28. However, at excessive optical injection ($\sim$ 1 mW) the laser ceases to be a mode-locked laser. Instead single mode CW operation is obtained (at the injection wavelength).

5.6.3.2 Injection locking of a passively mode-locked laser with a modulated CW laser.

In a second approach, hybrid mode-locking can be avoided without loosing control over the repetition rate of the MLL. This can be achieved by modulation of the

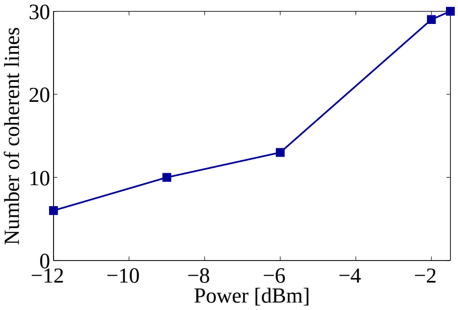

Figure 5.28: Number of coherent mode-locked laser lines as a function of CW seed power in the waveguide.

narrow line width seed at the repetition rate of the mode-locked laser. Optical injection locking of the MLL with a modulated seed narrows both the line width of the longitudinal modes and the RF beat notes.

Figure 5.29 shows the fundamental RF tone of the free running passive mode-locking (Fig. 5.29a), optical injection locking with a CW seed (passive mode-locking) (Fig. 5.29b) and optical injection locking with a modulated seed (passive mode-locking) (Fig. 5.29c). We can see that CW optical injection locking of the passive MLL already reduces the 3 dB line width from 55 kHz to 40 kHz. Using a modulated seed results in a sub-hertz 3 dB RF line width (Fig. 5.29c). A seed modulation depth of 11 dB was used in the experiment. In Fig. 5.29c side peaks can be observed more than 50 dB below the fundamental RF tone. The origin of these side peaks is not well understood.

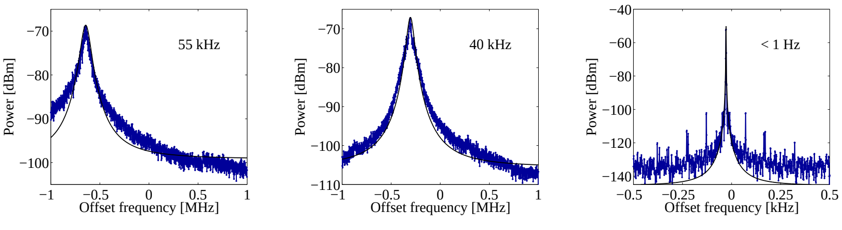

(a) (b) (c)

Figure 5.29: Modulation of the seed laser narrows the RF line width. Plot of the fundamental tone at 4.71 GHz under different locking conditions: (a) passive MLL without optical injection (RBW: 3 kHz), (b) passive MLL with optical injection (RBW: 3 kHz), (c) passive MLL with modulated injection (RBW: 1 Hz). Measurement data (red), Lorentzian fit (black). The measured 3 dB line width is indicated on all three graphs.

Being able to tune the repetition rate of the laser can be very useful when a deviation exist between the intended and the actual laser repetition rate (given by the optical length of the cavity). In case of pure passive mode-locking, the repetition rate can be slightly changed by changing the bias settings (saturable absorber voltage and gain current) of the mode-locked laser, but changes are smaller than 50 MHz ($<$ 1 % of the repetition rate). By tuning the modulation frequency of the seed laser we can tune the repetition rate of the MLL almost 100 MHz (2.1 % of the repetition rate) when the bias settings are fixed. This is illustrated in Figure 5.30. When the tuning is too far away from the ”natural” repetition rate, we can see this repetition rate also appear in the RF spectrum.

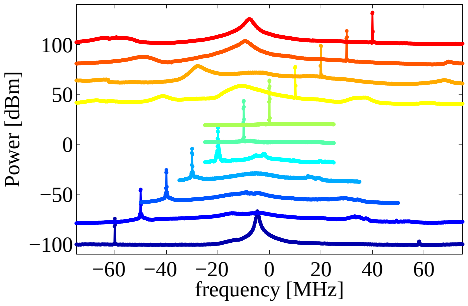

Figure 5.30: Tuning of the repetition rate of the mode-locked laser by tuning the modulation frequency of the seed laser.

The beat notes of the mode-locked laser with the filtered probe comb are depicted in Fig. 5.31. The CW injection power is 0.1 mW on chip and the center of the filter was positioned at 1579.4 nm. Similar as in Fig. 5.27a, we can distinguish 12 different beat notes. Line 1a and 1b result from two fiber frequency comb lines spaced f_a and $f_{\text{probe}} - f_a$ from the same MLL comb line. Line 2a and 2b result from the beating of the probe comb with the neighbouring MLL comb line and so on, meaning 6 mode-locked laser longitudinal modes are probed. Similar to the previous experiments, line widths $<$ 100 kHz are obtained from the Lorentzian fit, proving that the probed mode-locked laser lines are coherent with the seed laser.

When sweeping the probe comb over the different mode-locked laser lines, narrow beat notes can be measured from a center wavelength of 1578.3 nm to 1580.4 nm for an injection power of 0.1 mW on chip, indicating that 55 mode-locked laser lines are coherent with the seed laser. The beat notes measured at different center wavelengths are shown in Fig. 5.32. The positions of all measured beat notes correspond with equation 5.3 and can be understood in the same way as Fig. 5.31a, which is the same as Fig. 5.32c.

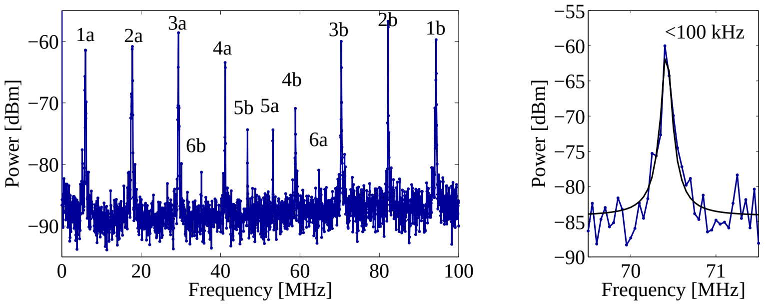

(a) **(b)**

Figure 5.31: (a) Beat notes recorded at the electrical spectrum analyzer, (b) Lorentzian fit of one of the beat notes with a 3 dB line width < 100 kHz (blue: experimental data, black: Lorentzian fit) (RBW: 50 kHz).

5.7 Conclusion

First we showed 3 different types of narrow linewidth, short-pulse InP QW-based III-V-on-silicon mode-locked lasers. We showed a 4.7 GHz linear MLL with a 36 kHZ 10 dB RF line width and a 1.5 ps pulse, a 4.7 GHz ring MLL with a 49 kHZ 10 dB RF line width and a 4.83 GHz anti-colliding MLL with a 5 kHZ 10 dB RF line width and a 3 ps pulse. The first two configurations are classical MLL implementations. However, the latter is a new approach, first proposed in [29] in order to achieve low timing jitter in combination with high output powers. We demonstrated the anti-colliding pulse MLL for the first time on a III-V-on-Si platform.

In order to meet the stringent requirements of terabits per second coherent communications in terms of line width and phase stability, we used hybrid mode-locking and injection locking techniques to improve the optical and electrical line width of the linear MLL. We have demonstrated that injection locked III-V-on-silicon mode-locked lasers can operate as coherent comb sources. It was shown that under optical injection locking the 3 dB optical line width is reduced from a ∼MHz line width to a 50 kHz line width. With a CW injection power as low as 0.1 mW, coherence between more than 50 mode-locked laser modes and the CW laser is experimentally confirmed. Such sources can be used for advanced optical transceivers, but also in other applications, such as microwave photonics and on-chip dual comb spectroscopy. While in these experiments the seed laser was external to the MLL chip, recently ultra-narrow line width (50 kHz) III-V-on-silicon tunable lasers were demonstrated [42], as well as on-chip optical isolators [43, 44], enabling the monolithic integration of such a frequency comb source.

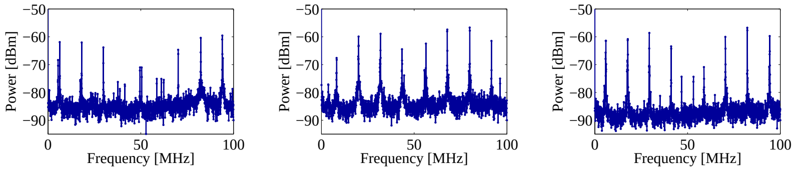

(a) λ_c = 1578.3 nm **(b)** λ_c = 1579.0 nm **(c)** λ_c = 1579.4 nm

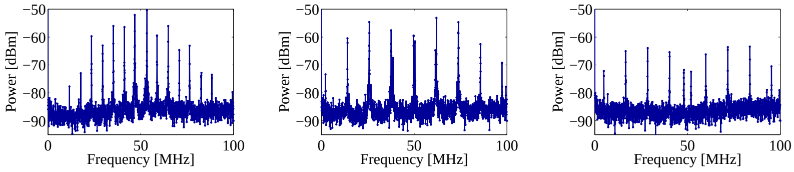

(d) λ_c = 1579.8 nm **(e)** λ_c = 1580.1 nm **(f)** λ_c = 1580.4 nm

Figure 5.32: Beat notes recorded on the electrical spectrum analyzer when sweeping the probe comb over the different mode-locked laser lines. The center wavelength λ_c of the filter is indicated for each graph. (RBW: 50 kHz)

References

[1] Friedrich Dausinger and Friedemann Lichtner. *Femtosecond technology for technical and medical applications*, volume 96. Springer Science & Business Media, 2004.

[2] Tibor Juhasz, Frieder H Loesel, Ron M Kurtz, Christopher Horvath, Josef F Bille, and Gerard Mourou. *Corneal refractive surgery with femtosecond lasers*. IEEE Journal of Selected Topics in Quantum Electronics, 5(4):902–910, 1999.

[3] George C Valley. *Photonic analog-to-digital converters*. Optics express, 15(5):1955–1982, 2007.

[4] Ian Coddington, Nathan Newbury, and William Swann. *Dual-comb spectroscopy*. Optica, 3(4):414–426, 2016.

[5] Julien Mandon, Guy Guelachvili, and Nathalie Picqué. *Fourier transform spectroscopy with a laser frequency comb*. Nature Photonics, 3(2):99, 2009.

[6] M Mielke, GA Alphonse, and PJ Delfyett. *168 channels x 6 GHz from a multiwavelength mode-locked semiconductor laser*. IEEE Photonics Technology Letters, 15(4):501–503, 2003.

[7] Kasper Van Gasse, Z Wang, Sarah Uvin, Bert De Deckere, J Mariën, L Thomassen, and Günther Roelkens. *Ka-band to L-band frequency downconversion based on III–V-on-silicon photonic integrated circuits*. CEAS Space Journal, 9(4):531–541, 2017.

[8] Jianping Yao. *Microwave photonics*. Lightwave Technology, Journal of, 27(3):314–335, 2009.

[9] G Carpintero, K Balakier, Z Yang, RC Guzman, A Corradi, A Jimenez, G Kervella, MJ Fice, M Lamponi, M Chitoui, et al. *Microwave photonic integrated circuits for millimeter-wave wireless communications*. Journal of Lightwave Technology, 32(20):3495–3501, 2014.

[10] Paolo Ghelfi, Francesco Laghezza, Filippo Scotti, Giovanni Serafino, Amerigo Capria, Sergio Pinna, Daniel Onori, Claudio Porzi, Mirco Scaffardi,

Antonio Malacarne, et al. *A fully photonics-based coherent radar system*. Nature, 507(7492):341, 2014.

[11] Meint Smit, Xaveer Leijtens, Huub Ambrosius, Erwin Bente, Jos Van der Tol, Barry Smalbrugge, Tjibbe De Vries, Erik-Jan Geluk, Jeroen Bolk, Rene Van Veldhoven, et al. *An introduction to InP-based generic integration technology*. Semiconductor Science and Technology, 29(8):083001, 2014.

[12] Michael L Davenport, Songtao Liu, and John E Bowers. *Integrated heterogeneous silicon/III–V mode-locked lasers*. Photonics Research, 6(5):468–478, 2018.

[13] Valentina Moskalenko, Jeroen Koelemeij, Kevin Williams, and Erwin Bente. *Study of extra wide coherent optical combs generated by a QW-based integrated passively mode-locked ring laser*. Optics letters, 42(7):1428–1431, 2017.

[14] Tin Komljenovic, Michael Davenport, Jared Hulme, Alan Y Liu, Christos T Santis, Alexander Spott, Sudharsanan Srinivasan, Eric J Stanton, Chong Zhang, and John E Bowers. *Heterogeneous silicon photonic integrated circuits*. Journal of Lightwave Technology, 34(1):20–35, 2016.

[15] Gunther Roelkens, Amin Abassi, Paolo Cardile, Utsav Dave, Andreas De Groote, Yannick De Koninck, Sören Dhoore, Xin Fu, Alban Gassenq, Nannicha Hattasan, Q Huang, S Kumari, S Keyvaninia, B Kuyken, L Li, P Mechet, M Muneeb, D Sanchez, H Shao, T Spuesens, A Subramanian, S Uvin, M Tassaert, K Van Gasse, J Verbist, R Wang, Z Wang, J Zhang, et al. *III-V-on-Silicon Photonic Devices for Optical Communication and Sensing*. In Photonics, volume 2, pages 969–1004. Multidisciplinary Digital Publishing Institute, 2015.

[16] Michael L Davenport and John E Bowers. *Integrated Heterogeneous Silicon/III-V Mode-Locked-Laser Based Frequency Combs*. In 2018 IEEE International Semiconductor Laser Conference (ISLC), pages 1–2. IEEE, 2018.

[17] S Keyvaninia, S Uvin, M Tassaert, X Fu, S Latkowski, J Mariën, L Thomassen, F Lelarge, G Duan, P Verheyen, et al. *Narrow-linewidth short-pulse III-V-on-silicon mode-locked lasers based on a linear and ring cavity geometry*. Optics express, 23(3):3221–3229, 2015.

[18] Herman A Haus and Antonio Mecozzi. *Noise of mode-locked lasers*. Quantum Electronics, IEEE Journal of, 29(3):983–996, 1993.

[19] Fabien Kéfélian, Shane O'Donoghue, Maria Teresa Todaro, John G McInerney, and Guillaume Huyet. *RF linewidth in monolithic passively mode-locked*

semiconductor laser. IEEE Photonics Technology Letters, 20(16):1405–1407, 2008.

[20] Dennis J Derickson, Roger J Helkey, Alan Mar, Judy R Karin, John G Wasserbauer, and John E Bowers. *Short pulse generation using multisegment mode-locked semiconductor lasers*. IEEE Journal of Quantum Electronics, 28(10):2186–2202, 1992.

[21] Valentina Moskalenko. *Extended cavity passively mode-locked lasers in indium phosphide generic integration technology*. PhD thesis, Technische Universiteit Eindhoven, 2016.

[22] Herman A Haus. *Mode-locking of lasers*. Selected Topics in Quantum Electronics, IEEE Journal of, 6(6):1173–1185, 2000.

[23] EU Rafailov, MA Cataluna, and Wilson Sibbett. *Mode-locked quantum-dot lasers*. Nature photonics, 1(7):395–401, 2007.

[24] KA Williams, MG Thompson, and IH White. *Long-wavelength monolithic mode-locked diode lasers*. New Journal of Physics, 6(1):179, 2004.

[25] Sudharsanan Srinivasan, Michael Davenport, Martijn JR Heck, John Hutchinson, Erik Norberg, Gregory Fish, and John Bowers. *Low phase noise hybrid silicon mode-locked lasers*. Frontiers of Optoelectronics, 7(3):265–276, 2014.

[26] Mark G Thompson, Alastair R Rae, Mo Xia, Richard V Penty, and Ian H White. *InGaAs quantum-dot mode-locked laser diodes*. IEEE Journal of Selected Topics in Quantum Electronics, 15(3):661–672, 2009.

[27] Yohan Barbarin, Erwin AJM Bente, Martijn JR Heck, YS Oei, Richard Nötzel, and Meint K Smit. *Characterization of a 15 GHz integrated bulk InGaAsP passively modelocked ring laser at 1.53* μm. Optics Express, 14(21):9716–9727, 2006.

[28] DJ Jones, LM Zhang, JE Carroll, and DD Marcenac. *Dynamics of monolithic passively mode-locked semiconductor lasers*. IEEE Journal of Quantum Electronics, 31(6):1051–1058, 1995.

[29] Julien Javaloyes and Salvador Balle. *Anticolliding design for monolithic passively mode-locked semiconductor lasers*. Optics letters, 36(22):4407–4409, 2011.

[30] Jun-Ping Zhuang, Vincenzo Pusino, Ying Ding, Sze-Chun Chan, and Marc Sorel. *Experimental investigation of anti-colliding pulse mode-locked semiconductor lasers*. Optics letters, 40(4):617–620, 2015.

[31] Zhechao Wang, Kasper Van Gasse, Valentina Moskalenko, Sylwester Latkowski, Erwin Bente, Bart Kuyken, and Gunther Roelkens. *A III-V-on-Si ultra-dense comb laser*. Light: Science & Applications, 6(5):e16260, 2017.

[32] D Hillerkuss, R Schmogrow, T Schellinger, M Jordan, M Winter, G Huber, T Vallaitis, R Bonk, P Kleinow, F Frey, et al. *26 Tbit s-1 line-rate super-channel transmission utilizing all-optical fast Fourier transform processing*. Nature Photonics, 5(6):364–371, 2011.

[33] Brian R Washburn, Scott A Diddams, Nathan R Newbury, Jeffrey W Nicholson, Man F Yan, and Carsten G Jrgensen. *Phase-locked, erbium-fiber-laser-based frequency comb in the near infrared*. Optics Letters, 29(3):250–252, 2004.

[34] Matthias Seimetz. *Laser linewidth limitations for optical systems with high-order modulation employing feed forward digital carrier phase estimation*. In optical fiber communication conference, page OTuM2. Optical Society of America, 2008.

[35] Joerg Pfeifle, Victor Brasch, Matthias Lauermann, Yimin Yu, Daniel Wegner, Tobias Herr, Klaus Hartinger, Philipp Schindler, Jingshi Li, David Hillerkuss, et al. *Coherent terabit communications with microresonator Kerr frequency combs*. Nature photonics, 8(5):375–380, 2014.

[36] Brian Stern, Xingchen Ji, Yoshitomo Okawachi, Alexander L Gaeta, and Michal Lipson. *Battery-operated integrated frequency comb generator*. Nature, 562(7727):401–405, 2018.

[37] Isao Morohashi, Takahide Sakamoto, Hideyuki Sotobayashi, Tetsuya Kawanishi, Iwao Hosako, and Masahiro Tsuchiya. *Widely repetition-tunable 200 fs pulse source using a Mach–Zehnder-modulator-based flat comb generator and dispersion-flattened dispersion-decreasing fiber*. Optics Letters, 33(11):1192–1194, 2008.

[38] Atsushi Ishizawa, Tadashi Nishikawa, Akira Mizutori, Hidehiko Takara, Atsushi Takada, Tetsuomi Sogawa, and Masafumi Koga. *Phase-noise characteristics of a 25-GHz-spaced optical frequency comb based on a phase-and intensity-modulated laser*. Optics Express, 21(24):29186–29194, 2013.

[39] Ehsan Sooudi, Stylianos Sygletos, Andrew D Ellis, Guillaume Huyet, John G McInerney, François Lelarge, Kamel Merghem, Ricardo Rosales, Anthony Martinez, Abderrahim Ramdane, et al. *Optical frequency comb generation using dual-mode injection-locking of quantum-dash mode-locked lasers: Properties and applications*. Quantum Electronics, IEEE Journal of, 48(10):1327–1338, 2012.

[40] Yuanbing Cheng, Xianshu Luo, Junfeng Song, Tsung-Yang Liow, Guo-Qiang Lo, Yulian Cao, Xiaonan Hu, Xiaohui Li, Peng Huei Lim, and Qi Jie Wang. *Passively mode-locked III-V/silicon laser with continuous-wave optical injection*. Optics express, 23(5):6392–6399, 2015.

[41] Natalia Rebrova, Tatiana Habruseva, Guillaume Huyet, and Stephen P Hegarty. *Stabilization of a passively mode-locked laser by continuous wave optical injection*. Applied Physics Letters, 97(10):101105, 2010.

[42] Tin Komljenovic, Sudharsanan Srinivasan, Erik Norberg, Mike Davenport, Gregory Fish, and John Bowers. *Widely-tunable narrow-linewidth monolithically-integrated external-cavity semiconductor lasers*. IEEE Journal of Selected Topics in Quantum Electronics, 21(6), 2015.

[43] Xue Yin Sun, Qingyang Du, Taichi Goto, Mehmet C Onbasli, Dong Hun Kim, Nicolas M Aimon, Juejun Hu, and Caroline A Ross. *Single-Step Deposition of Cerium-Substituted Yttrium Iron Garnet for Monolithic On-Chip Optical Isolation*. ACS Photonics, 2(7):856–863, 2015.

[44] Samir Ghosh, Shahram Keyvaninia, Y Shirato, Tetsuya Mizumoto, Gunther Roelkens, and Roel Baets. *Optical isolator for TE polarized light realized by adhesive bonding of Ce: YIG on Silicon-on-Insulator waveguide circuits*. Photonics Journal, IEEE, 5(3):6601108–6601108, 2013.

6

InAs/GaAs quantum dot mode-locked lasers integrated on silicon

The global Internet traffic has grown spectacularly in the past two decades. This trend requires high-performance interconnects that can handle the massive amount of information that needs to be transported over the optical network. In order to use the available optical fiber bandwidth effectively, the spectral efficiency of these optical transceivers is of utmost importance.

There exist several multiplexing schemes that all aim to efficiently use the available optical fiber bandwidth. The conventional solution is to use highly parallel wavelength division multiplexing (WDM) with several tens of channels. The spectral efficiency of such a system is however below the theoretical limit, due to the guard bands inserted in between the wavelength channels. Moreover, the management of large arrays of single wavelength lasers is far from trivial. A second approach is to use short pulses to transmit a signal: different optical pulse trains are combined and transmitted together and on arrival separated again based on their different arrival times. This is called optical time division multiplexing (OTDM). Finally, coherent optical orthogonal frequency division multiplexing (OFDM) systems use one frequency band per signal. In contrast to WDM systems, OFDM frequency bands can overlap considerably. Because of this, the spectral efficiency can become much higher. Tbps optical OFDM communication systems with high spectral efficiency have been demonstrated [1]. However, such a system puts stringent requirements on the light source: it needs an optical frequency comb source to generate an array of narrow line width lines with a fixed phase relation and fixed frequency spacing.

All of the above systems show that there is a great need for multi-wavelength lasers. The frequency comb generated by a mode-locked laser, can be the perfect solution. Because of the mode-locking, the laser lines have inherently a distinct phase relation, while the frequency spacing is determined by the repetition rate of the laser. It has been shown that (stabilized) mode-locked fiber lasers can serve as a frequency comb source, however, these lasers have typically a low repetition rate (and hence too small frequency spacings for optical communication) because of the long laser cavity length [2]. Integrating mode-locked lasers on chip could overcome this problem, and has additionally a clear advantage in form factor and power consumption. The integration of mode-locked lasers on a silicon photonics platform allows using low-loss silicon waveguide structures to form the laser cavity, which positively affects the laser performance [3, 4].

Since the optical transceivers will be used in datacenters, the on-chip lasers need to operate at high ambient temperatures. Due to the three dimensional confinement of carriers, InAs/GaAs quantum dot (QD) lasers inherently have a more stable performance over the 20°C-100°C temperature range compared to quantum well lasers [5]. Furthermore, due to the inhomogeneous broadening during growth, they have a wider gain spectrum compared to conventional quantum well lasers making this material system an excellent candidate for creating multi-wavelength transmitters [6, 7]. Additionally, the ultra-fast gain recovery of the quantum dots allows for mode-locking with ultrashort pulse widths [8]. To achieve error-free transmission, low noise behavior is also important. Since every dot present in the active layer acts as an independent emitter and charge carriers cannot freely move between dots, neighboring modes will not compete for carriers. So mode partition noise is less of a problem in quantum dot lasers than in quantum well lasers [9].

This was also recognized by other research groups. In [10] a QD-based comb laser wafer bonded on a silicon substrate is demonstrated. The colliding pulse MLL with a repetition rate of 19 GHz showed error-free operation in the three highest-power modes with extinction ratios of 11.5 dB or more. The optical bandwidth of the MLL was limited to 1 nm, the cause of this was not fully understood. In [11] a 20 GHz passively mode-locked quantum dot laser grown on a CMOS compatible on-axis (001) silicon substrate is demonstrated. A RF 3 dB linewidth of 1.8 kHz is measured. The 3 dB optical bandwidth of the comb is 6.1 nm.

In this work we explored the potential of InAs/GaAs QD mode-locked lasers integrated on a silicon photonics platform. Based on the mode-locked lasers presented in chapter 5, we designed, fabricated and tested both linear colliding pulse MLLs (section 6.2) and ring MLLs (section 6.3). Quantum-dot-based comb lasers were shown with both constellations. Since this is a first iteration, the different design parameters of the laser cavity are not yet optimized and more research is necessary.

6.1 Mesa design and fabrication

A schematic cross-section of the InAs/GaAs QD III-V-on-silicon laser mesa is depicted in Fig. 6.1a. The laser consists of a planarized SOI wafer containing the silicon waveguides defined in a 400 nm-thick silicon waveguide layer using 193 nm deep UV lithography (180 nm etch depth) fabricated at imec. The GaAs quantum dot epitaxial layer stack is adhesively bonded to the planarized silicon-on-insulator (SOI) using a 60 nm-thick divinylsiloxane-bisbenzocyclobutene (DVS-BCB) bonding layer. Top to bottom, the III-V layers comprise a highly-doped p-type GaAs ohmic contact and a p-type AlGaAs top cladding layer, followed by the quantum dot region. This QD active region consists of nine dot-in-a-well (DWELL) layers (InAs/InGaAs) separated by GaAs barriers. Finally, there is an n-type AlGaAs bottom cladding layer and a n-type GaAs contact. The epitaxial layer stack is the same as the one we used to fabricate the DFB lasers from chapter 4 and is described in detail in table 2.1. An electric p-type contact (anode) is located on the top of the mesa, while the cathodes are located on top of the n-contact layer, symmetrically on both sides of the mesa.

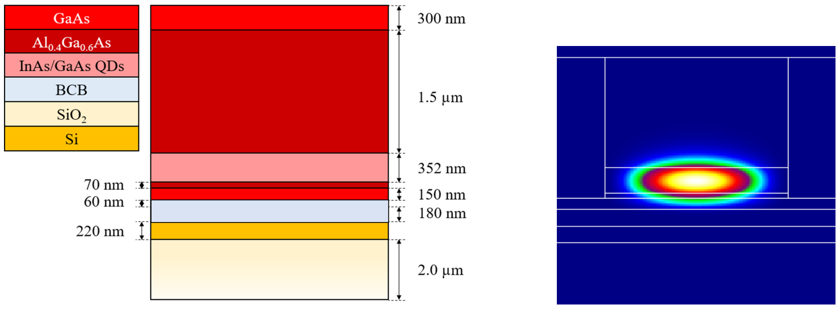

(a) **(b)**

Figure 6.1: (a) Cross-section of the InAs/GaAs QD-on-SOI mesa and (b) corresponding optical mode profile.

Note that no silicon waveguide is present underneath the III-V for most of the mesa length, the silicon is only present in the spotsize converters to couple the light from the III-V into the silicon waveguide. For a III-V mesa width of 3.7 μm, this results in an optical confinement of 69 % in the 352 nm-wide active layer or a 10.3 % confinement in the QD layers. This confinement factor is the same in both the gain section and the saturable absorber. The corresponding mode profile is plotted in figure 6.1b. By not putting a silicon waveguide underneath the quantum dot gain section, we opted for the highest possible confinement factor, since we wanted the highest possible modal gain. Although a higher confinement factor reduces the saturation power, achieving enough modal gain was our first objective.

A 215 μm-long tapered spotsize converter is used to couple the light from the gain section into the passive silicon waveguides. The III-V taper is a piecewise linear taper that quickly tapers (L = 35 μm) from a 3.7 μm mesa width to an 1.7 μm wide waveguide width after which a slower adiabatic taper (L = 180 μm) is implemented by tapering both the III-V and silicon waveguide structure. More information on the coupler design can be found in section 3.1.

The fabrication of the lasers is described in detail in section 2.3. One extra step was added to this process in order to make the saturable absorber. Right after the planarization and before the deposition of the p-contact, two 10 μm wide trenches have been etched through the p-GaAs contact layer and 100 nm deep into the p-AlGaAs cladding layer. In this way part of the active material is electrically isolated from the gain sections forming the saturable absorber. This is schematically illustrated in figure 6.2a. In figure 6.2b a picture of the absorber section is shown right after the p-contact deposition: the saturable absorber has its own p-contact, but shares a common ground with the gain sections of the laser.

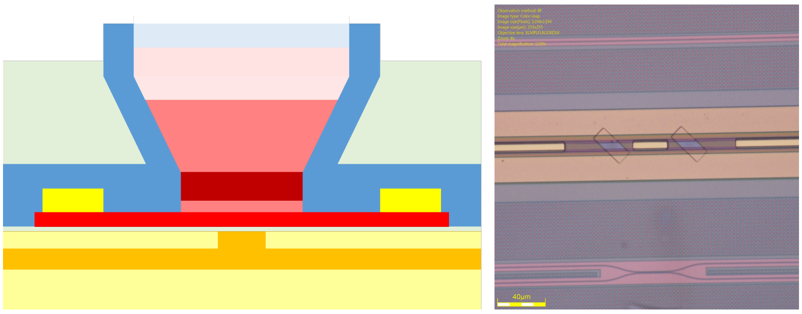

(a) (b)

Figure 6.2: (a) Cross-section of the absorber etch through the p-GaAs contact layer and into the p-AlGaAs cladding layer. (b) Microscope image of the saturable absorber section.

6.2 Linear colliding pulse mode-locked laser

First, we look at a linear mode-locked laser realized in a colliding pulse configuration. The structure of the laser comprises a saturable absorber (SA) section located in the middle of the resonator cavity between two semiconductor optical amplifier (SOA) sections, as is illustrated in figure 6.3. Two counter-propagating pulses circulate in the cavity and only interact in the saturable absorber. This leads to a doubling of the repetition frequency and thus a halving of the pulse period.

6.2.1 Implementation

The three-dimensional layout of the linear colliding pulse mode-locked (CPML) laser is shown in Fig. 6.3. The optical amplifier and the saturable absorber are implemented in the III-V-on-silicon waveguide section. The InAs/GaAs QD gain section is 2×1425 μm long (not including the 195 μm long spotsize converters), while the III-V saturable absorber, placed in the center of the laser cavity is 150 μm long, 5 % of the total SOA length. The remainder of the cavity length is formed by two silicon waveguides of 346 μm length each in order to reach a pulse repetition rate of about 20 GHz (18.83 GHz in the experiment) in colliding pulse mode. The laser cavity mirrors are also fabricated in the silicon waveguide layer. Two second order silicon distributed Bragg reflector (DBR) mirrors (period 400 nm, 75 % duty cycle, 10 periods) providing close to 85 % reflectivity are placed at both ends of the laser cavity.

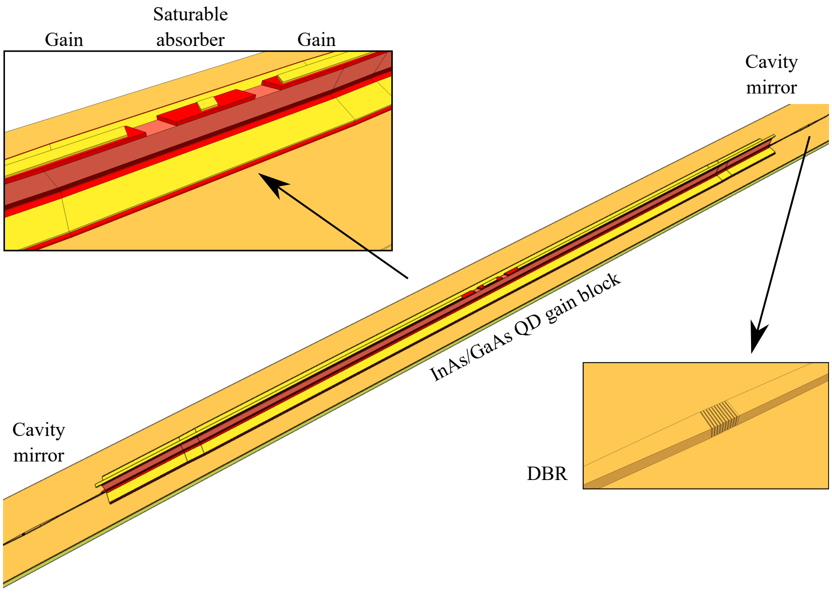

Figure 6.3: Illustration of the InAs/GaAs QD linear cavity colliding pulse mode-locked laser.

A microscope image of several fabricated linear MLLs is shown in figure 6.4. The electrical contacts are designed such that the laser can be probed with a PGSGP-probe.

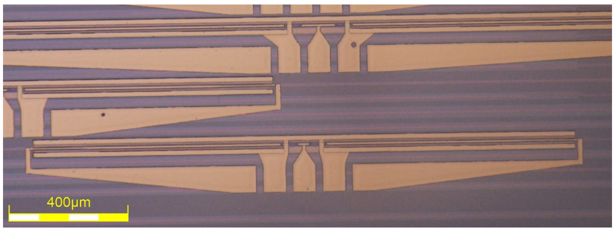

Figure 6.4: Microscope image of InAs/GaAs QD linear cavity colliding pulse MLLs fabricated on a 400 nm SOI platform.

6.2.2 Characterization

The measurements are carried out with the device on a thermo-electric cooler set at 20 °C. Figure 6.5 shows the schematic of the measurement set-up. The output of the mode-locked laser is coupled to an optical fiber through a fiber-to-chip grating coupler. The coupling efficiency is measured to be 8 dB. An optical isolator is used to prevent back-reflections into the laser. The performance of the laser is investigated by connecting the laser to an optical spectrum analyzer (OSA) or to a high-speed photodiode (40 GHz bandwidth) that is connected to a 50 GHz electrical spectrum analyzer (ESA).

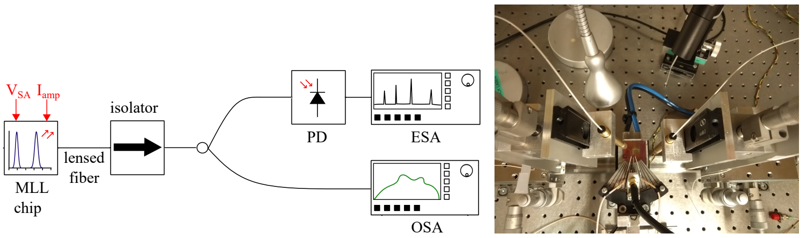

(a) **(b)**

Figure 6.5: (a) Schematic of the experimental set-up used for the characterization of the mode-locked laser. (b) Picture of the MLL chip: light is coupled from a grating coupler into the fiber on the left side. The electrical input is given via a PGSGP probe.

The light-current characteristic of the realized device is shown in figure 6.6, as a function of saturable absorber reverse bias. The laser had a threshold current ranging from 22 mA ($V_{SA} = 0V$) to 28 mA ($V_{SA} = -1.6V$), corresponding with threshold current densities of 198 A/cm^2 and 252 A/cm^2 respectively. The increase of the threshold current is caused by the increase of the optical loss with increasing saturable absorber voltage.

In [12] it was shown theoretically that many factors like the recovery time of the SA, the width of the gain curve and the relative detuning between the gain curve and the band-edge of the SA influence the performance of the comb laser. Since these parameters depend on the operating conditions, the laser was characterized over a wide range of amplifier currents and SA voltages in order to find the optimal conditions for passive mode-locking.

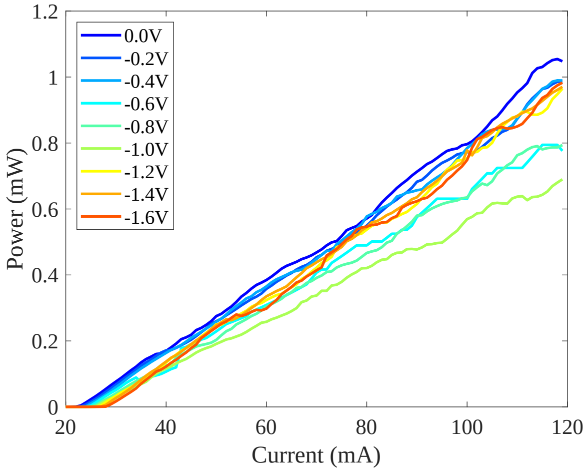

Figure 6.6: LI curve as a function of saturable absorber voltage. The optical power in the waveguide is plotted.

In figure 6.7 the optical 3 dB and 10 dB bandwidth are plotted as a function of amplifier current and saturable absorber voltage. We can see that the bandwidth is increasing with increasing current. The 3 dB bandwidth is limited to 2 nm and 10 dB bandwidth to 3 nm. This is much lower than expected, since quantum dot lasers are know for their broad gain spectrum. However, an even lower bandwidth of 1 nm is reported in [10] where they also fabricated comb lasers by integrating InAs/GaAs QD material on SOI. They believe that the bandwidth is limited by group velocity dispersion. Compensating for this dispersion could broaden the comb span [13, 14]. On top of dispersion, we can think of several other causes of the narrow comb: there might be not enough gain, the spectra of the amplifier and the saturable absorber can be misaligned, etc. Extensive research is necessary to better understand what is happening.

In figure 6.8a the optical spectrum of the laser is plotted at an amplifier bias current of 42 mA and a saturable absorber voltage of -1.6 V. Figure 6.8b shows the evolution of the optical spectrum as a function of the injection current of the optical amplifier. Here, the SA was biased at -1.6 V.

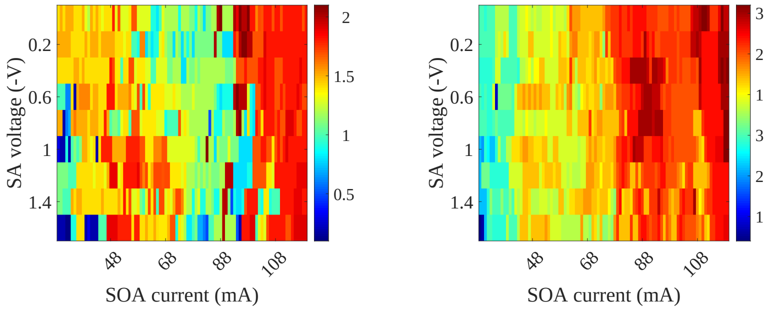

(a) Optical 3 dB bandwidth (nm)

(b) Optical 10 dB bandwidth (nm)

Figure 6.7: A map of the spectral bandwidth measured at (a) 3 dB and (b) 10 dB level as a function of biasing conditions applied to the SOA and SA sections.

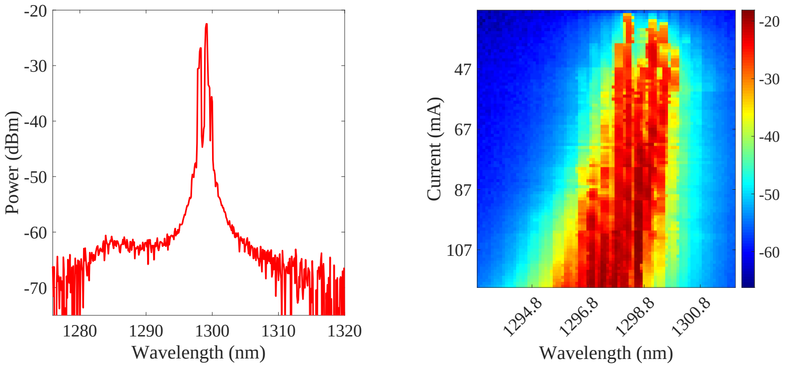

(a)

(b)

Figure 6.8: (a) The optical frequency comb recorded at an amplifier bias current of 42 mA and a saturable absorber voltage of -1.6 V. (b) Evolution of the optical spectrum as a function of amplifier current for a saturable absorber voltage of -1.6 V.

In figure 6.9b the height of the fundamental RF peak (around 18.8 GHz) is plotted as a function of the biasing conditions applied to the SOA and SA sections. The height of RF peak was taken as a ratio between the peak at fundamental frequency 20 GHz and the low frequency components [15]. The peak height is quite unstable with changing biasing conditions. Due to the fact that in the linear

CPML design two pulses travel in the laser cavity and couple to the same output, we can see a residual component at half the repetition rate. If the two pulses are not identical, a spurious tone occurs. In figure 6.9a the RF peak height around 9.4 GHz is mapped. The height of the residual component is always lower than the fundamental peak and seems to decrease with increasing saturable absorber voltage.

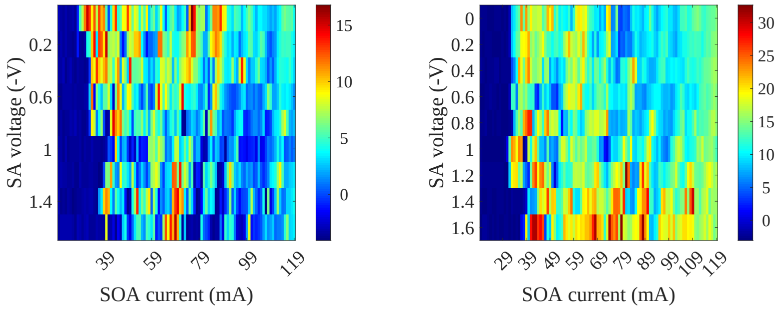

(a) RF peak height at 9.4 GHz (dB) **(b)** RF peak height at 18.8 GHz (dB)

Figure 6.9: A map of the RF peak height as a function of biasing conditions applied to the SOA and SA sections.

In figure 6.10a we see a wide span electrical spectrum of the comb laser at an amplifier bias current of 42 mA and a saturable absorber voltage of -1.6 V. We see a strong fundamental RF tone and a very weak RF tone at half the repetition rate. A more detailed plot of the fundamental tone is shown in figure 6.10b. The 3 dB line width was defined by fitting a Lorentzian curve to the RF spectrum and measured to be 623.6 kHz.

6.3 Ring mode-locked laser

An alternative manner to realize mode-locked lasers in a colliding pulse configuration is the ring laser as is shown in figure 6.11. Two pulses propagate in the ring cavity in opposite directions and collide in the SA. Since the two pulses couple to different output waveguides, the frequency is not doubled as is the case in linear colliding pulse configurations.

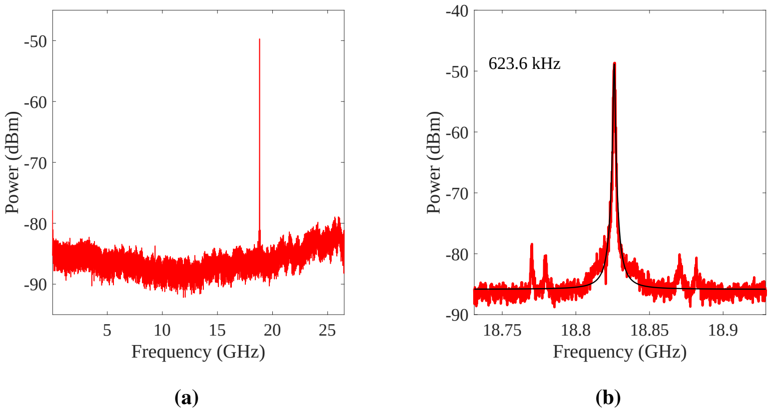

Figure 6.10: (a) Wide span electrical spectrum of the generated pulse train (Resolution bandwidth (RBW): 1 MHz and video bandwidth (VBW): 10 kHz). (b) Linewidth of the fundamental RF tone (resolution bandwidth and video bandwidth used to obtain the RF spectrum were 1 MHz and 10 kHz). The laser gain section was biased at 42 mA, while the saturable absorber had a reverse bias of -1.6 V.

6.3.1 Implementation

The three-dimensional layout of the ring mode-locked laser is shown in Fig. 6.11. The optical amplifier and the saturable absorber are implemented in the III-V-on-silicon waveguide section. The III-V gain section is 2×600 μm long (not including the 190 μm long spotsize converters), while the III-V saturable absorber, placed symmetrically in the laser cavity is 65 μm long. The other half of the cavity length is formed by the waveguides that make up the ring of around 2 mm length in total in order to reach a pulse repetition rate of about 20 GHz (20.318 GHz in the experiment). A directional coupler (coupling around 20 %) is used for the optical coupling between the laser cavity and the silicon output waveguide. A microscope image of several fabricated ring ML lasers is shown in figure 6.12. The device described below is the third one starting from the top of the picture. The picture shows that the 20 GHz ring MLL was also fabricated with a shorter InAs/GaAs QD mesa and long silicon spirals to make up the cavity (the two top devices), since long low-loss silicon waveguides reduce the RF linewidth compared to all-active devices [16, 17]. However, the shorter III-V mesa didn't provide enough gain to start lasing.

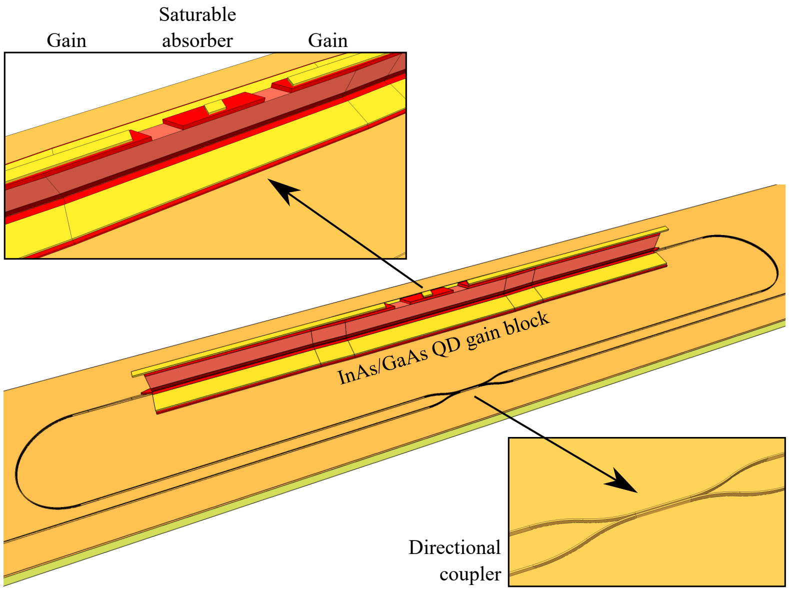

Figure 6.11: Illustration of the ring mode-locked laser.

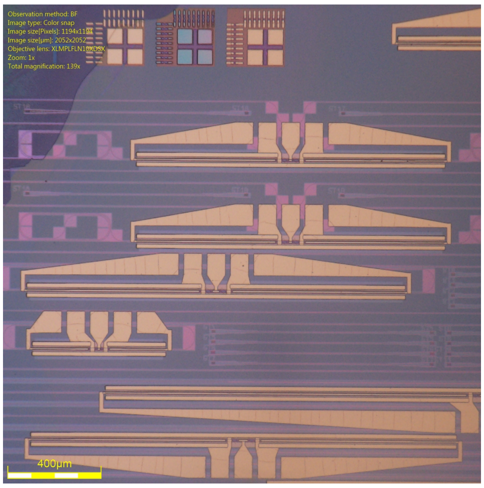

Figure 6.12: Microscope image of InAs/GaAs QD ring mode-locked lasers fabricated on a 400 nm SOI platform.

6.3.2 Characterization

To characterize the devices, the same measurement set-up as described in 6.2.2 was used. The light-current characteristic of the ring MLL is shown in figure 6.13, as a function of saturable absorber reverse bias. The laser had a threshold current ranging from 7.5 mA ($V_{SA} = 0V$) to 11 mA ($V_{SA} = -4V$), corresponding with threshold current densities of 156 A/cm^2 and 228 A/cm^2 respectively. The sudden drops in power correspond with with sudden jumps in the optical spectrum.

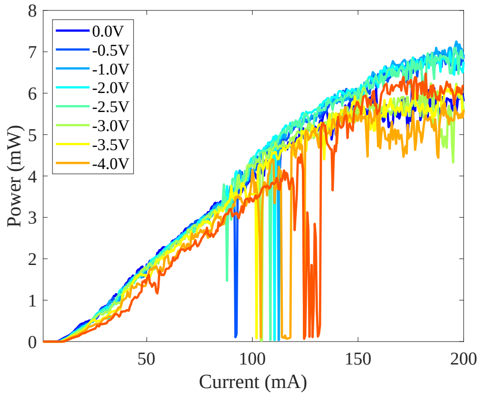

Figure 6.13: LI curve as a function of saturable absorber voltage. The optical power in the waveguide is plotted.

In figure 6.14 the optical 3 dB and 10 dB bandwidth are plotted as a function of amplifier current and saturable absorber voltage. Both the 3 dB and 10 dB bandwidth are limited to 4.5 nm. However, the broadest optical spectra close to threshold (the predominantly red regions in the maps) did not result in RF peaks at the fundamental tone, so the phases of the modes are not locked in this area. In the regions were mode-locking was observed, the 10 dB bandwidth was more around 3 nm. Since the optical spectrum is not always notably flat, the 10 dB bandwidth is more practical to measure [16, 18].

In figure 6.15a the optical spectrum of the laser is plotted at an amplifier bias current of 100 mA and a saturable absorber voltage of -3.1 V. Figure 6.15b shows the evolution of the optical spectrum as a function of the injection current of the optical amplifier. Here, the SA was biased at -3.1 V.

In figure 6.16 the height of the fundamental RF peak (around 20.318 GHz) is plotted as a function of the biasing conditions applied to the SOA and SA sections. We can see that there is a relation between the increase in RF peak height and the 10 dB bandwidth plotted in figure 6.14b. The strongest RF peaks are 40 dB above the noise floor.

In figure 6.17a we see a wide span electrical spectrum of the comb laser at an amplifier bias current of 100 mA and a saturable absorber voltage of -3.1 V. We see a strong fundamental RF tone and a smaller RF tone at the first harmonic. The

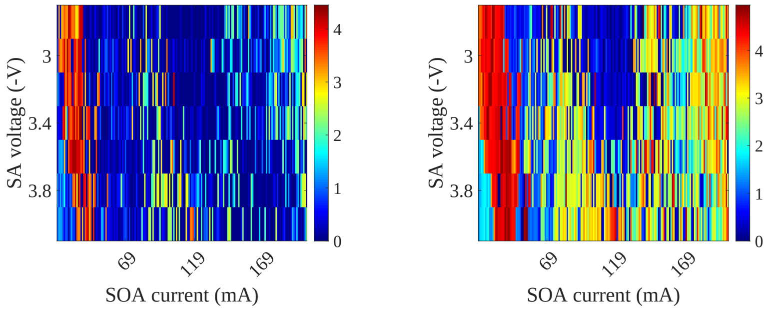

(a) Optical 3 dB bandwidth (nm) **(b)** Optical 10 dB bandwidth (nm)

Figure 6.14: A map of the spectral bandwidth measured at (a) 3 dB and (b) 10 dB level as a function of biasing conditions applied to the SOA and SA sections.

latter is at least partially caused by the losses of the photodiode at this speed. A more detailed plot of the fundamental tone is shown in figure 6.17b. The 3 dB line width was defined by fitting a Lorentzian curve to the RF spectrum and measured to be 3 kHz.

6.4 Conclusion

In this chapter we explored the potential of InAs/GaAs quantum dot mode-locked lasers integrated on a silicon photonics platform. We designed, fabricated and tested both linear colliding pulse MLLs and ring MLLs. Quantum-dot-based comb lasers were shown with both constellations. We showed a 18.8 GHz linear MLL with a 623 kHZ 3 dB RF line width and a 20.3 GHz ring MLL with a 3 kHZ 3 dB RF line width. However, the optical 10 dB bandwidth was disappointingly small, around 3 nm for both structures and the cause for this is not fully understood at the moment. Since this is a first iteration, the different design parameters of the laser cavity are not yet optimized and more research is necessary.

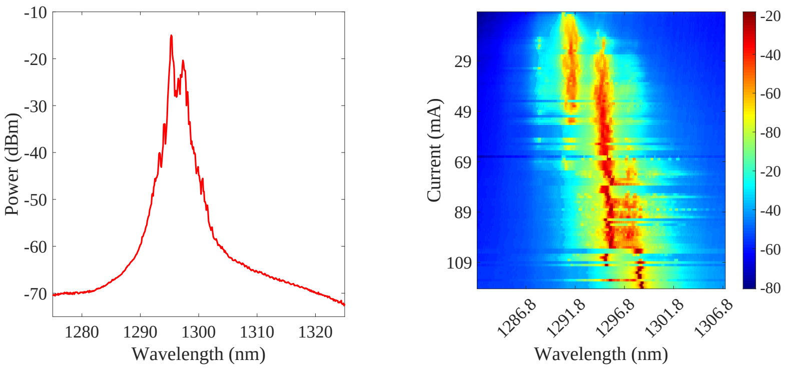

(a) **(b)**

Figure 6.15: (a) The optical frequency comb recorded at an amplifier bias current of 100 mA and a saturable absorber voltage of -3.1 V. (b) Evolution of the optical spectrum as a function of amplifier current for a saturable absorber voltage of -3.1 V.

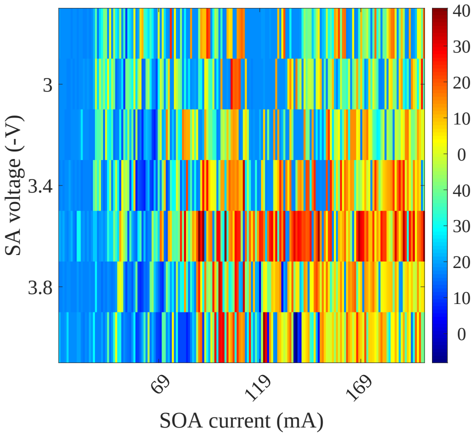

(a)

Figure 6.16: A map of the RF power at the fundamental tone as a function of biasing conditions applied to the SOA and SA sections.

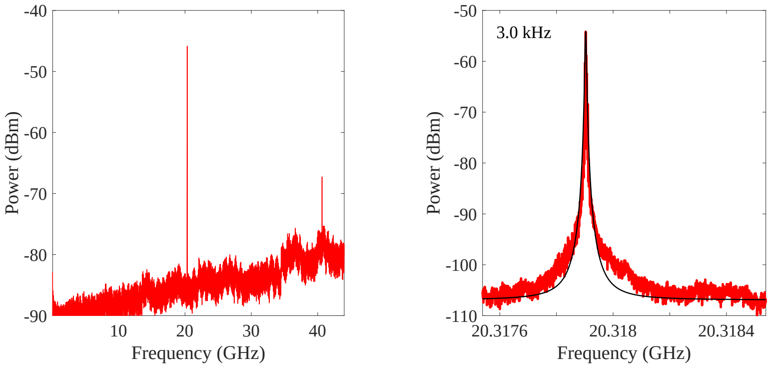

(a) **(b)**

Figure 6.17: (a) Wide span electrical spectrum of the generated pulse train (Resolution bandwidth (RBW): 1 MHz and video bandwidth (VBW): 10 kHz). (b) Linewidth of the fundamental RF tone (resolution bandwidth and video bandwidth used to obtain the RF spectrum were 2 kHz and 20 Hz). The laser gain section was biased at 100 mA, while the saturable absorber had a reverse bias of -3.1 V.

References

[1] D Hillerkuss, R Schmogrow, T Schellinger, M Jordan, M Winter, G Huber, T Vallaitis, R Bonk, P Kleinow, F Frey, et al. *26 Tbit s-1 line-rate superchannel transmission utilizing all-optical fast Fourier transform processing*. Nature Photonics, 5(6):364–371, 2011.

[2] Brian R Washburn, Scott A Diddams, Nathan R Newbury, Jeffrey W Nicholson, Man F Yan, and Carsten G Jrgensen. *Phase-locked, erbium-fiber-laser-based frequency comb in the near infrared*. Optics Letters, 29(3):250–252, 2004.

[3] S Keyvaninia, S Uvin, M Tassaert, X Fu, S Latkowski, J Mariën, L Thomassen, F Lelarge, G Duan, P Verheyen, et al. *Narrow-linewidth short-pulse III-V-on-silicon mode-locked lasers based on a linear and ring cavity geometry*. Optics express, 23(3):3221–3229, 2015.

[4] Michael Davenport. *Heterogeneous Silicon III-V Mode-Locked Lasers*. PhD thesis, University of California, Santa Barbara, 2017.

[5] Mitsuru Sugawara and Michael Usami. *Quantum dot devices: Handling the heat*. Nature Photonics, 3(1):30–31, 2009.

[6] ZG Lu, JR Liu, CY Song, J Weber, Y Mao, SD Chang, HP Ding, PJ Poole, PJ Barrios, D Poitras, et al. *High performance InAs/InP quantum dot 34.462-GHz C-band coherent comb laser module*. Optics express, 26(2):2160–2167, 2018.

[7] A Kovsh, A Gubenko, I Krestnikov, D Livshits, S Mikhrin, J Weimert, L West, G Wojcik, D Yin, C Bornholdt, et al. *Quantum dot comb-laser as efficient light source for silicon photonics*. In Photonics Europe, pages 69960V–69960V. International Society for Optics and Photonics, 2008.

[8] A Zeghuzi, H Schmeckebier, M Stubenrauch, C Meuer, C Schubert, C-A Bunge, and Dieter Bimberg. *25 Gbit/s differential phase-shift-keying signal generation using directly modulated quantum-dot semiconductor optical amplifiers*. Applied Physics Letters, 106(21):213501, 2015.

[9] Larry A Coldren, Scott W Corzine, and Milan L Mashanovitch. *Diode lasers and photonic integrated circuits*, volume 218. Wiley. com, 2012.

[10] Geza Kurczveil, M Ashkan Seyedi, Di Liang, Marco Fiorentino, and Raymond G Beausoleil. *Error-Free Operation In A Hybrid-Silicon Quantum Dot Comb Laser*. IEEE Photonics Technology Letters, 2017.

[11] Songtao Liu, Xinru Wu, Daehwan Jung, Justin C Norman, MJ Kennedy, Hon K Tsang, Arthur C Gossard, and John E Bowers. *High-channel-count 20 GHz passively mode-locked quantum dot laser directly grown on Si with 4.1 Tbit/s transmission capacity*. Optica, 6(2):128–134, 2019.

[12] Julien Javaloyes and Salvador Balle. *Mode-locking in semiconductor Fabry-Perot lasers*. IEEE Journal of Quantum Electronics, 46(7):1023–1030, 2010.

[13] Roger GMP Koumans and Raymond Van Roijen. *Theory for passive mode-locking in semiconductor laser structures including the effects of self-phase modulation, dispersion, and pulse collisions*. IEEE Journal of Quantum Electronics, 32(3):478–492, 1996.

[14] Alexander L Gaeta, Michal Lipson, and Tobias J Kippenberg. *Photonic-chip-based frequency combs*. Nature Photonics, 13(3):158, 2019.

[15] Valentina Moskalenko. *Extended cavity passively mode-locked lasers in indium phosphide generic integration technology*. PhD thesis, Technische Universiteit Eindhoven, 2016.

[16] Zhechao Wang, Kasper Van Gasse, Valentina Moskalenko, Sylwester Latkowski, Erwin Bente, Bart Kuyken, and Gunther Roelkens. *A III-V-on-Si ultra-dense comb laser*. Light: Science & Applications, 6(5):e16260, 2017.

[17] Michael L Davenport, Songtao Liu, and John E Bowers. *Integrated heterogeneous silicon/III–V mode-locked lasers*. Photonics Research, 6(5):468–478, 2018.

[18] V Corral, R Guzmán, C Gordón, XJM Leijtens, and G Carpintero. *Optical frequency comb generator based on a monolithically integrated passive mode-locked ring laser with a Mach–Zehnder interferometer*. Optics letters, 41(9):1937–1940, 2016.

7

Conclusion and outlook

While writing this conclusion the Coronavirus, SARS-CoV-2, keeps the whole world in its grip. Never more than now, we depend on our internet connection to do our jobs, to talk to our families, to go to school and to see other people. This has led to a very sudden burst of data usage. But despite the odd hiccup, the internet is doing fine. This is thanks to an industry and a community of researchers that has long been taking the increasing demand for higher bandwidth into account and prepared and adapted the systems accordingly. Instead of collapsing under this crisis, already planned expansions in datacenters can be moved forward to meet the current needs.

Since we do not expect the demand for higher bandwidth too slow down anytime soon, a new generation of high-performance interconnects that can sustain this high bandwidth without consuming exorbitant amounts of energy is needed. Silicon photonics is emerging as an important platform for the realization of power-efficient, high-speed optical transceivers. However, currently the lack of cost-effective integration of the light source limits silicon-based photonic integrated circuits (PIC) deployment in this field. In order to become the next-generation technology of preference, on-chip lasers operating at high ambient temperature and with low-loss coupling to the silicon waveguide circuits are of paramount importance.

To meet this demand, we have introduced InAs/GaAs quantum dot material to the silicon photonics ecosystem. We described the design, fabrication and characterization of InAs/GaAs quantum dot lasers integrated on silicon. Firstly, a new process is developed in order to integrate and fabricate InAs/GaAs QD lasers on

SOI by means of DVS-BCB assisted wafer bonding. We also explored the option of transfer-printed InAs/GaAs QD lasers. In parallel, extensive research has been carried out into various coupling mechanism to couple light from the III-V into the silicon waveguide. This has led to the world's first single mode InAs/GaAs QD laser integrated on and coupling to a silicon chip. Furthermore, the same QD epitaxial layerstack was also used to fabricate various types of InAs/GaAs quantum dot mode-locked lasers. In order to design these lasers, first InP quantum well based mode-locked lasers were characterized thoroughly to get a better understanding. In this chapter we want to formulate an overview of our research on advanced laser sources on silicon as well as provide the reader with the future prospects we anticipate.

7.1 Fabrication of heterogeneously integrated InAs/-GaAs quantum dot lasers

At the start of this work InAs/GaAs quantum dot material was never integrated onto a silicon chip with the ability to couple light from the III-V into the silicon waveguide. So first we developed a fabrication process to realize exactly this. We wanted to use the crystal orientation of the epi in order to get faceted surfaces in the mesa, since this can help to create good coupling structures. We investigated a lot of potential wet etchants before we got to the final process explained in full in chapter 2 and briefly summarized hereunder.

To fabricate the lasers, the InAs/GaAs QD epitaxial structure (typically a 1 cm by 1 cm die) is bonded to the planarized SOI using ultra-thin DVS-BCB adhesive bonding. After bonding, the GaAs substrate is removed. The major part of the GaAs substrate is removed by wet etching in HNO_3:H_2O_2:H_2O. The last 50 μm of the substrate is etched using more selective NH_4OH:H_2O_2. The III-V mesa and spotsize converters are defined through wet etching, using citric acid:H_2O_2 and KI:I_2:H_2O for the GaAs/InAs and AlGaAs layers, respectively. The reaction rate limited wet etching of the p-AlGaAs cladding layer in KI:I_2:H_2O results in a faceted surface structure dependent on the crystal orientation. This allows creating undercut structures in the spot-size converter, which relaxes the lithography requirements in the definition of the III-V spotsize converter, which was realized using 300 nm UV contact lithography. Next, the Ni/Ge/Au n-contact is defined through a lift-off process. The devices are passivated using a 300 nm-thick silicon nitride layer deposited by plasma-enhanced chemical vapor deposition (PECVD). The lasers are then planarized with DVS-BCB. Thereafter Ti/Au p-contacts are deposited on the p-GaAs contact layer and thermally annealed. Finally vias are formed and probe pad metal is deposited.

In an academic context, we developed a stable process. However, if we want to use this to mass produce QD lasers with a high yield, improvements need to be made. By far the most critical and challenging step is the wet etching in KI:I_2:H_2O. Since the solution is dark brown, it is not possible to see the surface of the chip during etching, let alone any color change. Furthermore, during wet etching an offset is created in the etch profile that can not be seen or measured from above, but needs to be removed completely. We have to rely mostly on timing, but the etchant behaves notoriously fickle. If we want to take these lasers to the next level, we have to improve this critical etch step. There are several ways to do this:

- We can define narrow taper tips during lithography if we use a system with a higher resolution. In that case we have no longer need of an undercut structure. Consequently, we can use dry etching processes to define the mesa.
- Dry etching processes can also be used when we change to a coupling structure where no narrow taper tips are needed. However this has other implications, e.g. it will become more challenging to define part of the laser cavity in the silicon waveguide layer.
- If we want to keep the undercut structures, KI:I_2:H_2O is unavoidable. We saw that the etch rate was very sensitive to the slightest changes in the mixture, to the amount of times we took the sample out to look under the microscope, to the way we rinsed it when etching was done, etc. So to improve the yield, very stable etch conditions are indispensable.
- Lastly, we noticed that there were a lot of defects present in the epi material. We think, these defects were also in part responsible for the fickle behavior of the etchant. So to improve the etch step, also the epi material quality should be improved.

In the course of this work, micro-transfer-printing emerged as a promising new integration technology. Although reliable, bonding is not very efficient in terms of III-V material usage. By using μTP, the efficiency of the use of source materials can be significantly improved and different materials/devices can be intimately integrated on a common substrate. We explored the possibility to use this technique with GaAs-based devices and have shown successful transfer-printing. Even though μTP is not used as integration technique in most of this PhD project, the presented devices are inherently compatible with the transfer-printing approach. The research presented here was therefore the starting point for the CALADAN project. CALADAN is an European H2020 project which focuses upon the micro-transfer-printing technology to integrate InAs/GaAs quantum dot lasers and high-speed SiGe BiCMOS chips onto 300 mm silicon photonic wafers.

7.2 Optical coupling schemes

Coupling light from the III-V mesa into a silicon waveguide is not trivial, especially if this needs to be done efficient, without back-reflections, with a high tolerance towards misalignment and both on planarized SOI and in the trench of a full platform silicon chip. Therefore we designed, simulated and tested several coupling structures.

The traditional spotsize converter used in many III-V-on-SOI lasers has excellent coupling efficiency, but is very sensitive to misalignment. Therefore this structure is well suited for wafer bonded lasers and we used it throughout this work. But for lasers that are transfer-printed with an alignment accuracy of 1.5 μm (3σ) the spotsize converter needs to be adapted to keep up its performance.

A first option for a more alignment tolerant coupler is the use of a polymer waveguide. The width of the III-V mesa is fixed and at the end a very wide polymer waveguide is attached. Underneath the polymer an inverted taper made in the silicon pulls all the light down into the silicon waveguide. Most challenging here is the need for clean lasing facets and a good anti-reflection (AR) coating to avoid back-reflections that may hamper good laser working.

Another approach that doesn't require narrow tapers to be etched in the III-V mesa, is the intracavity coupler. A silicon bend underneath the III-V mesa couples out some of the light. Unfortunately this technique doesn't allow us to make single mode lasers. So although this coupling mechanism has a lot of advantages like easy processing, this shortcoming makes it unsuitable for most applications.

When we want to integrate a laser on a full silicon platform, we have to take into account the back-end stack that contains the heaters and all metal. A trench is opened in this back-end so the laser can be printed close to the silicon waveguide circuits. For good heat-sinking, printing the laser directly onto the silicon substrate is a good idea. Then we need butt-coupling from the III-V into the silicon waveguide circuit. We explored three different techniques: an inverted taper, a big SiON waveguide and a trident-like structure. All show decent misalignment tolerance. However, in order to have a good coupling efficiency, it is important that both the III-V facet and the vertical facet of the etched well are smooth and clean. Up till now this structures were only compared in simulation. To get a better understanding, we also need to compare them in measurement.

Finally, we also researched coupling of light from III-V into silicon nitride waveguides. Due to the very low losses of silicon nitride waveguides, this is also a promising material platform. But the low refractive index of nitride prevents the use of a traditional spotsize converter. We proposed to use an amorphous silicon layer as an intermediate between the III-V and nitride. In simulation the coupling efficiency was promising, however the fabrication proved to be quite a challenge.

In the end there is no one coupling technology that fits all and depending on the application one or the other will be the better choice.

7.3 InAs/GaAs quantum dot DFB lasers on silicon

Based on the developments described above, we demonstrated the first single mode quantum dot DFB laser on a silicon substrate with efficient coupling of light to a silicon waveguide. We demonstrated high temperature operation with CW lasing up to 100°C. Threshold current densities as low as 205 A/cm^2 were measured. The laser showed single mode behavior with a side-mode suppression ratio of 47 dB. These devices are attractive candidates for uncooled WDM systems in data centers.

The low threshold current density proves the power of the quantum dot gain material. Especially since suboptimal III-V tapers caused residual reflections, extra losses and the existence of higher order modes. However, when we made the tapers narrower to improve them, many of them were taken out by defects in the III-V material. Improving the laser working will go hand in hand with improving the epitaxial material.

In the current mesa design higher order modes will always be present in the mesa, even if we do not see them because they cannot couple out. So further optimization is necessary. By playing both with the width of the mesa and the width of the silicon waveguide underneath, we should be able to avoid these higher order modes.

7.4 Mode-locked lasers integrated on silicon

In this work we designed, fabricated and characterized various types of mode-locked lasers as is shown in figure 7.1. A linear MLL realized in a colliding pulse configuration is shown in figure 7.1a. The structure of the laser comprises a saturable absorber (SA) section located in the middle of the resonator cavity between two semiconductor optical amplifier (SOA) sections. Two counter-propagating pulses circulate in the cavity and only interact in the saturable absorber. This leads to a doubling of the repetition frequency and thus a halving of the pulse period. Due to its geometry, this design is very sensitive to any mismatch in the saturable absorber position. When the symmetry is not perfect, the harmonic mode-locking can fail and tones at half the repetition frequency can appear. In figure 7.1b a ring mode-locked laser is depicted. Two pulses propagate in the ring cavity in opposite directions and collide in the SA. Since the two pulses couple to different output waveguides, the frequency is not doubled as is the case in linear colliding pulse configurations. This means that in the ring mode-locked laser no spurious tones appear when the SA is not placed exactly in the middle. Figure 7.1c shows a drawing of an anti-colliding pulse mode-locked laser. In this case the SA is placed next to the low reflectivity mirror. This leads to an increase in output power and a reduction in amplitude and timing jitter compared with the self-colliding pulse designs.

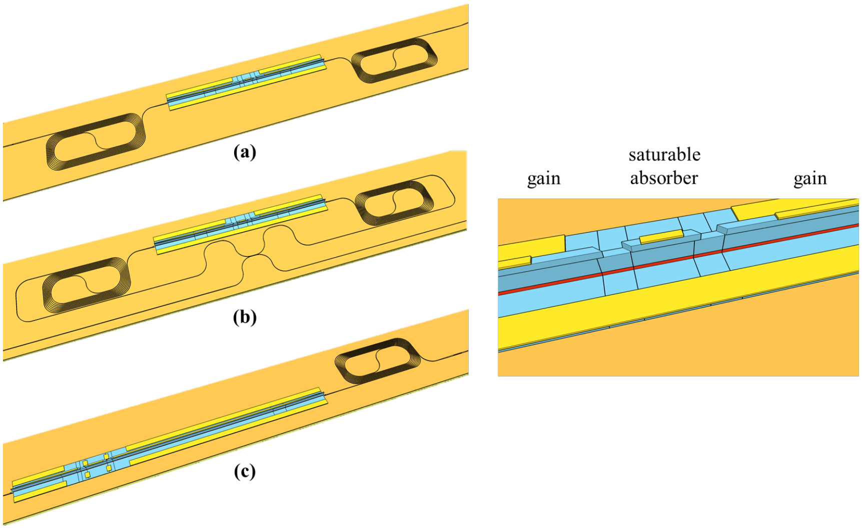

Figure 7.1: Illustration of (a) the linear cavity colliding pulse mode-locked laser, (b) the ring mode-locked laser and (c) the anti-colliding mode-locked laser.

Firstly we characterized 1550 nm InP quantum well mode-locked lasers of the different types. We showed a 4.7 GHz linear MLL with a 36 kHZ 10 dB RF line width and a 1.5 ps pulse, a 4.7 GHz ring MLL with a 49 kHZ 10 dB RF line width and a 4.83 GHz anti-colliding MLL with a 5 kHZ 10 dB RF line width and a 3 ps pulse. In order to meet the stringent requirements of terabits per second coherent communications in terms of line width and phase stability, we used hybrid mode-locking and injection locking techniques to improve the optical and electrical line width of the MLL. We demonstrated that under optical injection locking the 3 dB optical line width is reduced from a ~MHz line width to a 50 kHz line width. With a CW injection power as low as 0.1 mW, coherence between more than 50 mode-locked laser modes and the CW laser is experimentally confirmed.

Based on the InP quantum well lasers, we explored the potential of InAs/-GaAs QD mode-locked lasers integrated on a silicon photonics platform. We designed, fabricated and tested both linear colliding pulse MLLs and ring MLLs. Quantum-dot-based comb lasers were shown with both constellations. We showed a 18.8 GHz linear MLL with a 623 kHZ 3 dB RF line width and a 20.3 GHz ring

MLL with a 3 kHZ 3 dB RF line width. However, the optical 10 dB bandwidth was disappointingly small, around 3 nm for both structures and the cause for this is not fully understood at the moment. Since this is a first iteration, the different design parameters of the laser cavity are not yet optimized and more research is necessary.

List of Figures

List of Tables